An Investigation into the Design of the Helical Undulator for the International Linear Collider Positron Source

Thesis submitted in accordance with the requirements of
the University of Liverpool for the degree of Doctor in Philosophy

by

Duncan James Scott

February 2008

Accelerator Science and Technology Centre,
Science and Technology Facilities Council

and

The Cockcroft Institute of Accelerator Science,
Daresbury Science and Innovation Campus,
Warrington, WA4 4AD, UK

An Investigation into the Design of the Helical Undulator for the International Linear Collider Positron Source

Duncan James Scott

Abstract

Positrons are produced in the International Linear Collider via pair-production when multi-MeV photons are incident on a metallic conversion target. The multi-MeV photons are generated by the main electron beam, at an energy of 150 GeV, which passes through a ∼200 m long helical undulator magnet and generates synchrotron radiation. The circular polarisation of the helical undulator radiation can be used to create a polarised positron source. A derivation, from Maxwell's equations, of the radiation characteristics of a helical undulator is presented. After a comprehensive paper study of possible undulator designs the two pre-eminent ones were fabricated and tested. A super-conducting bifilar wires undulator was chosen instead of a permanent magnet design. This was because of its superior performance in terms of, magnetic field strength and quality, operational flexibility, risk of radiation damage, ease in achieving the required vacuum and cost. For a beam aperture of ∼5.85 mm and operational safety margin of ∼80% the period and strength of the undulator are 11.5 mm and 0.9 T, respectively. The magnetic field errors are shown to be acceptable for an unpolarised positron source. To meet the required vacuum level a series of photon collimators with a diameter of 4.4 mm are required. To mitigate impedance effects a smooth copper vessel with surface roughness ∼ 100 nm should be used. The impedance effects on the electron beam of the photon collimators and other tapered elements in the undulator line are also shown to be acceptable.

In Loving Memory of William Scott

Author's Contribution

The work described in this thesis has been undertaken as part of an international collaboration of scientists and engineers working on the International Linear Collider positron source for the past five years. The contribution of the author to the work presented here comprises of: general specification of the overall positron source design and layout (with the ILC positron source group); the design, testing and selection of helical undulators (with the scientists and engineers from the UK HeLiCal group); the analysis of magnetic field errors and their correction; calculations of the photon spectrum and synchrotron radiation power incident on the vessel walls (necessary for specifying the vacuum system, the vacuum science calculations were completed by Oleg Malyshev); specification of the photon collimators; calculations of the wakefields and their effects. In addition, the author was part of the SLAC Experiment-166 collaboration, which first demonstrated undulator-based polarised-positron production. The author was part of the shift team taking data during the experimental phase of the project.

Acknowledgement

First, and most importantly, thanks to my parents, Charles and Hilary, who have continually supported me throughout my life and instilled in me a life long love of learning. None of this would have been possible without them.

There are many other people who have helped me over the years I have been studying for this PhD and deserve mention. Jim Clarke, my line manager, who has supported me in this undertaking and always been helpful, encouraging and knowledgable. Mike Poole who, as director of ASTeC, allowed me to undertake this project and has supported me (financially and morally). John Dainton (who's always kept an interest in my work) and Tim Greenshaw (my supervisor and who read the manuscript) at Liverpool University for enabling this collaboration with Daresbury.

Members of the HeLiCal collaboration, especially, Simon Appleton, Ian Bailey, Elwyn Baynham, Tom Bradshaw, Amanda Brummitt, Steve Carr, Peter Cooke, Yuri Ivanushenkov, Leo Jenner, Oleg Malyshev, Gudi Moortgat-Pick and James Rochford.

All the people at ASTeC and the Cockcroft Institute who have helped me over the years, specifically, Dave Dunning, Dave Holder, Frank Jackson, James Jones, Roger Jones, Bruno Muratori, Hywel Owen, Ben Shepherd, Susan Smith, Neil Thompson and Naomi Wyles.

Members of the E-166 Collaboration, especially John Sheppard and Vinod Bharadwaj. Klaus Flöttmann and Nick Walker at DESY, who introduced us to the project and finally, the rest of the ILC positron source group.

Contents

Abstract **i**

Author's Contribution **iii**

Acknowledgement **iv**

Contents **xi**

List of Figures **xv**

List of Tables **xvii**

1 Introduction **1**

1.1 Open Questions from the Standard Model 2

1.2 Terascale Colliders 3

1.3 The Need for a *Linear* Collider 4

1.3.1 Synchrotron Radiation from Linear and Circular Accelerators 4

1.4 The International Linear Collider 6

1.4.1 The International Linear Collider Parameters 7

1.5 The International Linear Collider Positron Source 9

1.5.1 Layout of the Undulator Line 12

1.5.2 A Polarised Positron Source 14

1.5.3 Alternative Polarised Positron Source Designs 15

1.5.4 Experiment-166 16

1.6 Thesis Outline 17

2 Derivation of Synchrotron Radiation from an Undulator 18

2.1 Arbitrary Electron Motion 18

2.2 The Liénard-Wiechert Potentials 19

2.2.1 Maxwell's Equations 19

2.2.2 Scalar and Vector Potentials 20

2.2.3 Gauge Transformations 21

2.2.4 The Lorenz Gauge Condition 21

2.2.5 Green's Function Solution of the Wave Equation 22

2.2.6 Potentials for Moving Charges 23

2.2.7 Solution for the Scalar Potential 24

2.2.8 Solution for the Vector Potential 26

2.3 Calculating the Electric and Magnetic Fields 27

2.3.1 Differentiating the Equation for the Retarded Time 27

2.3.2 The Electric Field 27

2.3.3 The Magnetic Field 29

2.4 Radiated Power and Radiation Spectrum 30

2.4.1 The Poynting Vector and Energy Flow in the Far-Field 30

2.4.2 Radiated Energy Spectrum 31

2.4.3 Polarisation and the Stokes' Parameters 33

2.4.4 The Fourier Transform of the Acceleration Field 34

2.5 Electron Motion in an Undulator 36

2.6 Interference Effects in an Undulator 40

2.6.1 The Undulator Equation 40

2.6.2 Radiation Phase and the Line-Shape Function 41

2.7 Undulator Radiation 43

2.7.1 Expression for $\boldsymbol{n} \times [\boldsymbol{n} \times \boldsymbol{\beta}]$ 43

2.7.2 Expression for $\omega\left(t' - \frac{\boldsymbol{n}\cdot\boldsymbol{R}}{c}\right)$ 44

2.7.3 Substitution for Bessel Functions 45

2.7.4 On-Axis Radiation 47

2.8 Helical Undulator Radiation 48

2.8.1 Helical Undulator On-Axis Radiation and Polarisation 49

2.9 Example Figures 50

2.9.1 Numerical Codes for Synchrotron Radiation Calculations 53

2.10 The Photon Flux 54

2.11 Summary 55

3 Selection of the Optimum Undulator Magnet Technology 57

3.1 Pure Permanent Magnet Helical Undulators 58

3.1.1 Planar Helical Undulators 59

3.1.1.1 Planar Undulators 60

3.1.1.2 APPLE Undulator Designs 61

3.1.1.3 Multi-Mode Undulator Design 61

3.1.2 Permanent Magnet Ring Undulator 64

3.1.3 Choice of Permanent Magnet Undulator Design 66

3.2 Ten Period Permanent Magnet Ring Undulator Design 67

3.3 Permanent Magnet Ring Undulator Measurements 68

3.4 Super-Conducting Magnet Design 72

3.4.1 Super-Conducting Undulator Measurements 75

3.5 Photon Flux and Polarisation 77

3.6 Conclusions from the First Models 79

3.7 Further Super-Conducting Model Fabrication 81

3.7.1 International Linear Collider Reference Design Report Undulator Parameters 83

4 Achieving the Required Vacuum Pressure in the Undulator Vessel 84

4.1 The Fast Ion Instability and Vacuum Specification 84

4.2 Achieving the Required Vacuum Pressure 85

4.2.1 Incident Photon Spectra Calculation with SPECTRA 86

4.2.1.1 Verification of the SPECTRA Results 87

4.2.1.2 Dipole Radiation Approximation of the Undulator Radiation Spectrum 88

4.2.1.3 Total Number of Incident Photons 91

4.2.2 Photon Collimators 91

4.3 Conclusions and Further Work 92

5 Synchrotron Radiation Power Incident on the Vessel 94

5.1 Incident Synchrotron Radiation Power 94

5.1.1 Synchrotron Radiation Collimation 96

5.1.1.1 Collimator Alignment Errors 98

5.2 Conclusions and Further Work 99

6 Magnetic Field and Electron Trajectory Errors 101

6.1 Electron Trajectory Through the Undulator 101

6.1.1 Computer Modelled Field Errors of the Permanent Magnet Ring Undulator 102

6.1.2 Analytic Estimation of Off-Axis Field Deviation in the Super-Conducting Undulator 104

6.2 Estimation of the RMS Trajectory Error with Correction 104

6.2.1 Effect of an RMS Trajectory Error 105

6.3 Conclusions and Further Work 105

7 Resistive Wall Wakefields of the Vacuum Vessel **107**

7.1 Introduction to Wakefields 108

7.2 Resistive Wall Wakefields of an Infinitely Long Round Pipe 112

7.2.1 Models of Electrical Conductivity 112

7.2.1.1 DC Conductivity 112

7.2.1.2 AC Conductivity 114

7.2.1.3 The Anomalous Skin Effect 115

7.2.2 Longitudinal Resistive Wall Impedance for the Different Conductivity Models 118

7.2.2.1 DC Conductivity Impedance 118

7.2.2.2 AC Conductivity Impedance 118

7.2.2.3 Anomalous Skin Effect Impedance 119

7.2.3 Example Calculation 119

7.2.3.1 Longitudinal Resistive Wall Impedance 119

7.2.3.2 Longitudinal Wake Functions 119

7.2.3.3 Longitudinal Wake Potentials 121

7.2.4 Longitudinal Loss Factor, Energy Loss and Induced Energy Spread . 122

7.2.4.1 Average Energy Lost per Electron per Bunch 122

7.2.4.2 Induced Correlated Energy Spread 124

7.2.5 Transverse Resistive Wall Wake Potentials 126

7.2.6 Transverse Kick Factors 127

7.2.7 Emittance Growth due to Transverse Wakefields 127

7.3 Image Current Heating of the Vacuum Vessel 128

7.3.1 Surface Resistance in the Normal Conducting Regime 129

7.3.2 Residual Resistivity Ratio and Magneto-Resistance 129

7.3.3 Surface Resistance in the Anomalous Skin Effect Regime 129

7.3.4 Comparison with Energy Loss Due to Resistive Wall Wakefields . . . 130

7.3.5 Power Deposited in the Vessel Due to Image Current Heating 131

7.4 Conclusions and Further Work 132

8 Geometric Wakefields of the Vacuum Vessel 134

8.1 Surface Roughness Wakefields 134

8.1.1 Surface Roughness Wakefields Theory 134

8.1.2 Surface Roughness Specification 137

8.2 Wakefields of Tapered Elements in the Undulator Line 139

8.2.1 Electron Beam Properties 140

8.2.2 Geometry of the Tapered Sections 141

8.2.2.1 Photon Collimators 141

8.2.2.2 Undulator Transitions 141

8.2.3 Kick Factors 142

8.2.3.1 Photon Collimator Wakefield Kick Factors 143

8.2.3.2 Undulator Wakefield Kick Factors 143

8.2.3.3 Bunch Kick Factors 144

8.2.4 Emittance Growth 144

8.2.4.1 Emittance Growth with Perfectly Aligned Elements 144

8.2.4.2 Emittance Growth with Misaligned Elements 144

8.3 Conclusions and Further Work 146

9 Summary and Further Study 148

9.1 Summary 148

9.2 Further Study 150

A Electron Spin and the Stern-Gerlach Experiment 152

B Green's Function for the Time Dependent Wave Equation 154

C Derivation of the Panofsky-Wenzel Theorem **157**

Bibliography **160**

List of Figures

1.1 Schematic layout of the International Linear Collider 8

1.2 Electron-positron pair production 10

1.3 Undulator based positron production schematic 11

1.4 International Linear Collider Reference Design Report positron source components 13

1.5 Layout of an undulator cell 14

1.6 Electron motion through a helical undulator 15

1.7 Measured and expected positron polarisation from E-166 16

2.1 Definition of arbitrary electron motion and co-ordinate system 19

2.2 Periodic motion and the interference condition in an undulator 40

2.3 Co-ordinate system for electron motion in an undulator 44

2.4 Radiation intensity from helical undulators with varying K parameters . . . 51

2.5 Angular power distribution from helical undulators with varying K parameters 52

2.6 Intensity and circular polarisation rate from a $K = 1$ helical undulator into different angular acceptances 53

2.7 Photon number spectrum from a K=1 helical undulator 55

3.1 Two dimensional planar undulator field lines 61

3.2 APPLE-II and APPLE-III undulators 62

3.3 Transverse field vs phase in an APPLE-II undulator 62

3.4 Multi-mode undulator 62

3.5 Transverse field in a Multi-mode undulator vs phase 63

3.6 Optimisation of the Multi-mode undulator inner magnet block dimensions . 64

3.7 Example configuration of magnet blocks and magnetisation vectors for a permanent magnet dipole ring 64

3.8 Permanent Magnet Ring undulator blocks per ring optimisation. 65

3.9 Permanent Magnet Ring undulator magnetic forces 66

3.10 Permanent Magnet Ring undulator peak fields 67

3.11 Permanent Magnet Ring undulator assembly 68

3.12 Permanent Magnet Ring undulator photograph 69

3.13 Permanent Magnet Ring undulator magnetic fields 70

3.14 Permanent Magnet Ring undulator electron trajectory 70

3.15 Permanent Magnet Ring undulator wedge assembly 71

3.16 Permanent Magnet Ring undulator reverse fields 72

3.17 Field in cross-section of the super-conducting undulator wires 73

3.18 Super-conducting undulator conductor load lines 74

3.19 Super-conducting undulator winding 74

3.20 Super-conducting undulator photograph 75

3.21 Super-conducting undulator field measurements 76

3.22 Electron trajectory in the super-conducting undulator 76

3.23 Spectrum and polarisation from undulator models 78

3.24 Further super-conducting undulator models 82

3.25 Peak field of super-conducting models 82

4.1 Photon stimulated desorption yield vs ϵ_c 87

4.2 Total power incident on the vessel walls due to synchrotron radiation 88

4.3 ϵ_c of low energy dipole radiation 89

4.4 Example undulator spectrum calculated in SPECTRA and low and high ϵ_c DR approximations 90

4.5 Photon flux incident on the vessel walls 91

5.1 Synchrotron radiation power incident on the undulator vessel walls 95

5.2 Undulator half-cell used for incident synchrotron radiation power calculation 95

5.3 Collimated synchrotron radiation power downstream from a single undulator 96

5.4 Synchrotron radiation power incident on the undulator vessel walls with photon collimation 97

5.5 Peak synchrotron radiation power incident on the undulator vessel wall with photon collimation 98

5.6 Histograms of the synchrotron radiation power incident on the undulator vessel walls with photon collimation for 1 000 iterations 99

6.1 Uncorrected on and off-axis electron trajectory through a 1 m Permanent Magnet Ring undulator 103

6.2 Corrected on and off-axis electron trajectory through a 1 m Permanent Magnet Ring undulator 103

6.3 Relative transverse field strength in a bifilar wires helical undulator 105

6.4 Histograms of rms trajectory with and without correction 106

7.1 Co-ordinates for source and test charge in wakefield analysis 108

7.2 Electric field lines for $\cos(n\theta)$ charge rings 111

7.3 Ratio of anomalous skin effect to classical resistance and reactance at 273 K and 77 K 117

7.4 Impedance of a 2 mm copper pipe at 273 K and 77 K 120

7.5 Wake functions of a 2 mm copper pipe at 273 K and 77 K 121

7.6 Gaussian and trapezium charge distributions 121

7.7 Gaussian and trapezium wake potentials of a copper pipe at 273 K and 77 K 123

7.8 Average energy lost due to resistive wall wakefields in a steel vessel 124

7.9 Induced energy spread vs vessel radius due to resistive wall wakefields . . . 125

7.10 Peak increase in energy spread due to resistive wall wakefields 125

7.11 Comparison of methods for calculating the transverse wake potential 126

7.12 Transverse kick factors 127

7.13 Peak transverse kick factors 128

7.14 Image current heating and resistive wall wakefields energy lost comparison . 130

7.15 Image current heating of a copper vessel 132

8.1 Example surface roughness bump shapes 135

8.2 Induced energy spread for increasing surface bump size 138

8.3 Bump size and vessel radius required to induce an energy spread of 0.5 $\times 10^{-4}$ 138

8.4 Undulator half-cell β-functions 140

8.5 Electron beam size through the undulator cell 141

8.6 Undulator tapered section layout 142

8.7 Photon collimator geometric kick factors 143

8.8 Histogram of increase in ϵ_y for 10 000 random undulator lines 145

8.9 Mean growth in ϵ_x and ϵ_y 145

A.1 Schematic of the Stern-Gerlach experiment 153

List of Tables

1.1 Main International Linear Collider baseline beam parameters 9

1.2 Positron flux achieved at the Stanford Linear Collider and the required positron flux for the International Linear Collider 9

3.1 International Linear Collider Baseline Configuration Document undulator parameters 58

3.2 Example Multi-mode undulator dimensions 63

3.3 Permanent Magnet Ring undulator field measurements 69

3.4 Super-conducting undulator field measurement data 75

3.5 International Linear Collider beam parameters used for flux and polarisation calculation 77

3.6 Spectrum and polarisation data from undulator models 79

3.7 International Linear Collider Reference Design Report undulator parameters 83

4.1 Undulator and electron beam parameters used to calculate the photon spectrum incident on the vessel walls 87

4.2 Required distance between collimators to obtain acceptable gas density inside the undulator vacuum vessel 92

5.1 Undulator parameters for incident synchrotron radiation calculation 95

7.1 σ_{DC}, τ and λ for different materials 114

7.2 Γ for 2 mm radius vessels 115

7.3 Skin depth for different materials with different bunch lengths 115

7.4 Λ for different materials 117

7.5 Power deposited per metre in a 5.85 mm diameter copper vessel due to image current heating 131

8.1 Form factors for the different shaped bumps in Figure 8.1 136

8.2 Parameters for the surface roughness calculation 137

8.3 Taper dimensions for the unshielded bellows layout 142

8.4 K_b for the photon collimators and undulator 144

9.1 Power heating an undulator module due to image currents and synchrotron radiation 149

Chapter 1

Introduction

For over 100 years physicists have been accelerating particles to higher and higher energies to study the fundamental constituents of matter and how they interact with one another. The role of accelerator physicists is to create and accelerate particle beams with the desired properties and deliver them to an interaction point (IP) where they collide. At the IP, complicated particle detectors monitor the products of the collisions. The data are analysed, and, using theoretical considerations and other experimental results,[1] a physical model of fundamental particles and their interactions can be developed.

This discipline has come to be known as high energy particle physics, and by the late 20th century a theory which provided a self consistent description of the results of many experiments had been developed. This is known as the '*Standard Model*' of particle physics. In developing the Standard Model there have been two main types of particle collider that have been used, those that collide protons with anti-protons and those that collide electrons with positrons.[2]

For reasons that will be explained,[3] despite its larger mass, it is easier to accelerate protons in a circular motion than electrons. However, due to the composite nature of protons, (they have an internal structure comprising of quarks and gluons), the interactions involving them are significantly more complicated to interpret than collisions involving electrons. This is because a typical proton interaction involves only one of the constituent particles from each proton colliding together at a lower centre-of-mass energy than the

[1] E.g. astrophysics and cosmic ray experiments.

[2] In general the distinction between protons and anti-protons and electrons and positrons will not be made explicit.

[3] See section 1.3.1.

proton-proton centre-of-mass energy total. These interactions are almost always accompanied by debris from the remaining parts of the protons, making the interpretation of the interaction more difficult. In contrast to the proton, all experimental evidence indicates that electrons are fundamental particles with no internal structure. This makes interpreting electron-electron interactions easier. In general, proton colliders push the energy frontiers of particle physics and electron colliders make the precision measurements.

1.1 Open Questions from the Standard Model

Although the Standard Model has had great success in explaining experimental results, it is not a complete theory of fundamental physics: a number of questions remain unanswered. The detailed physics arguments are beyond the scope of this thesis, however a good overview of the main open questions in particle physics can be found in [1, 2]. It is still worthwhile highlighting a few outstanding questions from [1, 2].

Does the Higgs boson exist and if so what are its characteristics?

Present day experiments suggest that there is a new type of matter, the Higgs boson, that gives particles their mass. This particle is associated with the Higgs field that permeates the entire universe and conveys mass to matter. Although predicted by the Standard Model it is yet to be experimentally observed. It is also possible that the Higgs boson does not exist; if that is so then some alternative explanation for the origin of mass would need to be considered.

What is dark matter and can it be created in the laboratory?

Recent discoveries have indicated that only $\sim$4% of the universe is made of ordinary matter, the rest is made of unknown dark matter ($\sim$23%) and dark energy ($\sim$73%). Definitive evidence for dark matter has come from many sources. For example, observations of galaxies (including our own Milky Way) show that the gravitational attraction of the visible matter is not strong enough to keep the stars in their observed orbits. Therefore it is postulated that the gravitational effects of dark matter are holding these galaxies together. The exact nature of the dark matter is not known and so one of the challenges is to create it in the laboratory and study its nature.

One of the main dark matter candidates involves a possible new symmetry of nature, supersymmetry, (or SUSY). SUSY is a symmetry that relates elementary particles of one spin to another particle that differs by half a unit of spin and are known as superpartners, (or sparticles). Therefore, in a supersymmetric theory, for every type of boson there exists a corresponding type of fermion, and vice-versa. Exact unbroken supersymmetry would predict that a particle and its superpartners would have the same mass. No superpartners of the Standard Model particles have yet been found, implying that SUSY is not an exact, unbroken symmetry of nature and that the mass of a sparticle is greater than its particle superpartner. If a superpartner is found its mass would determine the scale at which SUSY is broken. There are many introductions to SUSY [3, 4].

One of the ways of answering these questions is to build new accelerators that can reach higher energies. It is anticipated that the energy required to make new discoveries is of the order of a tera electron volts (TeV). This is the energy an electron would gain if it passed through a potential difference of a million-million volts and is colloquially known as the terascale.

1.2 Terascale Colliders

There are a number of planned accelerators that will operate at the terascale. The Large Hadron Collider (LHC) is a 14 TeV proton collider under construction by the European Organization for Nuclear Research (CERN). It is expected that the LHC will make new and important discoveries, such as discovering the Higgs boson.[4] As well as a proton collider an electron collider is required to make precision measurements.

Currently there are two proposed terascale electron colliders. These are not yet funded projects, they are the subject of a large amount of worldwide research and development. They are the International Linear Collider (ILC) and the Compact Linear Collider (CLIC). Of these two proposals, the most mature is the ILC, but CLIC has the greatest energy reach. The ILC has two main stages, the first at a centre-of-mass energy of 0.5 TeV and the second at 1 TeV. The CLIC proposal has an approximate energy range of 0.5 to 3 TeV. A design study from the year 2000 for CLIC can be found in [5] and a general overview of the ILC and the potential for discovering new physics can be found in [2].

[4] Even if it does not make the anticipated discoveries, that in itself would be a significant discovery!

1.3 The Need for a *Linear* Collider

Both proposals for electron colliders are *linear* accelerators. In a linear accelerator (linac) particles are accelerated in a straight line. In a circular accelerator particles move in approximately a circle. Typically, the particles are bent into a circular orbit by magnetic fields. The advantage of circular accelerators over linacs is that as the particles can transit indefinitely they can pass the accelerating stage of the machine many times, gaining energy in each pass. It would therefore seem that a circular accelerator can be smaller than a linear accelerator of comparable power and so be generally cheaper, as a linac would have to be extremely long to accelerate a particle to the equivalent energy attainable by a circular accelerator. However, there is a technical limit that is reached with circular accelerators that makes them impractical to operate above a certain energy. This is to due to the emission of synchrotron radiation (SR), as first noted by M. Tigner in 1965 [6].

1.3.1 Synchrotron Radiation from Linear and Circular Accelerators

When charged particles are accelerated, they radiate electro-magnetic energy at a rate proportional to the square of the accelerating force and to the angle between the force and the particle's velocity. In the laboratory frame of reference, the power P radiated by a relativistic particle is [7]:

$$P = \frac{2}{3}\, r_c\, m\, c\, \gamma^6 [\dot{\boldsymbol{\beta}}^2 - (\boldsymbol{\beta} \times \dot{\boldsymbol{\beta}})^2], \tag{1.1}$$

where r_c is the classical radius of the particle, m is its mass, c is the speed of light, γ is the ratio of the particle's total energy to its rest mass energy, $\boldsymbol{\beta} = \frac{\boldsymbol{v}}{c}$ is the ratio of the particle's velocity to the speed of light and $\dot{\boldsymbol{\beta}}$ is the derivative of $\boldsymbol{\beta}$ w.r.t. time. The radiation power is dependent on the particle's trajectory through the quantities $\boldsymbol{\beta}$ and $\dot{\boldsymbol{\beta}}$. Decomposing the acceleration into parts parallel, $\dot{\beta}_{\parallel}$, and perpendicular, $\dot{\boldsymbol{\beta}}_{\perp}$, to $\boldsymbol{\beta}$ gives:

$$\dot{\boldsymbol{\beta}} = \dot{\beta}_{\parallel} + \dot{\boldsymbol{\beta}}_{\perp}. \tag{1.2}$$

By substituting Equation 1.2 into Equation 1.1, the total radiated power can be decomposed into contributions from parallel and perpendicular acceleration, ($P_{\parallel}$ and $P_{\perp}$ respectively):

$$P_{\parallel} = \frac{2}{3}\, r_c\, m\, c\, \gamma^6 \dot{\beta}_{\parallel}^2 \tag{1.3}$$

and

$$P_\perp = \frac{2}{3}\, r_c\, m\, c\, \gamma^4 \dot{\boldsymbol{\beta}}_\perp{}^2. \tag{1.4}$$

Equations 1.3 and 1.4 are similar except for a factor of γ^2. Parallel acceleration is related to the accelerating force by:

$$m\dot{v}_\parallel = \gamma^{-3}\frac{\mathrm{d}p_\parallel}{\mathrm{d}t},$$

where $\dot{v}_\parallel$ and $p_\parallel$ are the particle's longitudinal acceleration and longitudinal momentum, respectively. By substituting this expression into Equation 1.3, the total radiated power from linear acceleration becomes:

$$P_\parallel = \frac{2}{3}\frac{r_c}{m\, c}\left(\frac{\mathrm{d}p_\parallel}{\mathrm{d}t}\right)^2. \tag{1.5}$$

The SR power is independent of the particle's energy and depends only on the accelerating force.

For perpendicular acceleration the characteristics of the radiated power are very different. Dipole magnetic fields can be used to transversely deflect particles in circular machines. Assuming that the particle's velocity is orthogonal to the field, a pure dipole magnetic field deflects a charged particle of charge q into a circular path with bending radius, ρ, given by [8]:

$$\frac{1}{\rho} = \frac{c\, q\, B}{\beta E}, \tag{1.6}$$

where E is the particle's energy, B is the magnitude of the dipole field and β is the magnitude of $\boldsymbol{\beta}$. The transverse acceleration, $\dot{\boldsymbol{v}}_\perp$, is caused by the Lorentz force, and when there is no electric field present this gives:

$$\begin{aligned} \frac{\mathrm{d}\boldsymbol{p}_\perp}{\mathrm{d}t} &= \gamma m \dot{\boldsymbol{v}}_\perp \\ &= q(\boldsymbol{v}\times\boldsymbol{B}), \end{aligned} \tag{1.7}$$

where $\boldsymbol{B}$ is the magnetic field. Inserting this into Equation 1.4 and combining it with Equation 1.6 gives:

$$\begin{aligned} P_\perp &= \frac{2}{3}\frac{r_c}{mc}\gamma^2\frac{\mathrm{d}\boldsymbol{p}_\perp}{\mathrm{d}t}^2 \\ &= \frac{2 r_e m c^3 \beta^4 \gamma^4}{\rho^2}. \end{aligned} \tag{1.8}$$

From Equations 1.5 and 1.8, it can be seen that equal accelerating forces lead to higher SR power by a factor of γ^2 when the acceleration is perpendicular compared to parallel to the motion.

The SR power increases very fast for high energy particles and provides the most severe limitation on the maximum achievable energy of a circular accelerator. To reduce the SR power, smaller magnetic fields must be used which increases the radius of curvature of the machine, increasing its total circumference and therefore its total cost. The largest circular electron accelerator so far constructed was the Large Electron-Positron (LEP) Collider, built at CERN. For an electron energy of 50 GeV and given the circumference of 27 km, the total SR power was 1.4×10^{-7} watts per electron or approximately 80 MeV per electron per turn. To maintain the energy of the beam this energy loss must be replaced each turn.[5] To overcome these problems and to reach higher energies the consensus of opinion is that a future electron-positron collider must be a linear machine.

1.4 The International Linear Collider

The ILC is a proposed new 500 GeV centre-of-mass[6] electron-positron linear collider. It relies on super-conducting (SC) radio frequency (RF) technology to provide the main acceleration of the beams. For the 500 GeV machine, the nominal accelerating gradient of the RF cavities is 31.5 MV/m. Approximately 15 km of accelerating structures are required for each linac to be able to accelerate the particles to 250 GeV. A schematic layout is shown in Figure 1.1 and described below.

The ILC comprises of an electron source and injector that creates and accelerates electron bunches up to an energy of ∼5 GeV. These are then injected into the electron damping ring, (the central blue ellipse in Figure 1.1), where their phase space volume is damped. After extraction from the damping ring, the beam is transported to the start of the main electron linac. In the main linac the beam is accelerated to 250 GeV. At the 150 GeV point of the linac, there is an undulator insertion for positron production. The undulator is 100s of meters long. After the undulator and a further 100 GeV of acceleration the electrons pass through the beam delivery system (BDS), where they are collimated and

[5] Due to their much heavier mass, the SR power from protons is smaller to that from electrons by the fourth power of the mass ratio, approximately $1836^4 = 1.14 \times 10^{13}$, which explains why protons are easier to accelerate in circular machines. Despite this huge difference, substantial SR is expected from the 7 TeV proton beams in the LHC.

[6] Which can be upgraded to 1 TeV.

focussed to a small spot at the interaction point (IP).

When passing through the undulator, the electrons generate SR. This SR is in the gamma ray regime and is incident on a metallic conversion target. Electron-positron pairs are produced in the target and the positrons are then captured and accelerated to 5 GeV. The positrons are then transported to the positron damping ring. After damping in the positron damping ring, (central green ellipse in Figure 1.1), they are transported to the start of the positron main linac where they are accelerated to 250 GeV, through a positron BDS and to the IP where they collide with an electron bunch. As the positrons are created by an electron bunch passing through the undulator the two linacs are coupled: this places constraints on the geometry of the machine to ensure that the arrival of the positron bunch coincides with an electron bunch at the IP [9, 10].

As the ILC is currently being designed, the parameters are not fixed. However, for a number of years a range of likely parameters has been assumed and used in the research and development of the machine.

1.4.1 The International Linear Collider Parameters

The main ILC parameters are given in Table 1.1 and are taken from the ILC Baseline Configuration Document (ILC-BCD) [11][7] for three different proposed configurations. For the ILC, it was decided to have an operating range of parameters instead of the usual single operating point. In the past a collider project, in most cases, used to provide a unique set of parameters which were tuned to give the highest luminosity. In actual machine operations, however, unexpected or underestimated difficulties require the adoption of operating conditions different from those assumed in the initial design. It is desirable to provide for such changes in the initial design. Since these changes are not very predictable, an operating plane is defined, rather than an operating point. Accepting a wide range of parameters may introduce challenges in the machine design, but the resulting operational flexibility more than justifies the additional design effort required. If the machine, as built, works for a wide range of parameters within the operating plane, then it should be easier to reach the design luminosity.

[7] Correct as of Sept 1st 2006. Since this time the configurations have slightly changed, but not to an extent that significantly affects the conclusions in this thesis.

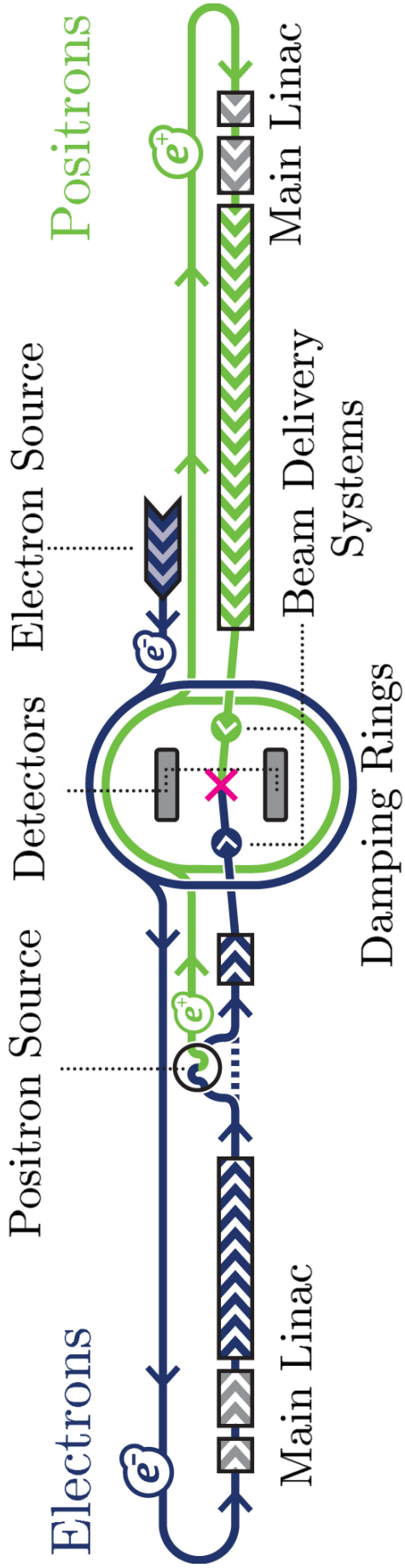

Figure 1.1: Schematic layout of the ILC showing the geometry and main subsystems.

Table 1.1: Main ILC baseline beam parameters.

			Configuration		
Parameter	Symbol	Unit	1	2	3
Bunch Charge	N	10^{10}	1	2	2
Number of bunches	n_b		1330	2820	5640
Linac bunch interval	t_b	ns	154	308	461
Bunch length at IP	σ_z	μm	150	300	500
Vertical Emittance at IP	$\gamma\epsilon_y$	mm mrad	0.03	0.04	0.08
Repetition Frequency		Hz	5	5	5

1.5 The International Linear Collider Positron Source

One of the main challenges facing future electron colliders is producing sufficient quantities of positrons to achieve the desired number of collisions at the IP. The ILC requires a positron intensity a factor of ∼60 greater than the most intense sources currently available, for example the one used for the Stanford Linear Collider (SLC) at the Stanford Linear Accelerator Centre (SLAC) [12]. The positron flux achieved at the SLC and that required for the ILC is given in Table 1.2.

Table 1.2: Positron flux achieved at the SLC and the required positron flux for the ILC.

	Positron Flux ($e^+\ s^{-1}$)
SLC	$\sim 5 \times 10^{12}$
ILC	$\sim 3 \times 10^{14}$

In an SLC-type (conventional) positron source a multi-GeV electron beam is incident on a thick rotating metal target and produces bremsstrahlung photons. These photons, via a process known as '*pair production*,' illustrated in Figure 1.2, create electron-positron pairs. The positrons exiting the back-face of the target are captured. To extend this technology for the ILC a more intense electron drive beam is required and this results in too much power deposited in the target and downstream elements [13], leading to thermal and radiation damage. Therefore this type of source is deemed to be unfeasible for the ILC [14]. In the ILC-BCD design the photons are generated upstream of the target in a magnetic device called a helical undulator via SR [11], instead of in the target via bremsstrahlung. This means that a thinner target can be used and there is less scattering of secondary particles [15]. Consequently, the amount of power deposited in the target and downstream elements is significantly less than for a conventional positron source of equivalent intensity, and the ILC requirements can be met.

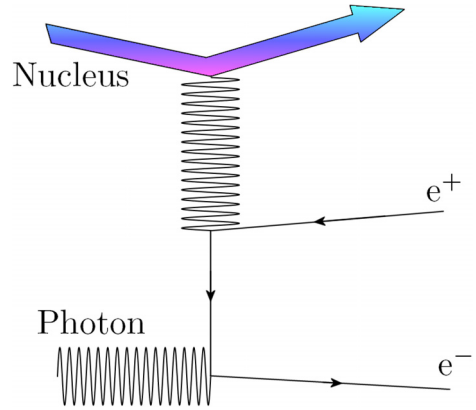

Figure 1.2: Schematic of the pair production process. A high-energy photon interacts with the field from an atomic nucleus producing an electron-positron pair.

The incident photons must have enough energy to be able to create the total mass of the electron-positron pair, that is its energy must be ≥1.022 MeV. Any remaining energy from the initial photon transfers into the kinetic energy of the pair, but is not necessarily equally distributed between the particles. The probability of a photon producing an electron-positron pair in the target is not 100% and so many more photons must impinge on the target than the required number of positrons. Approximately 90% of the incident photons are transmitted through the target [16]. This means that a multiple target system can be considered, but has generally been disregarded due to the increased operational difficulty and cost.[8]

Photons in the MeV energy range are difficult to produce in a controlled manner. For the ILC, the photons are created when the main electron beam, at an energy of 150 GeV, passes through a periodic magnetic device called a helical undulator. This device creates an on-axis helical magnetic field with period λ_u, typically of the order of tens of millimeters. Electrons passing through this field are accelerated and describe a helical trajectory. When any charged particle is accelerated it emits electromagnetic radiation. If the acceleration is due to a magnetic field and the electron is relativistic then the radiation is known as synchrotron radiation (SR). The wavelength of the radiation from the undulator is proportional to the electron energy, λ_u and the strength of the magnetic field. Qualitatively, the periodic motion of the electrons with a ∼cm wavelength in the laboratory frame results in gamma-ray wavelength radiation because λ_u is Lorentz contracted by a factor of γ and there is also a relativistic doppler shift, giving another factor of $\sim 2\gamma$. For 150 GeV

[8] A significant portion of the cost of the positron source for the ILC is the civil engineering required for the target hall area and remote handling of the target and capture optics due to the high radiation levels.

electrons $\gamma \simeq 2.9 \times 10^5$ and therefore the cm period of the magnetic field results in ∼MeV energy photons. A general layout of the scheme is shown in Figure 1.3. A source of this kind was first described in 1977 [17] and adopted and studied further for the TESLA[9] collider project [15, 18, 19].

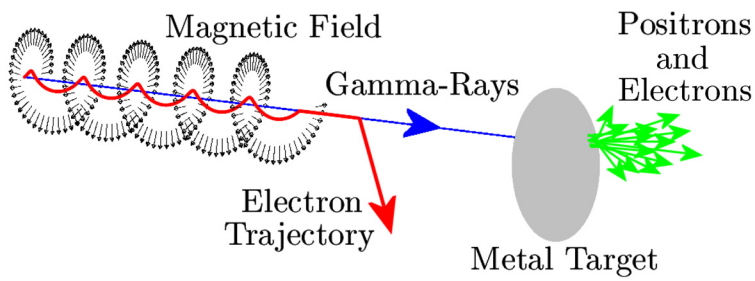

Figure 1.3: Schematic of the undulator based positron production process. A high energy electron beam (red line) passes through a helical magnetic field (black arrows) generating gamma-rays (blue line). The gamma-rays are incident on a metal target and electron-positron pairs are created. The positrons (green arrows) are then captured and accelerated.

The ILC Reference Design Report [20][10] (ILC-RDR) positron production scheme is shown in Figure 1.4. The photon beam is produced by passing the main electron linac beam through an undulator ∼200 m long. The electron beam loses ∼3 GeV in this process. The photon beam is then transported ∼500 meters to the positron source target hall where it is incident on a ∼0.4 radiation length thick Ti-alloy target producing showers of electrons and positrons. The resulting beam is captured using an optical matching device (OMD) and normal conducting (NC) RF linac with solenoidal focusing and accelerated to 125 MeV. The electrons and remaining photons are separated from the positrons and dumped. The positrons are accelerated to 400 MeV in a NC linac with solenoidal focusing. They are transported ∼5 km to the central damping ring complex, where they are boosted to 5 GeV in a linac using SC RF and injected into the positron damping ring. The positron source system also includes a *keep-alive source* to generate a low intensity positron beam that can be injected into the SC linac. This allows various beam feedback-systems to remain active if the main electron beam, and hence the undulator-based positron beam, is lost. ILC availability studies show that the keep-alive source makes an improvement in accelerator uptime and delivered luminosity by as much as 7% [20]. The keep alive source is a conventional positron source using a 500 MeV electron drive beam impinging on a tungsten-rhenium target to produce positrons which are then captured and accelerated to 400 MeV similar

[9] TeV-Energy Super-conducting Linear Accelerator.
[10] An update of the ILC-BCD published in 2007.

to the main positron source. The intensity of the keep-alive source is approximately 10% of the main source.

The specification of the conversion target is a significant research topic with many technical issues that need to be addressed. Many of these technicalities are coupled to the design and performance of the helical undulator and downstream capture optics and so deciding exact specifications is complicated. One of the issues that is directly related to the helical undulator performance is the optimum photon spot size on the target. Studies have shown that decreasing the spot size on the target increases the positron capture efficiency [15]; however, this increases the power density incident on the target. The spot size on the target is determined by the distance between the undulator and target, the natural opening angle of SR generated in the undulator and the trajectory of the electron beam through the undulator. These issues are discussed further in Chapter 6.

The electron beam will have a polarisation of ∼80% [20]. When passing through the undulator, the beam will emit SR photons stochastically and this random effect could de-polarise the beam. It has been shown analytically that for a high energy electron beam and for an undulator where $K \leq 1$ there are no significant electron de-polarisation effects [21]. As yet no computer simulations of the de-polarising effects of the undulator have been made, this is because existing codes do not currently model the helical undulator magnetic field.

1.5.1 Layout of the Undulator Line

In the ILC-RDR design, the undulator is in a chicane whose axis is 2.5 m off the main linac axis to give adequate space between the undulator photon beam and the linac for the conversion target and capture optics. The undulator line is comprised of FODO cells with undulator modules between the quadrupoles. The need for quadrupoles to focus the beam through the undulator is not well established and they could contribute to an emittance growth of the electron beam. In the present layout, which is developed throughout this thesis, there are three undulator modules between each quadrupole and in the space between undulator modules there are photon collimators. A schematic cell layout is shown in Figure 1.5. For each cell there is ∼12 m of active undulator for a cell length of ∼15 m. The length of undulator, and hence the number of cells required, is determined by many factors, such as the performance of the undulator, conversion target and downstream capture optics. It is expected that a few hundred meters of active undulator will be required.

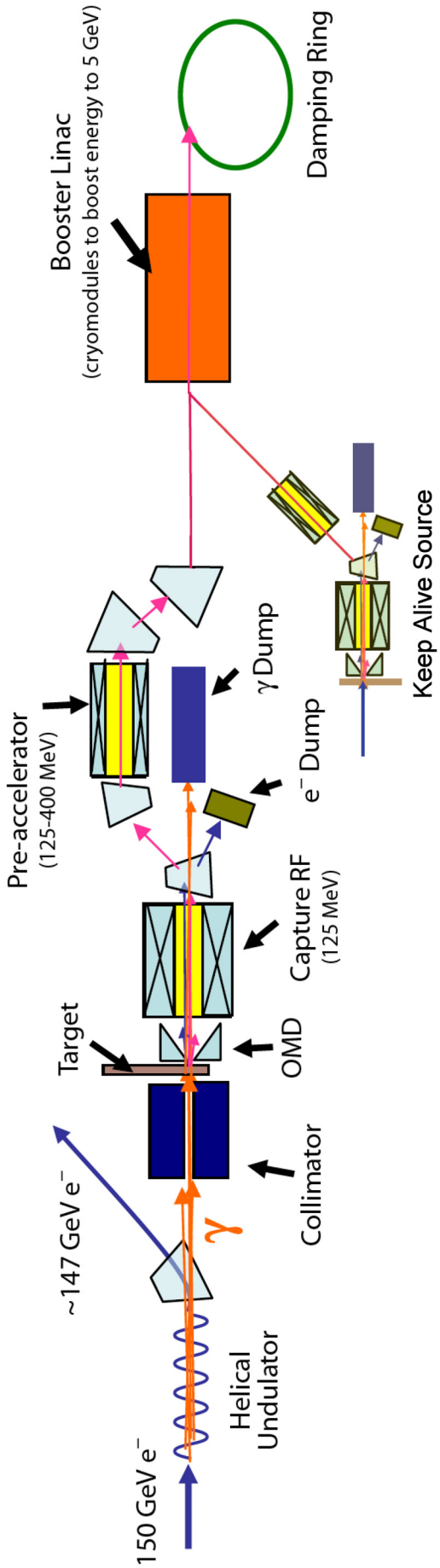

Figure 1.4: Layout of the ILC-RDR Positron Source.

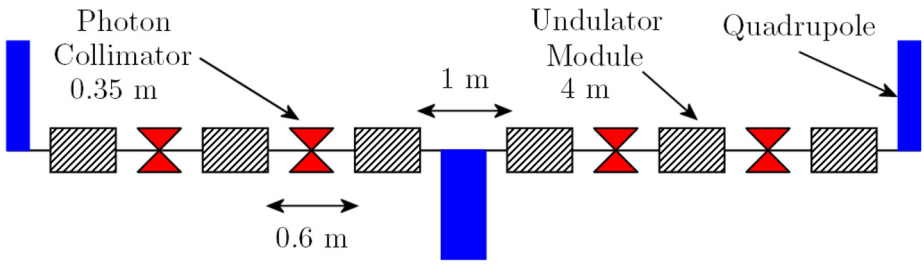

Figure 1.5: Schematic layout of an undulator cell.

1.5.2 A Polarised Positron Source

As well as being able to produce the required number of positrons a helical undulator based source with its associated target can also produce a polarised positron beam. The polarisation of a beam is related to the intrinsic spin of the beam particles. Spin is a quantum mechanical property of matter that was discovered in experiments such as those performed by Stern and Gerlach in the 1920's.[11] The polarisation, P, of a particle beam in a particular direction is defined as [15]:

$$P = \frac{N^+ - N^-}{N^+ + N^-},$$

where N^+ and N^- denote the number of particles with their spin parallel and antiparallel to that direction, respectively. A positron source that is spin-polarised in the longitudinal direction can be achieved as a natural consequence of using a helical undulator to produce the photons. If viewed end-on, electrons travelling in a helical orbit describe a circle and the radiation they emit is therefore circularly polarised. If viewed at a slight angle, the electron trajectory is an ellipse and emitted radiation is elliptically polarised, as shown in Figure 1.6.

In the pair production process, the circular polarisation of the photon is transferred to the longitudinal polarisation of the particle with the highest energy. The particle with the lower energy has a polarisation of opposite sign [22, 23, 24]. This means that by using circularly polarised photons, and then energy selection of the resultant positrons, a longitudinally polarised positron beam can be created.

Initially the ILC will have an unpolarised positron source that will use all of the

[11] For an introduction to electron spin see Appendix A.

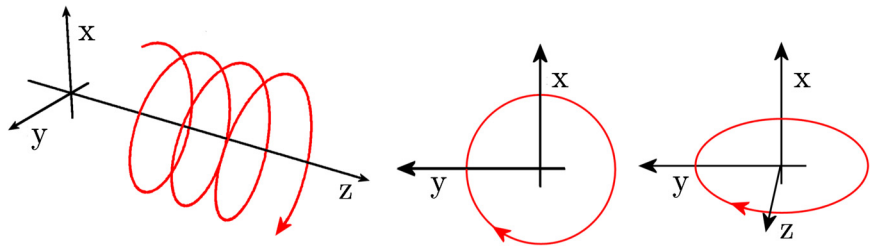

Figure 1.6: A helical trajectory in the z direction, viewed from the side (left), the negative z direction (centre) where the trajectory can be seen to describe a circle and in the negative direction from above (right) where the trajectory can be seen to describe an ellipse.

photons from the helical undulator (circularly and non-circularly polarised).[12] The source will then be upgraded to provide polarised positrons, which can be achieved by collimating non-circularly polarised photons. To maintain positron intensity the collimated gamma-rays need to be replaced by increasing the length of the undulator, thus providing more initial photons. The physics case for a polarised positron beam at the ILC has been made in references [27, 28]. As well as new physics, a polarised positron beam has the advantage of reducing the number of uncertainties in the interactions therefore reducing the systematic errors in the experiment.

1.5.3 Alternative Polarised Positron Source Designs

Conventional sources, such as the one used at the SLC, cannot produce polarised positrons and are not suitable for the ILC. However, there are positron source designs alternative to the conventional and undulator-based source that can produce polarised positrons and could work for the ILC. These alternative schemes differ in their exact detail but all rely on inverse Compton scattering of laser light off an electron beam. If the laser light is circularly polarised then a polarised positron beam can be created [29, 30]. Undulator radiation can be thought of as Compton backscattering of the virtual photons of the undulator, and hence the photon spectrum and the polarisation characteristics of Compton backscattered laser photons are very similar to those of undulator radiation. The requirements for the laser system to implement positron production are extremely demanding, so the use of the electron beam plus undulator offers significant technical advantages compared to Compton backscattering of real photons. The advantage of laser-based sources is that the positrons can be created independently of the main electron linac.

[12] Estimates suggest that the baseline source will provide ∼30% polarisation of the positron beam [25]. If need be, there are a number of techniques which can reduce this polarisation to zero, for example the use of RF deflectors in the damping rings [26].

1.5.4 Experiment-166

Recently a proof of principle experiment, Experiment-166 [31], demonstrating polarised positron production using a helical undulator has been completed at SLAC. A ∼50 GeV electron beam was passed through a 1 m long helical undulator, generating circularly-polarised gamma-rays. These were then incident on a metal target, producing electron positron pairs. The positrons were captured, focussed and then passed through an energy spectrometer to select a particular energy. The polarisation of the positrons was measured using a polarimeter. In this device, the positrons annihilate[13] to form polarised photons which then pass through a block of magnetised iron. The intensity of the transmitted photons is measured in downstream CsI crystals. The attenuation of the intensity of the photons in the iron depends on their polarisation and the direction of the magnetic field in the iron. By reversing the polarity of the magnetic field and measuring the asymmetry in the intensity of the transmitted photons, the degree of polarisation of the positrons can be inferred. The results of Experiment-166 indicate that polarised positrons have been created and detected [32, 33]. Figure 1.7 shows the polarisation of different energy positron and electron beams from the experiment.

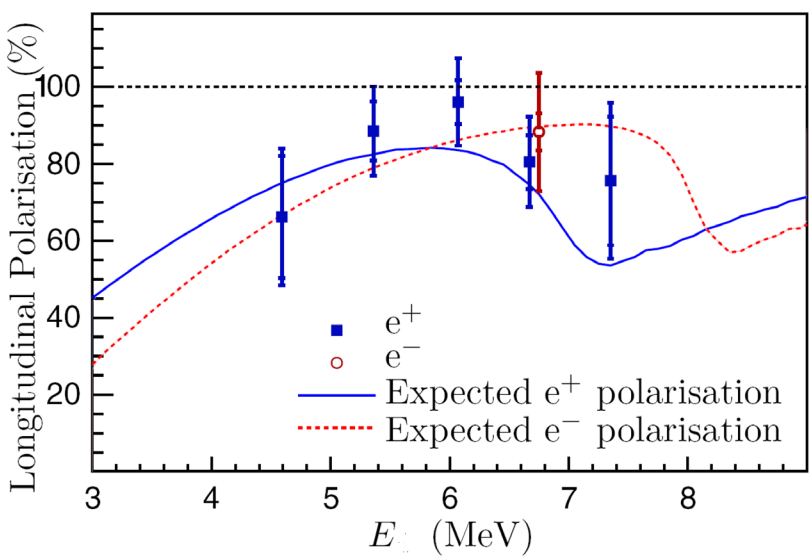

Figure 1.7: Longitudinal polarisation vs energy, E, of positrons and electrons as determined from the asymmetries observed in the CsI crystal. Also shown are predictions by a Geant4 [34, 35] simulation of the experiment.

[13] Via a process similar to pair production.

1.6 Thesis Outline

The main subject of this thesis is the design of the helical undulator magnet required to produce the photons for positron production and its effects on the electron beam.

In Chapter 2 there is a detailed derivation of synchrotron radiation from an undulator, starting from Maxwell's equations.

Chapter 3 describes a paper study into possible undulator designs and the fabrication and testing of the two most promising designs, from which the optimum is selected. The undulator parameters chosen for the ILC-RDR, which were based on further prototyping, are given.

To keep the photon stimulated desorption rates acceptable for the vacuum specification photon collimators are required. These are also needed to mask upstream undulator modules from synchrotron radiation that would otherwise cause excessive heating of the modules. In Chapter 4 the vacuum requirements are discussed and the synchrotron radiation heating is discussed in Chapter 5.

The magnitude of magnetic field errors on the electron beam trajectory and trajectory correction are discussed in Chapter 6. It is important to understand these errors to ensure that the electron beam can be transmitted through the undulator. The electron beam trajectory also has a direct effect on the photon-beam spot-size on the conversion target, this couples to the positron capture efficiency and so is important to understand.

As well as the magnetic design of the undulator the effects of the magnet on the electron beam also needs to be considered. As the high quality electron beam of the ILC is used to generate the photons before it reaches the IP, any possible deleterious effects on its quality must be understood and mitigated. One of the main areas of possible beam degradation is due to the impedance of the undulator line, this is discussed in Chapters 7 and 8.

Finally, Chapter 9 summarises the conclusions reached and highlights areas for further study.

In general, unless otherwise stated, all the calculations have been performed using Mathematica [36].

Chapter 2

Derivation of Synchrotron Radiation from an Undulator

In this chapter a derivation of the synchrotron radiation produced when an electron passes through the periodic magnetic field of an undulator is presented. Starting from Maxwell's equations, the vector and scalar potentials for an arbitrarily moving charge are derived, the Liénard-Wiechert potentials. These potentials are used to calculate the electric and magnetic field seen by an observer due to arbitrary electron motion. The frequency content of the far-field radiation is found by taking the Fourier transform of the electric field in the time domain. Then, the particular motion of an electron in an undulator field is used to calculate the radiation spectrum from an undulator. The derivation is fairly involved. A comprehensive introduction to classical electromagnetism can be found in [37] and in other general physics books [38, 39, 40]. The theory of synchrotron radiation and undulators is described in numerous places, for example in [41, 42, 43]. The mathematics required can be found in many text books, such as here [44] .

2.1 Arbitrary Electron Motion

Figure 2.1 illustrates the variables used to describe electron motion. The motion of the charge is described by the vector $\boldsymbol{R}$ which is a function of time. The position of the observer (field point) is given by the vector $\boldsymbol{r}$. The observer measures the field due to the electron at time t which, it transpires, is due to the electron's motion at the earlier time t'. This is because electromagnetic information travels at a finite speed, the speed of light.

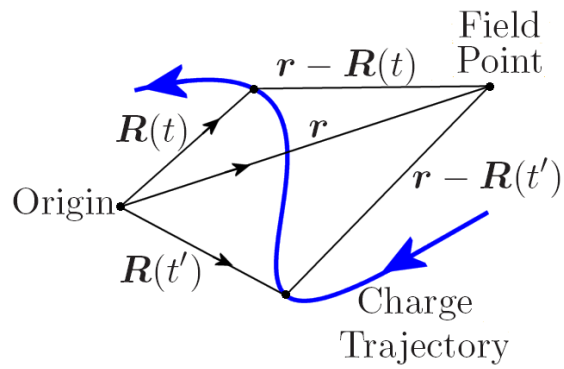

Figure 2.1: Definition of arbitrary electron motion and co-ordinate system.

2.2 The Liénard-Wiechert Potentials

Having defined the motion in general terms, the starting point for the derivation of the radiation from a moving charge is to derive the Liénard-Wiechert potentials. Maxwell's equations are expressed in terms of vector and scalar potentials and two inhomogenous wave equations are obtained in the Lorenz gauge.[14] These wave equations are then solved using a Green's function technique, giving the potentials for moving charges.

2.2.1 Maxwell's Equations

Maxwell's equations expressed in terms of the electric and magnetic fields, $\boldsymbol{E}$ and $\boldsymbol{B}$, are (in SI units):

$$\boldsymbol{\nabla} \cdot \boldsymbol{B} = 0, \tag{2.1}$$

$$\frac{\partial \boldsymbol{B}}{\partial t} + \boldsymbol{\nabla} \times \boldsymbol{E} = 0, \tag{2.2}$$

$$\boldsymbol{\nabla} \cdot \boldsymbol{E} = \frac{\rho}{\epsilon_0}, \tag{2.3}$$

$$-\frac{1}{c^2}\frac{\partial \boldsymbol{E}}{\partial t} + \boldsymbol{\nabla} \times \boldsymbol{B} = \mu_0 \boldsymbol{J}, \tag{2.4}$$

where ρ and $\boldsymbol{J}$ are the charge and current densities, respectively, and ϵ_0 and μ_0 are the vacuum permittivity and permeability. Equations 2.1 and 2.2 are homogenous and Equations 2.3 and 2.4 are inhomogenous, (i.e. in the former there is no source term while in the latter there is).

[14] This gauge is sometimes erroneously attributed to the Dutch physicist H. A. Lorentz [45], in the following Lorenz shall be used.

2.2.2 Scalar and Vector Potentials

The homogenous equations imply that the vector fields $\boldsymbol{E}$ and $\boldsymbol{B}$ can be expressed in terms of scalar and vector potentials ϕ and $\boldsymbol{A}$. The divergence of the curl of a vector field, $\boldsymbol{A}$, is zero:

$$\boldsymbol{\nabla} \cdot (\boldsymbol{\nabla} \times \boldsymbol{A}) = 0,$$

applying this to Equation 2.1:

$$\begin{aligned} \boldsymbol{\nabla} \cdot \boldsymbol{B} &= \boldsymbol{\nabla} \cdot (\boldsymbol{\nabla} \times \boldsymbol{A}) \\ &= 0. \end{aligned}$$

therefore:

$$\boldsymbol{B} = \boldsymbol{\nabla} \times \boldsymbol{A}. \tag{2.5}$$

Substituting this into Equation 2.2 gives:

$$\begin{aligned} \boldsymbol{\nabla} \times \boldsymbol{E} &= -\frac{\partial}{\partial t}(\boldsymbol{\nabla} \times \boldsymbol{A}) \\ &= -\boldsymbol{\nabla} \times (\frac{\partial \boldsymbol{A}}{\partial t}). \end{aligned} \tag{2.6}$$

The curl of the gradient of a scalar field, ϕ, is also zero:

$$\boldsymbol{\nabla} \times (\boldsymbol{\nabla}\phi) = 0,$$

which implies that the gradient of an arbitrary scalar field can be added to the argument of the curl in Equation 2.6:

$$\boldsymbol{\nabla} \times \boldsymbol{E} = -\boldsymbol{\nabla} \times \left(\frac{\partial \boldsymbol{A}}{\partial t} + \boldsymbol{\nabla}\phi \right), \tag{2.7}$$

giving:

$$\boldsymbol{E} = -\left(\frac{\partial \boldsymbol{A}}{\partial t} + \boldsymbol{\nabla}\phi \right). \tag{2.8}$$

Therefore the vector field $\boldsymbol{E}$ can be expressed in terms of another vector field, $\boldsymbol{A}$, and a scalar field, ϕ. $\boldsymbol{B}$ can be related to $\boldsymbol{A}$ through Equation 2.5.

2.2.3 Gauge Transformations

In general *any* vector field, $\boldsymbol{C'}$, can be expressed in terms of another vector and scalar field, $\boldsymbol{C}$ and Φ, by:

$$\boldsymbol{C'} = \boldsymbol{C} + \boldsymbol{\nabla}\Phi, \tag{2.9}$$

and any scalar field, Ψ', by:

$$\Psi' = \Psi + \frac{\partial \Phi}{\partial t}. \tag{2.10}$$

Equations 2.9 and 2.10 represent gauge transformations. Any gauge can be chosen when solving Maxwell's equations and choosing the right gauge can simplify many problems in electromagnetism whilst not changing the underlying physics.

2.2.4 The Lorenz Gauge Condition

A useful gauge when dealing with radiation is the Lorenz gauge. Equation 2.11, known as the Lorenz condition, shows how the scalar and vector potentials are related in this gauge.

$$\boldsymbol{\nabla} \cdot \boldsymbol{A} + \frac{1}{c^2}\frac{\partial \phi}{\partial t} = 0 \tag{2.11}$$

Using this gauge and Maxwell's equations, two inhomogenous wave equations that are functions of the current and charge densities can be derived. The electric field in Gauss' law (Equation 2.3) can be substituted for a scalar and vector potential:

$$\begin{aligned} \boldsymbol{\nabla} \cdot \left(-\frac{\partial \boldsymbol{A}}{\partial t} - \boldsymbol{\nabla}\phi \right) &= -\frac{\partial}{\partial t}(\boldsymbol{\nabla} \cdot \boldsymbol{A}) - \nabla^2 \phi \\ &= \frac{\rho}{\epsilon_0}. \end{aligned}$$

Applying the Lorenz condition gives:

$$\begin{aligned} \nabla^2 \phi - \frac{1}{c^2}\frac{\partial^2}{\partial t^2}(\phi) &= \Box^2 \phi \\ &= -\frac{\rho}{\epsilon_0}, \end{aligned} \tag{2.12}$$

where, $\Box^2 \equiv \nabla^2 - \frac{1}{c^2}\frac{\partial^2}{\partial t^2}$, is the second order differential operator known as the d'Alembertian operator. Using the vector triple product identity:

$$\boldsymbol{\nabla} \times (\boldsymbol{\nabla} \times \boldsymbol{A}) = \boldsymbol{\nabla}(\boldsymbol{\nabla} \cdot \boldsymbol{A}) - \nabla^2 \boldsymbol{A}, \tag{2.13}$$

a similar procedure can be performed for Equation 2.4. Substituting in the scalar and vector potentials and the Lorenz condition gives:

$$-\frac{1}{c^2}\frac{\partial}{\partial t}\left(-\frac{\partial \boldsymbol{A}}{\partial t} - \boldsymbol{\nabla}\phi\right) + \boldsymbol{\nabla}\times(\boldsymbol{\nabla}\times\boldsymbol{A}) = \mu_0\boldsymbol{J}$$

and

$$\begin{aligned}\boldsymbol{\nabla}(\boldsymbol{\nabla}\cdot\boldsymbol{A}) + \nabla^2\boldsymbol{A} + \frac{1}{c^2}\frac{\partial^2}{\partial t^2}\boldsymbol{A} - \boldsymbol{\nabla}(\boldsymbol{\nabla}\cdot\boldsymbol{A}) &= \Box^2\boldsymbol{A} \\ &= -\mu_0\boldsymbol{J}. \end{aligned} \tag{2.14}$$

Equations 2.12 and 2.14 are two inhomogenous wave equations that describe the potentials due to stationary and moving charges. These differential equations can be solved using a Green's function method.

2.2.5 Green's Function Solution of the Wave Equation

The general form of the wave equation is:

$$\Box^2 u(\boldsymbol{r},t) = v(\boldsymbol{r},t), \tag{2.15}$$

where $v(\boldsymbol{r},t)$ is a general source function and $u(\boldsymbol{r},t)$ is the associated potential. The potential obeys the boundary conditions $u(\boldsymbol{r},t)\to 0$ as $|r|\to\infty$ and $|t|\to\infty$. By assuming that Equation 2.15 is linear[15] the Green's function method can be used to write the solution of Equation 2.15 in the form:

$$u(\boldsymbol{r},t) = \int G(\boldsymbol{r}-\boldsymbol{r'},t-t')v(\boldsymbol{r'},t')\mathrm{d}\tau' \tag{2.16}$$

where the Green's function, $G(\boldsymbol{r}-\boldsymbol{r'},t-t')$, is the potential generated by a point source located at $\boldsymbol{r}=\boldsymbol{r'}$ and at time $t=t'$, which obeys the differential equation:

$$\Box^2 G(\boldsymbol{r},t) = \delta(\boldsymbol{r})\delta(t).$$

[15] I.e. the solutions obey the principle of linear superposition.

The solution can be written as:[16]

$$G(\boldsymbol{r}-\boldsymbol{r'},t-t') = \frac{1}{4\pi|\boldsymbol{r}-\boldsymbol{r'}|}\delta\left(t-t'\pm\frac{|\boldsymbol{r}-\boldsymbol{r'}|}{c}\right).$$

The delta function means that an observer at $\boldsymbol{r}$ only measures a non-zero potential at two particular times:

$$t = t' \pm \frac{|\boldsymbol{r}-\boldsymbol{r'}|}{c}.$$

One of the solutions relates to the *advanced* time, here a spherical wave is travelling backwards in time. The advanced time solution raises questions about the principles of causality and so will be disregarded for the remainder of the derivation. Instead the *retarded* time solution, which represents a spherical wave travelling forwards in time, will be considered:

$$t = t' + \frac{|\boldsymbol{r}-\boldsymbol{r'}|}{c}. \tag{2.17}$$

Here, t is the time at which the impulse was applied at position $\boldsymbol{r'}$ plus the time taken for a light signal to travel between the points $\boldsymbol{r'}$ and $\boldsymbol{r}$. For $t > t'$, the locus of all points at which the potential is non-zero is simply:

$$|\boldsymbol{r}-\boldsymbol{r'}| = c(t-t').$$

This is a sphere centred on $\boldsymbol{r'}$ whose radius is the distance travelled by the light in the time interval since the impulse was applied. The Green's function describes a spherical wave that emanates from position $\boldsymbol{r'}$ at t' and propagates at the speed of light. The amplitude of the wave is inversely proportional to the distance from the source.

A solution corresponding to a distribution of point sources can now be found by integration of the point source response over the entire distribution. This requires an integration over all space and time.

2.2.6 Potentials for Moving Charges

Using Equations 2.17 and 2.16, Equations 2.12 and 2.14 can be solved:

$$\phi(\boldsymbol{r},t) = \frac{1}{4\pi\epsilon_0}\int_{-\infty}^{\infty}\int_{space}\delta\left(t-t'-\frac{|\boldsymbol{r}-\boldsymbol{r'}|}{c}\right)\frac{\rho(\boldsymbol{r'},t')}{|\boldsymbol{r}-\boldsymbol{r'}|}\mathrm{d}V'\mathrm{d}t' \tag{2.18}$$

[16] See Appendix B.

and

$$\boldsymbol{A}(\boldsymbol{r},t) = \frac{\mu_0}{4\pi} \int_{-\infty}^{\infty} \int_{space} \delta\left(t - t' - \frac{|\boldsymbol{r}-\boldsymbol{r'}|}{c}\right) \frac{\boldsymbol{J}(\boldsymbol{r'},t')}{|\boldsymbol{r}-\boldsymbol{r'}|} \mathrm{d}V'\mathrm{d}t'. \tag{2.19}$$

For a moving charge q, the current and charge distributions are:

$$\rho(\boldsymbol{r'},t') = q\delta(\boldsymbol{r'} - \boldsymbol{R}(t')) \tag{2.20}$$

and

$$\boldsymbol{J}(\boldsymbol{r'},t') = q\boldsymbol{v}\delta(\boldsymbol{r'} - \boldsymbol{R}(t')), \tag{2.21}$$

where $\boldsymbol{R}(t')$ is the position of the charge at time t' and $\boldsymbol{v}$ is its velocity:

$$\begin{aligned} \boldsymbol{v}(t') &= \frac{\mathrm{d}}{\mathrm{d}t}\boldsymbol{R}(t') \\ &= \dot{\boldsymbol{R}}(t'). \end{aligned} \tag{2.22}$$

2.2.7 Solution for the Scalar Potential

Substituting Equation 2.20 into Equation 2.18 and considering first only the spatial integration gives:

$$\int_{space} \delta\left(t - t' - \frac{|\boldsymbol{r}-\boldsymbol{r'}|}{c}\right) \frac{q\,\delta(\boldsymbol{r'} - \boldsymbol{R}(t'))}{|\boldsymbol{r}-\boldsymbol{r'}|} \mathrm{d}V' = q\,\delta\left(t - t' - \frac{|\boldsymbol{r}-\boldsymbol{R}(t')|}{c}\right) \frac{1}{|\boldsymbol{r}-\boldsymbol{R}(t')|}.$$

Due to the integration over all space, the delta function is now a more complicated function of t': it depends directly on t' but also on $\boldsymbol{R}(t')$ and it only contributes to the integration over time when:

$$t' = t - \frac{|\boldsymbol{r}-\boldsymbol{R}(t')|}{c}.$$

The retarded time is now a function of the time and position at which the field is *seen*. It is an implicit function of $(\boldsymbol{r},t)$ and represents the time at which the field must have left the source point to arrive at the field point. To calculate the scalar potential the integration over time must now be completed:

$$\phi(\boldsymbol{r},t) = \frac{q}{4\pi\epsilon_0} \int_{-\infty}^{\infty} \delta\left(t - t' - \frac{|\boldsymbol{r}-\boldsymbol{R}(t')|}{c}\right) \frac{1}{|\boldsymbol{r}-\boldsymbol{R}(t')|} \mathrm{d}t'. \tag{2.23}$$

This integral is of the form:

$$\int_{\infty}^{\infty} f(t')\delta(g(t')-a)\mathrm{d}t'.$$

Some manipulation gives:

$$\begin{aligned}\int_{\infty}^{\infty} f(t')\delta(g(t')-a)\frac{\mathrm{d}t'}{\mathrm{d}g}\mathrm{d}g &= \int_{\infty}^{\infty}\frac{f(t')}{\dot{g}(t')}\delta(g(t')-a)\\ &= \frac{f(g^{-1}(a))}{\dot{g}(g^{-1}(a))},\end{aligned}$$

where $g^{-1}(a)$ is the value of t' satisfying $g(t')=a$. To find $\dot{g}(t')$ let:

$$g(t') = t' - t + \frac{|\boldsymbol{r}-\boldsymbol{R}(t')|}{c}.$$

Differentiating w.r.t. t' gives:

$$\frac{\mathrm{d}}{\mathrm{d}t'}g(t') = 1 + \frac{\partial}{\partial t'}\frac{|\boldsymbol{r}-\boldsymbol{R}(t')|}{c}. \tag{2.24}$$

The partial differentiation in Equation 2.24 can be carried out by considering $|\boldsymbol{r}-\boldsymbol{R}(t')|^2$. Directly differentiating this expression gives:

$$\frac{\partial}{\partial t'}|\boldsymbol{r}-\boldsymbol{R}(t')|^2 = 2|\boldsymbol{r}-\boldsymbol{R}(t')| \times \frac{\partial}{\partial t'}|\boldsymbol{r}-\boldsymbol{R}(t')|. \tag{2.25}$$

The expression can also be expanded:

$$|\boldsymbol{r}-\boldsymbol{R}(t')|^2 = \boldsymbol{r}\boldsymbol{r} - 2\boldsymbol{r}\boldsymbol{R}(t') + \boldsymbol{R}(t')\boldsymbol{R}(t')$$

and then differentiated:

$$\frac{\partial}{\partial t'}|\boldsymbol{r}-\boldsymbol{R}(t')|^2 = -2\boldsymbol{r}\dot{\boldsymbol{R}}(t') + 2\boldsymbol{R}(t')\dot{\boldsymbol{R}}(t'). \tag{2.26}$$

Combining Equation 2.25 and Equation 2.26 and re-arranging gives:

$$\frac{\partial}{\partial t'}|\boldsymbol{r}-\boldsymbol{R}(t')| = -\frac{\dot{\boldsymbol{R}}(t')(\boldsymbol{r}-\boldsymbol{R}(t'))}{|\boldsymbol{r}-\boldsymbol{R}(t')|}. \tag{2.27}$$

Substituting back into Equation 2.24 results in the expression:

$$\frac{\mathrm{d}}{\mathrm{d}t'}g(t') = \frac{|\boldsymbol{r} - \boldsymbol{R}(t')| - c^{-1}\dot{\boldsymbol{R}}(t') \cdot (\boldsymbol{r} - \boldsymbol{R}(t'))}{|\boldsymbol{r} - \boldsymbol{R}(t')|},$$

which is all that is needed to perform the integration in Equation 2.23. The equation for the scalar potential is now:

$$\phi(\boldsymbol{r}, t) = \frac{q}{4\pi\epsilon_0}\left(\frac{1}{|\boldsymbol{r} - \boldsymbol{R}(t')| - c^{-1}\dot{\boldsymbol{R}}(t')(\boldsymbol{r} - \boldsymbol{R}(t'))}\right),$$

where t' must satisfy the equation for the retarded time (Equation2.17) to preserve causality. By defining the following terms, the equation for the scalar potential can be simplified:

- The retarded position vector: $\boldsymbol{r}' = \boldsymbol{r} - \boldsymbol{R}(t')$.
- The retarded distance: $r' = |\boldsymbol{r} - \boldsymbol{R}(t')|$.
- The unit vector in the direction of the retarded position vector: $\boldsymbol{n}' = \frac{\boldsymbol{r}'}{r'}$.
- The scaled velocity of the particle: $\boldsymbol{\beta}(t') = \frac{\dot{\boldsymbol{R}}(t')}{c}$.

For this derivation $\boldsymbol{\beta}$ will always be evaluated at the retarded time so the t' dependence will be dropped from hereon. With these definitions the scalar potential is:

$$\phi(\boldsymbol{r}, t) = \frac{q}{4\pi\epsilon_0}\frac{1}{r'(1 - \boldsymbol{\beta} \cdot \boldsymbol{n}')}, \tag{2.28}$$

which is very similar to the Coulomb potential except for the relativistic factor.

2.2.8 Solution for the Vector Potential

The vector potential is derived in a similar way. In this case there is a velocity term in the numerator. The equivalent expression for the vector potential is:

$$\boldsymbol{A}(\boldsymbol{r}, t) = \frac{\mu_0 q}{4\pi}\frac{\dot{\boldsymbol{R}}(t')}{r'(1 - \boldsymbol{\beta} \cdot \boldsymbol{n}')}. \tag{2.29}$$

This can also be written in terms of the scalar potential, thereby relating magnetic and electric fields:

$$\boldsymbol{A}(\boldsymbol{r}, t) = \frac{\boldsymbol{\beta}\phi(\boldsymbol{r}, t)}{c}. \tag{2.30}$$

Equations 2.28 and 2.29 represent the Liénard-Wiechert potentials.

2.3 Calculating the Electric and Magnetic Fields

In the previous section the potentials for moving charges were derived. From these, the physically measurable electric and magnetic fields need to be calculated. The scalar and vector potentials at the position of the observer at time t are those excited by the charge distribution at time t', not the charge distribution at time t. This can be understood because electromagnetic information travels at a finite speed, the speed of light. To determine the radiation at the observer's position the electric and magnetic fields due to the scalar and vector potentials must be calculated. This requires that the fields ϕ and $\boldsymbol{A}$ must be differentiated with respect to the co-ordinates and time at which the observation is made. However, ϕ and $\boldsymbol{A}$ are expressed as functions of t': only through the relationship between t and t' is their dependence on $\boldsymbol{r}$ and t apparent (Equation2.17). Hence, the derivatives of t' with respect to $\boldsymbol{R}$ and t need to be calculated.

2.3.1 Differentiating the Equation for the Retarded Time

First consider differentiating Equation 2.17 with respect to t:

$$\frac{\partial}{\partial t}t' + \frac{1}{c}\frac{\partial}{\partial t}|\boldsymbol{r} - \boldsymbol{R}(t')| = 1.$$

Multiplying the second term on the LHS by $\frac{\partial t'}{\partial t'}$ and then substituting for $\frac{\partial}{\partial t'}|\boldsymbol{r} - \boldsymbol{R}(t')|$ (Equation2.27) gives:

$$\frac{\partial t'}{\partial t} - \frac{\dot{\boldsymbol{R}}(t') \cdot (\boldsymbol{r} - \boldsymbol{R}(t'))}{c|\boldsymbol{r} - \boldsymbol{R}(t')|}\frac{\partial t'}{\partial t} = 1.$$

After some re-arrangement:

$$\frac{\partial t'}{\partial t} = \frac{1}{(1 - \boldsymbol{\beta} \cdot \boldsymbol{n}')}. \tag{2.31}$$

The spatial derivative is calculated in a similar way:

$$\begin{aligned} \boldsymbol{\nabla} t' &= \boldsymbol{\nabla}\left(t - \frac{|\boldsymbol{r} - \boldsymbol{R}(t')|}{c}\right) \\ &= -\frac{\boldsymbol{n}'}{c(1 - \boldsymbol{\beta} \cdot \boldsymbol{n}')}. \end{aligned} \tag{2.32}$$

2.3.2 The Electric Field

The electric field can now be calculated from Equation 2.8. Care must be taken to ensure that the partial derivatives are evaluated at the correct time and position. Firstly some

manipulation of Equation 2.8 is required:

$$\begin{aligned} \boldsymbol{E} &= -\frac{\partial \boldsymbol{A}}{\partial t} - \boldsymbol{\nabla}\phi \\ &= -\boldsymbol{\nabla}\phi\Big|_{t'} - \frac{\partial \phi}{\partial t'}\boldsymbol{\nabla}t' - \frac{\partial \boldsymbol{A}}{\partial t'}\frac{\partial t'}{\partial t}. \end{aligned} \tag{2.33}$$

The scalar potential can be substituted for the vector potential using Equation2.30 giving:

$$\begin{aligned} \boldsymbol{E} &= -\boldsymbol{\nabla}\phi\Big|_{t'} - \frac{\partial \phi}{\partial t'}\boldsymbol{\nabla}t' - \frac{\partial}{\partial t'}\left(\frac{\boldsymbol{\beta}\phi}{c}\right)\frac{\partial t'}{\partial t} \\ &= -\boldsymbol{\nabla}\phi\Big|_{t'} - \frac{\partial \phi}{\partial t'}\boldsymbol{\nabla}t' - \left(\frac{\boldsymbol{\beta}}{c}\frac{\partial \phi}{\partial t'} + \frac{\phi}{c}\dot{\boldsymbol{\beta}}\right)\frac{\partial t'}{\partial t} \\ &= -\boldsymbol{\nabla}\phi\Big|_{t'} - \frac{\partial \phi}{\partial t'}\left(\boldsymbol{\nabla}t' + \frac{\boldsymbol{\beta}}{c}\frac{\partial t'}{\partial t}\right) - \frac{\phi}{c}\dot{\boldsymbol{\beta}}\frac{\partial t'}{\partial t}. \end{aligned} \tag{2.34}$$

Consider each term in Equation 2.34 separately, starting with $\frac{\partial \phi}{\partial t'}$:

$$\begin{aligned} \frac{\partial \phi}{\partial t'} &= \frac{q}{4\pi\epsilon_0}\frac{\partial}{\partial t'}\left(\frac{1}{r'(1-\boldsymbol{\beta}\cdot\boldsymbol{n'})}\right) \\ &= -\left(\frac{q}{4\pi\epsilon_0}\right)(r' - \boldsymbol{\beta}\boldsymbol{r'})^{-2}\frac{\partial}{\partial t'}(r' - \boldsymbol{\beta}\boldsymbol{r'}) \\ &= -\left(\frac{q}{4\pi\epsilon_0}\right)(r' - \boldsymbol{\beta}\boldsymbol{r}')^{-2}\left[\frac{\partial r'}{\partial t'} - \boldsymbol{\beta}\frac{\partial \boldsymbol{r'}}{\partial t'} - \boldsymbol{r}'\frac{\partial}{\partial t'}\boldsymbol{\beta}\right]. \end{aligned} \tag{2.35}$$

It is simple to show that $\frac{\partial \boldsymbol{r'}}{\partial t'} = -c\boldsymbol{\beta}$ and $\frac{\partial r'}{\partial t'} = -c\boldsymbol{\beta}\cdot\boldsymbol{n}'$, therefore Equation2.35 becomes:

$$\frac{\partial \phi}{\partial t'} = \frac{q}{4\pi\epsilon_0}\frac{(c\boldsymbol{\beta}\cdot\boldsymbol{n'} - c\beta^2 - r'\dot{\boldsymbol{\beta}}\cdot\boldsymbol{n}')}{(r'(1-\boldsymbol{\beta}\cdot\boldsymbol{n}'))^2}. \tag{2.36}$$

The second term in Equation 2.34 that must be differentiated is $\boldsymbol{\nabla}\phi|_{t'}$:

$$\begin{aligned} \boldsymbol{\nabla}\phi|_{t'} &= \frac{q}{4\pi\epsilon_0}\boldsymbol{\nabla}\left(\frac{1}{r' - \boldsymbol{\beta}\cdot\boldsymbol{r'}}\right) \\ &= \frac{q}{4\pi\epsilon_0}\left(-(r' - \boldsymbol{\beta}\cdot\boldsymbol{r'})^{-2}\boldsymbol{\nabla}(r' - \boldsymbol{\beta}\cdot\boldsymbol{r'})\right) \\ &= \frac{q}{4\pi\epsilon_0}\left(-(r' - \boldsymbol{\beta}\cdot\boldsymbol{r'})^{-2}\left(\boldsymbol{\nabla}r' - \frac{1}{c}\boldsymbol{\nabla}\frac{\mathrm{d}\boldsymbol{R'}}{\mathrm{d}t}\boldsymbol{r'}\right)\right) \\ &= -\frac{q}{4\pi\epsilon_0}\frac{(\boldsymbol{n'} - \boldsymbol{\beta})}{(r'(1-\boldsymbol{\beta}\cdot\boldsymbol{n}'))^2}. \end{aligned} \tag{2.37}$$

The differentiation required to determine the electric field has now been completed, all that is required is some further algebraic manipulation of the formulae. This can be tricky: there are many terms to consider. However, by combining Equations 2.31, 2.32, 2.34, 2.36

and 2.37, the correct answer can be obtained:

$$\boldsymbol{E} = \frac{q}{4\pi\epsilon_0}\left[\frac{(\boldsymbol{n}' - \boldsymbol{\beta})}{(r'(1-\boldsymbol{\beta}\cdot\boldsymbol{n}'))^2}\left(1 - \beta^2 + \boldsymbol{\beta}\cdot\boldsymbol{n}' - \frac{r'\dot{\boldsymbol{\beta}}\cdot\boldsymbol{n}'}{c}\right) - \frac{\dot{\boldsymbol{\beta}}}{cr'(1-\boldsymbol{\beta}\cdot\boldsymbol{n}')}\right]$$

or

$$\boldsymbol{E} = \frac{q}{4\pi\epsilon_0}\left[\frac{(1-\beta^2)(\boldsymbol{n}' - \boldsymbol{\beta})}{r'^2(1-\boldsymbol{\beta}\cdot\boldsymbol{n}')^3} + \frac{\boldsymbol{n}' \times [(\boldsymbol{n}' - \boldsymbol{\beta}) \times \dot{\beta}]}{r'(1-\boldsymbol{\beta}\cdot\boldsymbol{n}')^3}\right]. \tag{2.38}$$

Here the vector triple product identity has been used. If there is no acceleration, $\dot{\boldsymbol{\beta}} = 0$ and only the first term contributes. This is the Coulomb field of the charge corrected for relativistic effects, sometimes called the velocity field, and is inversely proportional to r'^2. If there is acceleration, there is a component of the electric field inversely proportional to r'. This term is called the radiation, or acceleration, field.

2.3.3 The Magnetic Field

The magnetic field can be evaluated without as much algebra, starting from Equation 2.5:

$$\begin{aligned}
\boldsymbol{B} &= \boldsymbol{\nabla} \times \boldsymbol{A} \\
&= \boldsymbol{\nabla} \times \boldsymbol{A}\Big|_{t'} + \boldsymbol{\nabla} t' \times \frac{\partial \boldsymbol{A}}{\partial t'} \\
&= \boldsymbol{\nabla} \times \left(\frac{\boldsymbol{\beta}\phi}{c}\right)\Bigg|_{t'} + \boldsymbol{\nabla} t' \times \frac{\partial \boldsymbol{A}}{\partial t'}.
\end{aligned} \tag{2.39}$$

Using the vector identity, $\boldsymbol{\nabla} \times (\phi\boldsymbol{A}) = \phi(\boldsymbol{\nabla} \times \boldsymbol{A}) + (\boldsymbol{\nabla}\phi) \times \boldsymbol{A}$ gives:

$$\boldsymbol{\nabla} \times \left(\frac{\boldsymbol{\beta}\phi}{c}\right)\Bigg|_{t'} = \frac{1}{c}(\boldsymbol{\nabla}\phi\big|_{t'}) \times \boldsymbol{\beta}. \tag{2.40}$$

The result for $\boldsymbol{\nabla}\phi|_{t'}$ (Equation 2.37) can be used:

$$\boldsymbol{\nabla}\phi\big|_{t'} = \lambda(\boldsymbol{n}' - \boldsymbol{\beta}),$$

where, for simplicity in the algebraic manipulation, the scalar factors are represented by λ. Making use of another identity, $(\boldsymbol{A} - \boldsymbol{B}) \times \boldsymbol{A} = (\boldsymbol{A} - \boldsymbol{B}) \times \boldsymbol{B}$, enables the cross product to be expressed in terms of $\boldsymbol{n}'$:

$$\frac{1}{c}(\lambda(\boldsymbol{n}' - \boldsymbol{\beta})) \times \boldsymbol{\beta} = \frac{1}{c}(\lambda(\boldsymbol{n}' - \boldsymbol{\beta})) \times \boldsymbol{n}'.$$

This can be substituted back into Equation 2.40, (this is also useful as it enables $\boldsymbol{\nabla} t'$ to be expressed in terms of $\boldsymbol{n}'$, allowing terms in Equation 2.39 that have a factor of $\boldsymbol{n}'$ to be collected together):

$$\frac{1}{c}(\boldsymbol{\nabla}\phi\big|_{t'}) \times \boldsymbol{\beta} = \frac{1}{c}(\boldsymbol{\nabla}\phi\big|_{t'}) \times \boldsymbol{n}'.$$

Equation 2.32 for $\boldsymbol{\nabla} t'$ can be used with Equation 2.31 to give:

$$\boldsymbol{\nabla} t' = -\frac{1}{c}\boldsymbol{n}' \times \frac{\partial t'}{\partial t}.$$

Equation 2.39 is now:

$$\begin{aligned} \boldsymbol{B} &= \frac{1}{c}(\boldsymbol{\nabla}\phi\big|_{t'}) \times \boldsymbol{n}' - \frac{1}{c}\boldsymbol{n}' \times \frac{\partial \boldsymbol{A}}{\partial t'}\frac{\partial t'}{\partial t} \\ &= -\frac{1}{c}\boldsymbol{n}' \times \left(\boldsymbol{\nabla}\phi\big|_{t'} + \frac{\partial \boldsymbol{A}}{\partial t}\right). \end{aligned}$$

If this is compared to Equation 2.33 for the electric field, it can be seen that magnetic fields can be expressed in terms of electric fields:

$$\boldsymbol{B} = \frac{1}{c}\boldsymbol{n}' \times \boldsymbol{E}. \tag{2.41}$$

Equation 2.41 holds for both the velocity and acceleration electric fields and implies that the magnetic fields are always perpendicular to the electric fields.

2.4 Radiated Power and Radiation Spectrum

Equations 2.38 and 2.41 represent the electric and magnetic fields in the time domain due to moving charges. To calculate the energy flow and power radiated, the Poynting vector must be used. For the spectral content of the radiation, the Fourier transform of the fields in the time domain must be calculated.

2.4.1 The Poynting Vector and Energy Flow in the Far-Field

The Poynting vector $\boldsymbol{S}$ describes how the energy in the electromagnetic field moves through space. In terms of $\boldsymbol{E}$ and $\boldsymbol{B}$ fields it is defined as:

$$\boldsymbol{S} = \epsilon_0 c^2 (\boldsymbol{E} \times \boldsymbol{B}).$$

An important point to note about $\boldsymbol{S}$ is that it is not necessarily unique, for example the curl of any vector field can be added to it and the general physics of the problem will not be changed [37]. In this derivation, the customary expression for $\boldsymbol{S}$ is used. The Poynting vector can be expressed in terms of the electric field only using Equation 2.41:

$$\begin{aligned} \boldsymbol{S} &= \frac{\boldsymbol{E} \times (\boldsymbol{n}' \times \boldsymbol{E})}{\mu_0 c} \\ &= \frac{1}{\mu_0 c}(E^2 \boldsymbol{n}' - (\boldsymbol{E} \cdot \boldsymbol{n}')\boldsymbol{E}). \end{aligned} \tag{2.42}$$

Equation 2.38 has acceleration and velocity terms. Far from the source the terms proportional to r^{-1} will dominate over those proportional to r^{-2}. Therefore in the far-field $\boldsymbol{E}$ is:

$$\boldsymbol{E} = \frac{q}{4\pi\epsilon_0}\left[\frac{\boldsymbol{n'} \times [(\boldsymbol{n'} - \boldsymbol{\beta}) \times \dot{\beta}]}{r'(1 - \boldsymbol{\beta} \cdot \boldsymbol{n'})^3}\right]. \tag{2.43}$$

Making this approximation also simplifies the expression for the Poynting vector because, for the acceleration field, $\boldsymbol{E}$ is always perpendicular to $\boldsymbol{n}'$:

$$\boldsymbol{E} \propto \boldsymbol{n}' \times [(\boldsymbol{n}' - \beta) \times \dot{\boldsymbol{\beta}}]].$$

This implies that $\boldsymbol{E} \cdot \boldsymbol{n}' = 0$ and that the Poynting vector is:

$$\boldsymbol{S} = \frac{1}{\mu_0 c} E^2 \boldsymbol{n}'. \tag{2.44}$$

There are therefore equal amounts of electric and magnetic energy moving at the speed of light in the direction of $\boldsymbol{n}'$.

2.4.2 Radiated Energy Spectrum

The spectrum, i.e. frequency content, of the radiation can be determined by taking the Fourier transform of the electric field in the time domain. Decomposing the electric field into two orthogonal basis vectors, $\boldsymbol{e_1}$ and $\boldsymbol{e_2}$, so that:

$$\boldsymbol{E}(t) = E_1(t)\boldsymbol{e_1} + E_2(t)\boldsymbol{e_2},$$

gives the Fourier transform pair:

$$E_\alpha(\omega) = \int_{-\infty}^{\infty} E_\alpha(t)\mathrm{e}^{\mathrm{i}\omega t}\mathrm{d}t \tag{2.45}$$

and

$$E_\alpha(t) = \frac{1}{2\pi}\int_{-\infty}^{\infty} E_\alpha(\omega)\mathrm{e}^{-\mathrm{i}\omega t}\mathrm{d}t,$$

where $\alpha = 1, 2$ depending on the transverse direction of interest. Applying the constraint that the electric field in the time domain should be real means that:

$$E_\alpha(-\omega) = E_\alpha^*(\omega).$$

The Poynting flux is simply the energy flux per unit time, t, per unit area, a:

$$\begin{aligned} \frac{\mathrm{d}^2 W}{\mathrm{d}t\mathrm{d}a} &= \epsilon_0 c E(t)^2 \\ &= \epsilon_0 c (E_1(t)^2 + E_2(t)^2), \end{aligned} \tag{2.46}$$

where W has been used to stand for energy to avoid confusion. Taking the Fourier transform of this expression gives the frequency spectrum of the energy density. The total energy per unit area is:

$$\frac{\mathrm{d}W_\alpha}{\mathrm{d}a} = \epsilon_0 c \int_{-\infty}^{\infty} E_\alpha(t)^2 \mathrm{d}t.$$

Using Parseval's theorem [44], the electric field as a function of time can be related to the electric field as a function of frequency:

$$\int_{-\infty}^{\infty} E_\alpha(t)^2 \mathrm{d}t = \frac{1}{2\pi}\int_{-\infty}^{\infty} |E_\alpha(\omega)|^2 \mathrm{d}\omega.$$

For the negative frequency components:

$$\begin{aligned} E_\alpha(-\omega)E_\alpha^*(-\omega) &= E_\alpha(\omega)E_\alpha^*(\omega) \\ &= |E_\alpha(\omega)|^2, \end{aligned} \tag{2.47}$$

so:

$$\int_{-\infty}^{\infty} E_\alpha(t)^2 \mathrm{d}t = \frac{1}{\pi}\int_{0}^{\infty} |E_\alpha(\omega)|^2 \mathrm{d}\omega.$$

Hence the total energy radiated per unit area of the electric field into each α is:

$$\begin{aligned} \frac{\mathrm{d}W_\alpha}{\mathrm{d}a} &= \epsilon_0 c \int_{-\infty}^{\infty} E_\alpha(t)^2 \mathrm{d}t \\ &= \frac{\epsilon_0 c}{\pi}\int_{0}^{\infty} |E_\alpha(\omega)|^2 \mathrm{d}\omega. \end{aligned} \tag{2.48}$$

The spectral components of the Poynting flux are therefore:

$$\frac{\mathrm{d}^2 W_\alpha}{\mathrm{d}\omega \mathrm{d}a} = \frac{\epsilon_0 c}{\pi}|E_\alpha(\omega)|^2.$$

If the surface da is far from the distance over which the particle is moving when emitting the radiation, then $\mathrm{d}a = r^2 \mathrm{d}\Omega$, where Ω denotes a solid angle, and the energy radiated per unit angular frequency per unit solid angle is:

$$\frac{\mathrm{d}^2 W_\alpha}{\mathrm{d}\omega \mathrm{d}\Omega} = \frac{\epsilon_0 c r^2}{\pi}|E_\alpha(\omega)|^2. \tag{2.49}$$

2.4.3 Polarisation and the Stokes' Parameters

Although not directly needed for the derivation, it is now worth introducing the concept of polarisation and the Stokes' parameters. The polarisation of electro-magnetic radiation can be defined in many ways, which are somewhat arbitrary but essentially describe the same thing. One convention is to use the Stokes' parameters. These can be defined in terms of the components of the electric field vectors in the arbitrary basis vectors:

$$S_0 = E_1(\omega)E_1^*(\omega) + E_2(\omega)E_2^*(\omega), \tag{2.50}$$

$$S_1 = E_1(\omega)E_1^*(\omega) - E_2(\omega)E_2^*(\omega), \tag{2.51}$$

$$S_2 = E_1^*(\omega)E_2(\omega) + E_1(\omega)E_2^*(\omega), \tag{2.52}$$

$$S_3 = \mathrm{i}[E_1^*(\omega)E_2(\omega) - E_1(\omega)E_2^*(\omega)], \tag{2.53}$$

and

$$S_0^2 = S_1^2 + S_2^2 + S_3^2.$$

The total intensity is S_0. S_1 is the difference in intensity transmitted by a linearly polarised filter in orientation $\boldsymbol{e_1}$ and $\boldsymbol{e_2}$. S_2 is the difference in intensity for the components polarised at $\pm 45°$ to $\boldsymbol{e_1}$ and $\boldsymbol{e_2}$ and S_3 is the difference in the intensity of right- and left-handed circularly polarised components. The above parameters are defined for a single monochromatic wave. In general the radiation is a summation of many waves and can be divided into a polarised and unpolarised part. For the unpolarised part a similar decomposition can be made and it follows that:

$$S_0 = \sqrt{S_1^2 + S_2^2 + S_3^2} + S_4,$$

where S_4 is the intensity of the unpolarised component of the radiation. Dividing through by S_0 gives:

$$1 - P_4 = \sqrt{P_1^2 + P_2^2 + P_3^2},$$

where $P_1 = \frac{S_1}{S_0}$ etc. The overall polarisation is $\sqrt{P_1^2 + P_2^2 + P_3^2}$ and the fraction of unpolarised radiation is P_4. The values of P_1, P_2 and P_3 are the *polarisation rates* for the particular component.

2.4.4 The Fourier Transform of the Acceleration Field

The Fourier transform of the electric field due to moving charges must now be completed. Substituting Equation 2.43 into Equation 2.45 gives:

$$\boldsymbol{E}(\omega) = \frac{q}{4\pi\epsilon_0 r'} \int_{-\infty}^{\infty} \left[\frac{\boldsymbol{n}' \times [(\boldsymbol{n}' - \boldsymbol{\beta}) \times \dot{\beta}]}{(1 - \boldsymbol{\beta} \cdot \boldsymbol{n}')^3} \mathrm{e}^{\mathrm{i}\omega t} \mathrm{d}t \right].$$

As the fields are due to the charge density at the retarded time the integration must be performed over $\mathrm{d}t'$ using Equation 2.31, hence:

$$\boldsymbol{E}(\omega) = \frac{q}{4\pi\epsilon_0 r} \int_{-\infty}^{\infty} \left[\frac{\boldsymbol{n}' \times [(\boldsymbol{n}' - \boldsymbol{\beta}) \times \dot{\beta}]}{(1 - \boldsymbol{\beta} \cdot \boldsymbol{n}')^3} \mathrm{e}^{\mathrm{i}\omega t} (1 - \boldsymbol{\beta} \cdot \boldsymbol{n}') \mathrm{d}t' \right]. \tag{2.54}$$

The exponential must also be expressed in terms of t'. This can be done by considering the approximation:

$$r' = |\boldsymbol{r} - \boldsymbol{R}(t')| \approx r,$$

for $\boldsymbol{r} \gg \boldsymbol{R}(t')$, allowing the exponential to be written as:

$$\mathrm{e}^{\mathrm{i}\omega t} \approx \mathrm{e}^{\left[\mathrm{i}\omega\left(t' + \frac{r'}{c}\right)\right]}.$$

Expanding r' to first order in $\boldsymbol{R}(t')$:

$$r' = r + (\boldsymbol{\nabla} r') \cdot \boldsymbol{R}(t')$$

and

$$\boldsymbol{\nabla} r' = -\frac{(\boldsymbol{r} - \boldsymbol{R}(t'))}{r'}.$$

Hence:

$$r' = r - \boldsymbol{n} \cdot \boldsymbol{R}(t')$$

and the exponential can now be expressed as:

$$\exp\left[\mathrm{i}\omega\left(t' + \frac{r - \boldsymbol{n} \cdot \boldsymbol{R}(t')}{c}\right)\right] = \exp\left[\mathrm{i}\omega\left(t' + \frac{\boldsymbol{n} \cdot \boldsymbol{R}(t')}{c}\right)\right] \exp\left(\frac{\mathrm{i}\omega r}{c}\right). \tag{2.55}$$

When the factor of $\exp\left(\frac{\mathrm{i}\omega r}{c}\right)$ is multiplied by its complex conjugate it will equal unity and is therefore unimportant in the derivation. This also explains why the next to leading order term is taken in the expansion, not just the leading order term. Equation 2.54 can be solved by taking the derivative w.r.t. time of the vector $\boldsymbol{n} \times [\boldsymbol{n} \times \boldsymbol{\beta}]$ divided by the scalar $(1 - \boldsymbol{\beta} \cdot \boldsymbol{n})$:

$$\frac{\mathrm{d}}{\mathrm{d}t'}\left(\frac{\boldsymbol{n} \times [\boldsymbol{n} \times \boldsymbol{\beta}]}{(1 - \boldsymbol{\beta} \cdot \boldsymbol{n})}\right) = \frac{\boldsymbol{n} \times [\boldsymbol{n} \times \dot{\boldsymbol{\beta}}](1 - \boldsymbol{\beta} \cdot \boldsymbol{n}) - \boldsymbol{n} \times [\boldsymbol{n} \times \boldsymbol{\beta}](\dot{\boldsymbol{\beta}} \cdot \boldsymbol{n})}{(1 - \boldsymbol{\beta} \cdot \boldsymbol{n})^2}.$$

As cross products are distributive this can be written as:

$$\frac{\mathrm{d}}{\mathrm{d}t'}\left(\frac{\boldsymbol{n} \times [\boldsymbol{n} \times \boldsymbol{\beta}]}{(1 - \boldsymbol{\beta} \cdot \boldsymbol{n})}\right) = \left(\frac{\boldsymbol{n} \times (\boldsymbol{n} \times \dot{\boldsymbol{\beta}})}{(1 - \boldsymbol{\beta} \cdot \boldsymbol{n})^2}\right) + \frac{\boldsymbol{n} \times (\boldsymbol{n} \times [(\boldsymbol{\beta} \cdot \boldsymbol{n})\dot{\boldsymbol{\beta}} - (\dot{\boldsymbol{\beta}} \cdot \boldsymbol{n})\boldsymbol{\beta}])}{(1 - \boldsymbol{\beta} \cdot \boldsymbol{n})^2}.$$

The expression in square brackets is another vector triple product giving:

$$\frac{\mathrm{d}}{\mathrm{d}t'}\left(\frac{\boldsymbol{n} \times [\boldsymbol{n} \times \boldsymbol{\beta}]}{(1 - \boldsymbol{\beta} \cdot \boldsymbol{n})}\right) = \frac{\boldsymbol{n} \times [\boldsymbol{n} \times \dot{\boldsymbol{\beta}}]}{(1 - \boldsymbol{\beta} \cdot \boldsymbol{n})^2} + \frac{\boldsymbol{n} \times (\boldsymbol{n} \times [\boldsymbol{n} \times (\boldsymbol{\beta} \times \dot{\boldsymbol{\beta}}])}{(1 - \boldsymbol{\beta} \cdot \boldsymbol{n})^2}.$$

Using $\boldsymbol{n} \times (\boldsymbol{n} \times [\boldsymbol{n} \times (\boldsymbol{\beta} \times \dot{\boldsymbol{\beta}}]) = -\boldsymbol{n} \times (\boldsymbol{\beta} \times \dot{\boldsymbol{\beta}})$, to give:

$$\frac{\mathrm{d}}{\mathrm{d}t'}\left(\frac{\boldsymbol{n} \times [\boldsymbol{n} \times \boldsymbol{\beta}]}{(1 - \boldsymbol{\beta} \cdot \boldsymbol{n})}\right) = \frac{\boldsymbol{n} \times [(\boldsymbol{n} - \boldsymbol{\beta}) \times \dot{\boldsymbol{\beta}}]}{(1 - \boldsymbol{\beta} \cdot \boldsymbol{n})^2}. \tag{2.56}$$

Equations 2.55 and 2.56 can now be substituted into Equation 2.54:

$$\boldsymbol{E}(\omega) = -\frac{q}{4\pi c \epsilon_0 r} \mathrm{e}^{\frac{\mathrm{i}\omega r}{c}} \int_{-\infty}^{\infty} \frac{\mathrm{d}}{\mathrm{d}t'}\left(\frac{\boldsymbol{n} \times [\boldsymbol{n} \times \boldsymbol{\beta}]}{(1 - \boldsymbol{\beta} \cdot \boldsymbol{n})}\right) \mathrm{e}^{\mathrm{i}\omega\left(t' - \frac{\boldsymbol{n} \cdot \boldsymbol{R}(t')}{c}\right)} \mathrm{d}t',$$

which can immediately be simplified as:

$$\frac{\mathrm{d}}{\mathrm{d}t'} \mathrm{e}^{\mathrm{i}\omega\left(t' - \frac{\boldsymbol{n} \cdot \boldsymbol{r}(t')}{c}\right)} = \mathrm{i}\omega(1 - \boldsymbol{\beta}' \cdot \boldsymbol{n}) \mathrm{e}^{\mathrm{i}\omega\left(t' - \frac{\boldsymbol{n} \cdot \boldsymbol{R}(t')}{c}\right)},$$

and cancelling a further factor of $(1 - \boldsymbol{\beta}' \cdot \boldsymbol{n})$ gives:

$$\boldsymbol{E}(\omega) = -\frac{\mathrm{i}\omega q}{4\pi c \epsilon_0 r} \mathrm{e}^{\frac{\mathrm{i}\omega r}{c}} \int_{-\infty}^{\infty} \boldsymbol{n} \times [\boldsymbol{n} \times \boldsymbol{\beta}] \mathrm{e}^{\mathrm{i}\omega\left(t' - \frac{\boldsymbol{n} \cdot \boldsymbol{R}(t')}{c}\right)} \mathrm{d}t'. \tag{2.57}$$

$\boldsymbol{E}$ is in the plane defined by $\boldsymbol{n}$ and $\boldsymbol{\beta}$ and perpendicular to $\boldsymbol{n}$.

Combining Equations 2.49 and 2.57 gives the energy radiated per unit solid angle per unit angular frequency:

$$\frac{\mathrm{d}^2 W}{\mathrm{d}\Omega \mathrm{d}\omega} = \frac{\omega^2 q^2}{16\pi^3 c \epsilon_0} \left| \int_{-\infty}^{\infty} \boldsymbol{n} \times [\boldsymbol{n} \times \boldsymbol{\beta}] \mathrm{e}^{\mathrm{i}\omega\left(t' - \frac{\boldsymbol{n} \cdot \boldsymbol{R}(t')}{c}\right)} \mathrm{d}t' \right|^2. \tag{2.58}$$

This integral must now be solved for the particular motion of an electron moving through the periodic magnetic field of an undulator, which is analysed in the following section.

2.5 Electron Motion in an Undulator

The radiation characteristics are dependent upon the motion of the charge. An undulator is a magnetic device that creates a periodic magnetic field of wavelength λ_u in the longitudinal direction z. The transverse angles $\alpha_{x,\,y}(z)$ and positions x or y of an electron passing through an arbitrary magnetic field $B_{x,\,y}(z)$ can be found by using the first and second

field integrals $I_{x,\,y}$ and $J_{x,\,y}$, respectively [41]:

$$I_{x,y} = \int_{-\infty}^{\infty} B_{x,y}(z)\mathrm{d}z, \tag{2.59}$$

for the second integral, a dummy variable z' is required:

$$J_{x,y} = \int_{-\infty}^{\infty}\int_{-\infty}^{z} B_{x,y}(z')\mathrm{d}z'\mathrm{d}z. \tag{2.60}$$

These give:

$$\alpha_{x,y} = \frac{e}{\gamma m_0 c} I_{x,y}, \tag{2.61}$$

$$x, y = \frac{e}{\gamma m_0 c} J_{x,y}. \tag{2.62}$$

In the following perfectly sinusoidal magnetic fields in the planes transverse to the electron's initial velocity are considered. The longitudinal field, B_z, is zero and arbitrary sinusoidal fields in both transverse planes, B_x and B_y, with magnitudes $B_{0,x}$ and $B_{0,y}$ can be defined by:

$$B_x = B_{0,x}\sin(k_u z + \Psi),$$

$$B_y = B_{0,y}\sin(k_u z),$$

where $k_u = \frac{2\pi}{\lambda_u}$ and Ψ is an arbitrary phase difference between the two fields. With no electric fields present these magnetic fields do not satisfy Maxwell's equations and are therefore not physical. The conclusions of this section would not be greatly affected by including the missing terms, and the simplification makes the derivation easier. The motion of a particle of charge e can be derived from the equation of motion for a particle in a magnetic field:

$$\boldsymbol{a} = \frac{e}{\gamma m}\boldsymbol{v} \times \boldsymbol{B},$$

where $\boldsymbol{a}$ is the acceleration, γ is the relativistic factor, m is the particle's mass and $\boldsymbol{v}$ its velocity. Hence:

$$\ddot{x} = -\frac{e}{\gamma m}\dot{z}B_y,$$

$$\ddot{y} = \frac{e}{\gamma m}\dot{z}B_x.$$

These expressions can be integrated to give the transverse velocities:

$$\begin{aligned}\dot{x} &= \int \ddot{x}\mathrm{d}t \\ &= -\int \frac{eB_{0,y}}{\gamma m}\frac{\mathrm{d}z}{\mathrm{d}t}\sin(k_u z)\mathrm{d}t \\ &= \frac{eB_{0,y}}{\gamma m k_u}\cos(k_u z)\end{aligned}$$

and

$$\dot{y} = -\frac{eB_{0,x}}{\gamma m k_u}\cos(k_u z + \Psi).$$

In terms of the scaled velocity $\boldsymbol{\beta}$ and the undulator deflection parameters $K_x = \frac{eB_{0,x}\lambda_u}{2\pi mc}$ and $K_y = \frac{eB_{0,y}\lambda_u}{2\pi mc}$ the transverse motion of the particle is given by:

$$\beta_x = \frac{K_y}{\gamma}\cos(k_u z),$$

and

$$\beta_y = -\frac{K_x}{\gamma}\cos(k_u z + \Psi).$$

The longitudinal component of $\boldsymbol{\beta}$ can be calculated by assuming that the energy of the electron remains constant using the expression:

$$\beta^2 = \beta_x^2 + \beta_y^2 + \beta_z^2.$$

This gives:

$$\beta_z^2 = \beta^2 - \left(\frac{K_y}{\gamma}\cos(k_u z)\right)^2 - \left(-\frac{K_y}{\gamma}\cos(k_u z + \Psi)\right)^2.$$

Using the trigonometric identity $2\cos^2(\theta) \equiv \cos(2\theta) + 1$ gives:

$$\beta_z^2 = \beta^2 - \frac{K_y^2}{2\gamma^2}(\cos[2k_u z] + 1) - \frac{K_x^2}{2\gamma^2}(\cos[2k_u z + 2\Psi] + 1).$$

To find β_z, the square root must be taken. This can be approximated using the series expansion, $\sqrt{1-x} \approx 1 - \frac{x}{2}$, giving:

$$\beta_z \approx \beta - \frac{K_y^2}{4\gamma^2}(\cos[2k_u z] + 1) - \frac{K_x^2}{4\gamma^2}(\cos[2k_u z + 2\Psi] + 1) \quad \text{for} \quad \beta \approx 1.$$

Hence the velocity in the z direction is a constant with oscillatory terms relating to the motion in the transverse planes. The mean velocity in the z direction, $\langle\beta_z\rangle$, is:

$$\langle\beta_z\rangle \approx \beta\left(1 - \frac{K_x^2}{4\gamma^2} - \frac{K_y^2}{4\gamma^2}\right), \tag{2.63}$$

and, as $\beta = \sqrt{1 - \frac{1}{\gamma^2}}$, β can be expanded in terms of γ using the same series as above:

$$\langle\beta_z\rangle \approx 1 - \frac{1}{2\gamma^2} - \frac{K_x^2}{4\gamma^2} - \frac{K_y^2}{4\gamma^2}. \tag{2.64}$$

For a high energy electron in an undulator $\frac{K}{\gamma} \ll 1$, enabling the argument of the cosine terms of the transverse velocity to be approximated as:

$$\begin{aligned} k_u z &\approx \frac{2\pi\langle\beta_z\rangle ct}{\lambda_u} \\ &= \Omega t. \end{aligned}$$

This gives, for each component of the velocity:

$$\dot{x} = \frac{cK_y}{\gamma}\cos(\Omega t),$$

$$\dot{y} = \frac{cK_x}{\gamma}\cos(\Omega t + \Psi)$$

and

$$\dot{z} = \langle\beta_z\rangle c - \frac{c}{4\gamma^2}[K_y^2\cos[2\Omega t] - K_x^2\cos(2\Omega t 2\Psi)].$$

These expressions can be directly integrated to give the particle's co-ordinates:

$$\begin{aligned} x &= \int \dot{x}\mathrm{d}t \\ &= \int \frac{cK_y}{\gamma}\cos(\Omega t)\mathrm{d}t \\ &= \frac{cK_y}{\gamma\Omega}\sin(\Omega t), \end{aligned} \tag{2.65}$$

$$y = -\frac{cK_x}{\gamma\Omega}\sin(\Omega t + \Psi) \tag{2.66}$$

and

$$z = \langle\beta_z\rangle ct - \frac{c}{8\gamma^2\Omega}[K_y^2\cos[2\Omega t] + K_x^2\sin(2\Omega t + 2\Psi)]. \tag{2.67}$$

The motion of the particle in the magnetic field has now been completely characterised. More simplifications can be made as the motion is periodic. This periodicity leads to interference effects.

2.6 Interference Effects in an Undulator

The multiple periods in an undulator mean there are evenly spaced multiple source points. These give rise to interference effects that depend upon the periodicity of the undulator and the angle of observation, analogous to those observed in a diffraction grating.

2.6.1 The Undulator Equation

The interference of radiation produced by the same electron at different points along its trajectory is now considered. The time taken for an electron to travel one period is $\frac{\lambda_u}{\langle\beta_z\rangle c}$. In this time, the radiation wave-front has travelled a distance $\frac{\lambda_u}{\langle\beta_z\rangle}$. If the radiation is emitted at an arbitrary angle θ, then the distance d between the electron beam and the radiation wave-front is (see Figure 2.2):

$$d = \frac{\lambda_u}{\langle\beta_z\rangle} - \lambda_u \cos\theta.$$

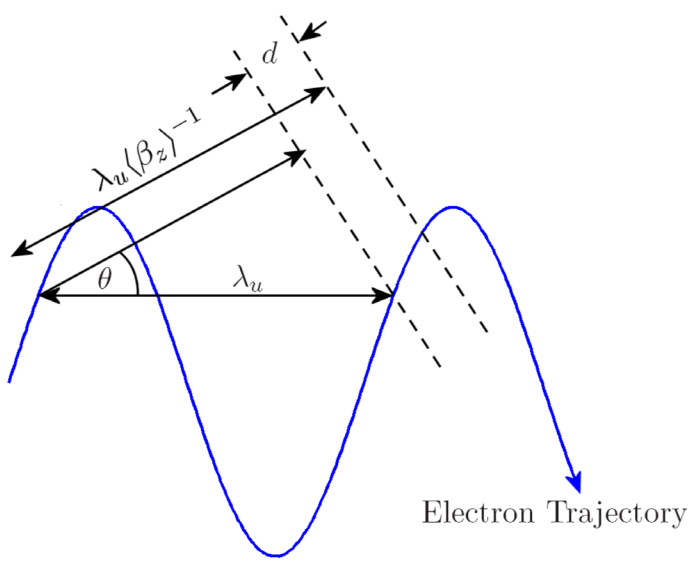

Figure 2.2: Geometry for periodic motion and the interference condition in an undulator.

If d is an integral number of radiation wavelengths, λ_{rad}, then there will be constructive interference, that is if:

$$\frac{\lambda_u}{\langle\beta_z\rangle} - \lambda_u \cos\theta = n\lambda_{rad}, \tag{2.68}$$

where n is a natural number. The quantity $\langle\beta_z\rangle^{-1}$ can be expressed as a power series:

$$\langle\beta_z\rangle^{-1} \approx 1 + \frac{1}{2\gamma^2} + \frac{K_x^2}{4\gamma^2} + \frac{K_y^2}{4\gamma^2},$$

and the cosine function replaced with a sine using the identity $\cos(\theta) \equiv 1 - 2\sin^2\left(\frac{\theta}{2}\right)$:

$$\lambda_u\left(1 + \frac{1}{2\gamma^2} + \frac{K_x^2}{4\gamma^2} + \frac{K_y^2}{4\gamma^2}\right) - \lambda_u\left(1 - 2\sin^2\left(\frac{\theta}{2}\right)\right) = n\lambda_{rad}.$$

For small angles:

$$\lambda_{rad} = \frac{\lambda_u}{2n\gamma^2}\left(1 + \frac{K_x^2}{2} + \frac{K_y^2}{2} + \gamma^2\theta^2\right).$$

It is seen that the wavelength of the emitted radiation only depends upon the amplitudes and wavelengths of the two transverse fields and not their relative phase difference Ψ.

2.6.2 Radiation Phase and the Line-Shape Function

The electron motion is periodic through an undulator and so the integral over each successive period must be the same, except for a phase factor. The time taken for the electron to travel one period is $\frac{\lambda_u}{c\langle\beta_z\rangle}$. Using this time for the limits of the integration[17] in Equation 2.58 and considering N periods, this equation becomes:

$$\begin{aligned}\frac{\mathrm{d}^2W}{\mathrm{d}\Omega\mathrm{d}\omega} &= \frac{\omega^2 q^2}{16\pi^3 c\epsilon_0}\left|\int_{-\frac{\lambda_u}{2c\langle\beta_z\rangle}}^{\frac{\lambda_u}{2c\langle\beta_z\rangle}} \boldsymbol{n}\times[\boldsymbol{n}\times\boldsymbol{\beta}]\mathrm{e}^{\mathrm{i}\omega\left(t'-\frac{\boldsymbol{n}\cdot\boldsymbol{R}(t')}{c}\right)}\mathrm{d}t'\right|^2 \\ &\quad\times\left(1 + \mathrm{e}^{\mathrm{i}\omega\frac{d}{c}} + \mathrm{e}^{\mathrm{i}\omega\frac{2d}{c}} + ... + \mathrm{e}^{\mathrm{i}\omega\frac{(N-1)d}{c}}\right)^2.\end{aligned} \tag{2.69}$$

The set of phase factors is a geometric series of the form:

$$\sum_{n=0}^{N-1} \mathrm{e}^{2\mathrm{i}\Lambda n} = 1 + \mathrm{e}^{2\mathrm{i}\Lambda} + \mathrm{e}^{4\mathrm{i}\Lambda} + ... + \mathrm{e}^{2\mathrm{i}\Lambda(N-1)},$$

[17] This analysis assumes that the motion of the electron is entirely periodic, for a real device there are end effects that are not considered here. For large numbers of periods the correction due to end effects is small.

which is of the form [44]:

$$\begin{aligned} S_n &= \sum_{n=0}^{N-1} ar^n \\ &= \frac{a(1-r^N)}{(1-r)}. \end{aligned}$$

Substituting $a = 1$ and $r = \mathrm{e}^{2\mathrm{i}\Lambda}$ gives:

$$\begin{aligned} S_n &= \frac{1-\mathrm{e}^{2\mathrm{i}\Lambda N}}{1-\mathrm{e}^{2\mathrm{i}\Lambda}} \\ &= \frac{\mathrm{e}^{\mathrm{i}\Lambda N}(\mathrm{e}^{-\mathrm{i}\Lambda N}-\mathrm{e}^{\mathrm{i}\Lambda N})}{\mathrm{e}^{\mathrm{i}\Lambda}(\mathrm{e}^{-\mathrm{i}\Lambda}-\mathrm{e}^{\mathrm{i}\Lambda})} \\ &= \frac{\sin(N\Lambda)}{\sin(\Lambda)}\mathrm{e}^{\mathrm{i}\Lambda(N-1)}. \end{aligned}$$

When multiplied by its complex conjugate, this expression is the familiar grating function:

$$S_n^2 = \frac{\sin^2(N\Lambda)}{\sin^2(\Lambda)},$$

which is associated with interference from successive periods of multiple source points, as in a diffraction grating or undulator. The relevant form of Λ for an undulator must now be found. The increase in phase over one period is:

$$\begin{aligned} \omega\left(t' - \frac{\boldsymbol{n}\cdot\boldsymbol{R}(t')}{c}\right) &= \frac{\omega\lambda_u}{c}\left(\frac{1}{\langle\beta_z\rangle} - \cos(\theta)\right) \\ &= \frac{2\pi\omega}{\omega_1(\theta)}. \end{aligned}$$

The function $\omega_1(\theta)$ is the fundamental frequency, which is a dependent on the observation angle. The grating function is now:

$$\frac{\sin^2\left(\frac{N\pi\omega}{\omega_1}\right)}{\sin^2\left(\frac{\pi\omega}{\omega_1}\right)}.$$

This function is analogous to the grating function used when analysing diffraction from gratings or crystals. Physically, it represents the interference between succsessive sources (periods of the undulator). It selects frequencies that are near the harmonics and decreases rapidly as ω changes in either direction, corresponding to the electromagnetic waves moving further and further out of phase at the observation point. Letting $\Delta\omega = \omega - n\omega_1(\theta)$

and normalising the function to unit amplitude, the so-called line-shape function can be defined:

$$L\left(\frac{N\Delta\omega}{\omega_1(\theta)}\right) = \frac{\sin^2\left(\frac{N\pi\Delta\omega}{\omega_1(\theta)}\right)}{N^2\sin^2\left(\frac{\pi\Delta\omega}{\omega_1(\theta)}\right)}.$$

Equation 2.69 is now:

$$\frac{\mathrm{d}^2W}{\mathrm{d}\Omega\mathrm{d}\omega} = \frac{\omega^2q^2}{16\pi^3c\epsilon_0}L\left(\frac{N\Delta\omega}{\omega_1(\theta)}\right)\left|\int_{-\frac{\lambda_u}{2c\langle\beta_z\rangle}}^{\frac{\lambda_u}{2c\langle\beta_z\rangle}} \boldsymbol{n}\times[\boldsymbol{n}\times\boldsymbol{\beta}]\mathrm{e}^{\mathrm{i}\omega\left(t'-\frac{\boldsymbol{n}\cdot\boldsymbol{R}(t')}{c}\right)}\mathrm{d}t'\right|^2. \tag{2.70}$$

The next step is to find suitable expressions to solve the remaining integral.

2.7 Undulator Radiation

Having now characterised the motion of an electron through an undulator, Equation 2.70 can be solved by finding the relevant forms for $\boldsymbol{n}\times[\boldsymbol{n}\times\boldsymbol{\beta}]$ and $\omega\left(t'-\frac{\boldsymbol{n}\cdot\boldsymbol{R}(t')}{c}\right)$.

2.7.1 Expression for $\boldsymbol{n}\times[\boldsymbol{n}\times\boldsymbol{\beta}]$

The unit vector pointing from the particle to the observation point is $\boldsymbol{n}$ and it can be defined simply from Figure 2.3:

$$\boldsymbol{n} = (\sin(\theta)\cos(\phi),\ \sin(\theta)\sin(\phi),\ \cos(\theta)).$$

The vector triple product $\boldsymbol{n}\times[\boldsymbol{n}\times\boldsymbol{\beta}]$ can be calculated if it is assumed that θ is small and the sine and cosine terms are expanded:

$$\boldsymbol{n}\times[\boldsymbol{n}\times\boldsymbol{\beta}] = (\beta_z\theta\cos(\phi)-\beta_x,\ \beta_z\theta\sin(\phi)-\beta_y,\ \beta_x\theta\cos(\phi)+\beta_y\theta\sin(\phi)).$$

Assuming $\beta_x \ll \beta_z$, $\beta_y \ll \beta_z$ and $\beta_z \approx 1$ gives:

$$\boldsymbol{n}\times[\boldsymbol{n}\times\boldsymbol{\beta}] = (\theta\cos(\phi)-\beta_x,\ \theta\sin(\phi)-\beta_y,\ 0). \tag{2.71}$$

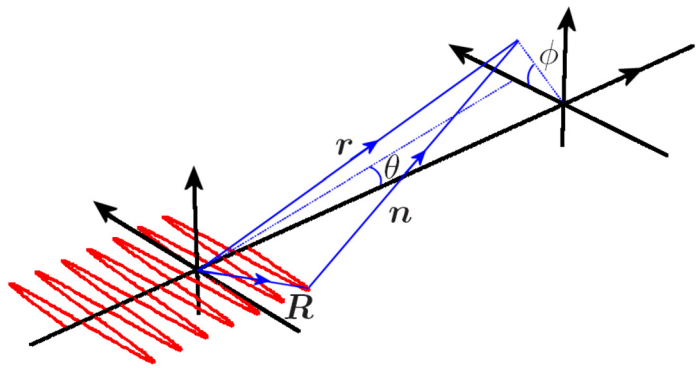

Figure 2.3: Co-ordinate system for electron motion in an undulator (red line): $\boldsymbol{R}$ is the vector from the origin to the particle, $\boldsymbol{r}$ is the vector from the origin to the observation point.

2.7.2 Expression for $\omega\left(t' - \frac{\boldsymbol{n}\cdot\boldsymbol{R}}{c}\right)$

The exponential in Equation 2.70 can now be replaced by the relevant expression for electron motion through an undulator. From Equations 2.65, 2.66 and 2.67 and Figure 2.3 the vector $\boldsymbol{R}$ is:

$$\begin{aligned}\boldsymbol{R} &= (x,\ y,\ z)\\ &= \left(\frac{cK_y}{\gamma\Omega}\sin(\Omega t),\ -\frac{cK_x}{\gamma\Omega}\sin(\Omega t+\Psi),\right.\\ &\quad \left.\langle\beta_z\rangle ct - \frac{c}{8\gamma^2\Omega}[K_y^2\sin(2\Omega t)+K_x^2\sin(2\Omega t+2\Psi)]\right),\end{aligned}$$

giving:

$$\begin{aligned}\omega\left(t' - \frac{\boldsymbol{n}\cdot\boldsymbol{R}}{c}\right) &= \left(\omega t - \frac{\omega K_y}{\gamma\Omega}\theta\cos(\phi)\sin(\Omega t) + \right.\\ &\quad \frac{\omega K_x}{\gamma\Omega}\theta\sin(\phi)\sin(\Omega t+\Psi) - \langle\beta_z\rangle\omega t\cos(\theta) - \\ &\quad \left.\frac{\omega}{8\gamma^2\Omega}[K_y^2\sin(2\Omega t)+K_x^2\sin(2\Omega t+2\Psi)]\cos(\theta)\right). \qquad (2.72)\end{aligned}$$

For large values of N, ω need only be evaluated at harmonic frequencies of the fundamental, using Equations 2.68 and 2.65:

$$\begin{aligned}n\omega_1 &= \frac{2\pi nc}{\lambda_{rad,1}}\\ &= 2\pi nc\left(\frac{\lambda_u}{\langle\beta_z\rangle} - \lambda_u\cos(\theta)\right)^{-1}\\ &= \frac{n\Omega}{1-\langle\beta_z\rangle\cos(\theta)}.\end{aligned}$$

Using Equation 2.63 to substitute for $\langle\beta_z\rangle$ and expanding the cosine terms gives:

$$\frac{n\Omega}{1-\langle\beta_z\rangle\cos(\theta)} = \frac{n\Omega}{1-\beta\left(1-\frac{K_x^2}{4\gamma^2}-\frac{K_y^2}{4\gamma^2}\right)\left(1-\frac{\theta^2}{2}\right)}.$$

For relativistic electrons $\beta \approx 1$, and dropping terms $\propto K^2\theta^2$ gives:

$$n\omega_1 = \frac{2n\Omega\gamma^2}{1+\frac{K_y^2}{2}+\frac{K_x^2}{2}+\gamma^2\theta^2}.$$

These values of ω need to be substituted back into Equation 2.72. Going through the algebra and using the relationship:

$$\sin(\theta) = \frac{\tan(\theta)}{\sqrt{1+\tan^2(\theta)}},$$

gives the result:

$$\omega\left(t' - \frac{\boldsymbol{n}.\boldsymbol{R}}{c}\right) = n\Omega t - X\sin(\Omega t - \Phi) + Y\sin(2\Omega t + \Psi), \tag{2.73}$$

Here:

$$X = \frac{2n\gamma\theta K}{A}\sqrt{K_y^2\cos^2(\phi) + K_x^2\sin^2(\phi) - 2K_xK_y\sin(\phi)\cos(\phi)\cos(2\Psi)}, \tag{2.74}$$

$$Y = \frac{n}{4A}\sqrt{K_y^4 + K_x^4 + 2K_y^2K_x^2\cos(2\Psi)}, \tag{2.75}$$

$$A = 1 + \frac{K_y^2}{2} + \frac{K_x^2}{2} + \gamma^2\theta^2, \tag{2.76}$$

$$\tan(\Phi) = -\frac{K_x\sin(\phi)\sin(\psi)}{K_x\sin(\phi)\cos(\psi) - K_y\cos(\phi)} \tag{2.77}$$

and

$$\tan(\Psi) = \frac{K_x^2\sin(2\psi)}{K_x^2\cos(2\psi) + K_y^2}. \tag{2.78}$$

2.7.3 Substitution for Bessel Functions

The expression for the exponential term in Equation 2.70 is:

$$\mathrm{e}^{\mathrm{i}(n\Omega t - X\sin(\Omega t-\Phi) + Y\sin(2\Omega t+\Psi))}. \tag{2.79}$$

Functions of the form $\mathrm{e}^{\mathrm{i}\sin(\theta)}$ can be expanded in terms of a series of Bessel functions, $J_p(x)$, using the following relationship [46]:

$$\mathrm{e}^{\mathrm{i}\sin(\theta)} = \sum_{p=-\infty}^{\infty} J_p(x)\mathrm{e}^{\mathrm{i}p\theta}.$$

For Equation 2.79 this gives:

$$\mathrm{e}^{\mathrm{i}[n\Omega t - X\sin(\Omega t-\Phi)+Y\sin(2\Omega t+\Psi)]} = \sum_{p=-\infty}^{\infty}\sum_{p'=-\infty}^{\infty} J_{p'}(X)J_p(Y)\mathrm{e}^{\mathrm{i}[n\Omega t - p'(\Omega t-\Phi)+p(2\Omega t+\Psi)]}, \quad (2.80)$$

Substituting Equations 2.71 and 2.80 into Equation 2.70 gives:

$$\begin{aligned}\frac{\mathrm{d}^2W}{\mathrm{d}\Omega\mathrm{d}\omega} &= \frac{\omega^2q^2}{16\pi^3c\epsilon_0}L\left(\frac{N\Delta\omega}{\omega_1(\theta)}\right)\sum_{p-\infty}^{\infty}\sum_{p'-\infty}^{\infty} J_{p'}(X)J_p(Y)\mathrm{e}^{\mathrm{i}[p\Psi-p'\Phi]} \\ &\times \int_{-\frac{\lambda_u}{2\langle\beta_z\rangle}}^{\frac{\lambda_u}{2c\langle\beta_z\rangle}} (\theta\cos(\phi)-\beta_x,\ \theta\sin(\phi)-\beta_y)\mathrm{e}^{\mathrm{i}\Omega t[n-p'+2p]}\mathrm{d}t \qquad (2.81)\end{aligned}$$

The integral now contains only terms dependent on t. The two terms are due to the polarisation in the two transverse planes. For the terms constant in the transverse planes, the integral over a complete period must equal zero, except when the exponential term is 1, i.e. when:

$$n - p' - 2p = 0$$

For the β_x term there is an additional factor of $\frac{K_y}{\gamma}\cos(\Omega t)$ to deal with. The argument of the integral is of the form:

$$\cos(\Omega t)\mathrm{e}^{\mathrm{i}(n\Omega t - p'\Omega t+2p\Omega t)} = \frac{1}{2}\left(\mathrm{e}^{\mathrm{i}\Omega t(n-p'+2p-1)}\right)\left(1+\mathrm{e}^{2\mathrm{i}\Omega t}\right).$$

Again, this factor will equal zero when integrated over a complete period unless:

$$n - p' + 2p = \pm 1.$$

A similar condition is found for the β_y term, which contains a factor of $\frac{K_x}{\gamma}\sin(\Omega t+\Psi)$. An $\exp^{\pm\mathrm{i}\psi}$ term can be factored out of the integral and the same procedure followed as for β_x, giving the condition where the integral is non-zero as:

$$n - p' + 2p = q \qquad \text{where} \qquad q = -1,\ 0,\ 1.$$

The integrals are now simple to perform, substituting for ω, rearranging (noting that some terms have been factored into the square) and including all the terms that did not depend upon t for the integration gives:

$$\frac{\mathrm{d}^2W}{\mathrm{d}\Omega\mathrm{d}\omega} = \frac{q^2\gamma^2n^2}{4\pi\epsilon_0 cA^2}L\left(\frac{N\Delta\omega}{\omega_1(\theta)}\right)|A_x, A_y|^2,$$

where:

$$A_x = 2\gamma\theta\cos(\phi)Q_0 - K_y(Q_{-1} + Q_1)$$

and

$$A_y = 2\gamma\theta\sin(\phi)Q_0 - K_x(\mathrm{e}^{-\mathrm{i}\psi}Q_{-1} + \mathrm{e}^{\mathrm{i}\psi}Q_1).$$

By substituting for p', Q_q is defined as:

$$Q_q = \sum_{p=-\infty}^{\infty} J_p(Y)J_{n+2p+q}(X)\mathrm{e}^{\mathrm{i}\Phi(n+2p+q)}\mathrm{e}^{\mathrm{i}p\Psi}. \tag{2.82}$$

2.7.4 On-Axis Radiation

On-axis $\theta = 0$ and so $X = 0$. Hence, the only contributing term is when $n + 2p + q = 0$ as:

$$J_k(0) = 0 \text{ for all } k \text{ except when } k = 0 \text{ as } J_0(0) = 1. \tag{2.83}$$

Therefore, $p = -\frac{n+q}{2}$, which can be substituted into Equation 2.82 to give:

$$Q_q = J_{-\frac{n+q}{2}}(Y)\mathrm{e}^{-\mathrm{i}\Psi\frac{(n+q)}{2}}.$$

Only integral orders were in the Bessel function expansion and so the index n must be restricted to odd values and $q = \pm 1$ (therefore $Q_0 = 0$). Hence, there are no even harmonics on axis. The expression can be further simplified by using the fact that:

$$J_{-n}(x) = (-1)^n J_n(x)$$

to handle the negative order Bessel functions. This gives:

$$A_x = K_y\left(J_{\frac{n+1}{2}}(Y)\mathrm{e}^{\mathrm{i}\Psi\frac{n+1}{2}} - J_{\frac{n-1}{2}}(Y)\mathrm{e}^{\mathrm{i}\Psi\frac{n-1}{2}}\right) \tag{2.84}$$

and

$$A_y = K_x \left(-J_{\frac{n+1}{2}}(Y) \mathrm{e}^{\mathrm{i}\Psi \frac{n+1}{2}} \mathrm{e}^{-\mathrm{i}\psi} + J_{\frac{n-1}{2}}(Y) \mathrm{e}^{\mathrm{i}\Psi \frac{n-1}{2}} \mathrm{e}^{\mathrm{i}\psi} \right). \tag{2.85}$$

2.8 Helical Undulator Radiation

For helical undulator radiation, $K_x = K_y = K$ and $\psi = \frac{\pi}{2}$. Substituting these values into Equations 2.74, 2.75, 2.77 and 2.78 gives $X = \frac{2n\gamma\theta K}{A}$, $Y = 0$, $\Psi = 0$ and $\Phi = \phi$. Therefore Q_q is:

$$Q_q = \sum_{p=-\infty}^{\infty} J_p(Y) J_{n+2p+q}(X) \mathrm{e}^{\mathrm{i}\phi(n+2p+q)}.$$

Using Equation 2.83, this expression can be simplified, as the only contributing term is when $p = 0$:

$$Q_q = J_{n+q}(X) \mathrm{e}^{\mathrm{i}\phi(n+q)}.$$

Substituting this back into Equations 2.84 and 2.85 gives:

$$A_x = 2\gamma\theta \cos(\phi) J_n(X) \mathrm{e}^{\mathrm{i}\phi n} - K \left(J_{n-1}(X) \mathrm{e}^{\mathrm{i}\phi(n-1)} + J_{n+1}(X) \mathrm{e}^{\mathrm{i}\phi(n+1)} \right),$$

$$A_y = 2\gamma\theta \sin(\phi) J_n(X) \mathrm{e}^{\mathrm{i}\phi n} + \mathrm{i}K \left(J_{n+1}(X) \mathrm{e}^{\mathrm{i}\phi(n+1)} - J_{n-1}(X) \mathrm{e}^{\mathrm{i}\phi(n-1)} \right).$$

By making the assumption that the radiation is cylindrically symmetric any value for ϕ can be chosen, zero for instance, to give:

$$A_x = 2\gamma\theta J_n(X) - K \left(J_{n-1}(X) + J_{n+1}(X) \right), \tag{2.86}$$

$$A_y = \mathrm{i}K \left(J_{n+1}(X) - J_{n-1}(X) \right). \tag{2.87}$$

This can be re-written using the following relations:

$$J_{n-1}(X) + J_{n+1}(X) = \frac{2n}{X} J_n(X)$$

and

$$J_{n-1}(X) - J_{n+1}(X) = 2J'_n(X),$$

where $J'_n(X) = \frac{\partial}{\partial X} J_n(X)$, to give:

$$A_x = \left(2\gamma\theta - \frac{2nK}{X} \right) J_n(X)$$

and

$$A_y = -2\mathrm{i}KJ_n'(X).$$

The total intensity is then proportional to:

$$\begin{aligned} |A_x + A_y|^2 &= |A_x|^2 + |A_y|^2 \\ &= 4K^2[J_n'(X)]^2 + [J_n(X)]^2\left(\frac{\gamma\theta}{K} - \frac{n}{X}\right)^2. \end{aligned} \tag{2.88}$$

There are no cross terms from the square as the two directions are orthogonal. Hence the expression for the energy radiated per electron, per unit solid angle per unit circular frequency through a perfectly helical field is:

$$\begin{aligned} \frac{\mathrm{d}^2W}{\mathrm{d}\Omega\mathrm{d}\omega} &= \frac{q^2\gamma^2 4K^2}{4\pi\epsilon_0 c(1+K^2)^2} L\left(\frac{N\Delta\omega}{\omega_1(\theta)}\right) \times \\ & \sum_{n=1}^{h} n^2\left(J_n'(X)^2 + J_n(X)^2\left(\frac{\gamma\theta}{K} - \frac{n}{X}\right)^2\right), \end{aligned} \tag{2.89}$$

In this expression, which is the same as that obtained by Kincaid [47], h is the number of harmonics to be included. For the full spectrum $h \longrightarrow \infty$.

2.8.1 Helical Undulator On-Axis Radiation and Polarisation

On-axis $\theta = 0$, therefore $X = 0$ and so only the $n = 1$ harmonic contributes to the series (from Equation 2.86 and Equation 2.87). The transverse amplitudes of the electric field are thus:

$$A_x = -K \text{ and } A_y = -\mathrm{i}K,$$

and the total intensity is:

$$\frac{\mathrm{d}^2W}{\mathrm{d}\Omega\mathrm{d}\omega} = \frac{q^2\gamma^2 2K^2}{4\pi\epsilon_0 c(1+K^2)^2} L\left(\frac{N\Delta\omega}{\omega_1(\theta)}\right).$$

The polarisation of the radiation is determined by the phase relationship between the transverse components of the electric field. For on-axis helical undulator radiation the Stokes' parameters can be found from Equations 2.51, 2.52 and 2.53 and are simply:

$$S_1 = S_2 = 0 \text{ and } |S_3| = 1.$$

This implies that the radiation is purely circularly polarised on-axis.

2.9 Example Figures

Equation 2.89 gives the energy radiated at a particular frequency and angle. It can be integrated over all angles to give the total energy radiated as a function of frequency [47]:

$$\frac{\mathrm{d}W}{\mathrm{d}\omega} = \frac{Ne^2K^2\gamma}{\epsilon_0 c}\sum_{n=1}^{\infty}\left(J_n'(x_n)^2 + \left(\frac{\alpha_n}{K} - \frac{n}{x_n}\right)J_n(x_n)^2\right)\Theta(\alpha_n^2), \tag{2.90}$$

where:

$$\alpha_n^2 = \frac{2n\gamma^2\omega_0}{\omega} - 1 - K^2,$$

$$x_n = \frac{2K\alpha_n\omega}{2\gamma^2\omega_0},$$

and $\Theta(\alpha_n^2)$ is the step function.

Equation 2.90 is plotted in Figure 2.4 for different K parameters, where the intensity has been normalised to the peak intensity and the frequency normalised to the fundamental (on-axis). The different harmonics have been plotted separately to show how for higher K parameters the significance of the higher harmonics increases.

Alternatively, Equation 2.89 can be integrated over all frequencies to give the angular distribution of the energy (or power) radiated from a helical undulator:

$$\begin{aligned}\frac{\mathrm{d}W}{\mathrm{d}\Omega}(\theta) &= \frac{2Ne^2\gamma^4\omega_u}{4\pi\epsilon_0 c}\frac{K^2}{(1+K^2+\gamma^2\theta^2)^3} \\ &\quad\times\sum_{n=1}^{\infty}n^2\left(J_n'^2(x_n) + \left(\frac{\gamma\theta}{K} - \frac{n}{x_n}\right)^2 J_n^2(x_n)\right).\end{aligned} \tag{2.91}$$

Here, $x_n = \frac{2Kn\gamma\theta}{1+K^2+\gamma^2\theta^2}$.

The angular power distribution is plotted in Figure 2.5 for different K parameters, where the power has been normalised to the on-axis power. The different harmonics have been plotted separately to show how for higher K parameters the significance of the higher harmonics increases.

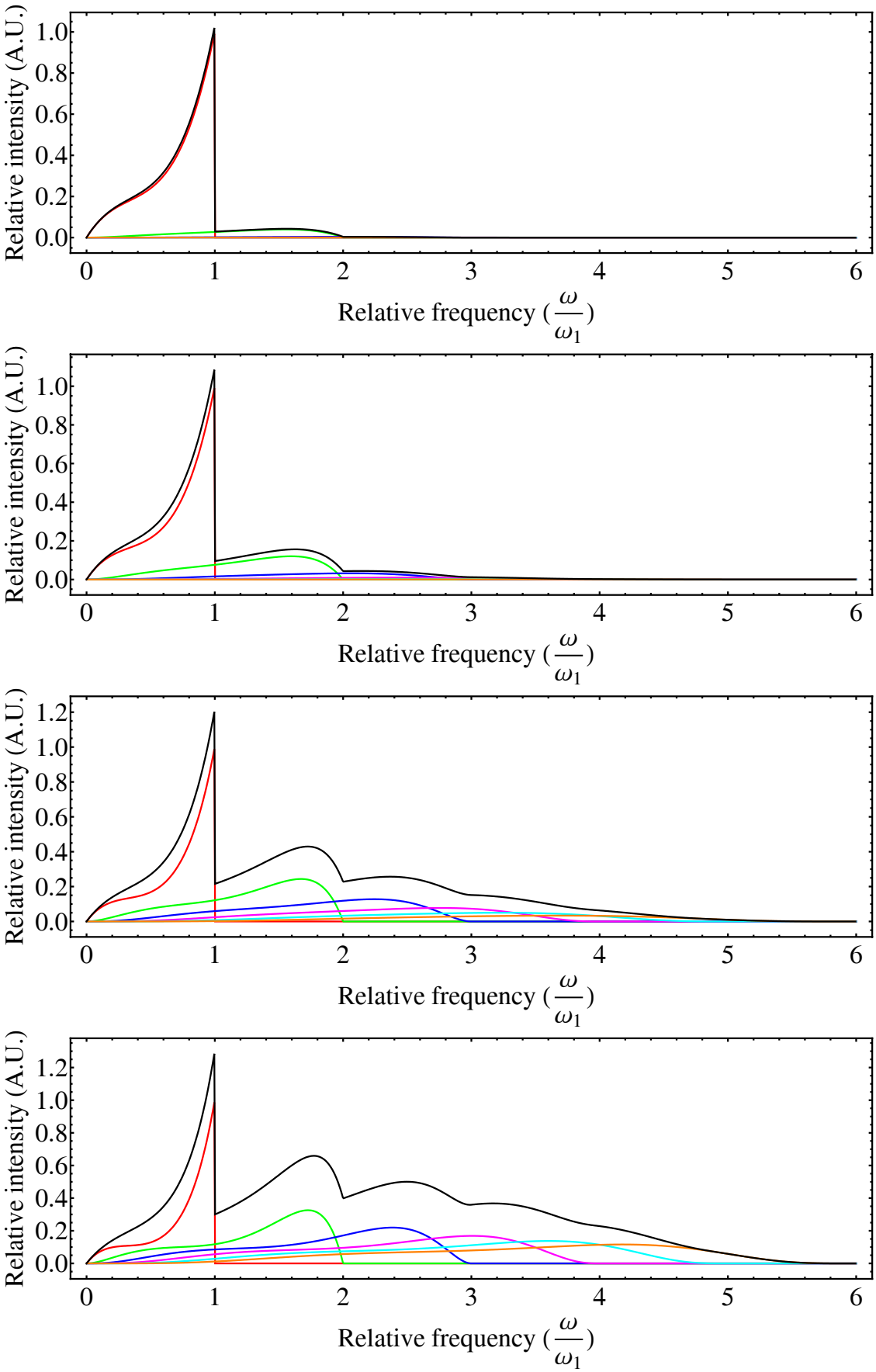

Figure 2.4: Relative intensity in total (black) and into the first six harmonics (red, green, blue, magenta, cyan, orange) from a helical undulator vs relative frequency for K=0.25, 0.5, 1 and 2 (top to bottom).

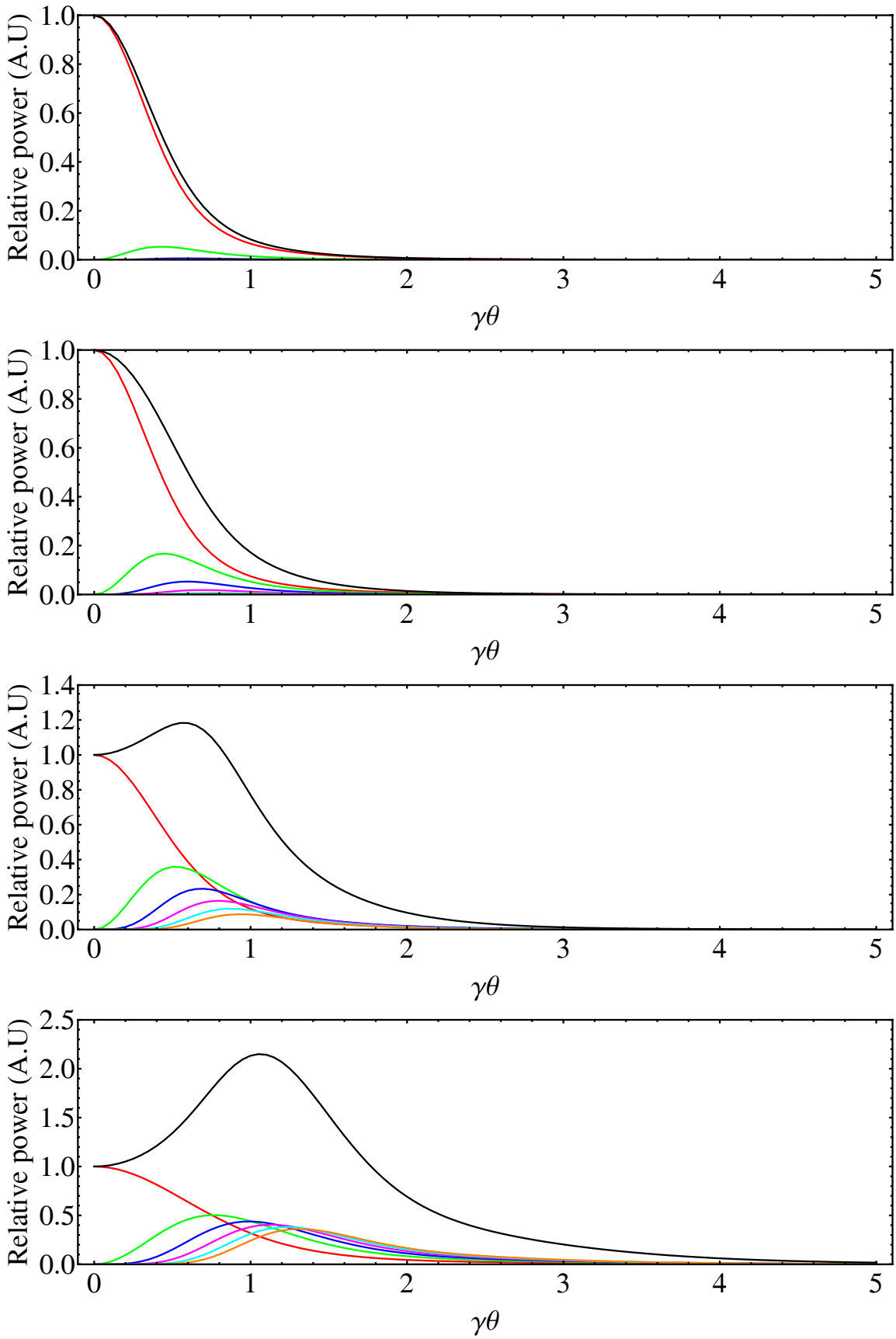

Figure 2.5: Relative angular power distribution in total (black) and in the first six harmonics (red, green, blue, magenta, cyan, orange) from a helical undulator vs observation angle for K=0.25, 0.5, 1 and 2 (top to bottom).

2.9.1 Numerical Codes for Synchrotron Radiation Calculations

The above derivation has been for a single electron. To include an electron beam with a non-zero size and divergence, a convolution with these properties is required. Often, calculations of the radiation into a particular aperture are also required which necessitates numerical integration of Equation 2.89.[18] There are a number of numerical codes available that have been developed over many years to perform these types of calculations [48, 49, 50]. As an example, Figure 2.6 shows the relative flux and circular polarisation (CP) rate into varying angular apertures for a $K = 1$ helical undulator as calculated by the code SPECTRA [50].

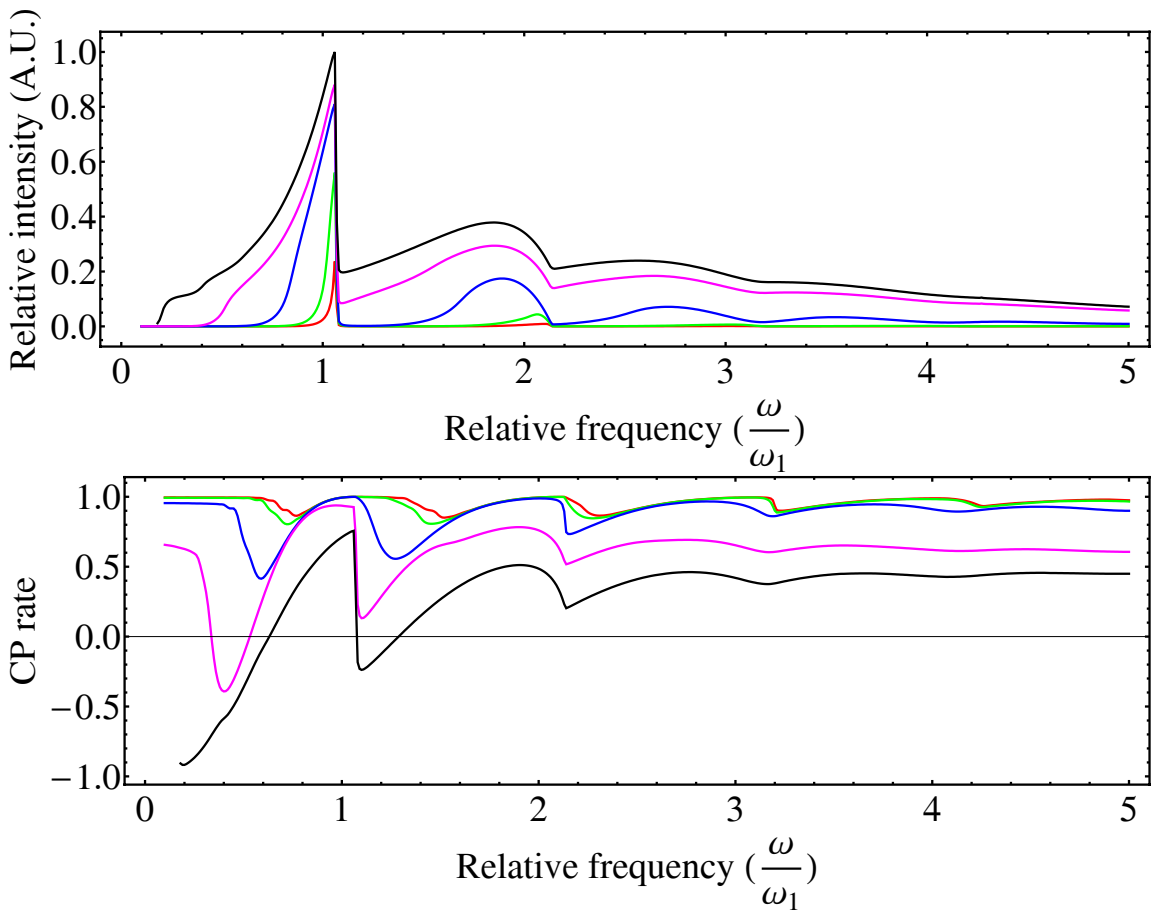

Figure 2.6: Relative intensity (top) and CP rate (bottom) of a $K = 1$ undulator into angular apertures of 1 μrad (red), 2 μrad (green), 5 μrad (blue), 10 μrad (magenta) and 20 μrad (black).

One of the objectives in performing the detailed derivation outlined in this chapter is to understand where assumptions have been made to enable codes that calculate SR to be refined. Equation 2.38 is used by SPECTRA to calculate the near-field radiation spectrum, however the radiated power per unit area is calculated using Equation 2.44 and not Equa-

[18] Or one of the equations earlier in the derivation, for example Equation 2.38.

tion 2.42. In SPECTRA, $\boldsymbol{E} \cdot \boldsymbol{n}$ is tacitly assumed to be zero [51]. This assumption may not be valid for accurate calculation of the SR at large angles and short distances downstream of the undulator. For the ILC, these types of calculations are necessary for specification of the vacuum system,[19] that is why the assumptions need to be well understood for any future code development.

2.10 The Photon Flux

In order to obtain the photon flux, the above expressions must be converted using the Planck relationship between energy and frequency, $E = \hbar\omega$. Letting $\dot{N}_\gamma$ be the photon flux, then the number of photons emitted into a fractional energy range[20] $\frac{\mathrm{d}E}{E}$ is simply:

$$\frac{\mathrm{d}\dot{N}_\gamma}{\frac{\mathrm{d}E}{E}} = \frac{E\mathrm{d}\dot{N}_\gamma}{\mathrm{d}E},$$

The quantity $E\mathrm{d}\dot{N}_\gamma$ is just the power emitted at that particular energy. This means that:

$$\frac{E\mathrm{d}\dot{N}_\gamma}{\mathrm{d}E} = \frac{\mathrm{d}P}{\mathrm{d}E} = \frac{1}{\hbar}\frac{\mathrm{d}P}{\mathrm{d}\omega}.$$

The number of photons emitted into the fractional energy range $\frac{\mathrm{d}E}{E}$ is thus:

$$\mathrm{d}\dot{N}_\gamma = \frac{1}{\hbar}\frac{\mathrm{d}P}{\mathrm{d}\omega}\frac{\mathrm{d}E}{E},$$

where $\frac{\mathrm{d}P}{\mathrm{d}\omega}$ is simply $\frac{\mathrm{d}I}{\mathrm{d}\omega}$ multiplied by the number of electrons passing through the undulator per second, $\dot{N}_{e^-}$. This finally gives:

$$\mathrm{d}\dot{N}_\gamma = \frac{\mathrm{d}I}{\mathrm{d}\omega}\frac{\mathrm{d}E}{E}\frac{\dot{N}_{e^-}}{\hbar}. \tag{2.92}$$

The relative number of photons for each harmonic for a $K = 1$ undulator is shown in Figure 2.7 as a function of frequency.

[19] See Chapter 4

[20] Typically the energy bandwidth is taken to be 0.1%.

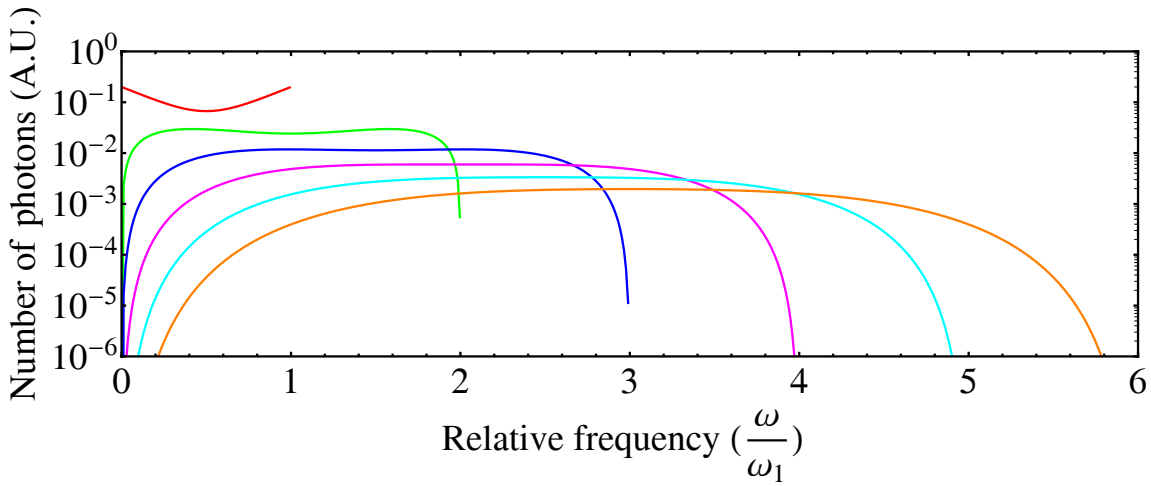

Figure 2.7: Relative number of photons into the first six harmonics (red, green, blue, magenta, cyan, orange) for a K=1 undulator.

2.11 Summary

The far-field radiation spectrum for charges moving through an undulator has been shown. The explicit case of helical motion has been considered and used to derive expressions for the angular distribution of energy as a function of radiation frequency. For this case it has been shown that the on-axis radiation must be circularly polarised. The key points in this derivation are:

- Maxwell's equations for the electric and magnetic fields are written in terms of scalar and vector potentials in the Lorenz gauge.
- The four Maxwell equations expressed using scalar and vector potentials are shown to be two inhomogenous wave equations with source terms provided by the charge and current densities.
- These equations are solved using the Green's function technique for both stationary and moving charges. (The potentials for moving charges are known as the Liénard-Wiechert potentials.)
- From these potentials, the electric and magnetic fields at an arbitrary point due to arbitrary motion of a charge are derived.
- The concept of energy flow of an electromagnetic field is used to calculate the radiation spectrum at a point. This is done by taking the Fourier transform of the acceleration field of the electric field components.

- The Stokes' parameters and polarisation rates are defined.
- The motion of an electron through the periodic magnetic field of an undulator is characterised.
- The radiation due to this periodic motion of charges is calculated.

Chapter 3

Selection of the Optimum Undulator Magnet Technology

In this chapter, having developed the necessary formilism, helical undulator designs that are suitable for the ILC positron source are considered. Permanent and super-conducting (SC) magnet designs are considered.

The parameters for the positron source undulator in the ILC Baseline Configuration Document (ILC-BCD) are shown in Table 3.1 [11]. These parameters were based on theoretical and computational models only [15, 52] and so an experimental model was required to demonstrate their feasibility. Therefore, a programme of work was undertaken to try and produce a suitable undulator. It is only through the building of test models that realistic undulator parameters can be specified and then their consequences for the overall source performance evaluated. Even though exact values for some parameters, such as the degree of circular polarisation (CP), beam aperture and undulator field integrals, are not yet fixed, it is still possible to evaluate the alternative solutions. Generally, increasing the length of the undulator will solve most issues. For example, if the degree of CP is not high enough then more photon collimation will be required and therefore an increased length of active undulator will be needed to maintain the positron intensity. The length of undulator required is ∼100 m for an unpolarised positron source and is anticipated to be ∼200 m for a polarised positron source, although these numbers depend upon many assumptions that have yet to be confirmed, such as the performance of realistic undulators.

The issues that are of obvious concern are the ease of fabrication of the undulator, achieving a suitable magnetic field strength and quality, the operational reliability and

Table 3.1: ILC-BCD undulator parameters.

Parameter	Unit	Value
Undulator Type		Helical
Undulator Period, λ_u	mm	10
Undulator K Parameter		1
Undulator Length (Unpolarised Source)	m	100

flexibility of the device and, lastly, cost. As described below, after a comprehensive paper study [53, 54, 55, 56, 57, 58, 59, 60] short test pieces of the two most promising designs were fabricated, one based on permanent magnet technology and the other on SC magnet technology [61]. These test devices were then measured and compared. The SC undulator was chosen instead of the permanent magnet alternative. This was because of its superior performance in terms of magnetic field strength and quality, operational flexibility, risk of radiation damage and cost [62]. The results from further prototypes, (that included iron to increase the on-axis magnetic field) are also presented [63, 64]. Based on these prototypes, the undulator parameters used for the ILC Reference Design Report (ILC-RDR) were determined.

3.1 Pure Permanent Magnet Helical Undulators

A magnet is said to be permanent if it can support a useful flux into an air gap without an external power source. It is not permanent if it can only do so with the aid of an external electrical or magnetic input. A good introduction to permanent magnets is given in [65]. Descriptions of their use in undulators can also be found in a number of places [41, 42, 43]. Permanent magnet (PM) materials have been used in undulator designs for over 25 years because they offer a number of benefits over electromagnets:

- A small amount of material can provide strong fields in a small volume.
- The magnets are immersible in other fields.
- They require no power supplies and no cooling, therefore there are virtually no running costs.

There are also disadvantages:

- They can be de-magnetised, reducing their field strength irrecoverably.
- They are susceptible to radiation damage.
- They may have to operate at high temperatures during a vacuum system bake-out.
- They are expensive.

Two different designs of pure PM helical undulators are considered here: planar helical undulators and a design based on PM dipole rings. Planar helical undulators are so called because there are planar magnet arrays above and below the vacuum vessel, whereas the PM Ring undulator has magnetic material completely surrounding the vacuum vessel.

The different undulator designs explained below were modelled using the magnetostatics code RADIA [66, 67] to find the peak on-axis magnetic field B_0 as a function of the undulator period, λ_u. In all cases, the PM material used was the nonlinear material NdFeB (in-built in RADIA) with a remanent magnetisation, B_r, of 1.3 T. The minimum magnetic gap was chosen to be 4 mm. Generally, the amount of magnetic material was not cost-optimised in the modelling. Instead excessive amounts were used to give the highest achievable on-axis field. Effects due to the termination of the magnetic material at the ends of the undulators were negated by only considering the central 5 periods of a 10 period device.

3.1.1 Planar Helical Undulators

Planar helical undulators have been used in synchrotron light sources for over 15 years and there are a number of different designs [68, 41, 42]. Each design requires a combination of *planar undulators* to create a helical field distribution. The helical field is usually achieved by adjusting the longitudinal position of one or more of the arrays. For synchrotron light sources, the planar configuration suits the large horizontal-to-vertical beam size ratio. Planar helical undulators offer a number of advantages over other possible magnet designs for the ILC positron source undulator:

- They are a proven technology with well understood engineering solutions.
- They allow easy access to the vacuum vessel, which may be required if a non-evaporable getter (NEG) coated vessel is needed to achieve the desired vacuum.

- The polarisation of the radiation can be changed to be vertical, horizontal, elliptical and circular (left and right).
- The emitted photon energy can be changed as a function of the magnetic field, (which is adjusted by changing the magnetic gap).
- Increasing the gap sufficiently gives zero field on-axis, effectively 'switching the undulator off'.
- The field quality can be maintained along the length of the undulator by using techniques such as 'magnetic shimming' [69].

The main disadvantage of a planar helical undulator design are:

- The on-axis field strength will not be as high as other designs because there is not magnetic material totally surrounding the vacuum vessel.
- They are permanent, and so providing zero field on-axis could be difficult.
- There can be many tonnes per meter of magnetic forces to handle in a controlled manner.

Three different planar helical PM undulators were considered, the Advanced Planar Polarized Light Emitter-II (APPLE-II) undulator [70], a new APPLE design, the APPLE-III [71] and the Multi-mode undulator [72, 73]. In the following, a description of planar undulators is given and then details of the modelling of each design using RADIA presented.

3.1.1.1 Planar Undulators

The on-axis periodic magnetic field required for a planar undulator can be created by two arrays of PM blocks above and below the axis. Each array consists of a series of M blocks per period and each block's magnetisation vector rotates sequentially by $\frac{2\pi}{M}$ radians [74]. For $M = 4$,[21] the magnetisation vector is in opposite directions for the horizontally magnetised blocks in the upper and lower arrays. The vertically magnetised blocks are aligned in both arrays. This arrangement creates loops of flux providing an alternating field on the axis between the arrays. A schematic of the field lines forming magnetic flux loops is shown in Figure 3.1 (for $M = 4$).

[21] The most typical number of blocks per period used in planar undulator design.

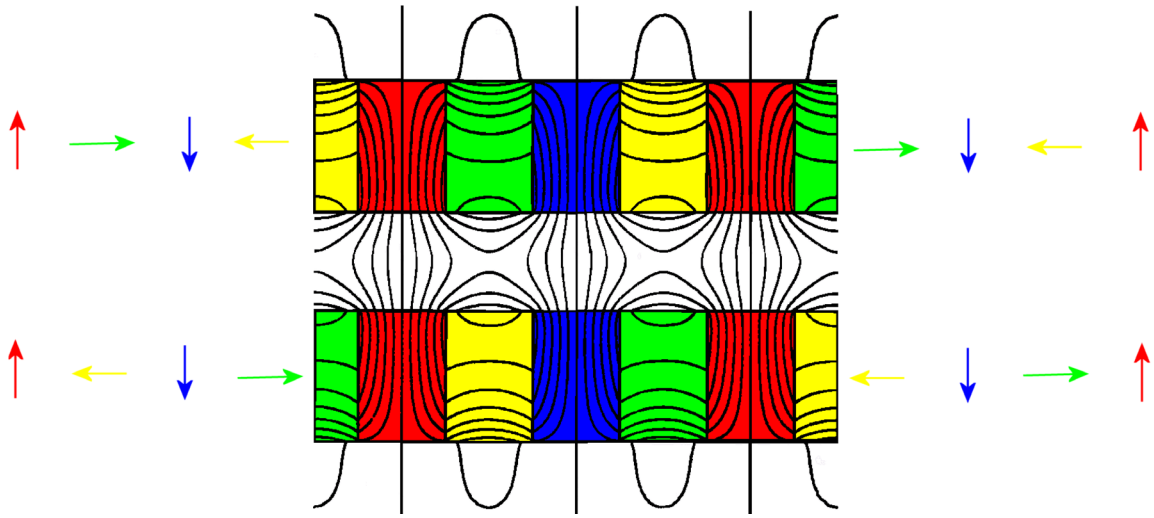

Figure 3.1: Two dimensional planar undulator field lines for M=4. Coloured arrows indicate the direction of magnetisation for each coloured block. The magnetic gap is the shortest distance between the two arrays.

3.1.1.2 APPLE Undulator Designs

In these designs there are four PM arrays, two above and two below the electron beam axis. Each array can move independently, described as changing the phase of the undulator, to create the required on-axis transverse magnetic field distribution. By adjusting the relative longitudinal position of the arrays, the polarisation of the emitted radiation can be changed from linear vertical to linear horizontal through circular and elliptical. Figure 3.2 shows the APPLE-II arrangement with a phase of $\frac{1}{2}\lambda_u$. A relatively new design, the APPLE-III [71, 75] has also been considered. This provides the same flexibility concerning the polarisation control as an APPLE-II but the maximum field on-axis is larger at the expense of reduced access to the vacuum vessel from the side and increased complexity of block shape. This can be seen in Figure 3.2. The effective magnetic field is a factor of ~1.4 higher than for an APPLE-II with a gap of 10.4 mm [71, 75]. The magnitudes of the transverse fields as a function of phase can be seen in Figure 3.3. For each model, the phase was chosen so that the undulator was in CP mode. Each block has dimensions (x, y, z) equal to (λ_u, 60 mm, $\frac{1}{4}\lambda_u$).

3.1.1.3 Multi-Mode Undulator Design

Figure 3.4 shows a schematic of the Multi-mode undulator [72, 73]. There are six planar arrays, three above and three below the axis. The blocks in the four outer arrays have different x and y dimensions to the blocks in the two inner arrays. This device achieves a

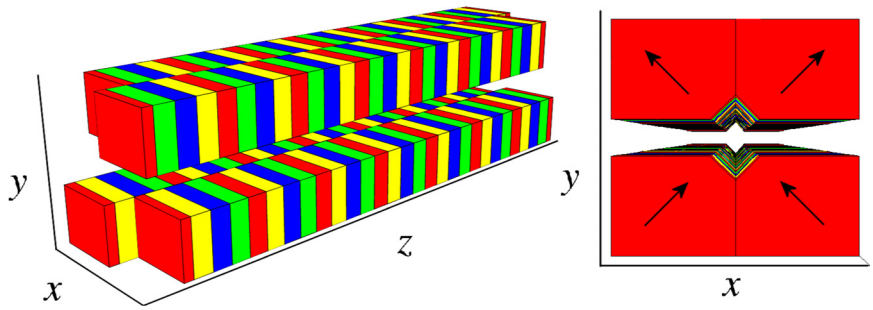

Figure 3.2: APPLE-II undulator with a $\frac{1}{2}\lambda_u$ phase change, (left). APPLE-III showing the block shape and magnetisation vectors, (right).

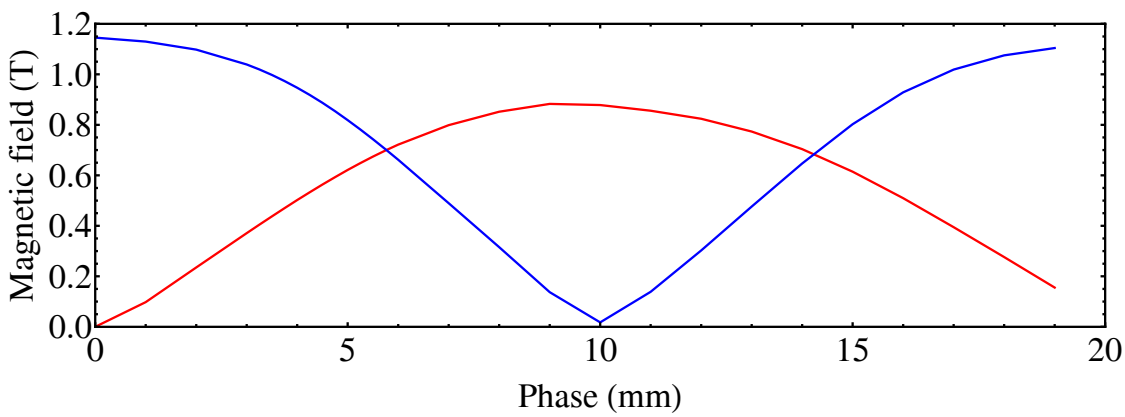

Figure 3.3: On-axis B_x (red) and B_y (blue) for a λ_u =20 mm APPLE-II undulator vs phase.

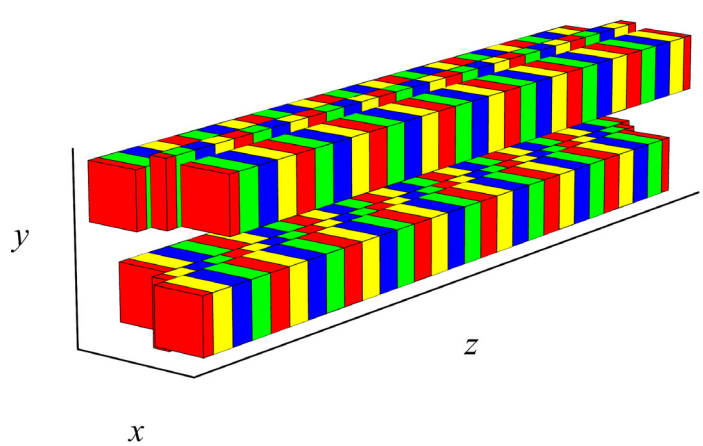

Figure 3.4: Schematic of the Multi-mode undulator.

slightly higher on-axis magnetic field compared to the APPLE-II and APPLE-III devices, due to the extra central array. Also, it has been designed specifically to create a high percentage of CP light off-axis [72, 73]. If it was to be used for the polarised positron source, this would be an advantage. The four outer arrays move in the longitudinal direction to produce the required transverse field while the inner arrays remain stationary.

Figure 3.5 shows how the transverse magnetic fields change as a function of the phase between the arrays for a model with the parameters given in Table 3.2.[22] To give the maximum field in CP mode, the length of the x dimension of the inner array blocks must be optimised. Figure 3.6 shows how the magnitude of the transverse field components change as the x dimension of the central block is changed for an undulator with the parameters given in Table 3.2. For this example, the peak field in CP mode is for a length of 2 mm. For each different undulator period considered, the x dimension of the inner array blocks has been optimised.

Table 3.2: Magnet block dimensions used for calculating the on-axis fields in Figure 3.5.

Parameter	Unit	Value
Undulator Period	mm	20
Block z Dimension	mm	5
Outer Array Block x Dimension	mm	20
Outer Array Block y Dimension	mm	20
Inner Array Block x Dimension	mm	1
Inner Array Block y Dimension	mm	40

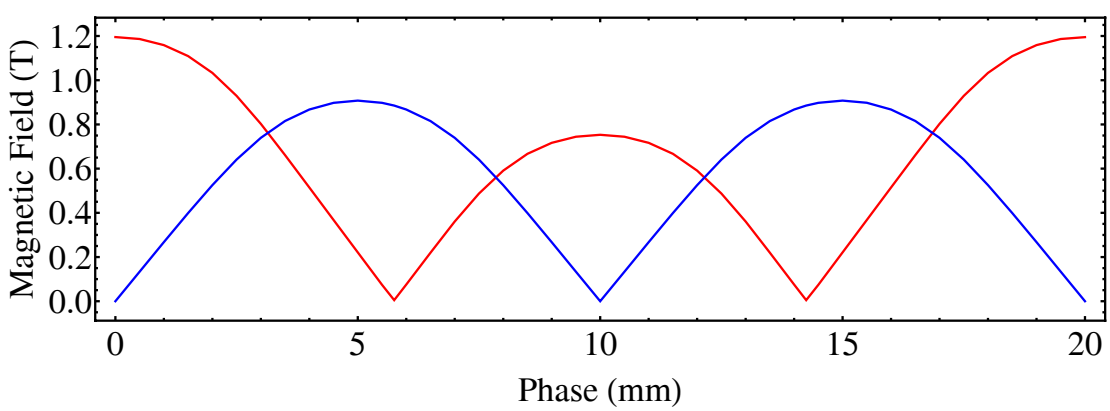

Figure 3.5: On-axis B_x (blue) and B_y (red) field components for a 20 mm period Multi-mode undulator vs phase.

[22] The values given in Table 3.2 would produce an odd shaped undulator, they are used solely to calculate the maximum attainable field.

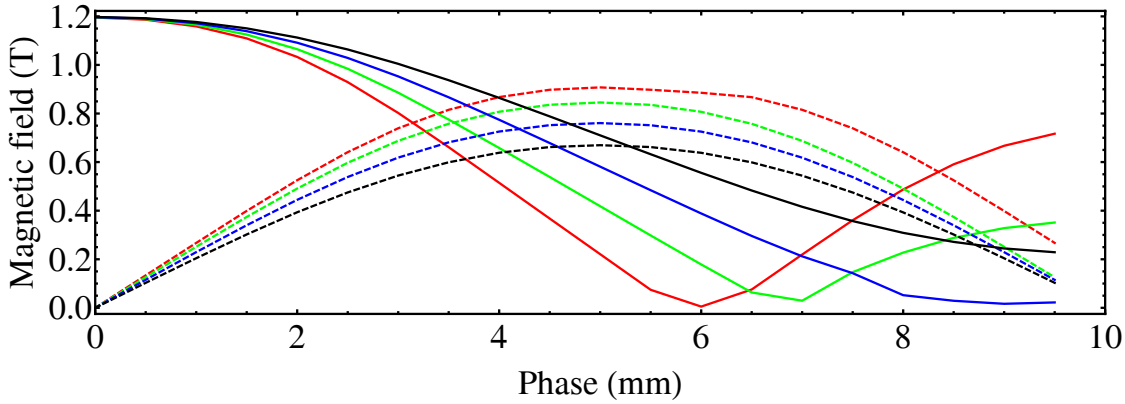

Figure 3.6: Magnitude of B_y (solid lines) and B_x (dashed lines) vs phase for 1 mm (red), 2 mm (green), 3 mm (blue) and 4 mm (black) x dimension of the central array.

3.1.2 Permanent Magnet Ring Undulator

A helical field can also be created by using an array of stacked PM rings. Each ring is comprised of PM blocks that produce an on-axis transverse dipole field by rotation of their magnetisation vectors by 4π radians around the ring [76], (shown in Figure 3.7 for 14 magnet blocks in a ring). Multiple rings are then placed together and the dipole field of each ring is rotated with respect to the preceding one so that over one period the total rotation of the on-axis dipole field is 2π radians [77].

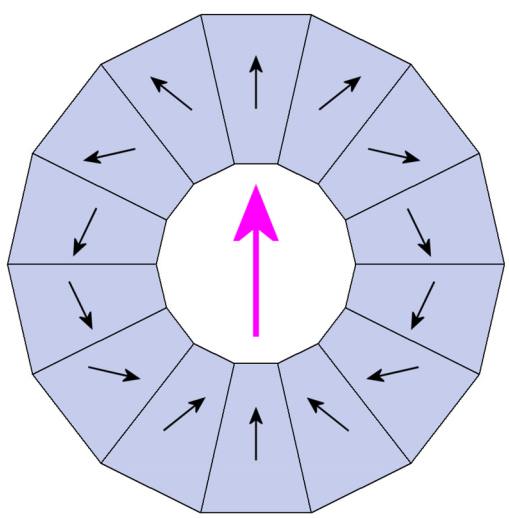

Figure 3.7: PM ring comprising of 14 blocks. The magnetisation vectors (black arrows) rotate $\frac{2\pi}{7}$ radians from block to block to produce a dipole field in the aperture (magenta arrow).

For curved blocks,[23] not trapezoidal ones as in Figure 3.7, an analytic expression for the peak transverse field on-axis, B_0 can be derived [74]:

$$B_0 = B_r \left(\frac{\sin(\pi/N)}{\pi/N}\right)\left(\frac{\sin(2\pi/M)}{2\pi/M}\right)\left(T\left(\frac{2\pi r_1}{\lambda_u}\right) - T\left(\frac{2\pi r_2}{\lambda_u}\right)\right), \tag{3.1}$$

where, M is the number of blocks per ring, N is the number of rings per period, r_1 and r_2 are the inner and outer radius of the ring, $T(x) = K_0(x) + \frac{x}{2}K_1(x)$ and K_0 and K_1 are modified Bessel functions. Optimisation of the numbers of blocks and block dimensions was carried out using Equation 3.1 and RADIA [53, 55, 56]. In the RADIA model the trapezoidal block shape was used, as machining a curved block would not be economical. As an example, the effect of the number of blocks per ring on the peak on-axis magnetic field can be seen in Figure 3.8. The difference between the analytic expression and the RADIA result is due to the block shape and non-unit permeability of the magnetic material that is accounted for in RADIA but not in Equation 3.1.

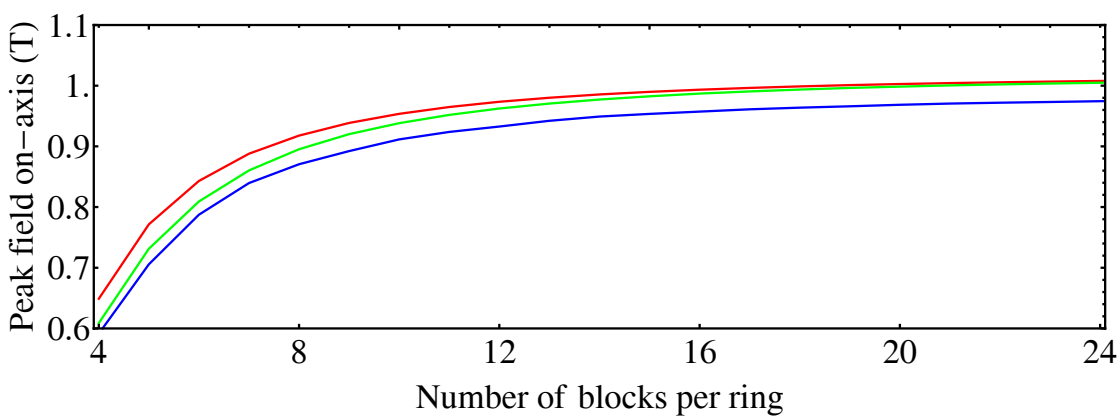

Figure 3.8: Magnetic field vs the number of blocks per ring, for a linear (green) and non-linear (blue) RADIA model and Equation 3.1 (red).

Initially, a design with 14 blocks per ring was considered [53]. However, it was found that to achieve the required vacuum pressure[24] the vessel would need to have a non-evaporable getter (NEG) coating [78]. This requires activation by bakeout and so access to the vessel with no surrounding magnetic material would be required.[25] Therefore the undulator was designed to be split in half. To keep the design regular (i.e. smooth along the opposing faces of each half) the number of blocks per ring must be an even number and

[23] i.e. the inner and outer edges of the ring are smooth circles.
[24] See Chapter 5.
[25] Since the baking required to activate the NEG coating would otherwise demagnetize the NdFeB PM blocks.

the number of rings per period must be a factor, or multiple, of the number of blocks per ring [56].

As the rings need to be split in half, the magnetic forces between the halves must be considered. These can be considerable and depend on the detailed configuration of the magnet blocks [57, 59]. Figure 3.9 shows the magnetic forces between the arrays for ten periods of a 14 mm period device as a function of the array gap for different magnet block configurations. It can be seen that the force between the two halves can be either repulsive or attractive, depending upon the configuration. A typical length for a PM undulator is ∼5 m and so the forces between the arrays could be as high as 30 kN at zero magnetic gap. This would make the engineering of the support girders and gap control mechanism quite demanding.

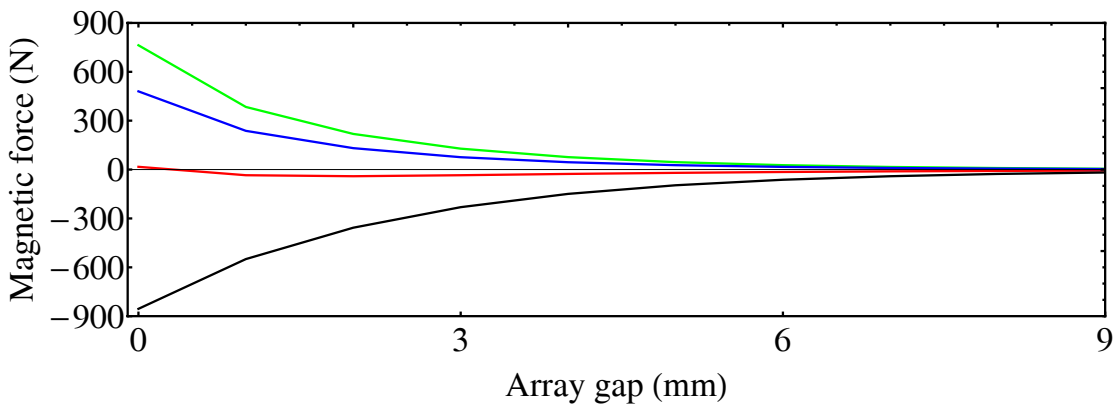

Figure 3.9: Magnetic force vs array gap for 10 periods of different PM Ring undulator configurations: 8 blocks per ring 8 rings per period (red), 12 blocks per ring 6 rings per period (green), 10 blocks per ring 5 rings per period (blue), 6 blocks per ring 6 rings per period (black).

3.1.3 Choice of Permanent Magnet Undulator Design

Figure 3.10 shows λ_u vs B_0 for each model as well as the required period and field to produce 20 MeV photons with a 250 GeV beam and 10 MeV photons with a 150 GeV beam. As expected, the PM Ring undulator out-performs the planar helical undulators, as there is magnetic material surrounding the entire vacuum chamber which drives more flux into the aperture. The Multi-mode undulator has 6 arrays compared to the APPLE-II and APPLE-III's four arrays, which means it can produce a high on-axis field in CP mode. The APPLE-III design has notches cut into the magnet blocks so that they are closer to the magnetic axis, giving a higher field than the APPLE-II design. To minimise the total length

of undulator required, the 14 mm period PM Ring undulator was chosen.[26] To make the supporting structure as simple as possible, an eight blocks per ring, eight rings per period configuration was chosen as this minimises the forces between each array at all gaps.

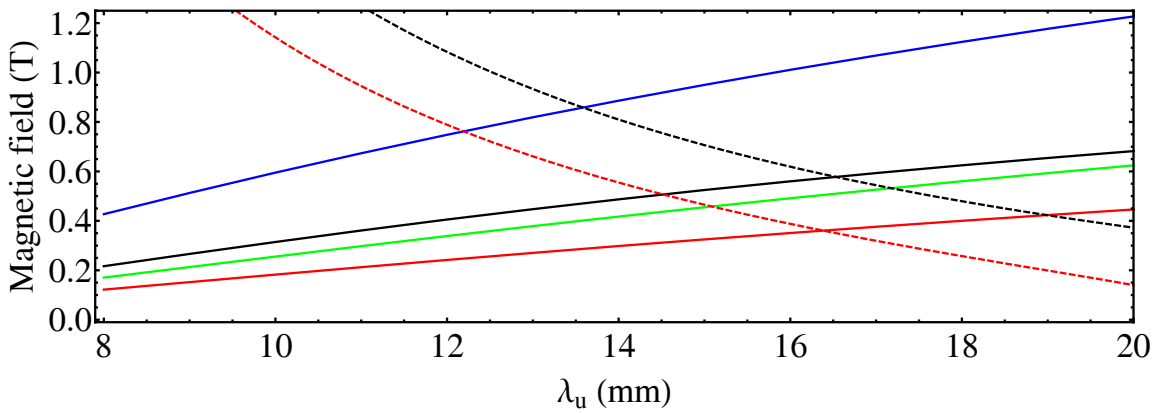

Figure 3.10: Computer modelled peak on-axis magnetic field vs λ_u for APPLE-II (solid, red), APPLE-III (green), Multi-mode (solid, black) undulators in CP mode and for the PM Ring undulator (blue). The field and λ_u required to produce 10 MeV photons (at the first harmonic) with 150 GeV electrons (dashed, red) and 20 MeV photons (at the first harmonic) with 250 GeV electrons (dashed, black) is also shown.

3.2 Ten Period Permanent Magnet Ring Undulator Design

A ten period model was chosen for construction to allow measurement of the magnetic field away from any end effects. An assembly drawing of the model undulator is shown in Figure 3.11 [79]. Wedges of PM material were made up of identically shaped blocks with a progressively rotating axis of magnetisation (left side of Figure. 3.11). From wedge A to B, the order the individual blocks is cycled by one (i.e. from {1, 2, 3, 4, 5, 6, 7, 8} to {8, 1, 2, 3, 4, 5, 6, 7} etc). Four wedges were then glued into aluminium holders to make half of a ring (centre of Figure 3.11). The aluminium holders were then aligned and fastened to top and bottom array base plates, which are then fitted together in the final assembly (right side of Figure 3.11). A photograph of the completed undulator is shown in Figure 3.12.

For each block the tolerance on the deviation of the magnetisation vector direction from the ideal direction was specified to be $\pm 3°$, (after thermal stabilisation), compared to

[26] Some of the parameter choices made in this study reflect the fact that this work was initially started for the TESLA project and may not be fully-optimised for the ILC baseline. In the TESLA design the undulator was at the 250 GeV point of the electron linac and was required to produce 20 MeV photons at the first harmonic.

the ±1.5° commonly used in undulators for synchrotron light sources. This is because it was decided, after discussions with PM block manufacturers, that it would be difficult to do much better due to the small z dimension without incurring excessive costs. It was also decided that no block sorting algorithm would be used. Typically, undulator magnet blocks are sorted (i.e. their exact orientation and position in the undulator array is specified) to minimise an objective function comprised of field integrals, phase errors and other relevant parameters [80, 81]. This process is time consuming and for long undulators is impractical. For this design, there would be nearly half a million magnet blocks to sort for 100 m of undulator. This approach has also been proposed for the European X-ray Free Electron Laser project undulators that are of a similar scale [82].

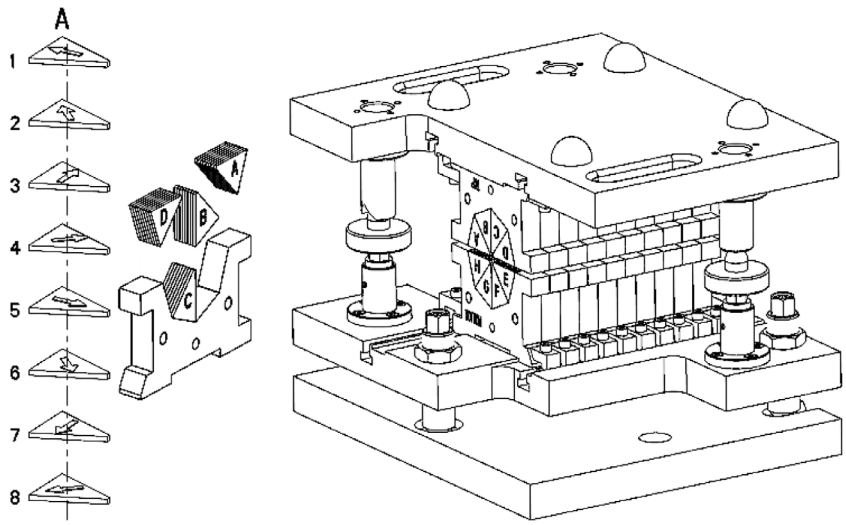

Figure 3.11: Assembly drawing of the 10 period PM Ring undulator.

3.3 Permanent Magnet Ring Undulator Measurements

The direction and magnitude of the magnetisation vector for each individual block was measured before assembly and their position in the assembly recorded. From this data, the expected magnetic field was calculated using RADIA. The on-axis field of the assembled magnet was measured using a conventional Hall probe measuring bench. The probe was mounted on a stiff carbon fibre shaft and aligned to the axis of the bench. The ratio of planar Hall effect coefficient to normal Hall effect coefficient for the Hall probe is a maximum of 8×10^{-4}. This means that the maximum magnetic field error will be ∼0.3 mT when measuring a zero field perpendicular to the Hall probe. Figure 3.13 shows the measured

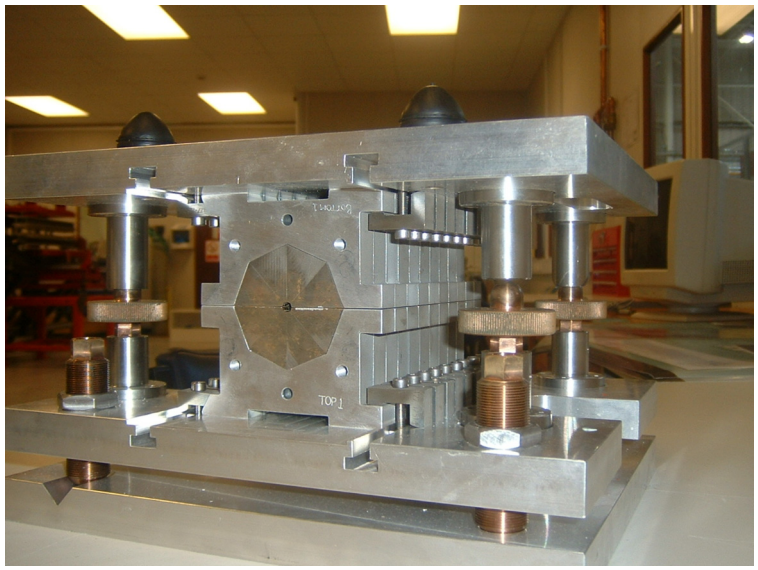

Figure 3.12: Photograph of the completed PM Ring undulator assembly.

field, expected measurements (from the individual block data) and ideal field in the two transverse directions. First and second field integrals ($I_{x,y}$, $J_{x,y}$, Equations 2.59 and 2.60), undulator K parameters and the mean on-axis peak field (neglecting the ends) are given in Table 3.3. For a 150 GeV electron beam entering the undulator on-axis, the angle of the beam direction at the end of the undulator is 3.9 and 6.4 nrad in the x and y directions respectively. The final displacements are 460 and 652 nm in the x and y directions respectively. The beam trajectory (calculated using Equation 2.62) is shown in Figure 3.14.

Table 3.3: PM Ring undulator field measurement data.

Parameter	Unit	Value
I_x, I_y	T m	-1.9 10^{-6}, -3.2 10^{-6}
J_x, J_y	T m^2	-2.3 10^{-4}, -3.3 10^{-4}
K_x, K_y		0.39, 0.47
On-Axis Peak Field	T	0.30, 0.36

The computer modelled field is less than the ideal field by ∼0.25 T due to the magnetisation errors of the individual magnet blocks. As the ILC polarised positron source requires an undulator ∼200 m in length, it is important to minimize the costs of individual magnets where possible. Relaxed specifications requiring lower production costs were therefore chosen for the permanent magnets in order to ascertain whether the required field could be realised economically. The modelling indicates that high quality magnet blocks should be used if the ideal peak field is to be obtained.

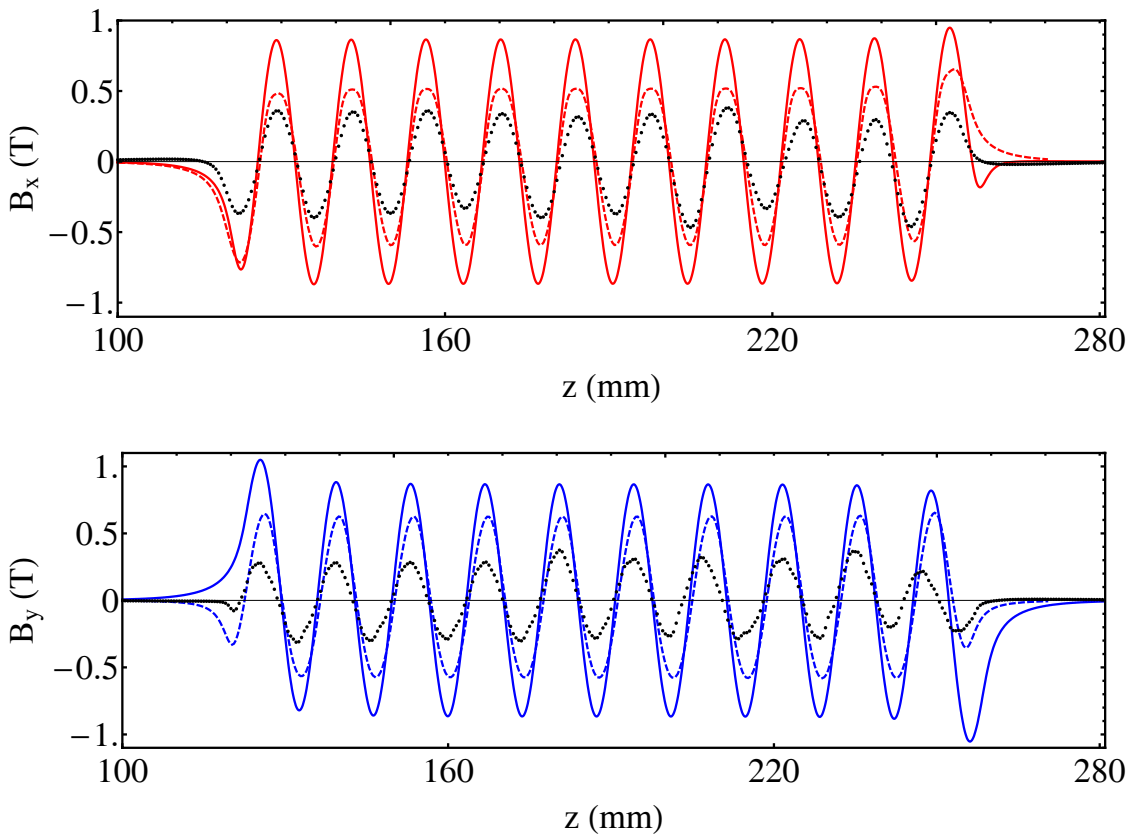

Figure 3.13: Ideal (solid), computer model based on actual block measurements (dashed) and measured (points) on-axis magnetic field in the x direction (top) and y direction (bottom) for the PM Ring undulator.

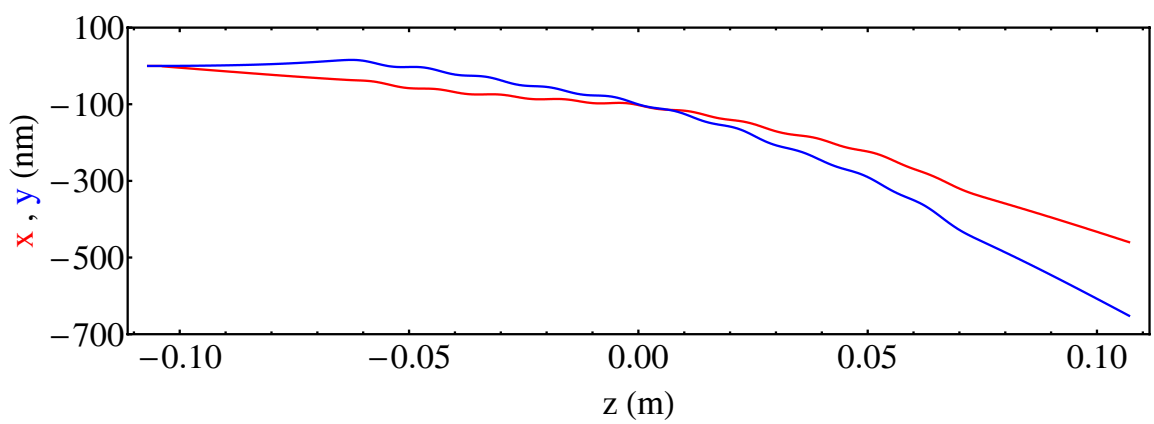

Figure 3.14: Calculated electron trajectory in the x (red) and y (blue) directions for the PM Ring undulator.

The measured field is less than was expected from the computer model: this could be due to a number of effects. Although every effort was made to ensure each block was measured accurately and aligned correctly in the assembly, mistakes may have been made. This cannot be checked as the blocks are now bonded together. Also, the strong demagnetising field that blocks experience when compiling the wedges, assembling the wedges into the holders and then bringing the two arrays together could have reduced their remanent field strength and working point. To check this hypothesis the maximum reverse field in a single block was calculated as the nearby magnet blocks were assembled. The assembly of the wedge and the two adjacent wedges is shown in Figure 3.15. Using the numbers in Figure 3.11 to represent the different orientations of the block magnetisation vector, the first block in Figure 3.15 is of type 5, the second (red) block is of type 6, the third block is of type 7, etc.

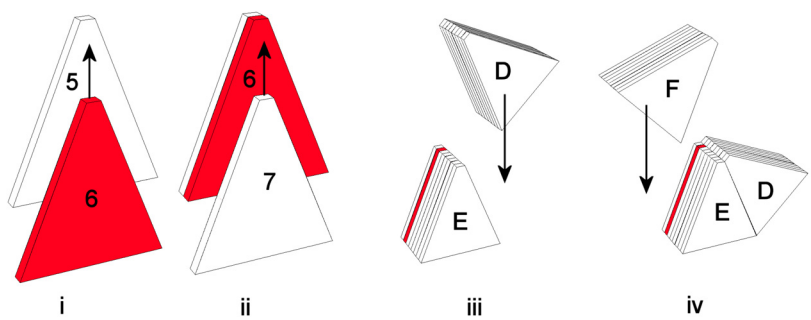

Figure 3.15: The maximum reverse field in the red block was calculated as it is assembled into a wedge (i), as the rest of the blocks in the wedge are added, (not all blocks are shown) (ii), and as the two adjacent wedges are added (iii and iv). The block numbers and wedge letters are defined in Figure 3.11.

The peak reverse fields in the red block as it is slid into place, as the other blocks are slid over it to form a complete wedge, and then as the two adjacent wedges are also slid into place, are shown in Figure 3.16. A peak reverse field of 1080 kA m^{-1} is experienced when blocks 7 and 8 are slid into position. After the other blocks and adjacent wedges are added, the peak reverse field is only 800 kA m^{-1}. The specification of the coercivity was 950 kA m^{-1} which is adequate for the peak reverse fields in the blocks in their final position, but is not sufficient given the reverse fields experienced by the magnet blocks in assembling the wedges and periods. The effect of a reverse field of this strength is to reduce the remanent field strength irreversibly, and hence the total on-axis field provided by the undulator. Blocks with a lower remanent field but higher coercivity should have been chosen to negate any de-magnetising effects.

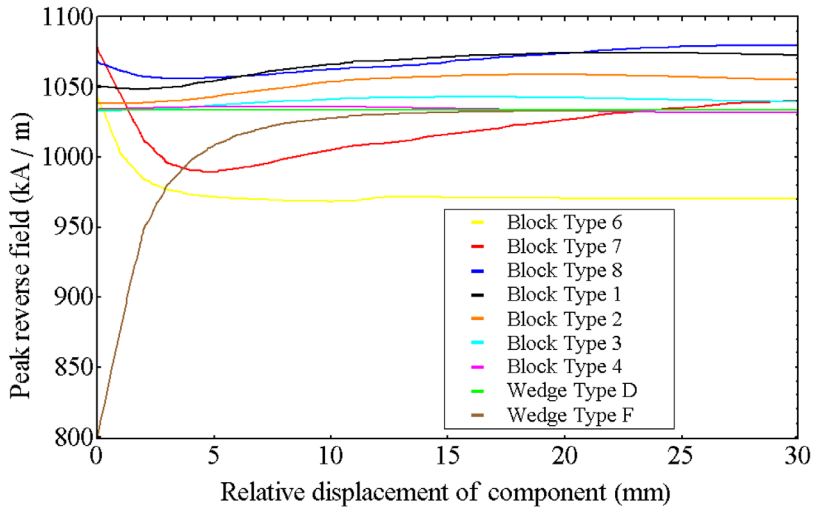

Figure 3.16: The peak de-magnetising field inside the sample block as other blocks and wedges (shown in Figure. 3.15) are slid into position.

To accurately re-test the de-magnetisation of each of the blocks would require the magnet to be disassembled and the magnetic field strength and direction of the individual blocks re-measured. However, this is impractical due to the strength of the bonding and the low intrinsic strength of the individual magnet blocks. Further de-magnetisation would probably occur in disassembly. Unfortunately, as no block sorting was done, no spare blocks were purchased on which further tests could be performed.

3.4 Super-Conducting Magnet Design

This undulator design is based on two helical SC coils wound around a vacuum vessel. The windings are spatially shifted by half a period in the longitudinal direction and current is passed through each winding in opposite directions. With current flowing, the on-axis longitudinal magnetic field cancels, leaving only a helical transverse field. A number of devices have been made in this manner [83, 84].

Extensive magnetic modelling was carried out in order to select the winding geometry of the undulator [85]. The software packages OPERA 2D and 3D from Vector Fields Ltd. [86] were used for the modelling studies. The results of the magnetic modelling indicate that:

- A winding with a flat shape (with the minimal radial height to width ratio) creates maximal field on-axis for a given current density. However, taking into consideration the peak field in the conductor, a square shape was found to be optimal.

- The peak field in the conductor is about twice the field on the undulator axis. The highest field in the conductor is always in the internal layers of the winding (Figure 3.17).

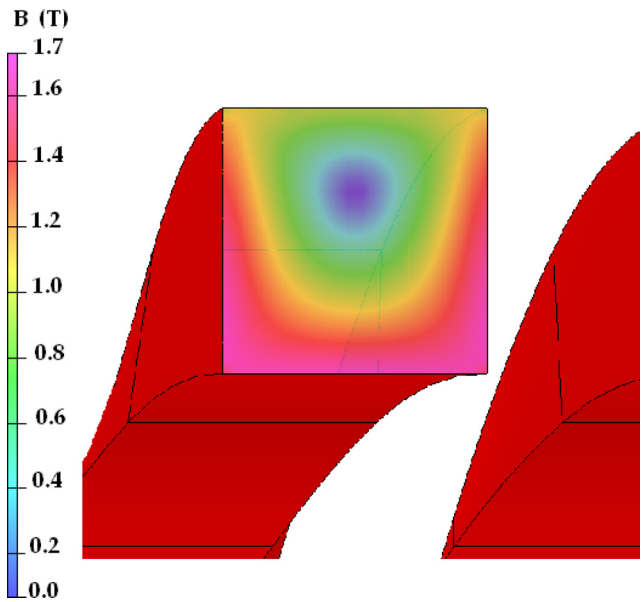

Figure 3.17: Calculated magnetic field, B, through a cross-section of the conductor windings for a current density of 1000 A mm^{-2}. The highest field is in pink near the axis of the magnet and is 1.75 T. The lowest field is in blue near the centre of the winding and is 77 mT.

Undulator conductor load lines, shown in Figure 3.18, were calculated and are expressed as a percentage of the short sample critical current,[27] for a winding geometry of 8 layers with 8 wires in a layer and for 8 layers with 9 wires in a layer. The 9 by 8 winding operates at 86% of the critical current giving a safety margin of 14%. The 8 by 8 winding operates at 94% of the critical current and the safety margin is 6%. The prototype uses an 8 by 8 winding geometry as it was not possible to fit a 9-wire ribbon into the rectangular groove of the former. A period of 14 mm was chosen as the computer model predicted the required field could be achieved with this period. This also allowed for a fair comparison with the PM Ring undulator.

The undulator was wound with VACRYFLUX 5001 type F54 [87] NbTi SC wire, onto an aluminium former 20 periods long. The internal bore of the former was 4 mm and the winding bore was 6 mm. Preliminary work indicated that winding the undulator with a wire ribbon rather than a single wire could significantly reduce technical difficulties encountered at the ends of the multi-wire winding. A similar approach is used at CERN for

[27] I.e. the current where a material has a phase transition from a SC phase to a non-SC phase.

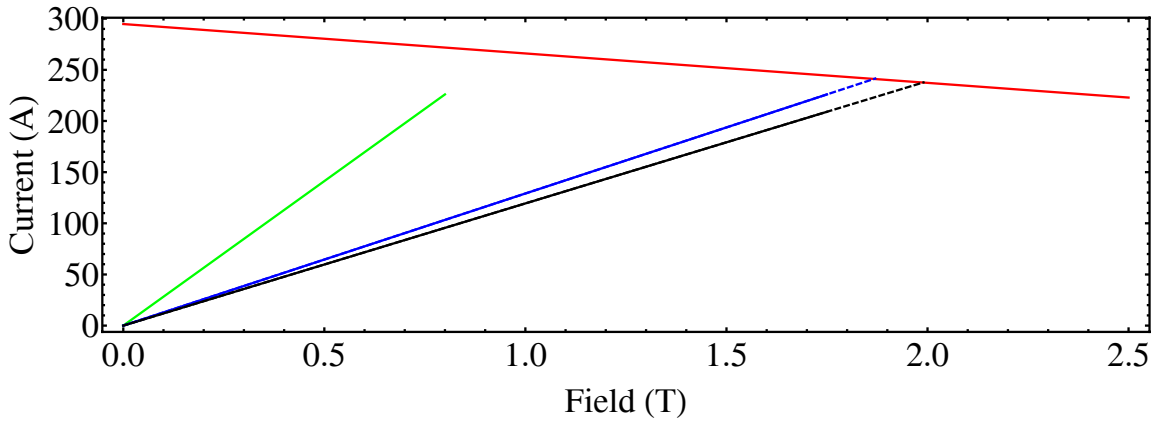

Figure 3.18: SC wire critical current at 4.2 K (red), calculated undulator conductor load lines for 8 layers 8 wires (blue) and 8 layers 9 wires (black) with safety margins (blue and black dashed), and the field achieved on-axis (green).

the winding of LHC corrector magnets [88]. Eight 0.44 mm diameter wires were bonded in a flat ribbon with a width of approximately 4 mm and a thickness of 0.5 mm. The ribbon was then wound into a spiral groove in the former. To achieve a continuous winding of two helices in one operation, two sets of pegs were used at the ends of the undulator for the return of the ribbon into the adjacent helical groove, shown in Figure 3.19.

Figure 3.19: Photograph of undulator winding showing the return pegs to allow for continuous winding.

After winding, the undulator coil was vacuum impregnated with epoxy resin and the wires in the ribbon were interconnected at the terminal block to form the series winding. As a result, the undulator coil forms a multi-layer, continuous, double-helical winding with two leads for connection to a power supply. The final view of the undulator before installation into the cold test rig is shown in Figure 3.20.

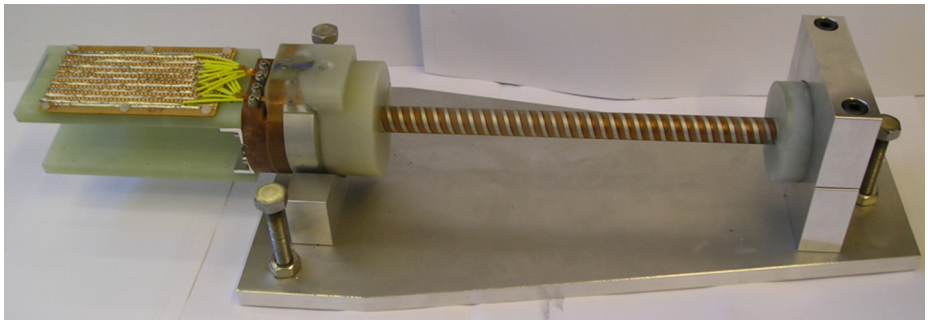

Figure 3.20: Photograph of the completed SC undulator before field measurement, with twenty 14 mm periods.

3.4.1 Super-Conducting Undulator Measurements

The undulator was mounted vertically in a liquid-helium bath. The level of liquid helium in the cryostat was monitored with discrete level sensors to ensure that liquid helium covered both the undulator coil and the SC current leads. The temperature of the undulator was monitored during cool-down and operation. Voltage taps were used to measure the resistive voltage across the undulator coil with a nano-voltmeter when the undulator was powered. In the cold test, the undulator reached the maximum current of the power supply at 225 A without quenching. The voltage across the complete undulator coil was approximately 10^{-6} V. This indicates that the wire interconnections have a total resistance $< 10^{-8}$ Ω. The undulator field profile, measured at a current of 220 A, is shown in Figure 3.21 and has the expected peak field. It was measured using a Hall probe (in a manner similar to that used for the PM undulator measurements) that was calibrated for 4 K operation by the manufacturers [89]. The first and second field integrals, K parameters and mean on-axis peak field are given in Table 3.4. For a 150 GeV electron beam entering the undulator on-axis, the angles of the beam to the axis at the end of the undulator are 14 and 762 prad in the x and y directions, respectively. The final displacements are 30.9 and 54.9 nm in the x and y directions, respectively. (Although these numbers seem incredibly small, it must be remembered that the electron beam is extremely rigid and that the total length of the undulator tested here is only ~0.3 m.) The beam trajectory is shown in Figure 3.22.

Table 3.4: SC undulator field measurement data.

Parameter	Unit	Value
I_x, I_y	T m	6.8 10^{-9}, 3.8 10^{-7}
J_x, J_y	T m^2	1.5 10^{-5}, 2.7 10^{-5}
K_x, K_y		1.06, 1.06
On-Axis Peak Field	T	0.81, 0.81

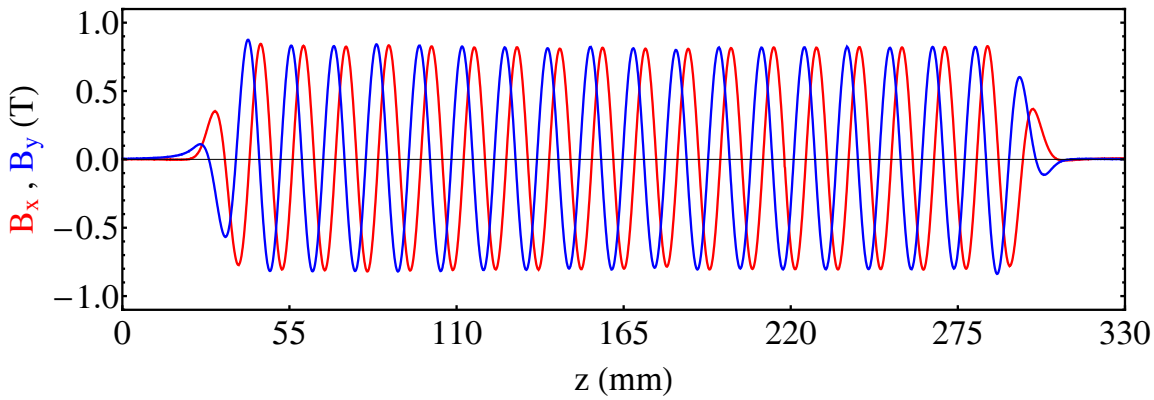

Figure 3.21: Measured on-axis magnetic field in the x (red) and y (blue) directions for the SC undulator.

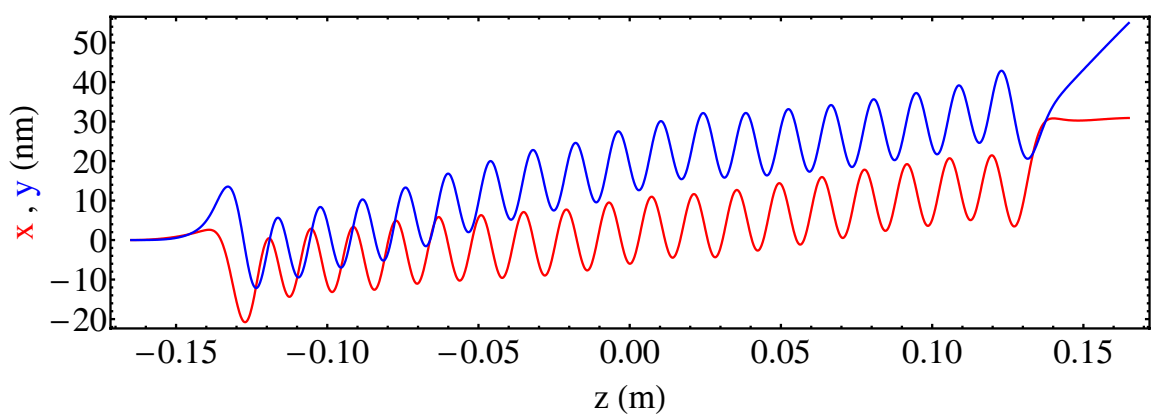

Figure 3.22: Calculated electron trajectory in the x (red) and y (blue) directions for the SC undulator.

3.5 Photon Flux and Polarisation

From the measured magnetic field of the undulators, the radiation spectrum and polarisation can be calculated. This was done using the numerical code SPECTRA [50] and is shown in Figure 3.23 for an ILC beam with parameters as given in Table 3.5 for the two different models. Two different beam energies have been considered to show the difference between the TESLA and ILC designs. Table 3.6 gives the peak flux and CP rate.

Interference effects, (characteristic of all undulator radiation), result in some broadening of the photon spectrum, due to the finite length of the undulator. The full width half-maximum (FWHM) of the ten period PM undulator device is approximately a factor of two larger than the FWHM of the twenty period SC device for each harmonic peak, as can be seen in the widths of the first harmonics in Figure 3.23. For the real ILC undulator, this would not be a significant factor as each module would have hundreds of periods. The difference between the total number of photons for the two undulators is explained by the differing K parameters. The total photon flux scales linearly with the undulator length and determines the maximum positron intensity in the ILC positron source. As the PM undulator produces less photons per unit length it would have to be longer to produce the same positron intensity as the SC undulator. The CP rates are between 0.78 and 0.93 and although there is no specification for the ILC it is assumed that these rates are acceptable, being close to the ideal value of 1. The polarisation rates for the SC undulator are higher than those for the PM undulator because the magnetic field quality in the SC undulator is better.

Table 3.5: ILC beam parameters used for flux and polarisation calculation.

Parameter	Unit	Value
Beam Energy	GeV	150, 250
Average Current	μA	45
Natural Emittance	nm rad	$2\ 10^{-2}$
Average β	m	25
Relative Energy Spread		0.0006

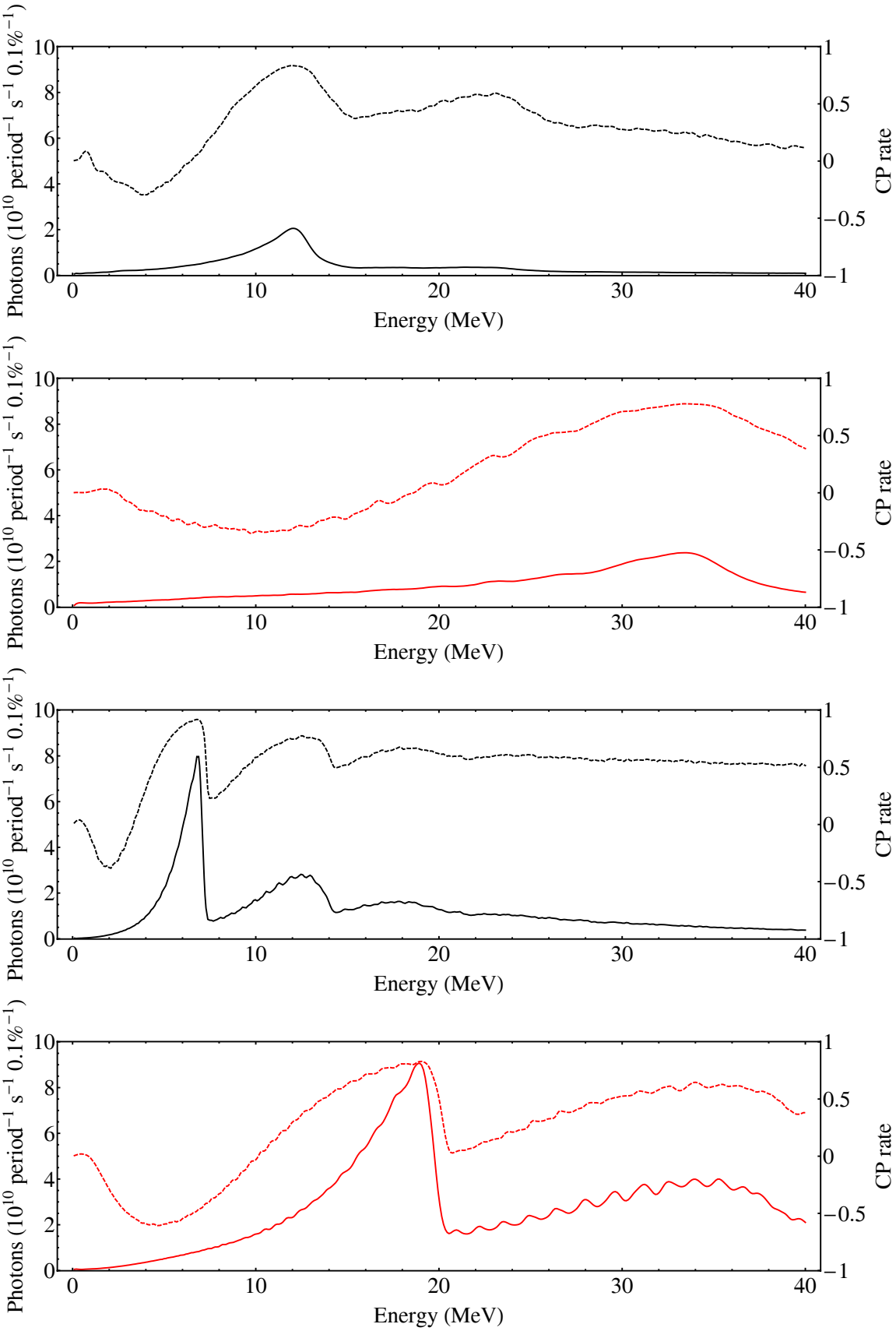

Figure 3.23: Photon spectrum per period (solid) and CP rate (dashed) from PM Ring undulator (top) and SC undulator (bottom) for 150 (black) and 250 GeV (red) electrons. Calculated using the measured magnetic field data.

Table 3.6: Peak flux and CP rate for the SC and PM undulators.

Parameter	Unit	PM (150 GeV)	PM (250 GeV)	SC (150 GeV)	SC (250 GeV)
Peak Flux Energy	MeV	12.1	33.4	6.8	19.0
Peak Flux	10^{10} Ph. 0.1% /period s^{-1}	2.1	2.4	7.8	9.1
Peak CP Energy	MeV	12.0	33.4	6.8	19.1
Peak CP rate		0.84	0.78	0.92	0.83

3.6 Conclusions from the First Models

An investigation into possible helical undulator designs for the ILC positron source has been carried out. Based on a paper design study, two model undulators, one using permanent and the other SC magnet technology, were constructed to assess their ease of fabrication and magnetic field quality. Both undulators produced a helical field distribution. The SC undulator performed to expectations but the PM Ring one did not. For the PM Ring undulator, the field quality and strength were both less than expected. This was due to the large number of components leading to possible assembly errors and certainly to de-magnetisation of the individual PM blocks during assembly. A tighter specification of magnet block errors would have ameliorated some of these problems, whilst the de-magnetisation effects would have been reduced if blocks with a higher coercivity had been manufactured, at the expense of a lower remanent field. The effects of magnet field errors could have been reduced by use of a block sorting algorithm. However, this is not a practical solution for the full length ILC magnet as any sorting of the many hundreds of thousands of blocks required would be too time consuming. Exactly specifying the position and orientation of each block would also greatly increase the assembly timescale and complexity.

The reduction in field strength for the PM Ring undulator means that a longer magnet would be required to achieve the required positron intensity for the ILC. In one positron source layout[28] an undulator with a K value of 0.4 must create ∼180 photons to produce a single positron at the IP. For a K value of 1 only ∼160 photons are required to produce a similar positron [90]. This is due to the different energy and angular spread of the photons. Therefore, if the PM Ring undulator was to be used it would need to be ∼13% longer than the SC undulator to give the same positron intensity at the IP. As the degree of CP is higher for the SC undulator radiation it would produce a higher positron polarisation rate in general.

[28] With particular assumptions for target thickness, target material, capture efficiency etc.

The trajectory of the electron beam through the SC undulator is significantly straighter than through the PM Ring magnet. Although the values for the field integrals are very small, it must be remembered that the undulators are both short, approximately 30 cm and 15 cm respectively. Field correction along the length is not practicable for either design and so the best field homogeneity must be achieved during manufacture. Simple trajectory correction can be done by using dipole correctors placed at the start and end of each module (typically every 4 m). A solution of this type is possible for the ILC undulator because of the very high energy beam and very small beam size.[29] The SC undulator outperforms the PM Ring undulator in terms of field homogeneity along the length. This means that the amount of dipole correction required and the possibility of deleterious trajectory walk-off of the electron beam is smaller.

In terms of operational aspects the SC undulator is also favored as the on-axis magnetic field can be controlled easily, allowing for a variable undulator K parameter if required. The SC undulator is also easy to switch off, whereas the PM Ring undulator would have to have a gap control mechanism and support for the vacuum chamber to reduce the field on-axis to negligible levels. This is achievable but more complicated than for the SC undulator. The ability to switch off the undulators will be beneficial during the commissioning of the ILC.

Another operational aspect that is difficult to quantify but could be important is the effect of radiation damage on the permanent magnets. The exact level of background radiation is not known. The undulator will be protected by a machine protection system and upstream collimators to reduce the risk of catastrophic damage but there will always be residual background radiation and beam halo particles to contend with. Radiation damage to PM undulators has been observed at the Advanced Photon Source [91]. The effects of radiation damage can be ameliorated by conditioning of the magnet, use of higher coercivity blocks, and operating the magnet at lower temperatures, e.g. 150 K [92]. Operating the magnet at lower temperatures also has the benefit of increasing the remanent field [93], however doing this would significantly increase the complexity of the engineering design to ensure that the temperature induced contraction of all the components was handled appropriately. It is not anticipated that the SC undulator would suffer from any significant radiation damage since these materials are already successfully used in high radiation environments. This means that the SC undulator has a much lower risk of radiation damage.

[29] Trajectory errors are further discussed in Section 6.1.

To achieve the required vacuum pressure the vacuum chamber[30] of the PM Ring undulator would need to have a NEG coating [78]. The SC undulator relies on cryo-pumping to achieve the required pressure. To date, a round vessel a few metres in length with a ∼4 mm diameter has not been NEG coated. Coating a vessel of these dimensions would be a significant research activity in its own right. It is also unclear at the present time what the impedance effects of the NEG coating on the electron beam would be.

For all of these reasons (summarised below) the SC undulator has now been selected for the ILC positron source. In summary:

- It performs better magnetically, resulting in a shorter overall length required to provide the same positron intensity.
- The field homogeneity is better, meaning that the amount of correction needed is less and the trajectory-wander of the electron beam is also be less.
- The undulator K factor can be adjusted and the magnet is easy to switch off.
- The SC undulator is less susceptible to radiation damage.
- There is a clear solution to provide the required vacuum needed for emittance preservation, requiring little further research and development.
- It has a better scope for further field enhancement since iron poles and an iron sleeve can be added relatively simply.
- The overall capital cost of the magnet is less, although the running cost would be higher.

3.7 Further Super-Conducting Model Fabrication

Since the fabrication and testing of the first SC undulator, the HeLiCal Collaboration [94] has produced more short models, with different apertures, periods and some with iron poles [63, 64]. A photograph of four of the test models is shown in Figure 3.24 and some data on the peak field versus λ_u (at a nominal 220A current) is shown in Figure 3.25.

[30] See Section 4.2.

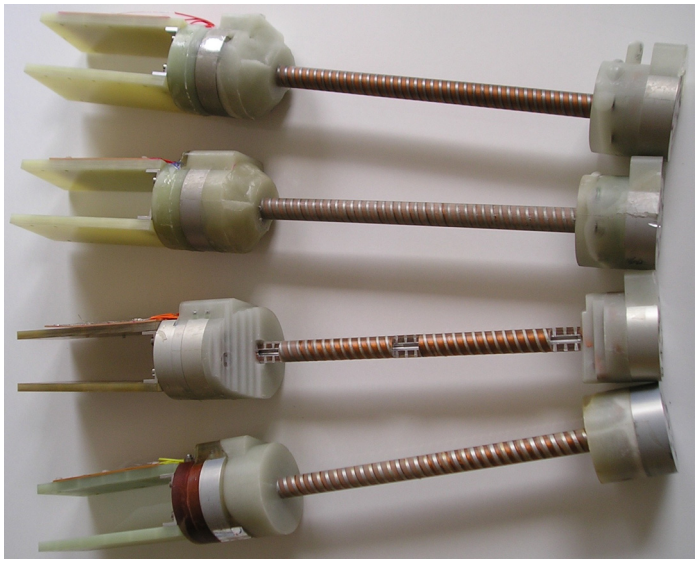

Figure 3.24: Photograph of four of the SC undulator prototypes that have been built and tested.

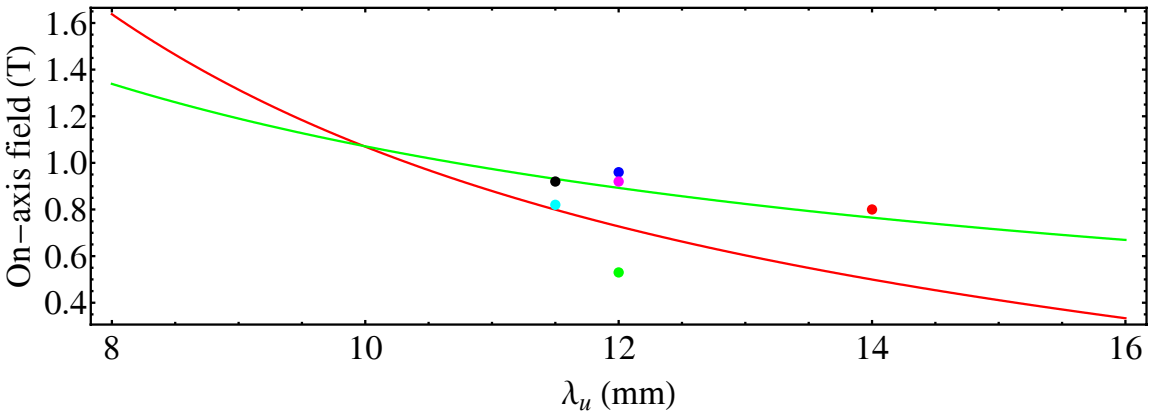

Figure 3.25: Peak field achieved for different SC undulator prototypes (points), also shown are the field and period required for a $K = 1$ undulator (green line) and to produce 10 MeV photons at the first harmonic with a 150 GeV electron beam (red line).

3.7.1 International Linear Collider Reference Design Report Undulator Parameters

Using a range of realistic numbers for the period and peak field achieved by these models, and others being considered at Cornell [95], calculations of the expected yield of positrons[31] were performed at Argonne National Laboratory [96]. Based on this work, the ILC-RDR undulator parameters were changed from those in the ILC-BCD and are shown in Table 3.7. The parameters are those suggested by the HeLiCal group. It is worth noting that, due to the increase in λ_u, the entire length of undulator has increased. The specification for the beam aperture is based on combining the prototype results with those from the surface roughness wakefields calculations.[32]

Table 3.7: ILC-RDR undulator parameters.

Parameter	Unit	Value
Undulator Period	mm	11.5
Undulator K		0.92
Field on-axis	T	0.86
Beam Aperture	mm	5.85
Undulator Length (Unpolarised Source)	m	147

[31] I.e. the number of positrons that arrive at the injection to the damping ring per electron through the undulator.

[32] See Section 8.1.

Chapter 4

Achieving the Required Vacuum Pressure in the Undulator Vessel

The magnetic design of the ILC positron source helical undulator was studied in the previous chapter and a super-conducting (SC) bifilar wires design chosen. This chapter considers the required vacuum system for the undulator. After specifying the vacuum pressure required and the main sources of outgassing, the photon spectrum incident on the vessel walls is calculated. This information is necessary to perform the vacuum science calculations. The vacuum science calculations were performed by Oleg Malyshev as part of the HeLiCal collaboration. In a single pass machine such as the ILC the main effect of a poor vacuum is to increase the beam emittance. If this emittance growth is too much then the design luminosity of the machine will not be achieved. Introductions to vacuum science and technology can be found in [97, 98, 99]. In this study no consideration of beam halo and tails has been made. These particles could impinge on the vessel and create secondary emission that worsens the vacuum system. It is assumed that there will be a collimator system upstream of the undulator that will absorb many of the beam halo particles, nevertheless there will be some present that could have an impact on the vacuum system.

4.1 The Fast Ion Instability and Vacuum Specification

As the electron beam passes through the undulator it can ionise residual gas molecules. These positively-charged ions can be attracted to subsequent negatively charged bunches. This may result in a perturbation of the beam trajectory which could result in an emittance

growth. This problem can be overcome by having a sufficiently low vacuum pressure, resulting in too few ions to disrupt the beam [100]. The main gas species in the system is hydrogen and it was found that hydrogen ions are not trapped with a vacuum pressure of 100 nTorr ($\sim 1.3 \times 10^{-10}$ bar) [101]. As the ions are not trapped, the vacuum pressure required to mitigate the fast ion instability could be greater, however it is felt that this pressure is a reasonable specification. If, at a later date the vacuum system needs to be modified then this specification for the vacuum pressure could be revised. Achieving such a vacuum in a long, narrow-bore SC magnet vessel is not trivial and is described in the next section.

4.2 Achieving the Required Vacuum Pressure

A detailed study into the vacuum performance of the SC undulator vessel has been carried out [102, 103]. There are two physical processes that are the main sources of gas within the vessel and that have to be managed; thermal- and photon-stimulated desorption.

- **Thermal-stimulated desorption**. All materials placed in vacuum desorb molecules of gas and are therefore sources of gas in a vacuum chamber. The desorption rate depends on many factors including the material, its cleaning, treatment, and prehistory. For example, thermal desorption rates for stainless steel, well known as a good vacuum material, can reach the level of 10^{-12} mbar litre s^{-1} cm^{-2} after bake-out at 300° C and several weeks of pumping. Therefore, suitable processing of the vacuum vessel before installation should reduce much of the residual gas produced via thermal-stimulated desorption.

- **Photon-stimulated desorption**. In photon stimulated desorption (PSD) at cryogenic temperatures, an incident photon desorbs a gas molecule from subsurface layers of the vessel. The desorbed molecules are then cryo-sorbed on the surface with a lower binding energy which leads to two effects:

  - The PSD of these cryo-sorbed molecules has a much higher desorption yield.
  - The vapour equilibrium gas density increases.

Generally, in a SC magnet, an ultra-high vacuum can be achieved by cryo-pumping. Cryo-pumping relies on gas molecules being cryo-sorbed onto the vessel walls, resulting in

a good vacuum in the aperture. However, due to the length of undulator required, PSD needs to be considered. This is because some photons generated in the upstream undulator modules will be incident on the walls of the downstream modules. In order to ameliorate the effect of any PSD, photon collimators will be required. The collimators are a cylindrically-symmetric aperture smaller than the undulator vacuum vessel aperture, combined with a pumping port. It is important to minimise the number of collimators to reduce any adverse effects on the electron beam[33] and to keep the overall length of the undulator line short.

In vacuum systems for traditional undulators, PSD has not generally been a significant factor, due to the relatively short length of the undulators. The PSD yield depends on the vessel material, cleaning, treatment, pre-history and accumulated photon dose. There are a number of experimental results published in the literature for PSD yields measured as a function of accumulated photon dose for different materials, and measured up to certain photon doses (for example, see [104, 105, 106]). The PSD yield also depends upon the photon energy. Empirical studies, using the synchrotron radiation from a dipole magnet, dipole radiation (DR), have shown that the PSD yield changes with the photon critical energy, ϵ_c, of the DR, such that it:

- is directly proportional to ϵ_c when ϵ_c <1 keV [107].
- weakly increases with ϵ_c when 1 keV< ϵ_c <100 keV [107, 108].
- is directly proportional to ϵ_c when ϵ_c >100 keV [108].

Schematically, this dependence is shown in Figure 4.1. The value of ϵ_c, (in eV), can be calculated from the energy of the electrons, E, (in GeV), and the strength of the magnetic field, B, (in T), using [41]:

$$\epsilon_c \cong 655E^2B.$$

Therefore to specify accurately the vacuum system the photon spectrum incident on the vessel walls must be calculated.

4.2.1 Incident Photon Spectra Calculation with SPECTRA

The synchrotron radiation spectrum from a helical undulator per metre along the length of the undulator line was calculated using the numerical code SPECTRA [50]. A helical un-

[33] Such as wakefield effects, discussed in Section 8.2.

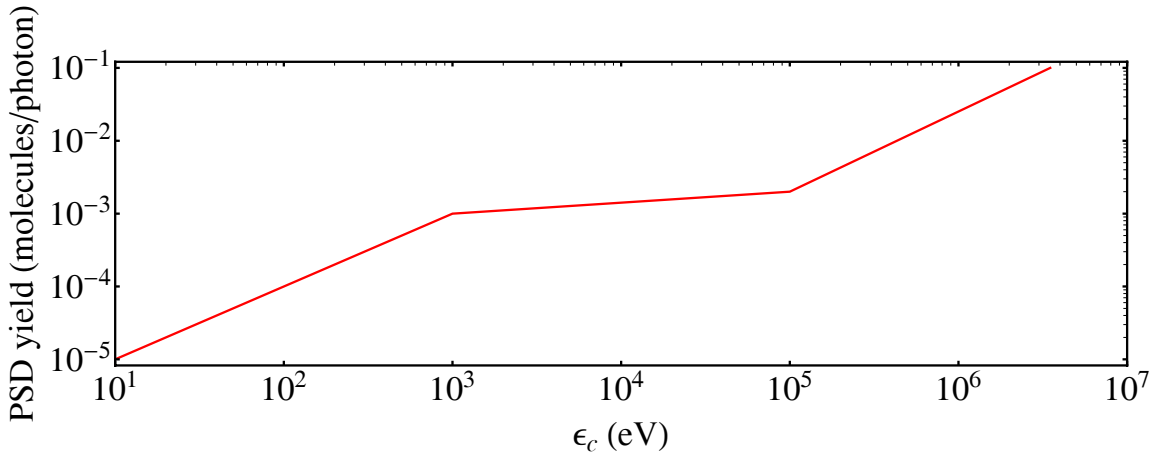

Figure 4.1: Photon stimulated desorption yield vs ϵ_c.

dulator and electron beam with the parameters given in Table 4.1 were assumed.[34] These parameters are significantly different to those of a typical undulator operating in a synchrotron light source. Due to these differences, it was found that at low photon energies (<100 keV), which correspond to large angles or distances less than ∼30 m from the undulator module, SPECTRA was too time consuming on a standard desktop computer for accurate calculation of the spectrum. This effect is not normally noticed because large angles are generally not important for short undulators. Therefore only SPECTRA results at distances above 30 m from the beginning of the first undulator module have been considered.

Table 4.1: Undulator and electron beam parameters used to calculate the photon spectrum incident on the vessel walls.

Parameter	Symbol	Unit	Value
Energy		GeV	150
Current		μA	45
Undulator Period	λ_u	mm	12
Undulator K Parameter	K_x, K_y		0.84,0.84
Undulator Aperture		mm	4
Undulator Length		m	100
Undulator Module Spacing		m	0
Electron Beam-Size	σ_x, σ_y	μm	66.75, 4.45
Electron Beam Divergence	$\sigma_{x'}, \sigma_{y'}$	μrad	0.3 4.45

4.2.1.1 Verification of the SPECTRA Results

To check the SPECTRA results, particularly given the limitations described above, a comparison with the analytic expression for the angular distribution of the power was made.

[34] At the time these calculations were performed the parameters in Table 4.1 were the best estimate for the ILC.

For a helical undulator with N periods this can be calculated from Equation 2.91, which assumes a beam with zero transverse size and energy spread. A comparison of the incident power per metre calculated with Equation 2.91 and from the photon spectrum calculated in SPECTRA is shown in Figure 4.2 for a single undulator of length 2 m, and with other parameters as given in Table 4.1. The discrepancies arise because the analytic expression does not include the beam-size or divergence, and for each point in the SPECTRA calculation there are no data for the preceding 30 m of undulator. There is a reasonable agreement between the two methods.

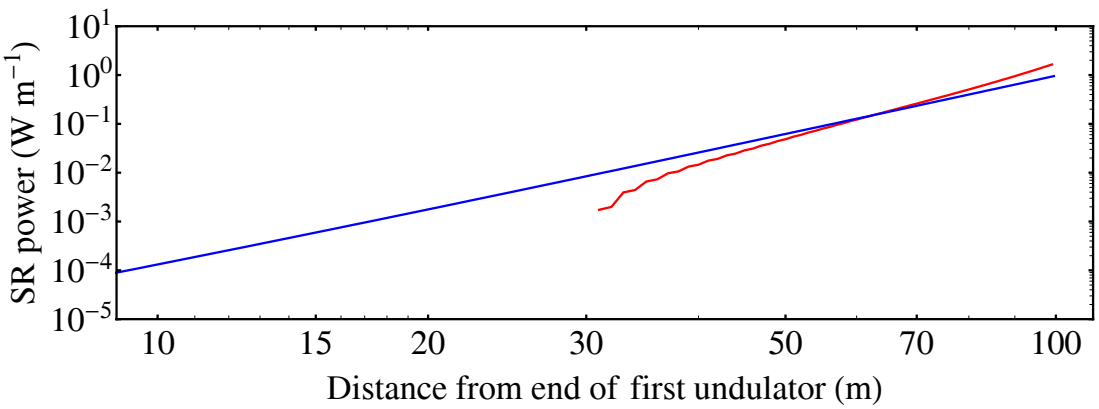

Figure 4.2: SR power per meter deposited in the walls from a beam and undulator with parameters given in Table 4.1, using Equation 2.91 (blue) and SPECTRA (red).

4.2.1.2 Dipole Radiation Approximation of the Undulator Radiation Spectrum

The experimental data on PSD yields are for DR, which has different characteristics to undulator radiation (UR). DR can be completely described by the critical photon energy ϵ_c and the SR power and so approximate values for ϵ_c and the SR power for the UR need to be determined. The UR has been approximated by modelling it as a superposition of two separate DR spectra, one with a high ϵ_c and one with a low ϵ_c. For the low energy DR, ϵ_c is defined as the photon energy at the peak of the spectrum of UR incident on the wall of the vacuum vessel, (see Figure 4.4). For the high energy DR ϵ_c is defined as the energy of the peak flux at approximately $\sim$10 MeV (the UR first harmonic cutoff energy). Figure 4.3 shows how the energy of the peak flux of the SPECTRA data changes with distance along the undulator. Also shown is a fit that matches the data well over the range 30 to 100 m.

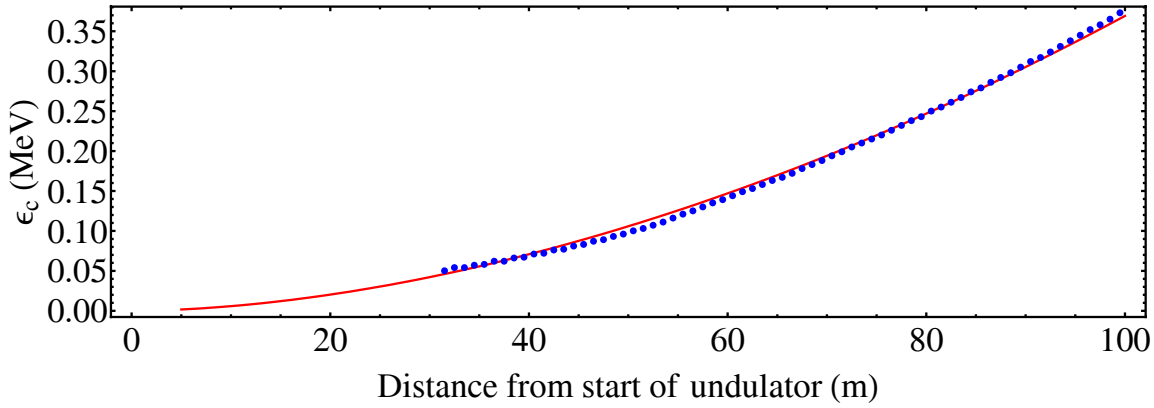

Figure 4.3: Value for low energy equivalent DR ϵ_c from SPECTRA data (points) and line of best fit (line) as a function of the distance from the start of the undulator.

As well as defining a value for ϵ_c a value for the SR power is required. This was obtained by first taking the value for the total power per metre from the SPECTRA data in Figure 4.2. The relative power for each DR spectrum was set by assuming that the ratio of the high ϵ_c power to the low ϵ_c power was the same as that of the power at the peak undulator flux to the power at ∼10 MeV. The total power P_t of SR from a dipole magnet, in kW, is [41]:

$$P_t = 88.46\frac{E^4 I_b}{\rho_0},$$

where I_b is the beam current in amperes and ρ_0 is the bending radius in metres. Examples of the photon energy spectrum from the undulator and for the DR approximations are shown in Figure 4.4 at 30, 40, 50, and 100 m downstream of the first metre of undulator. Figure 4.4 shows that, near the start of the undulator, it is the low energy photons that dominate but further down the device the higher energy photons become more significant, as expected. By inspection of Figure 4.4 it can be seen that there is a reasonable agreement between the SPECTRA data and the DR approximation. The main differences can be seen at lower photon energies: this is expected because of the assumptions made and the limitations in implementing the SPECTRA code outlined above.

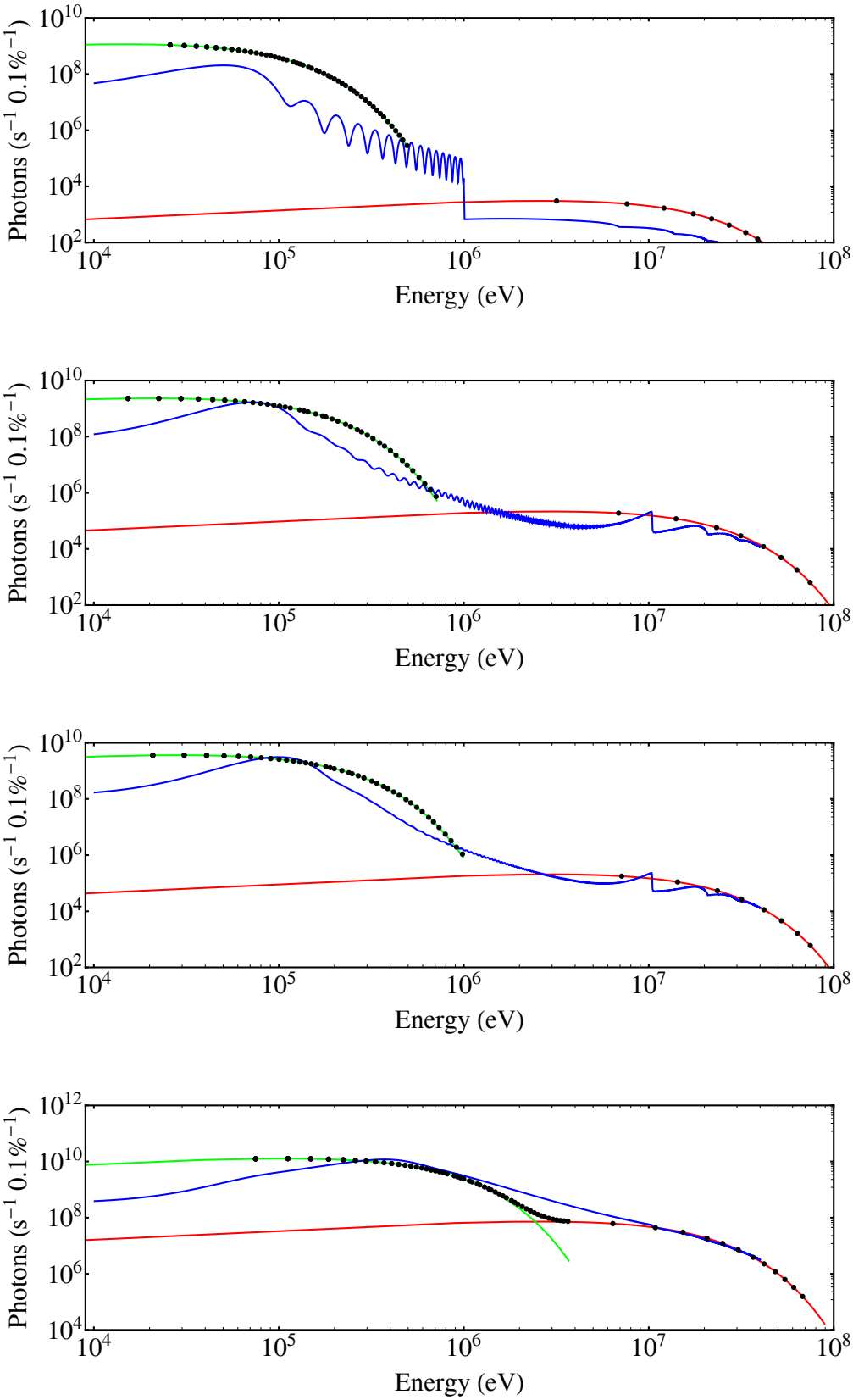

Figure 4.4: Energy spectrum of photons incident on the vessel walls after 30 (top), 40, 50 and 100 (bottom) m, SPECTRA data (blue) low ϵ_c DR (green), ϵ_c ∼10 MeV (red) and their superposition (points).

4.2.1.3 Total Number of Incident Photons

Using Equation 2.92 the total number of photons can be calculated from the spectra determined in the previous section. This is useful when determining the expected vacuum conditions. The numbers of photons are shown in Figure 4.5 for the SPECTRA data and DR approximations. The difference in the number of photons for the DR and UR cases can be explained by the fact that SPECTRA has not been used to calculate accurately the spectrum for energies less than ∼100 keV, due to the limitations in computer power mentioned above.

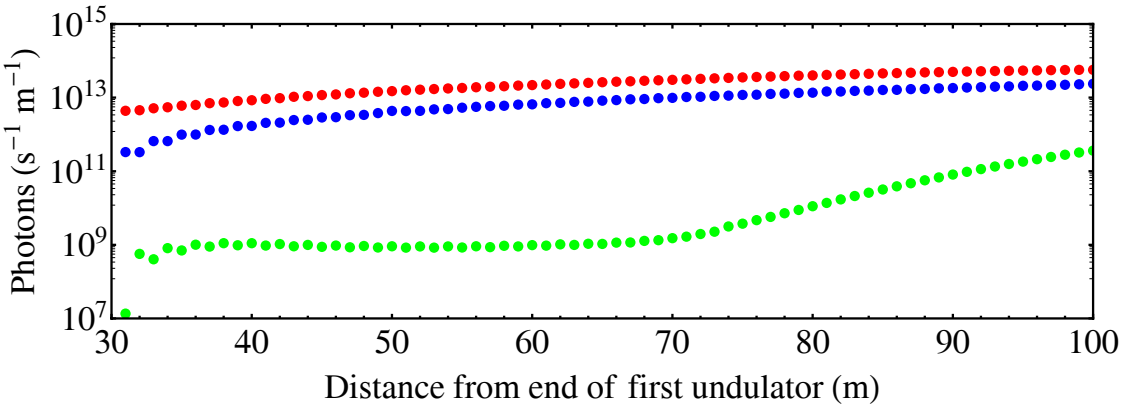

Figure 4.5: Photon flux incident on the vacuum vessel walls for the SPECTRA data (blue), low energy ϵ_c DR (red) and ϵ_c ∼10 MeV (green).

4.2.2 Photon Collimators

The vacuum design should allow for the continuous operation of the undulator for at least a half a year without warming up. In a study, based on the results of the number of incident photons, the power and ϵ_c of the DR approximations, with no collimators, and vacuum pumps every two meters, it was found that the pressure 100 m from the first undulator was too great after just one day of operation [102, 103]. Therefore, in order to achieve the specification photon collimators are required. The required spacing between the collimators has been estimated [102, 103]. The results of the vacuum science calculations performed by Oleg Malyshev are summarised in Table 4.2. In this cryogenic system the vacuum pressure will increase over time as there is always hydrogen diffusing into the vacuum chamber and, due to the ratio of vessel diameter to length, removing gas molecules in the vessel is unlikely [102]. To the criterion of continuous operation for at least 180 days was added the requirement that there be a reasonable distance between the collimators. This was assumed to be about 10 to 20 m. These two criteria are met for distances from the beginning of the

undulator of <30 m. Therefore, to keep the gas density at an acceptable level, the photon collimators must be installed in a few locations along the undulator vacuum chamber. The distance between collimators depends on the ratio of the diameter of the collimator d_c to that of the vacuum chamber, d. Simple geometry calculations show that the distance between collimators, L_c, should be:

$$L_c < 15 \text{ m for } d_c : d = 1 : 2$$

and

$$L_c < 7.5 \text{ m for } d_c : d = 3 : 4.$$

Table 4.2: Required distance between collimators to obtain acceptable gas density inside the undulator vacuum vessel.

	Distance Between Collimators (m)	
Distance from the start of the undulator (m)	Gas Density always below the required limit	Gas Density below the required limit for 150 days
10	≤20	<20
20	≤10	≤20
30	≤6	≤14
40	≤4	≤7.5
50	≤3	≤4.5

4.3 Conclusions and Further Work

To suppress the fast ion instability, the vacuum pressure in the beam line should be 100 nTorr. Although it is noted that hydrogen ions are not trapped at this pressure it is a reasonable specification. To specify the vacuum system design the incident photon flux had to be calculated to estimate the photon stimulated desorption yield. As only experimental data based on the SR from a dipole magnet are available, the undulator radiation spectrum was approximated by using two dipole radiation spectra with high and low energy. This was done for each metre of undulator for a 100 m continuous device with an aperture of 4 mm. From the spectra and the incident photon flux it is estimated that the required vacuum pressure can be achieved if collimators with an aperture of three quarters the size of the undulator aperture are placed every 7.5 m. This can approximately be achieved

with the current lay-out of the undulator line. These calculations should be re-done to take into account changes in the undulator length, vessel dimensions and module spacing. The ILC-RDR parameters should be an improvement on those used in this study due to the larger beam aperture, however, the undulator is longer. Magnetic field errors should also be included to allow for deviations in the direction of synchrotron radiation from each module. For an undulator in excess of 200 m length this would require the development of new or existing software. Such software is also required for the polarised source design to accurately simulate the polarisation of the photons incident on the conversion target.

Every photon above an energy of ∼5 eV contributes to PSD [109] and low energy photons are also observed at larger angles and so are more likely to be incident on the vessel walls. The accurate calculation of the number and angular distribution of low energy photons is a significant problem for the specification of the vacuum system. It involves running existing SR codes over many orders of magnitude in photon energy and observation angle, which is time consuming and not what the existing codes were designed for. Therefore, to accurately calculate spectra at low photon energies and large angles a bespoke SR calculation code should be developed. As can be seen from Figure 4.4, using a DR approximation probably overestimates the numbers of low energy photons.

It is assumed that the collimators perfectly absorb the incident SR power. Initial studies have indicated that the incident photons can result in secondary particles[35] being emitted back into the vacuum vessel [110]. Accurate calculations of the number of secondaries and their properties need to be made before their influence on the main electron beam and vacuum pressure can be determined.

[35] E.g. electrons, positrons and photons.

Chapter 5

Synchrotron Radiation Power Incident on the Vessel

In the previous chapter it was demonstrated that photon collimators need to be included in the design to achieve a vacuum pressure of 100 nTorr. In this chapter heating of the vessel due to synchrotron radiation (SR) is considered. Any power deposited in the undulator vacuum vessel could cause quenching of the low temperature super-conducting (SC) magnets. There are two main sources of heat to be considered: the SR photons produced in the undulator that are incident on the vessel walls; and the image currents in the metal walls induced by the electron beam. The SR effects are discussed in the remainder of this chapter and the image current heating is discussed in Section 7.3.5.

5.1 Incident Synchrotron Radiation Power

The incident power along the length of the undulator due to SR from the undulator can be calculated from Equation 2.91 integrated over the relevant angles. In spherical co-ordinates, $\mathrm{d}\Omega = \sin(\theta)\mathrm{d}\theta\mathrm{d}\phi$ and the intensity of radiation into an axially symmetric angular acceptance defined by θ_0 and θ_1 is:

$$P = N_e 2\pi \int_{\theta_0}^{\theta_1} \frac{\mathrm{d}I}{\mathrm{d}\Omega}(\theta)\sin(\theta)\mathrm{d}\theta, \tag{5.1}$$

where N_e is the number of electrons per second passing through the undulator and the factor of 2π has come from the integration with respect to ϕ. Equation 5.1 is plotted in

Figure 5.1 for the ILC-BCD and ILC-RDR undulator parameters, given in Table 5.1. Also shown for comparison are some points calculated using the numerical code SPECTRA [50]. The ILC positron source could consist of up to 60 undulator modules, each consisting of two, 2 m undulators. The SR power from a system of undulators is also shown in Figure 5.1 for an undulator line consisting of 60 modules. The assumed undulator spacing is shown in Figure 5.2 for a half-cell: twenty such half-cells were used for the calculations.

Table 5.1: Undulator parameters used to calculate the SR power incident on the vacuum vessel walls.

Parameter	Unit	ILC-BCD	ILC-RDR
Undulator Period	mm	10	11.5
Undulator K		1	0.92
Undulator Aperture	mm	5.85[a]	5.85
Undulator Length	m	2	2
N_e		2.82×10^{-14}	2.82×10^{-14}

[a]The ILC-BCD did not specify an aperture the same value given in the ILC-RDR has been used.

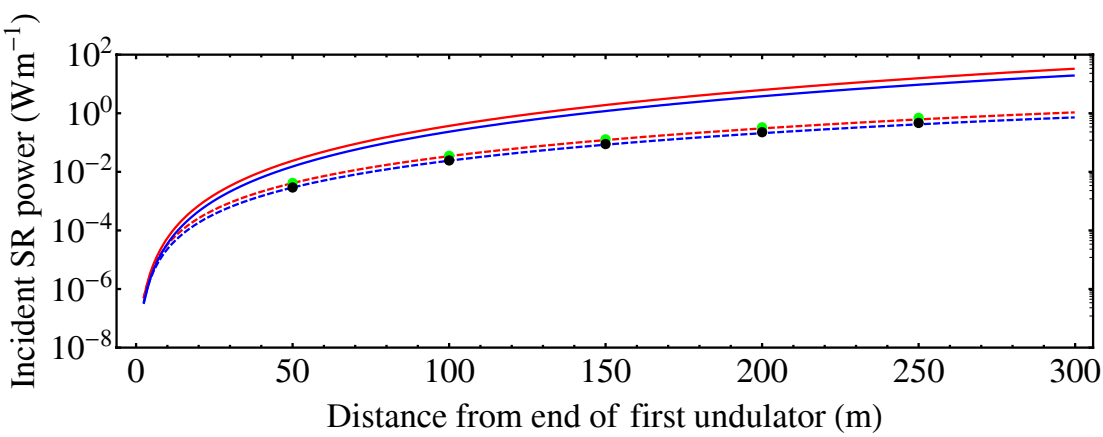

Figure 5.1: Incident SR power on the vessel walls calculated using Equation 2.91 (lines) and SPECTRA (points) from a single undulator (dashed lines) and a line of 20 half-cells from Figure 5.2 (solid lines) for ILC-BCD (blue lines, black points) and ILC-RDR (red lines, green points) undulator parameters.

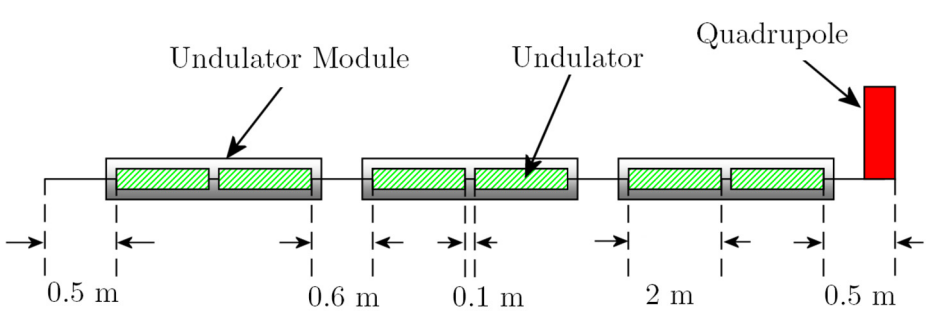

Figure 5.2: Schematic layout of a half-cell of the undulator line for incident SR power calculation.

5.1.1 Synchrotron Radiation Collimation

The peak SR power per metre is ∼33 W or ∼19.4 W for the ILC-BCD and ILC-RDR parameters, respectively, which is too great a heat load for the cryogenic system. A reasonable estimate of the maximum allowable heat load in the undulator is 1 W m^{-1} [111]. This means that photon collimators need to be placed along the length of the line to absorb some of this power. These are axially symmetric apertures with a smaller diameter than the undulator vacuum vessel, thereby screening downstream elements from some of the SR. Photon collimators are also required to achieve the required vacuum.[36] A photon collimator aperture of 4.4 mm has been chosen as that is what is required to achieve the necessary vacuum for the ILC-RDR undulator aperture. Figure 5.3 shows the incident power per metre if collimators are placed in the centre of the 0.6 m drift sections between undulator modules shown in Figure 5.2.

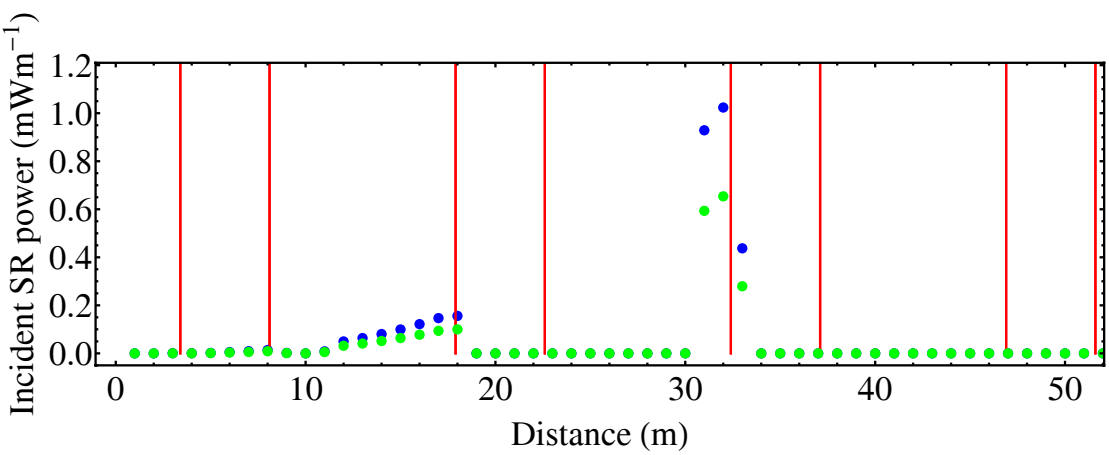

Figure 5.3: SR power incident on the downstream vessel walls from a single undulator with ILC-BCD (blue) and ILC-RDR (green) parameters with photon collimation. The red lines indicate the position of the collimators.

The effect of the collimation is quite dramatic: significant amounts of power are absorbed near the start of the line and the SR incident power from a single undulator is reduced to zero after ∼30 m. Figure 5.4 shows the incident power for a system of 20 half-cells with collimation. The peak incident power with collimation is 5.5 mW m^{-1} and 3.5 mW m^{-1} for the ILC-BCD and ILC-RDR undulator parameters, respectively.

[36] See Section 4.2.

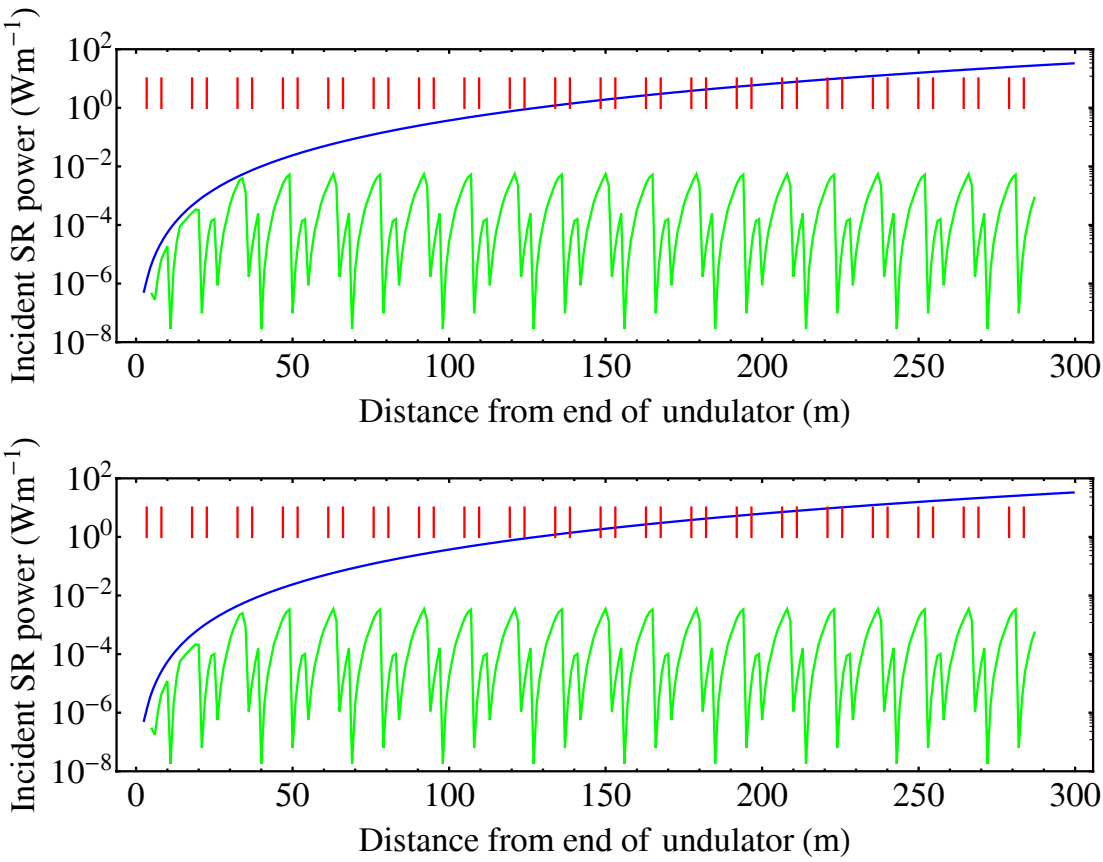

Figure 5.4: SR power incident on the vessel walls from a line of 20 half-cells with the ILC-BCD (top) and ILC-RDR (bottom) undulator parameters, with collimation (green) and with no collimation (blue). The red lines indicate the position of the collimators.

5.1.1.1 Collimator Alignment Errors

Due to engineering tolerances, there will be some spread in the actual size and alignment of the collimators. An attempt to account for this has been made by letting the radius of each collimator vary by a random amount following a Gaussian distribution with a σ value of 500 μm, truncated at $\pm 3\ \sigma$.[37] One thousand different 20 half-cell undulator lines were simulated with both ILC-BCD and ILC-RDR parameter sets. The maximum power per metre deposited in each of the sets of iterations was 0.27 W m^{-1} and 0.07 W m^{-1} for the ILC-BCD and ILC-RDR parameters, respectively. Figure 5.5 shows the incident power per metre along each line for the iteration containing this maximum. Histograms of the peak incident power per metre in the line for the 1 000 different iterations are shown in Figure 5.6. The mean of the peak incident power for the 1 000 iterations is 0.058 W m^{-1} and 0.014 W m^{-1} for the ILC-BCD and ILC-RDR undulator parameters, respectively.

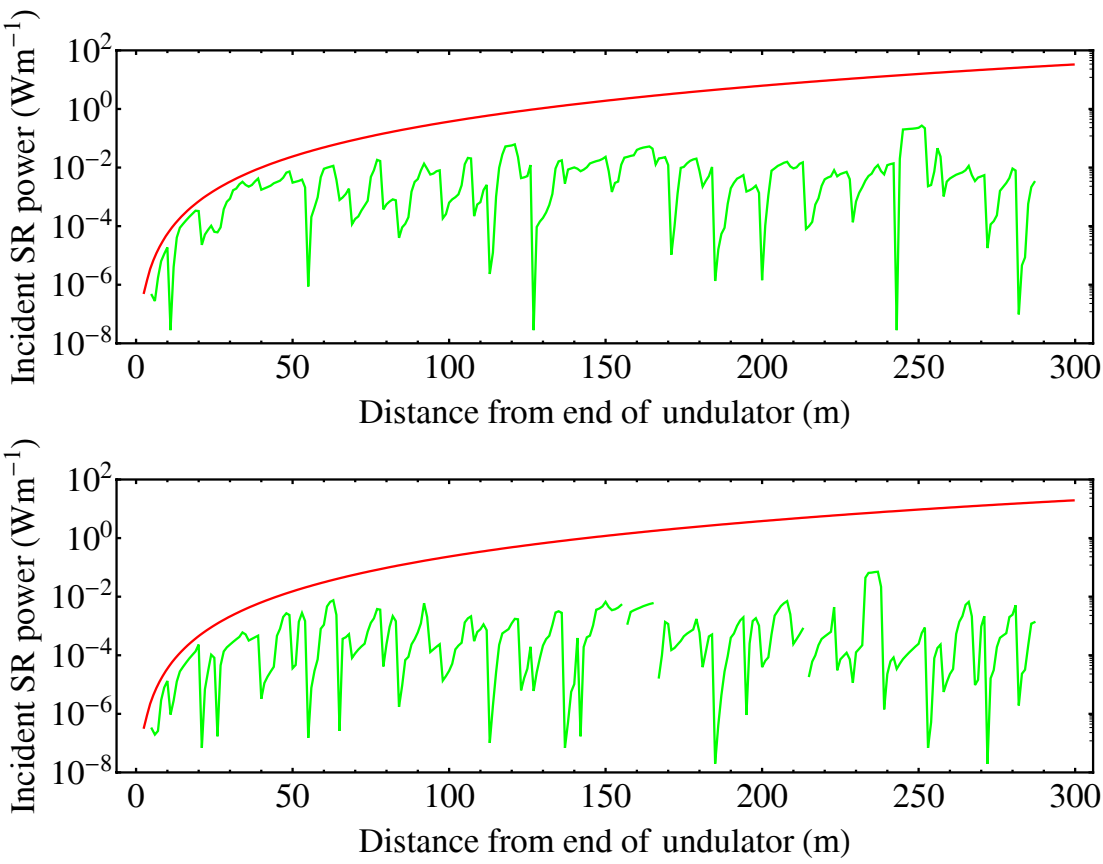

Figure 5.5: Iterations with the peak incident power per metre for the ILC-BCD (top) and ILC-RDR (bottom) undulator parameters and with misaligned collimators (green) and with no collimation (red)

[37] This amount of variation is excessively large and has been chosen for demonstration purposes.

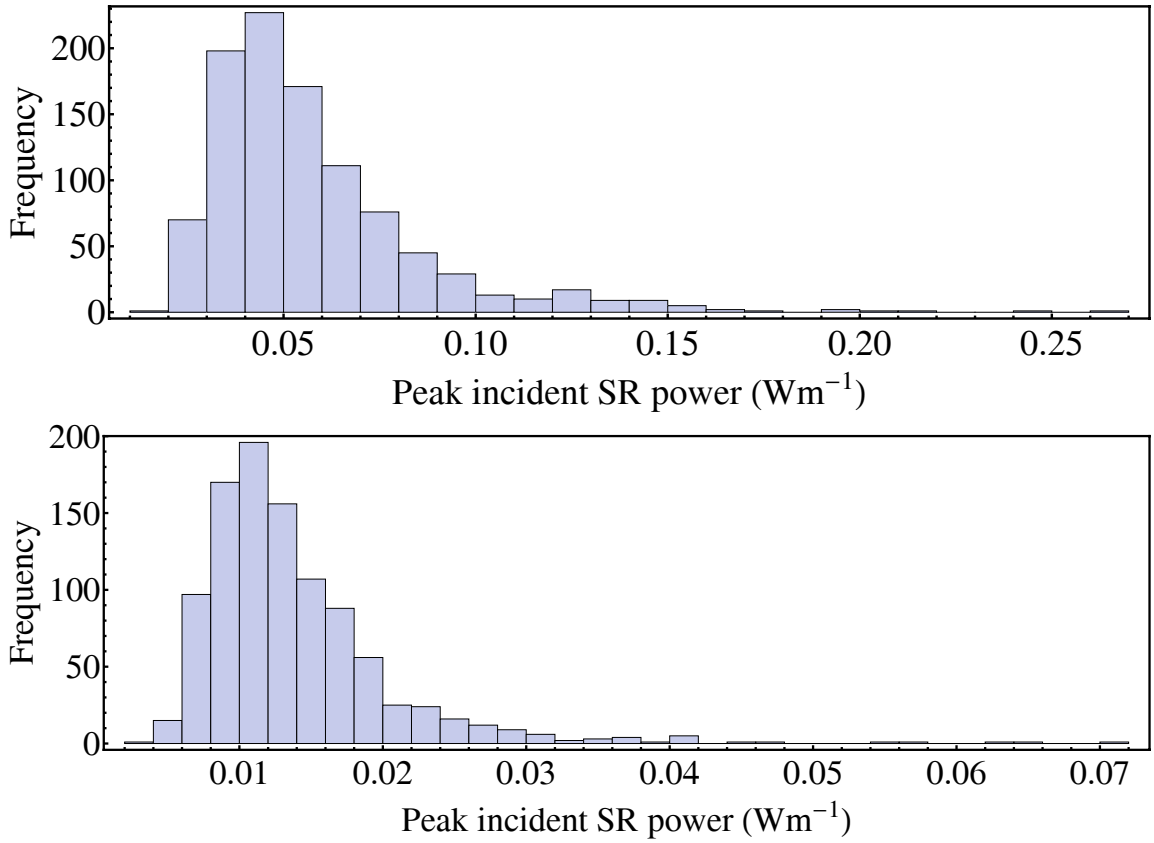

Figure 5.6: Histograms of the peak incident power per metre for 1 000 different iterations of the 20 half-cell undulator line with random misalignments of the collimators for the ILC-BCD (top) and ILC-RDR (bottom) parameters.

5.2 Conclusions and Further Work

The power deposited in the vacuum vessel due to SR has been calculated. The maximum power deposited an a 4 m module in line with ILC-BCD undulator parameters is ∼1.08 W for a 4 m long module. This is significant, however it is a worst case example and the mean peak power from 1 000 iterations was only 0.232 W deposited in a module. For the ILC-RDR undulator parameters the maximum power deposited in a module was 0.28 W and the mean peak power from the 1 000 iterations was 0.056 W. These powers must be combined with the heating due to image currents.[38]

For this study it has been assumed that the photon collimators perfectly absorb all the SR power. For a full engineering design of the collimator system a number of effects will need to be considered. These include, the consequences of photons back-scattered from the collimator surface, the number of photons transmitted through the collimator and the

[38] See Section 7.3.5.

production of secondary particles in the collimator. For these extended studies knowledge of the photon energy distribution is important. For example, photons with energies in the MeV range are harder to absorb than those with lower and higher energies.

The impact factor for a collimator system is defined as the distance between the incident photon and the collimator edge. Small impact factors increase the probability of secondary particles being ejected into the vessel and potentially disrupting the beam or of the particle not being collimated [112]. As there will be photons incident on the entire face of the collimators there will be arbitrarily small impact parameters.

Chapter 6

Magnetic Field and Electron Trajectory Errors

In the previous chapter the power incident on the vessel due to the SR produced in the undulator was calculated. The photon collimators required to achieve the necessary vacuum are also required to absorb the significant amounts of SR power that would quench the super-conducting (SC) magnet. In this chapter electron beam trajectory errors caused by initial off-axis injection into the undulator and magnetic field errors of the undulator are considered. It is necessary to quantify the trajectory errors for a number of reasons. The electron beam must be successfully transported through the 5.85 mm undulator bore. To achieve this it may be necessary to use dipole corrector magnets. From the results of the measured SC undulator models, this type of gross error is not foreseen. Off-axis trajectory deviations of the electron beam are correlated to the direction of the photon beam. With multiple wrongly aligned photon beams the photon-beam spot-size on the conversion target will be increased, affecting the downstream systems. A larger spot size will result in a larger emittance positron beam emerging from the target, and if this is too great there will be a loss of positron intensity [15]. The efficacy of the source will be reduced.

6.1 Electron Trajectory Through the Undulator

Magnetic field errors will result in deviations from the ideal trajectory through the undulator. Estimates of the trajectory errors for the Permanent Magnet (PM) Ring and SC undulator designs are given below.

6.1.1 Computer Modelled Field Errors of the Permanent Magnet Ring Undulator

Even though the SC undulator has been chosen it was decided that modelling of a PM Ring undulator has some benefit. This was because it is simpler to calculate magnetic fields for this design when errors are included. Full magnetic modelling to determine realistic fields that obey Maxwell's equations is CPU intensive and impractical for many iterations. However, a single 1 m long model of the PM Ring undulator was created in RADIA [67] with random errors assigned to the strength and direction of the magnetisation vector of each PM block. The measured range of the on-axis peak fields in the SC undulator is approximately $\pm 2.5\%$[39] and so the magnitude of the random errors of the PM blocks were constrained to give a similar range for the calculated on-axis peak fields. It was decided that the range of the on-axis peak fields the model should be similar to those measured for the SC undulator as it is only their effect on the electron beam trajectory that is under consideration here. Full magnetic modelling means that any off-axis fields considered will obey Maxwell's equations and hence be realistic.[40]

The trajectory of an electron entering the magnet on-axis and 0.5 mm off-axis in the positive and negative x and y directions was calculated using an in-built function in the RADIA code. This performs a 4th order Runge-Kutta integration of the Lorentz-force equation in the full 3D magnetic field, assuming relativistic charged particles [113]. The accuracy purely depends on the number of points in the longitudinal direction (with respect to the particle motion) and so this was increased until the trajectory was unaffected. The trajectories are shown in Figure 6.1. Using a dipole corrector placed at the start of the undulator with its field optimised to bring the displacement off-axis close to zero by the end of the undulator gives the trajectories shown in Figure 6.2. Even for such gross magnetic field errors and large initial displacements, there is very little difference between the trajectories. This indicates that considering only the on-axis field should be sufficient when determining the effect of field errors.

[39] These errors have been improved upon in later prototypes and so can be considered large.

[40] Of course the calculated off-axis fields are for the PM Ring undulator, here it assumed that these fields will also be good approximation for the off-axis fields associated with the SC undulator.

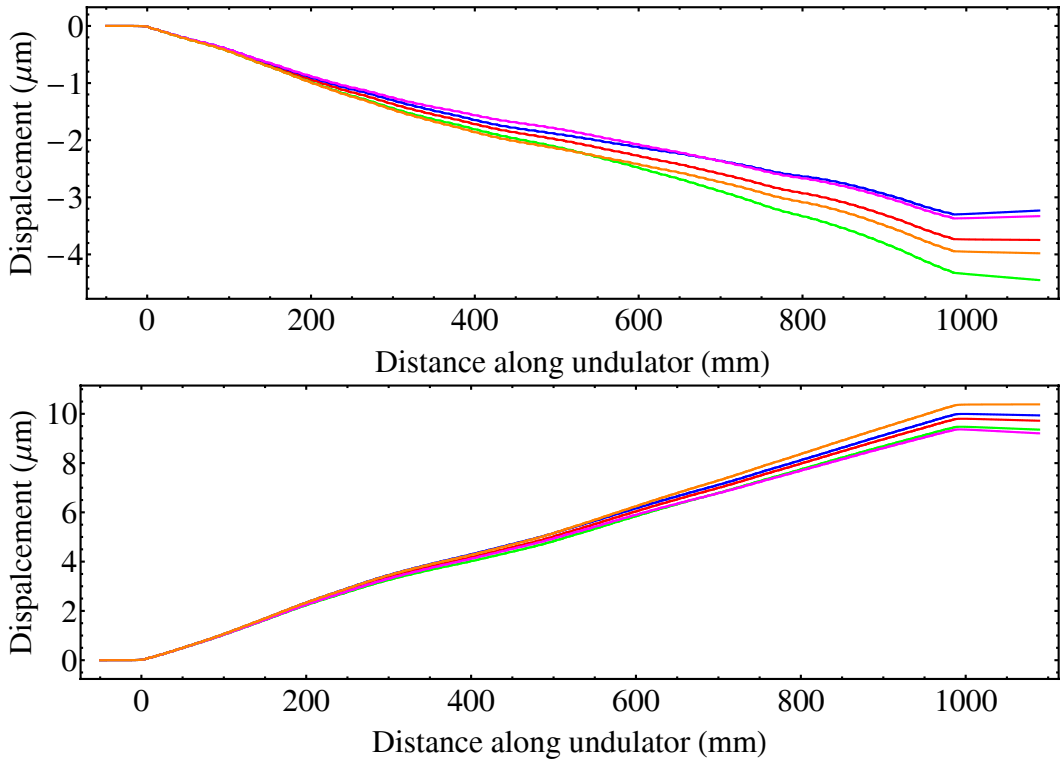

Figure 6.1: Trajectory of a 150 GeV electron (relative to the initial transverse displacement) in the x (top) and y (bottom) planes, with initial (x, y) displacements (in mm) of (0, 0) (red), (0.5, 0) (blue), (-0.5, 0) (green), (0, 0.5) (magenta) and (0, -0.5) (orange).

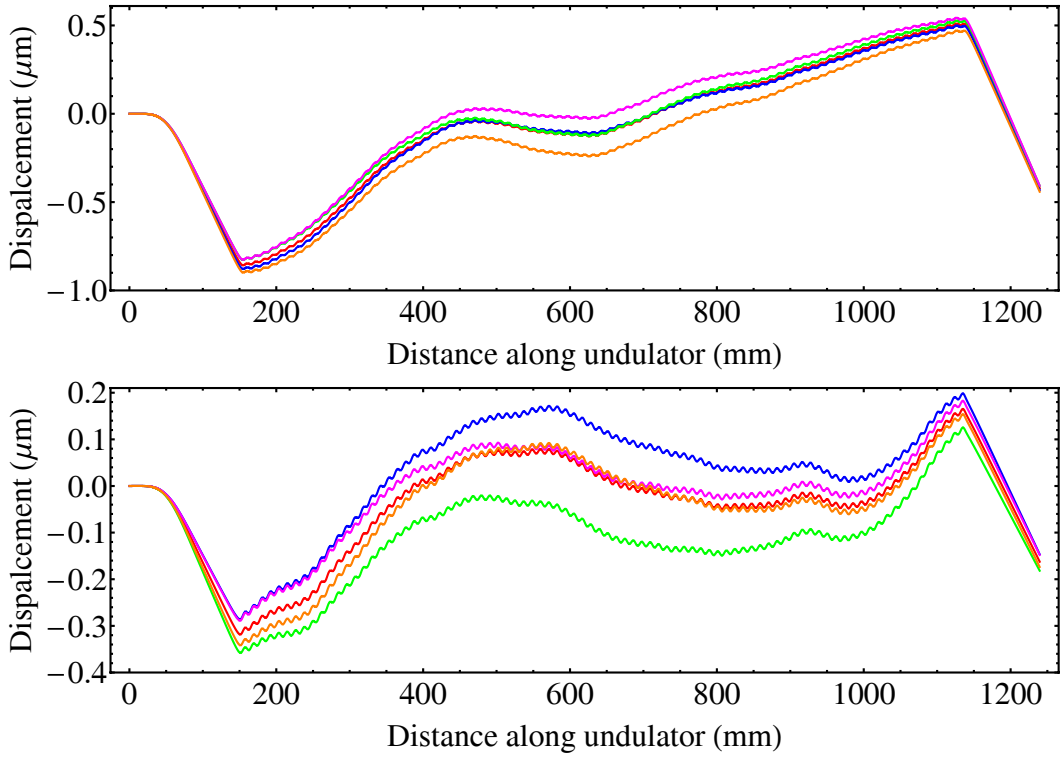

Figure 6.2: Corrected trajectory of a 150 GeV electron (relative to the initial transverse displacement) in the x (top) and y (bottom) planes with initial (x, y) displacements (in mm) of (0, 0) (red), (0.5, 0) (blue), (-0.5, 0) (green), (0, 0.5) (magenta) and (0, -0.5) (orange).

6.1.2 Analytic Estimation of Off-Axis Field Deviation in the Super-Conducting Undulator

It is expected that a similar result would be found for the SC undulator. However, full magnetic modelling of this device with errors would be too time consuming. As an example of the small change in field close to the axis analytic expressions for the magnetic field inside a double helix of two wires can be considered. In cylindrical co-ordinates, where r is the transverse distance off-axis, z the longitudinal position and θ the azimuthal angle, the radial, B_r, azimuthal, B_θ, and longitudinal, B_z, components of the magnetic field are [114]:

$$B_r = 2B_0 \left(I_0(k_u r) - \frac{1}{k_u r} I_1(k_u r) \right) \sin(\theta - k_u z),$$

$$B_\theta = \left(\frac{2B_0}{k_u r} \right) I_1(k_u r) \cos(\theta - k_u z),$$

$$B_z = -2B_0 I_1(k_u r) \cos(\theta - k_u z).$$

Here, B_0 is the transverse field amplitude on-axis, I_0 and I_1 are modified Bessel functions of the first kind and k_u is 2π divided by the undulator period. The transverse field amplitude $\boldsymbol{B}_\perp$ is given by:

$$\boldsymbol{B}_\perp = \sqrt{B_r^2 + B_\theta^2}.$$

Figure 6.3 shows how the transverse field amplitude increases as a function of r and θ. At a radius of 0.5 mm off-axis the peak increase in the field is less than 3 % of the on-axis value. Therefore, along with the results of modelling of the PM Ring undulator in Section 6.1.1, it is reasonable to assume that the trajectory of an electron will not vary greatly for small initial deviations off-axis.

6.2 Estimation of the RMS Trajectory Error with Correction

The SC undulator module for the ILC will comprise of two separate undulators with a small gap between them [64]. To analyse the effect of magnetic field errors on the trajectory through the undulator sample magnetic fields with errors were created. Modules consisting of two, 2 m long sinusoidal field distributions were simulated. For each period, the peak field and length was randomly chosen from Gaussian distributions with means of 0.82 T and 12 mm respectively.[41] The standard deviations used were 5% for the peak field and 0.1%

[41] At the time these calculations were performed these parameters were the best estimate for the ILC.

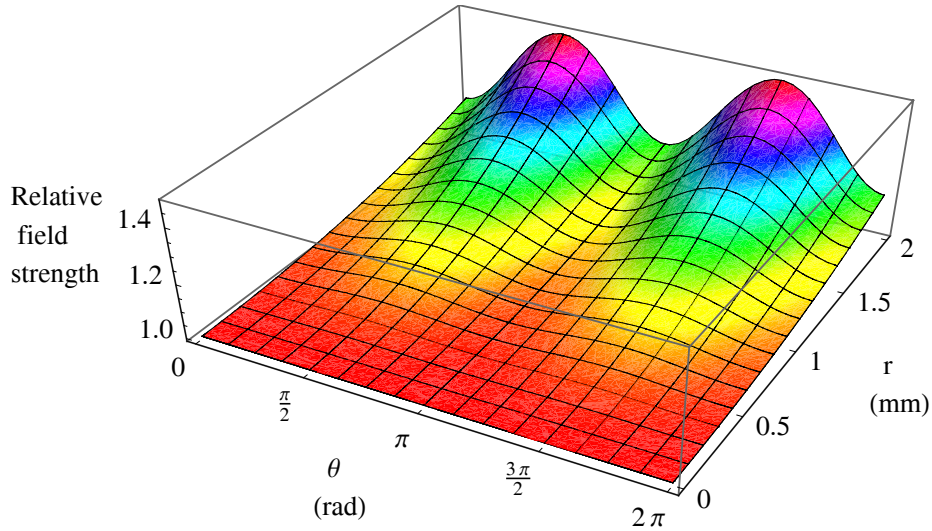

Figure 6.3: Transverse field strength relative to the on-axis transverse field strength as a function of r and θ.

for the length. The end field distributions measured from the SC undulator were added to these fields. Simple dipole steering magnets (modelled as racetrack coils in RADIA) were placed at the start of the module and in the gap between the two undulators and their strength adjusted to minimise the rms trajectory. This was done for 1 000 different initial field distributions. Histograms of the rms trajectory with and without correction are shown in Figure 6.4. The rms trajectory can be corrected to within a few microns over 4 m using these simple dipole steering magnets.

6.2.1 Effect of an RMS Trajectory Error

The effect of trajectory errors is to increase the spot size on the target. If it is assumed that the characteristic opening angle of the radiation is $\sim \frac{K}{\gamma}$ [41] then the spot size 500 m away from the undulator modules will be a circle of diameter ~3 mm. With a 3 μm offset over a 4 m module the locus of points at the target incorporating the radiation from each undulator will be a circle with diameter ~4 mm. This increase is probably acceptable [15], although further detailed simulation work (especially including polarisation effects) is required to confirm this.

6.3 Conclusions and Further Work

Simulations of the magnetic field of the PM Ring undulator with errors have shown that the field on axis can be used to approximate the field experienced by the beam, even with large

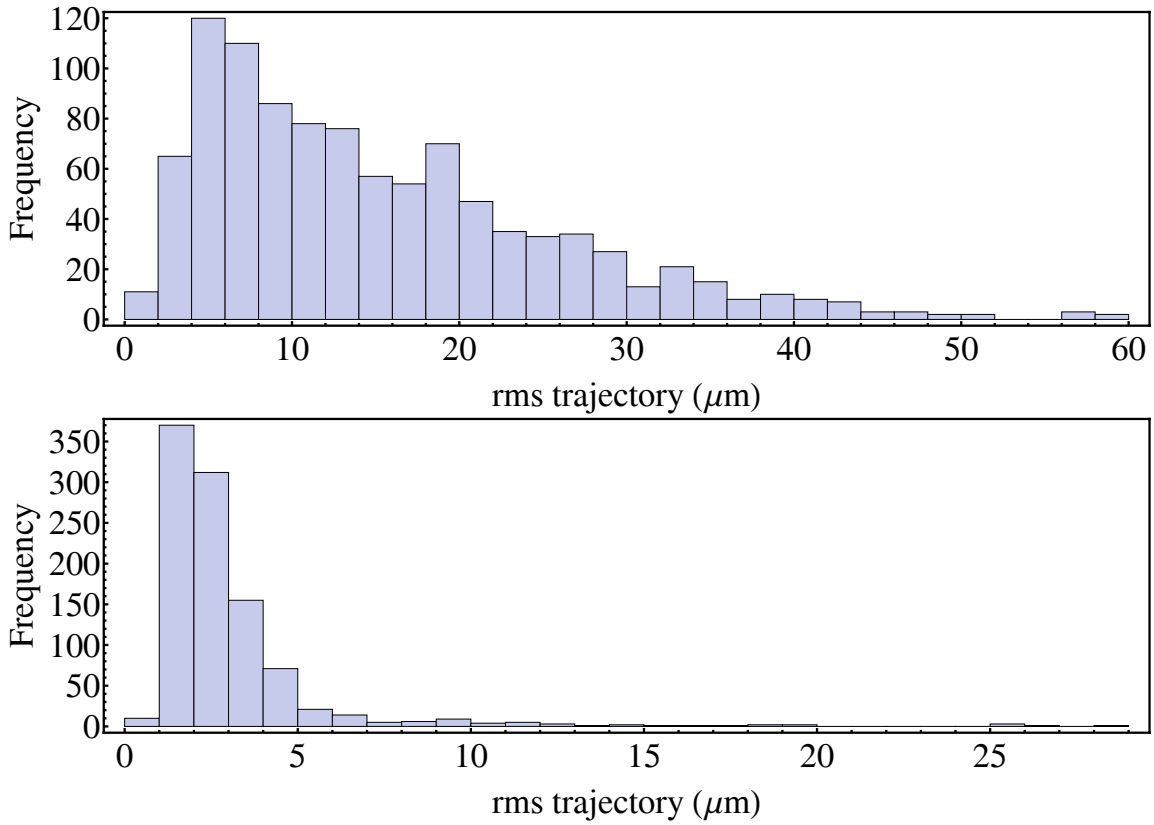

Figure 6.4: Histograms of the rms trajectory of a 150 GeV electron through 1 000 different field distributions, no correction (top), with correction (bottom).

displacements off axis. Analytic expressions for the variation of the transverse field with transverse distance from a bifilar wires arrangement also indicate that this assumption is reasonable. The rms deviation from the nominal trajectory is of the order of tens of microns, and with correction this can be reduced to a few microns. A specification for this value has not been made; however, from geometric arguments it seems likely that trajectory errors at this level will be acceptable for the unpolarised source. Due to the random nature of these errors, the effect on the polarisation is not clear and should be the subject of detailed further study for the polarised source design.

The work presented here takes no account of the beam position monitors (BPMs). These will be used to steer the beam through the undulator system and will result in trajectory errors. Reasonable assumptions for the BPM alignment tolerance and accuracy are 50 μm and 5 μm. With these values the trajectory (as calculated by the BPMs) will not be known accurately enough to prevent the photon spot size on the target increasing. However this could be mitigated by having other feedback systems, such as on the captured positron intensity or a dedicated screen upstream of the photon target to monitor the photon spot size directly.

Chapter 7

Resistive Wall Wakefields of the Vacuum Vessel

In Chapters 3 and 4 the magnetic and vacuum design of the undulator are considered. The heating effects of the SR and the consequence of magnetic field errors on the electron trajectory are considered in Chapters 5 and 6. In this chapter and the next the influence of the undulator vessel and photon collimators on the beam through their impedance is considered.

A beam of charged particles travelling through an accelerator will interact with its surroundings through self generated, co-propagating electromagnetic fields. These electromagnetic fields, that are produced by the beam and interact with the environment, are known as wakefields, and they can have harmful effects on the beam properties, such as changing the energy of the particles and driving instabilities that can increase the beam size. When the fields are described in the time domain, the concept of wake functions is used: when the fields are described in the frequency domain the concept of impedance is used. The wake function is the Fourier transform of the impedance. Impedance effects generally scale as an inverse power of the vessel radius and so are a concern for the (relatively) long narrow-gap undulator vacuum vessel. Two different types of impedance effect have been studied. Resistive wall wakefields are those due to the resistance of the vessel material for an infinitely long round pipe, and are discussed in this chapter. Impedances due to geometry, in particular the vessel surface roughness, are presented in Chapter 8. Further information on wakefields can be found in numerous books and reports, for example in [115, 116, 117].

7.1 Introduction to Wakefields

Consider a source and test charge, q_e and q_t, travelling at the speed of light, $v_e = v_t = c$, parallel to the axis of a vacuum vessel, as shown in Figure 7.1. The source charge and the test charge have coordinates $(\boldsymbol{r_e}, z_e)$ and $(\boldsymbol{r_t}, z_t)$, respectively, and the distance between the two charges is s. The Lorentz force acting on the test particle is:

$$\boldsymbol{F}(\boldsymbol{r_t}, z_t, t) = q_t[\boldsymbol{E}(\boldsymbol{r_t}, z_t, t) + \boldsymbol{v} \times \boldsymbol{B}(\boldsymbol{r_t}, z_t, t)].$$

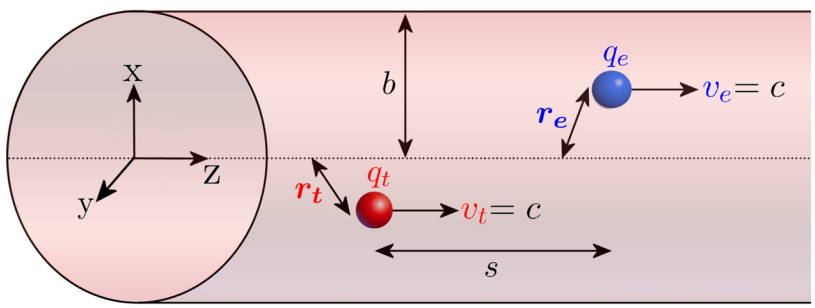

Figure 7.1: Axially symmetric geometry of a circular vacuum vessel of radius b, with an exciting charge, q_e, at (r_e, z_e) (blue) and a test charge, q_t, at (r_t, z_t) (red). Both charges travel at the speed of light parallel to the z axis.

The result of passing through the structure will be a modification of the energy and transverse momentum of both charges. If the particles are at high enough energy, any change in trajectory will only be a small perturbation, therefore it can be assumed that any change in the electromagnetic forces due to changes in the particle's trajectory is negligible. Making this assumption allows the forces to be to be treated as an impulse. The impulse is the integrated force along the length, L, of the structure, and the force associated with this impulse is known as the 'wake force'. The wake force on the test charge depends on the coordinates of both charges and is:

$$\boldsymbol{F}(\boldsymbol{r_t}, \boldsymbol{r_e}, s, t) = q_t[\boldsymbol{E}(\boldsymbol{r_t}, \boldsymbol{r_e}, z_t = vt - s, t) + v\,\boldsymbol{e_z} \times \boldsymbol{B}(\boldsymbol{r_t}, \boldsymbol{r_e}, z_t = vt - s, t)],$$

where $\boldsymbol{e_z}$ is a unit vector in the longitudinal direction. The change in momentum, $\triangle\boldsymbol{p}$, is

then equal to the impulse:

$$\triangle \boldsymbol{p}(\boldsymbol{r_e}, \boldsymbol{r_t}, s) = \int_L \boldsymbol{F}(\boldsymbol{r_t}, \boldsymbol{r_e}, s, t)\ \mathrm{d}t.$$

As s, z and t are not independent variables, the integration with respect to time can be replaced with an integration with respect to the longitudinal co-ordinate, z. This change of variables allows the 'wake function' to be defined:

$$\boldsymbol{w}(\boldsymbol{r_t}, \boldsymbol{r_e}, s) = \frac{1}{q_e} \int_L [\boldsymbol{E}(\boldsymbol{r_t}, \boldsymbol{r_e}, z, t) + v\boldsymbol{e_z}\boldsymbol{B}(\boldsymbol{r_t}, \boldsymbol{r_e}, z, t)]_{t=\frac{(z+s)}{c}}\ \mathrm{d}z,$$

so that:

$$\triangle \boldsymbol{p} = \frac{q_e q_t \boldsymbol{w}}{c}.$$

The wake for a longitudinal charge density, $\rho(s)$, is known as the 'wake potential', $\boldsymbol{W}(\boldsymbol{r_e}, s)$. At a distance s from a reference particle in the bunch and at $\boldsymbol{r_e} = \boldsymbol{r_t}$ it is obtained by convoluting the charge density with the wake function:

$$\boldsymbol{W}(\boldsymbol{r_e}, s) = \int_{-\infty}^{\infty} \rho(s')\boldsymbol{w}(\boldsymbol{r_e}, s - s')\ \mathrm{d}s'. \tag{7.1}$$

The charge distribution is normalised such that $\int_{-\infty}^{\infty} \rho(z)\ \mathrm{d}z = 1$. Wake potentials are normally expressed in terms of transverse, $\boldsymbol{W}_\perp$, and longitudinal, $W_\parallel$, components that are related by the Panofsky-Wenzel theorem [118]:

> *The transverse gradient of the longitudinal wake potential is equal to the longitudinal gradient of the transverse wake potential.*

Therefore, if either of these wakes is known, the other can be calculated from it. If the transverse electric fields are equal at the beginning and end of the structure being considered then the Panofsky-Wenzel theorem can be expressed as:[42]

$$\frac{\partial}{\partial s}\boldsymbol{W}_\perp(\boldsymbol{r_e}, s) = -\boldsymbol{\nabla}_\perp W_\parallel(\boldsymbol{r_e}, s).$$

The longitudinal component of the wake function describes the energy gain (or loss) of the test charge. If the source and test charge have the same sign then a positive wake

[42] See Appendix C.

function implies an accelerating electric field component. The energy lost by the exciting charge is the work done by the longitudinal electromagnetic force along the structure. The average energy lost, $\triangle E$, of a bunch of N particles of charge q is:

$$\triangle E = Nq^2\, k_{\parallel}, \tag{7.2}$$

where $k_{\parallel}$ is the longitudinal loss factor, which is a property of the environment, not of the beam. The longitudinal loss factor of a bunch is the integral of the longitudinal wake potential weighted by the charge distribution:

$$k_{\parallel} = -\int_{-\infty}^{\infty} \rho\,(s)\, W_{\parallel}(s)\ \mathrm{d}s. \tag{7.3}$$

The transverse component of the wake function gives a kick to the trailing particle in the transverse direction. A transverse loss factor (sometimes called the transverse kick factor), $k_{\perp}$, can also be defined as the average of the transverse wake:

$$k_{\perp} = \langle \boldsymbol{W}_{\perp} \rangle.$$

Generally speaking the discussion will now concentrate on the longitudinal wakefield but applies equally to the transverse wakefield.

In an axially symmetric system the beam can be represented as a superposition of charged rings where the charge density has a $\cos(n\theta)$ angular dependence, here n is an integer and θ is the azimuthal angle. Examples are shown in Figure 7.2. This representation means that the total wake function can be decomposed into a series expansion of nth-order wake functions:

$$w_{\parallel}(\boldsymbol{r_t}, \boldsymbol{r_e}, s) = \sum_{n=0}^{\infty} w_{n,\parallel}(\boldsymbol{r_t}, \boldsymbol{r_e}, s).$$

Wake functions that are created by geometric distortions or discontinuities of a real vacuum vessel are generally complicated functions of z and t. The integrals can be made much simpler if simple geometries are considered. For an infinitely long uniform pipe, the fields propagate with the bunch as a function of s. If it is assumed that the wake forces are constant along the vessel and the wake is linear with length then the wake function per

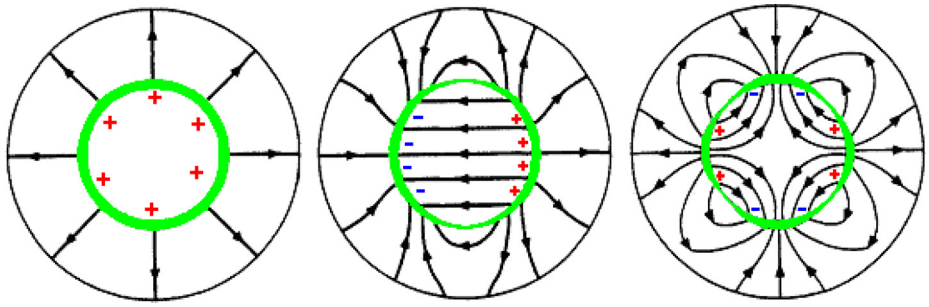

Figure 7.2: Electric field lines (black arrows) in a cylindrical vessel for transverse charge distribution (green) associated with a $\cos(n\theta)$ ring beam. Monopole, $n = 0$ (left), dipole, $n = 1$ (middle) and quadrupole, $n = 2$ (right), distributions are shown.

unit length is a convenient way of expressing the wake:

$$\frac{\mathrm{d}\boldsymbol{w}(\boldsymbol{r_t}, \boldsymbol{r_e}, s)}{\mathrm{d}z} = \frac{1}{q_e q_t}\boldsymbol{F}(\boldsymbol{r_t}, \boldsymbol{r_e}, s).$$

When the beam passes through structures before the section of interest, other wakefields will be created and these fields will enter the section under consideration along with the beam. In constructing the wake function per unit length these electromagnetic fields have been neglected as they are small.

The wake function is a function of distance, s. As it is assumed that the particles travel at the speed of light, the equations can be formulated as functions of time or space. The time difference T between the source and test charge is simply, $T = \frac{s}{c}$. The Fourier transform of the longitudinal wake function with respect to T defines the longitudinal impedance, $Z_\parallel$:

$$Z_\parallel(\boldsymbol{r_t}, \boldsymbol{r_e}, \omega) = -\int_{-\infty}^{\infty} w_\parallel(\boldsymbol{r_t}, \boldsymbol{r_e}, s = c\tau)\mathrm{e}^{\mathrm{i}\,\omega\,T}\ \mathrm{d}T,$$

and the wake function can be determined from the impedance via the inverse Fourier transform:

$$w_\parallel(\boldsymbol{r_t}, \boldsymbol{r_e}, s) = -\frac{1}{2\pi}\int_{-\infty}^{\infty} Z_\parallel(\boldsymbol{r_t}, \boldsymbol{r_e}, \omega)\mathrm{e}^{-\mathrm{i}\,\omega\,T}\ \mathrm{d}\omega.$$

Either the wake function in the time domain or the impedance in the frequency domain can be used to describe the interaction of the beam with its environment.

In general, the effects of impedances from different sources are calculated separately and then the effects of the total impedance on the bunch assessed. There are two main types of wakefield effects that have been considered: the resistive wall and geometric

wakefields of the vacuum vessel. The resistive wall wakefields arise due to the non-zero resistivity of the vacuum vessel wall material. The geometric wakefields are caused by the vessel geometry and discussed further in Chapter 8.

7.2 Resistive Wall Wakefields of an Infinitely Long Round Pipe

The resistive wall wakefields depend upon the conductivity of the vessel material. Vacuum vessels are generally made from stainless-steel or aluminium. These are often coated with copper to provide a higher conductivity surface for the fields of the beam to interact with. An assessment of the effects of different materials has been made in order to specify the required vacuum vessel material. Copper, gold, aluminium, iron and stainless steel have been considered. The conductivity of a material depends upon the frequency of the driving electromagnetic field. For the ILC this can be high due to the short bunch lengths, which are typically a few hundred microns (see Table 1.1). Conductivity is also temperature dependent and so there will be differences between room and cryogenic temperature calculations.

7.2.1 Models of Electrical Conductivity

In the Drude-Sommerfeld model of electron conductivity [119], conduction electrons are treated as an ideal gas. The conductivity is related to the mean free time between collisions (or metal relaxation time), τ, of the conduction electrons moving in an applied field, or equivalently the mean free path between collisions, λ. These quantities are related by the Fermi velocity, v_F, of the material:

$$\lambda = v_F \, \tau.$$

7.2.1.1 DC Conductivity

If the field the conduction electrons are moving in is constant during the time τ, then the conductivity is said to be DC. The DC conductivity of a metal, σ_{DC}, is given by [119]:

$$\sigma_{DC} = \frac{n \, e^2 \, \tau}{m_e}, \tag{7.4}$$

where n is the density of conduction electrons, e their charge and m_e the electron mass. Ideally, values at 4.2 K (the operating temperature of the super-conducting (SC) magnet) should be used, however at these temperatures the electrical properties are dependent on the levels of impurities in the material and are difficult to assess. For this reason, the wakefield effects have been calculated at 273 K and 77 K only. Values of τ, λ and σ_{DC} for various metals at 273 K and 77 K are given in Table 7.1 [119].

Values for stainless steel are difficult to obtain because the electrical properties greatly depend upon the level of impurities at all temperatures. The conductivity is relatively simple to measure and an estimation of τ can be made using the method described in the following. In order to obtain λ the Fermi velocity is needed, which is significantly more difficult to derive or measure experimentally. If σ_{DC} is known then, from Equation 7.4, only a value for the density of conduction electrons is required to calculate τ. The density of conduction electrons can be calculated from the mass density, ρ_m, atomic weight, A, and number of valence electrons, Z, of the material by using [119]:

$$n = \frac{N_A \, Z \, \rho_m}{A},$$

where N_A is Avogadro's number. The radius of a sphere whose volume is equal to the volume per conduction electron, r_{sphere}, is then:

$$r_{sphere} = \left(\frac{3}{4 \, \pi \, n} \right)^{\frac{1}{3}}.$$

This gives a convenient expression for the relaxation time in seconds [119]:

$$\tau = \frac{0.22}{\rho_\mu} \frac{r_{sphere}}{a_0} \times 10^{-14},$$

where ρ_μ is the resistivity in $\mu\,\Omega\,\mathrm{cm}$ and a_0 is the Bohr radius of the atom.

As an example, copper has a single valence electron, a density of 8.23 $\mathrm{g\,cm^{-3}}$ and an atomic weight of 63.6 g $\mathrm{mol^{-1}}$. This gives an electron density of 7.8×10^{22} $\mathrm{g\,cm^{-3}}$ and a relaxation time of 2.9×10^{-14} s, an often quoted value for copper is 2.7×10^{-14} s [119]. Stainless-steel type 316L has a density of 8 $\mathrm{g\,cm^{-3}}$, a resistivity of 74.5 $\mu\,\Omega\,\mathrm{cm}$ at room temperature and a number of valence electrons that is not well defined, but four shall be assumed as a reasonable estimate. These numbers give, $\tau_{StainlessSteel} = 1.38 \times 10^{-16}$ s. This is much shorter than the other pure materials in Table 7.1, which is expected due to the

high levels of impurities that act as scattering centres for the conduction electrons. As it is assumed that the value of τ for stainless steel is mainly due to impurities this value shall be used at all temperatures.

Table 7.1: Values of σ_{DC}, τ and λ for different materials at 273 K and 77 K [119].

	273 K			77 K		
Material	σ_{DC} ($\mathrm{M\Omega^{-1}\,m^{-1}}$)	τ (fs)	λ (nm)	σ_{DC} ($\mathrm{M\Omega^{-1}\,m^{-1}}$)	τ (fs)	λ (nm)
Copper	58.8	27	42	500	210	330
Gold	36.2	8.0	42	333	65	167
Aluminium	59.3	30.0	16	200	200	132
Iron	11.0	2.3	4.7	15.1	32	63
Stainless-Steel (Type 316L)	1.34	0.14	-	-	-	-

7.2.1.2 AC Conductivity

The DC conductivity model assumes that the applied field is constant between electron collisions. If the applied field changes significantly between the collisions then the conductivity is said to be AC and is given by [119]:

$$\sigma_{AC} = \frac{\sigma_{DC}}{1 - \mathrm{i}\,\omega\,\tau},$$

where ω is the angular frequency of the field. For AC conductivity wakefield calculations, a dimensionless parameter, Γ, can be defined which indicates the strength of the AC conductivity effects [120]:

$$\Gamma = \frac{\tau c}{s_0},$$

where s_0 is the characteristic length of the wakefields. This is a function of σ_{DC}, the pipe radius, b and the permittivity of free space, ϵ_0, and is given by [116]:

$$s_0 = \left(\frac{2\,c\,b^2\,\epsilon_0}{\sigma_{DC}}\right)^{\frac{1}{3}}.$$

Table 7.2 gives vales of Γ for a 2 mm radius vessel and the various materials considered. From the values of Γ it is expected that the AC effects at 77 K will be more significant than at 273 K for all materials. The material with the biggest temperature dependent difference will be iron followed by aluminium, copper and then gold.

Table 7.2: Values of Γ for 2 mm radius vessels at 273 K and 77 K.

	Γ (273 K)	Γ (77 K)
Copper	1.13	18
Aluminium	0.27	4.88
Gold	1.27	7.6
Iron	0.055	1.84

7.2.1.3 The Anomalous Skin Effect

If the frequency of the field is not too high then the field will penetrate into a metal a distance δ, the classical skin depth, given as a function of wavenumber, $k = \frac{\omega}{c}$, by [119]:

$$\delta(k) = \sqrt{\frac{2}{Z_0\,\sigma_{DC}\,k}}. \tag{7.5}$$

Here, $Z_0 = (c\,\epsilon_0)^{-1}$ is the vacuum impedance. The derivation of the skin depth of a material assumes that the field in the metal varies little over the mean free path, $\delta \gg \lambda$. When this assumption is not valid and $\delta \sim \lambda$ the theory of the anomalous skin effect (ASE) must be used. For cases where $\delta \ll \lambda$, the simple picture of an exponentially decaying field breaks down completely and is known as the extreme anomalous regime. Table 7.3 gives values of the skin depth for the various materials and the three ILC bunch lengths, calculated using Equation 7.5. When compared with the mean free path between collisions in Table 7.1, it can be seen that the ASE description will be most significant for short bunches at low temperatures. Also the effects for aluminium will be weaker than those for copper or gold. Iron and stainless steel will show the strongest ASE characteristics.

Table 7.3: Values for the skin depth, δ, for different materials with different ILC bunch lengths, σ_z, at 273 K and 77 K.

σ_z (μm)	T (K)	Copper (nm)	Aluminium (nm)	Gold (nm)	Iron (nm)	Stainless-Steel (316L) (nm)
150	273	46.4	59.2	46.2	107.4	307
	77	15.9	19.5	25.2	28.9	
300	273	65.7	83.7	65.4	152	435
	77	22.5	27.6	35.6	40.9	
500	273	84.8	108	84.4	196	561
	77	29.1	35.6	46.0	52.8	

The surface impedance, Z_{ASE}, resulting from the ASE can be derived [121]. In this model, Z_{ASE} is expressed in terms of a ratio to the normal, or classical, impedance Z_{cl}. The surface resistive, R, and reactive, X, parts of the impedance as a function of wavenumber k are:

$$\frac{R_{ASE}(k)}{R_{cl}(k)} = \frac{(4\sqrt{2\,\alpha(k)})(k\,c\,\tau\,\mathrm{Re}[I(k)] - \mathrm{Im}[I(k)])}{\pi\sqrt{3}(1+(k\,c\,\tau)^2)\sqrt{-k\,c\,\tau + \sqrt{1+(k\,c\,\tau)^2}}}, \tag{7.6a}$$

$$\frac{X_{ASE}(k)}{X_{cl}(k)} = \frac{(4\sqrt{2\,\alpha(k)})(k\,c\,\tau\,\mathrm{Re}[I(k)] + \mathrm{Im}[I(k)])}{\pi\sqrt{3}(1+(k\,c\,\tau)^2)\sqrt{k\,c\,\tau + \sqrt{1+(k\,c\,\tau)^2}}}. \tag{7.6b}$$

Here:

$$\alpha(k) = \frac{3}{2}\left(\frac{\lambda}{\delta}\right)^2 \tag{7.6c}$$

and

$$I(k) = \int_0^\infty \left(t^2 + \frac{2\,\mathrm{i}\,\alpha(k)[(1+t^2)\arctan(t) - t]}{(1+k\,c\,\tau)^3}\right)^{-1} \mathrm{d}t. \tag{7.6d}$$

The classical expressions for the surface resistance and reactance are:

$$R_{cl}(k) = \sqrt{\frac{k}{2\epsilon_0 c\,\sigma_{DC}}}\sqrt{-k\,c\,\tau + \sqrt{1+(k\,c\,\tau)^2}}, \tag{7.6e}$$

$$X_{cl}(k) = \sqrt{\frac{k}{2\epsilon_0 c\,\sigma_{DC}}}\sqrt{k\,c\,\tau + \sqrt{1+(k\,c\,\tau)^2}}. \tag{7.6f}$$

Figure 7.3 shows how the ASE changes the surface impedance for copper as a function of angular frequency. The resistive and reactive parts can decrease as well as increase. It can also be seen that the effects at lower temperatures are more important. This is to be expected as λ is greater at lower temperatures.

A dimensionless ASE strength parameter, Λ, can be defined that is also independent of frequency [120]:

$$\Lambda = \frac{\alpha(k)}{k\,c\,\tau}.$$

The higher the value Λ the stronger the effect of the ASE model. Table 7.4 gives vales of Λ for the various materials considered at 273 K and 77 K. From the values of Λ it is expected that the ASE will be more significant at lower temperatures. The biggest difference due to temperature will be seen in iron, then copper and aluminium with gold having the least difference.

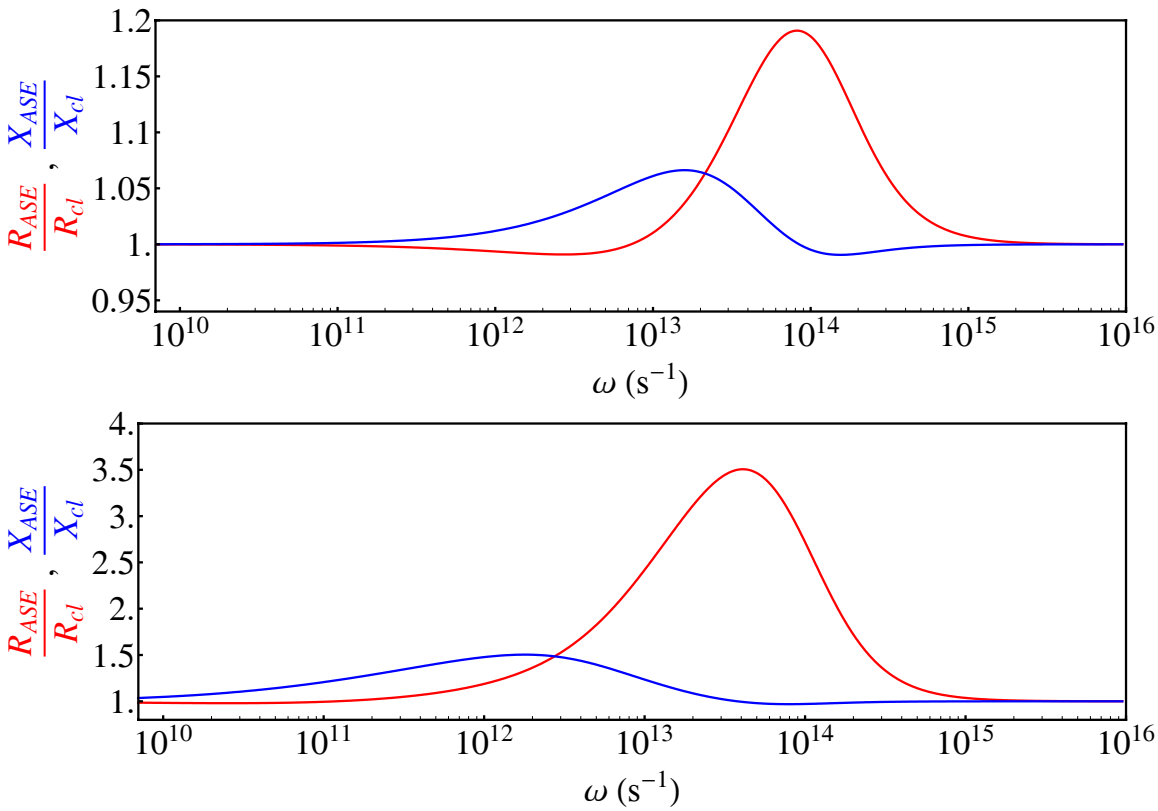

Figure 7.3: Ratio of the ASE resistance and reactance to the classical surface resistance and reactance (red and blue respectively), for copper at 273 K (top) and 77 K (bottom) as a function of the frequency of the applied field.

Table 7.4: Values of Λ for different materials at 273 K and 77 K.

	Λ (273 K)	Λ (77 K)
Copper	3.69	244
Aluminium	1.12	84
Gold	3.27	44
Iron	0.09	17.9

7.2.2 Longitudinal Resistive Wall Impedance for the Different Conductivity Models

The undulator vessel will be an axially symmetric system and the length to aperture ratio is high so the resistive wall impedance of an infinitely long round pipe can be used to model the impedance of the vessel. For this geometry, the surface impedance for the different conductivity models has been found and is outlined below.

7.2.2.1 DC Conductivity Impedance

For a round metallic pipe, the longitudinal impedance of the nth multi-pole of the beam using the DC conductivity model, $Z^n_{\parallel,DC}$, is [115]:

$$Z^n_{\parallel,DC}(k,\boldsymbol{r_e},\boldsymbol{r_t}) = \frac{Z_0\, s_0}{2\,\pi\, b^2}\left(\frac{\boldsymbol{r_e}\,\boldsymbol{r_t}}{b^2}\right)^n \times \left[\frac{1-\mathrm{i}\,\mathrm{sgn}(k\,s_0)}{|k\,s_0|^{\frac{1}{2}}} + \frac{\mathrm{i}\,k\,s_0}{n+1} + \left(\frac{s_0}{b}\right)^2\left\{\frac{|k\,s_0|^{\frac{1}{2}}}{1-\mathrm{i}\,\mathrm{sgn}(k\,s_0)} + \frac{\mathrm{i}\,n}{k\,s_0} + \left(\frac{s_0}{b}\right)^2\frac{n}{2}\right\}\right]^{-1}, \quad (7.7)$$

where n refers to the order of the multipole of the beam. The amplitude of the higher multipoles is proportional to the factor $\left(\frac{\boldsymbol{r_e}\boldsymbol{r_t}}{b^2}\right)^n$ and for small displacements off axis only the monopole term is important. For example, if the beam was displaced 500 μm off axis in a 2 mm radius vessel, then the dipole term is a factor of 125 less than the monopole term. Therefore, from now on, the $\boldsymbol{r_e}$ and $\boldsymbol{r_t}$ dependence of the wake function will be dropped and only the monopole wake will be considered. The terms in the curly brackets are also suppressed by the factor $\left(\frac{s_0}{b}\right)^2$. Typically, s_0 is of the order of microns and b is in millimeters so the expression in curly brackets in Equation 7.7 is suppressed by a factor of $\sim 10^{-6}$. Therefore, these terms are also neglected in the following analysis. This gives the monopole longitudinal DC impedance, $Z^0_{\parallel,DC}$, as:

$$Z^0_{\parallel,DC}(k) = \frac{Z_0\, s_0}{2\,\pi\, b^2}\left[\frac{1-\mathrm{i}\,\mathrm{sgn}(k\,s_0)}{|k\,s_0|^{1/2}}\right].$$

7.2.2.2 AC Conductivity Impedance

The monopole longitudinal AC impedance, $Z^0_{\parallel,AC}$, is given in terms of Γ and s_0 [120]:

$$Z^0_{\parallel,AC}(k) = \frac{Z_0\, s_0}{2\,\pi\, b^2}\left[\sqrt{\frac{t_\lambda}{\Gamma\, k^2}}(\mathrm{i}\sqrt{1+t_\lambda}) + \mathrm{sgn}(k)\sqrt{1-t_\lambda} - \frac{\mathrm{i}\,k}{2}\right]^{-1},$$

where:

$$t_\lambda = \frac{|ks_0|\Gamma}{\sqrt{1+(k\,s_0\,\Gamma)^2}}.$$

7.2.2.3 Anomalous Skin Effect Impedance

The monopole longitudinal ASE impedance $Z^0_{\parallel,ASE}$ is [120]:

$$Z^0_{\parallel,ASE}(k) = \frac{1}{2\pi\epsilon_0 c\,b}\left[\left(\frac{4\pi|k|}{cR_{ASE}(k)\mathrm{sgn}(k) - c\mathrm{i}\,X_{ASE}(k)}\right)k^{-1} - \frac{\mathrm{i}kb}{2}\right]^{-1}$$

where R_{ASE} and X_{ASE} can be found from Equations 7.6.

7.2.3 Example Calculation

As an example, the impedance, wake function and wake potential were calculated for a 2 mm radius copper vessel at 273 K and 77 K. Two different charge distributions were considered with a length of $\sigma_z = 150\,\mu$m.

7.2.3.1 Longitudinal Resistive Wall Impedance

Figure 7.4 shows the resistive, R, and reactive, X, parts of the longitudinal resistive wall impedance. The resonant peaks for the AC and ASE impedance are much narrower than for the DC impedance. The AC, and particularly the ASE, impedances are more pronounced at 77 K, as expected. The imaginary parts of the impedances are odd functions and the real parts are even functions.

7.2.3.2 Longitudinal Wake Functions

By definition, the longitudinal wake function, $w_\parallel$, is simply the Fourier transform of the longitudinal impedance, $Z_\parallel$:

$$w_\parallel(t) = \frac{1}{2\,\pi}\int_{-\infty}^{\infty} Z_\parallel(\omega)\mathrm{e}^{\mathrm{i}\,\omega\,t}\mathrm{d}\,\omega. \tag{7.8}$$

For the DC conductivity model the wake function has been found analytically by substituting $Z^0_{\parallel,DC}$, into Equation 7.8 and performing the integration in the complex plane. The

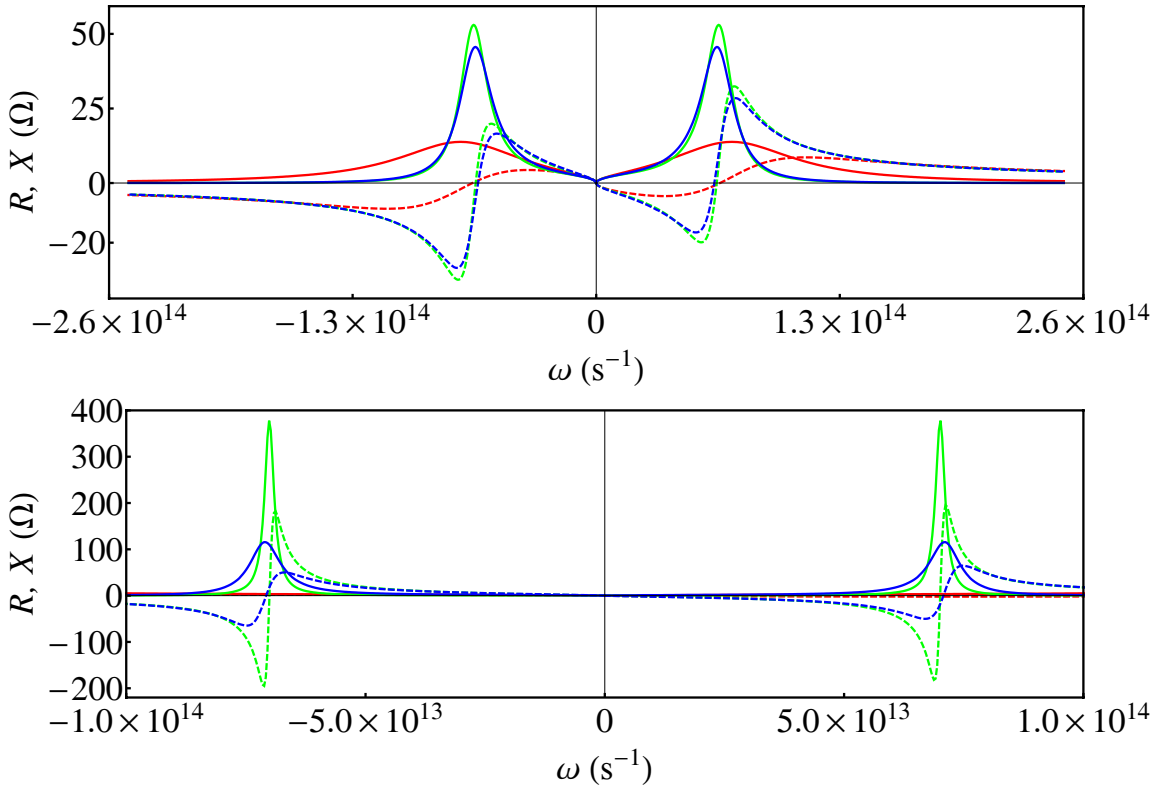

Figure 7.4: Resistive (solid) and reactive (dashed) parts of the impedance for the DC (red), AC (green) and ASE (blue) conductivity models vs ω, for copper at 273 K (top) and at 77 K (bottom).

result is [122]:

$$w_{\parallel}(s) = -\frac{4}{\pi\,\epsilon_0\,b^2}\left(\frac{1}{3}\,\mathrm{e}^{-\frac{s}{s_0}}\cos\left[\sqrt{3}\,\frac{s}{s_0}\right] - \frac{\sqrt{2}}{\pi}\int_0^{\infty}\frac{x^2}{x^6+8}\,\mathrm{e}^{-\frac{x^2\,s}{s_0}}\,\mathrm{d}x\right).$$

For the AC and ASE impedances, the wake functions have been found numerically and they are shown in Figure 7.5 for 273 K and 77 K. For the calculation, the Fourier transform can be simplified to:

$$w_{\parallel}(t) = \frac{2\,c}{\pi}\int_0^{\infty}\mathrm{Re}[Z_{\parallel}^0(k)]\cos(k\,s)\mathrm{d}k,$$

as only the real part of the impedance has a non-zero value when integrated from minus infinity to plus infinity.

The wake function is the wake potential left behind a delta function charge distribution. The charge is at $s = 0$ and is traveling in the negative s direction. At 273 K the AC and ASE wakes are similar and at 77 K they are quite different, as expected.

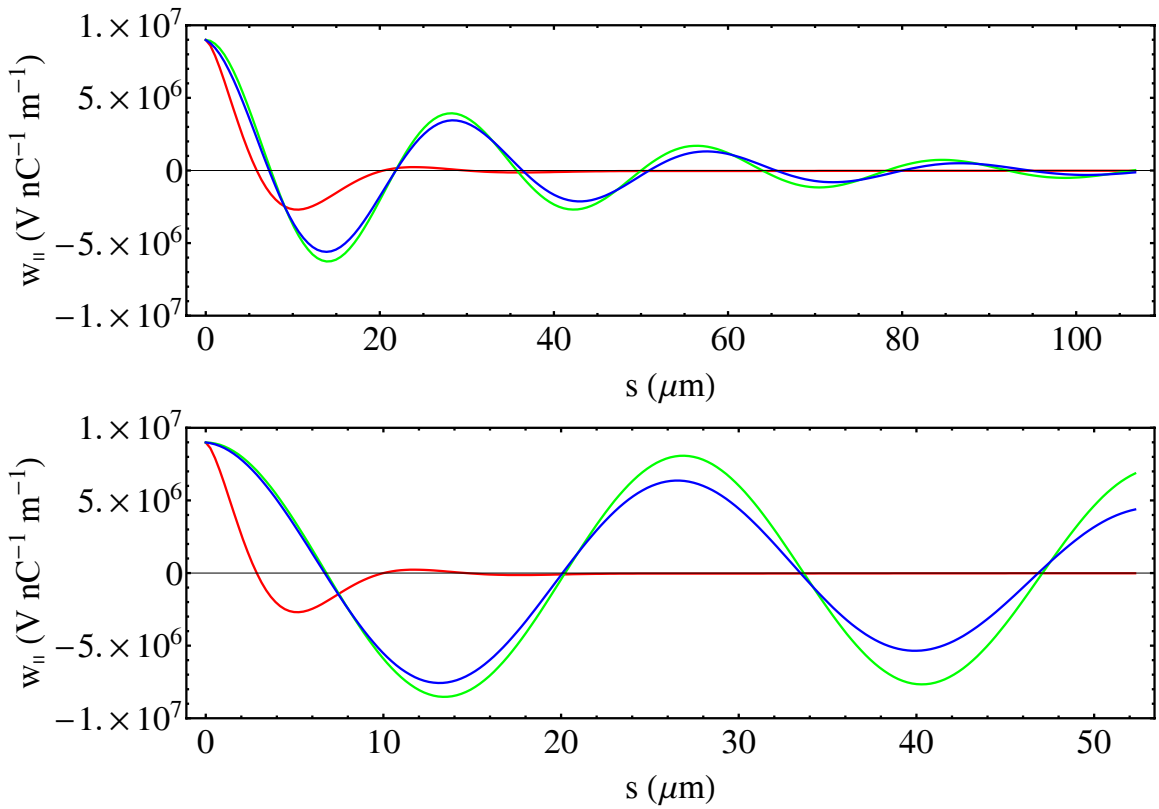

Figure 7.5: The DC (red), AC (green) and ASE (blue) wake functions for a 2 mm radius copper vessel at 273 K (top) and at 77 K (bottom).

7.2.3.3 Longitudinal Wake Potentials

The longitudinal wake potentials, $W_{\parallel}$, are found by convoluting the longitudinal wake function with a charge distribution, $\rho(s)$, (Equation7.1). The wakefield effects could be quite different for non-Gaussian charge distributions. Therefore a trapezium charge distribution has also been considered as an example. Both distributions are shown in Figure 7.6.

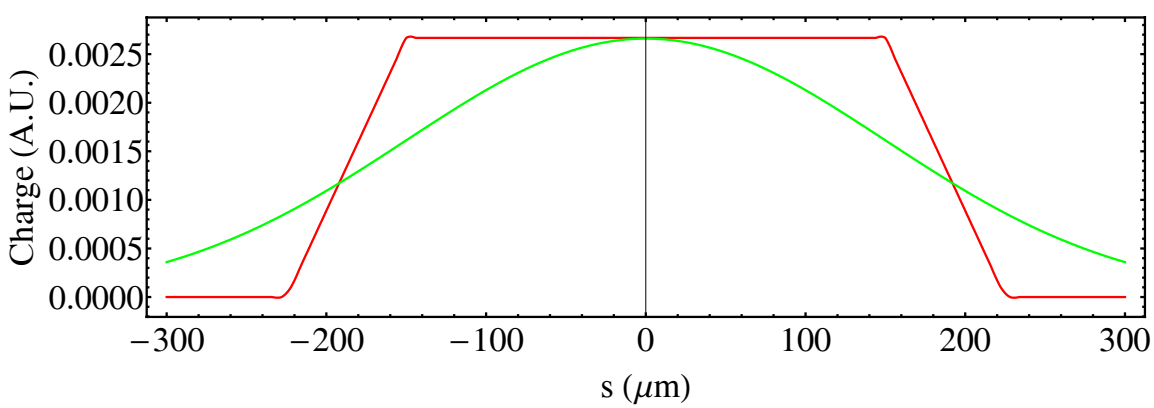

Figure 7.6: Gaussian (green) and trapezium (red) charge distributions, normalised so $\int \rho(s)\mathrm{d}s = 1$ for $\sigma_z = 150\,\mu$m).

Figure 7.7 shows the wake potentials from a 2 mm diameter copper vessel at 273 K and 77 K for Gaussian and trapezium shaped bunches, respectively. The difference between the AC and ASE wakes again becomes more prominent at 77 K, but the amplitude of the wakes is much smaller at 77 K. The wake for the trapezium shaped bunch has a higher oscillation frequency, due to the higher frequency components in the charge distribution. The wakes oscillate behind the bunch and so could affect the subsequent bunch. However, in the ILC the bunches are $\sim$ 100 m apart and the wake has decayed by a factor of 10^9 after about 0.4 m at 77 K so this is unlikely to be significant.

7.2.4 Longitudinal Loss Factor, Energy Loss and Induced Energy Spread

The longitudinal loss factor for a bunch of N particles, $k_{\|}$, is related to the average energy loss per particle, $\triangle E$, and can be calculated from Equations 7.2 and 7.3:

$$\begin{aligned} k_{\|} &= \frac{\triangle E}{N\,q^2} \\ &= -\langle W_{\|}\rangle \\ &= -\int_{-\infty}^{\infty} \rho(s) W_{\|}(s)\mathrm{d}s, \end{aligned}$$

from which the induced rms correlated energy spread of the bunch, σ_E, can be determined [117]:

$$\sigma_E = e^2\,N \left| \int_{-\infty}^{\infty} (\rho(s) W_{\|}^2(s) - k_{\|}^2)\mathrm{d}s \right|^{\frac{1}{2}}.$$

7.2.4.1 Average Energy Lost per Electron per Bunch

Figure 7.8 shows the calculated energy lost by a Gaussian and trapezium bunch ($\sigma_z = 150\ \mu$m) in a 200 m long stainless steel vacuum vessel at 273 K (the worst possible case). The average energy lost by an electron in the bunch is less than 30 MeV. The DC wake dominates for the Gaussian bunch whereas the AC dominates for the trapezium bunch. This is due to the higher frequency components in the trapezium charge distribution. In comparison to the $\sim$3 GeV lost by the beam due to SR in the undulator [20], this loss is not significant.

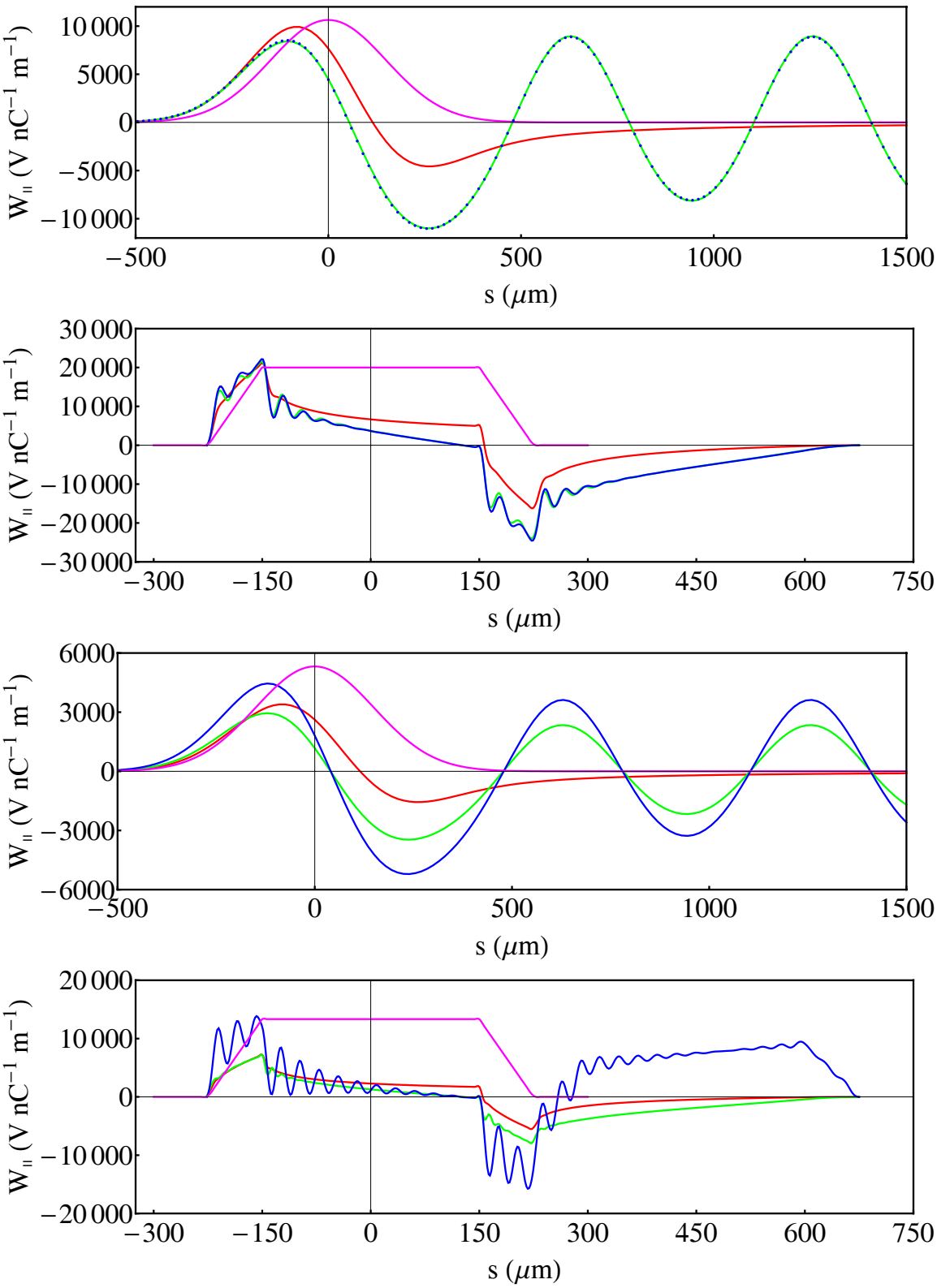

Figure 7.7: DC (red), AC (green), ASE (blue & points) wake potentials for Gaussian and trapezium charge distributions (magenta) for a 2 mm radius copper vessel at 273 K (top) and 77 K (bottom)

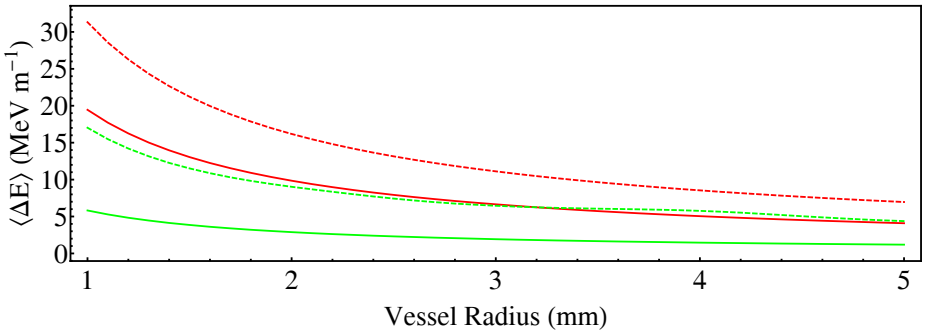

Figure 7.8: Average energy lost, $\langle E \rangle$, by an electron in a Gaussian (solid) and trapezium (dashed) charge distribution in a stainless steel vessel at 273 K for DC (red) and AC (green) wakes.

7.2.4.2 Induced Correlated Energy Spread

Figure 7.9 shows the induced energy spread, $\frac{\sigma_E}{E}$, for the three different conductivity models at 273 K and 77 K for 150 μm Gaussian and trapezium shaped bunches in a copper vessel. The induced energy spread is correlated with longitudinal position and so could potentially be corrected for. At these short bunch lengths the AC and ASE wakes are dominant, but in all cases the absolute values are not significant.

The induced energy spread has been calculated for all possible combinations of vessel material (Table 7.1), bunch charge and bunch length (Table 1.1) for Gaussian and trapezium shaped bunches as a function of the vessel radius. To give confidence in the results for different charge distributions, the numerical techniques were benchmarked against similar calculations for the Linac Coherent Light Source undulator vessel [120]. The effect on the energy spread is most significant for the 150 μm bunch length at 273 K. The worst material is stainless steel, and the increase in energy spread is probably too great for the ILC. There is little difference between copper, gold, aluminium or even iron at 77 K. Figure 7.10 shows the induced energy spread for 2.9 mm radius vessels of each material (approximately the vessel radius assumed for the ILC-RDR [20]). At 77 K the energy spread increases are all acceptable. Therefore the choice of vessel material depends on other factors, such as the required surface smoothness. Copper has been chosen since there are commercially available copper vessels that meet the surface smoothness specification.[43]

[43] See Chapter 8.

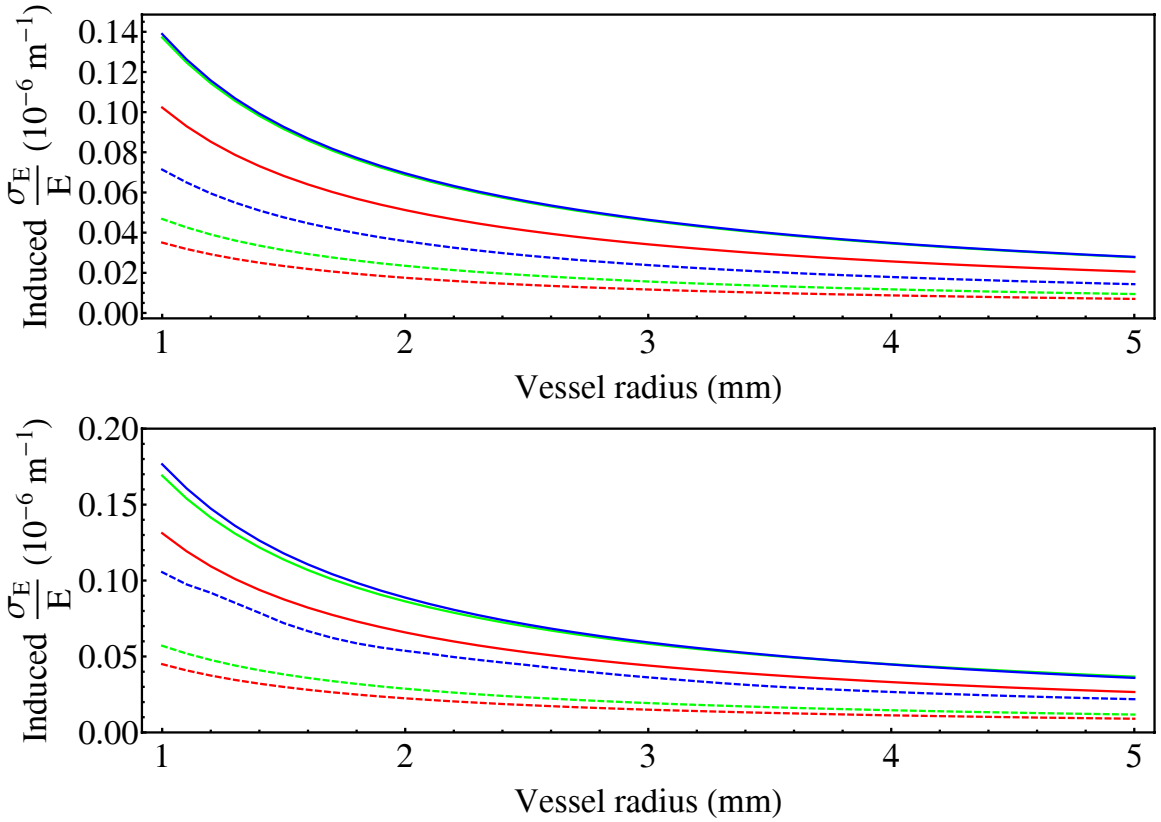

Figure 7.9: Induced correlated energy spread per meter for Gaussian (top) and trapezium (bottom) charge distributions using the DC (red), AC (green) and ASE (blue) conductivity models at 273 K (solid) and 77 K (dashed).

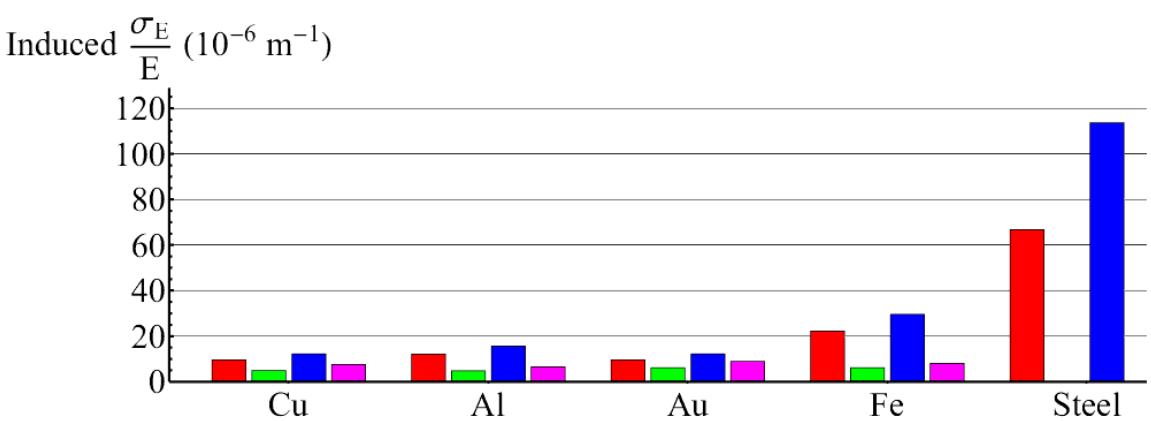

Figure 7.10: Peak induced energy spread per meter in a 2.9 mm radius vessel with a Gaussian charge distribution at 273 K (red) and 77 K (green) and a trapezium charge distribution at 273 K (blue) and 77 K (magenta).

7.2.5 Transverse Resistive Wall Wake Potentials

From the resistive wall monopole order longitudinal wake function, $w_{\parallel}^{0}$, the dipole order transverse wake function, $\boldsymbol{w}_{\perp}^{1}$, can be derived from the Panofsky-Wenzel theorem. The result is [123]:

$$\boldsymbol{w}_{\perp}^{1}(s) = \frac{2}{b^2} \int_0^s w_{\parallel}^{0}(s')\mathrm{d}s'.$$

This expression needs to be convoluted with a charge distribution to obtain the transverse wake potential:

$$\boldsymbol{W}_{\perp}^{1}(s) = \int_{-\infty}^{\infty} \rho(s)\boldsymbol{w}_{\perp}^{1}(s)\mathrm{d}s.$$

For a given charge distribution, $\rho(s)$, and transverse wake potential, a transverse kick factor, $k_{\perp}$, can then be defined:

$$k_{\perp}^{1} = \int_{-\infty}^{\infty} \rho(s)\boldsymbol{W}_{\perp}^{1}\mathrm{d}s.$$

This kick factor gives the strength of the transverse kick a particle receives per unit transverse displacement per metre longitudinally. This method can be checked for the DC wakes as an analytic expression for the dipole order wake function per unit length in a round resistive pipe has been computed [123]. For a distance r off-axis, it is found to be:

$$\boldsymbol{w}_{\perp}(s) = \frac{2\,s_0\,r}{3\,\pi\,\epsilon_0\,b^4}\left(\mathrm{e}^{-\frac{s}{s_0}}\left[\sqrt{3}\,\sin\left(\frac{s\sqrt{3}}{s_0}\right) - \cos\left(\frac{s\sqrt{3}}{s_0}\right)\right] + \frac{12\sqrt{2}}{\pi}\int_0^{\infty}\frac{\mathrm{e}^{-\frac{x^2\,s}{s_0}}}{x^6+8}\mathrm{d}x\right). \quad (7.9)$$

Figure 7.11 shows the results of an example calculation of the two methods for a copper vessel with two different diameters.

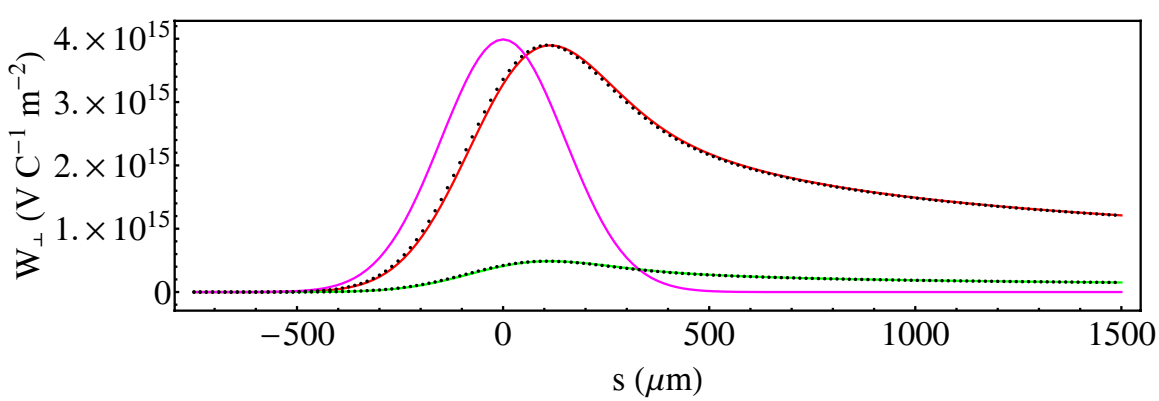

Figure 7.11: Transverse wake potential for a 150 μm Gaussian bunch (magenta) calculated using Equation 7.9 (points) and direct integration of the longitudinal wake for 1 mm radius (red) and 2 mm radius (green).

7.2.6 Transverse Kick Factors

As an example, the transverse kick factor as a function of vessel radius is plotted for the three different conductivity models for a 150 μm Gaussian bunch travelling 1 μm off-axis and 1 m longitudinally in Figure 7.12. From these graphs, and similar ones for the other bunch parameters and vessel materials, the maximum possible kick can be found. This is shown for a Gaussian bunch and a 5.85 mm diameter vessel at 273 K and at 77 K in Figure 7.13. The peak transverse kick is only 0.27 eV μm^{-1} m^{-1} for a Gaussian bunch and 0.29 eV μm^{-1} m^{-1} for a trapezium bunch in a copper vessel at 77 K.

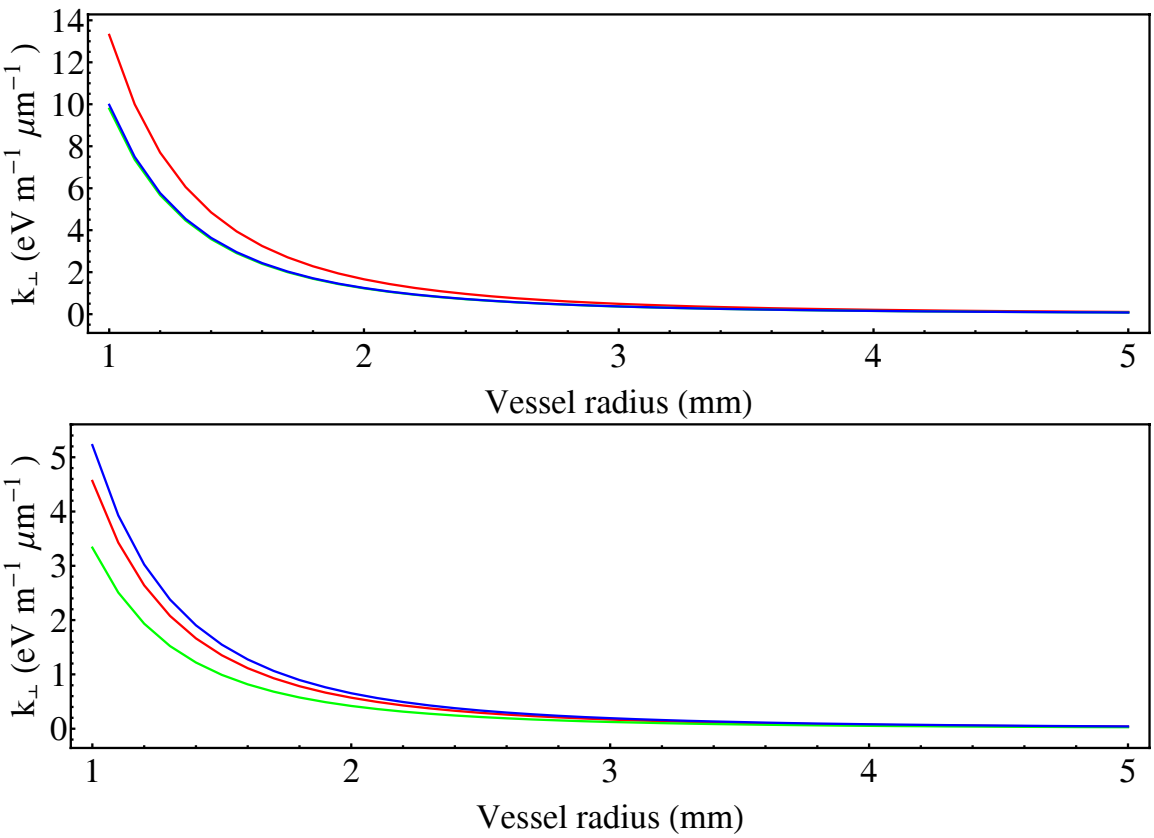

Figure 7.12: Transverse kick factor for a 150 μm Gaussian bunch per micron off-axis per metre vs vessel radius for DC (red), AC (green) and ASE (blue) wakes at 273 K (top) and 77 K (bottom) in a copper vessel.

7.2.7 Emittance Growth due to Transverse Wakefields

The transverse wakefields kick the beam transversely and this could cause an emittance growth. The calculation of this emittance growth is beyond the scope of this thesis although some initial studies have been made [124]. There is a dedicated group working on the low emittance transport of the electron beam throughout the ILC and the undulator line

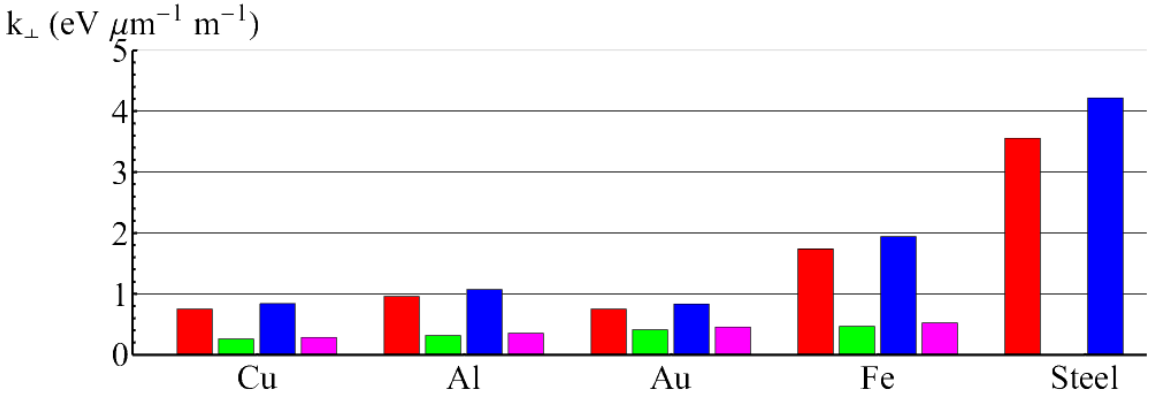

Figure 7.13: Peak kick factor, $k_\perp$, for a 2.9 mm radius vessel with a Gaussian charge distribution at 273 K (red) and 77 K (green) and a trapezium charge distribution at 273 K (blue) and 77 K (magenta).

has been included in some simulations. Currently these have looked at the effects of the undulator lattice, synchrotron radiation and a wakefield kick on the beam emittance and the increase is currently acceptable [125].

7.3 Image Current Heating of the Vacuum Vessel

In general, when a longitudinal charge distribution traverses an impedance it can lose energy to that impedance. For a resistive wall impedance, the amount of energy lost can be found by considering the heating of the vessel due to image currents induced by the beam or by considering the energy lost by the beam due to wakefields.[44] As it assumed that both these processes are correlated both should be similar in magnitude.

Equations for calculating the heating due to image currents have been determined for the LHC dipoles [126, 127] and also for a number of different SC planar undulators considered for light sources [128, 129, 130, 131]. To calculate the power dissipated in a conducting vessel due to the image currents, the surface resistance R_s of the vessel must be accurately modelled. The correct model to use depends on factors such as: the temperature of the metal T, the angular frequency of the applied field ω and the magnitude of any external magnetic field B. The total power dissipated due to image current heating, P_T, in W m^{-1}, from Gaussian bunches with rms bunch length σ_z in a circular vessel of radius b and surface resistance $R_s(\omega)$ is [129]:

$$P_T = \sum_{n=0}^{\infty} P_{s,n},$$

[44]The wakefield losses of the beam are considered in Section 7.2.

with

$$P_{s,0} = \frac{1}{2\pi b} R_s(0) I_0^2$$

and

$$P_{s,n} = \frac{1}{2\pi b} R_s(n\omega_0) 2 I_0^2 \mathrm{e}^{-\frac{n^2 \sigma_z^2 \omega_0^2}{c^2}}.$$

Here, ω_0 is 2π divided by the bunch spacing in seconds, I_0 is the time averaged current and c is the speed of light.

7.3.1 Surface Resistance in the Normal Conducting Regime

In the normal conducting regime, for example at room temperature, the surface resistance $R_{s,normal}$ is:

$$R_{s,normal} = \sqrt{\frac{\omega \mu_0 \rho}{2}},$$

where μ_0 is the vacuum permeability and ρ is the DC resistivity of the vessel. In this regime, the field penetrates into the metal a certain distance given by the skin depth, (Equation 7.5).

7.3.2 Residual Resistivity Ratio and Magneto-Resistance

If the vessel is cooled to cryogenic temperatures then the resistivity decreases by a factor determined by its residual resistivity ratio, RRR, to give a temperature dependent resistivity, ρ_T:

$$\rho_T = \frac{\rho}{RRR}.$$

Magneto-resistance is when the conductivity of a material is limited by an external magnetic field, B. Magneto-resistance is an effect seen in high purity metals, with a high RRR value, operating at low temperatures and in high magnetic fields. The resistivity of the material, ρ_{BT}, is determined by Köhler's rule [132]:

$$\rho_{BT} = \rho_T (1 + 10^{(1.055 \log_{10}(B.RRR) - 2.69)}).$$

7.3.3 Surface Resistance in the Anomalous Skin Effect Regime

As the resistivity decreases, the mean free path between collisions of the conduction electrons, λ, can eventually become greater than the skin depth and only the fraction of con-

duction electrons moving parallel to the metal surface are effective in carrying current. The classical theory of conductivity breaks down and the theory of the anomalous skin effect (ASE) must be used [121].[45] The surface resistance, $R_{s,anom}$, is then given by [133]:

$$R_{s,anom} = R_\infty(1 + 1.157\alpha^{-0.276}),$$

where:

$$\alpha = \frac{3}{4}\omega\mu_0(\rho_{BT}\lambda)^2\rho_{BT}^{-3},$$

$$R_\infty = \left(\frac{\sqrt{3}}{16\pi}\rho_{BT}\lambda(\omega\mu_0)^2\right)^{\frac{1}{3}}.$$

The value of $\rho_{BT}\lambda$ is a characteristic of the material: for copper it is 6.6×10^{-16} $\Omega\mathrm{m}^2$.

7.3.4 Comparison with Energy Loss Due to Resistive Wall Wakefields

The energy lost by the beam due to the resistive wall wakefield,[46] should be similar in magnitude to the energy deposited in the vessel. Figure 7.14 shows a comparison of the two methods for a copper pipe at 273 K using the DC conductivity model. There is reasonable agreement between the two methods. The resistive wakefield losses are slightly greater, probably due to limitations in the numerical techniques used, but this is not significant for the vessel radius being considered.

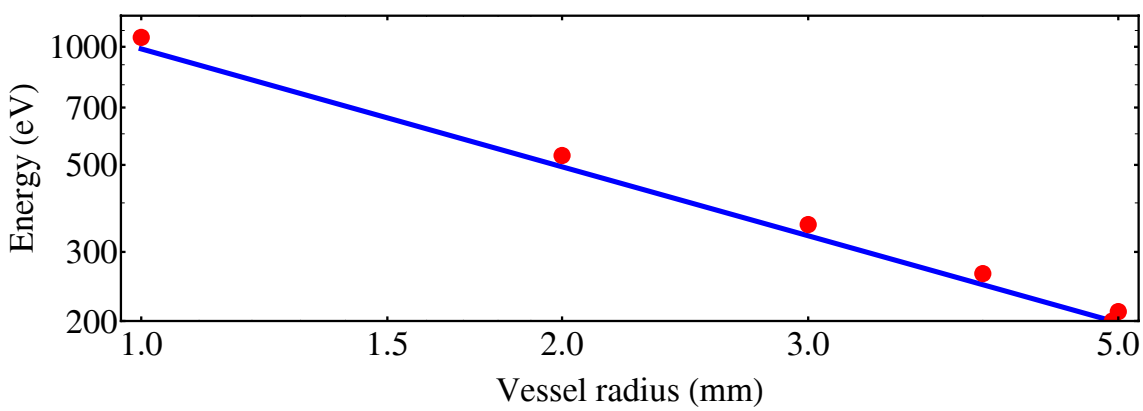

Figure 7.14: Comparison of energy lost per electron per metre (points) with the image current heating per electron per metre (line) for copper at 273 K.

[45] See Section 7.2.1.3

[46] Described in Section 7.2.

7.3.5 Power Deposited in the Vessel Due to Image Current Heating

Table 7.5 gives the power deposited per metre due to image currents for a 5.85 mm diameter copper vessel in a 1 T magnetic field, with a room temperature conductivity of $5.88\times10^{7}\ \Omega^{-1}\mathrm{m}^{-1}$ and an *RRR* value of 60. The magneto-resistance conductivity is therefore $3.06\times10^{9}\ \Omega^{-1}\mathrm{m}^{-1}$. The three different ILC electron beam fill patterns from Table 1.1 have been considered.

The ILC beam is pulsed at 5 Hz and so some assumptions have been made as to how this affects the overall heating. First, it was assumed that there was no 5 Hz pulsing for a particular pattern and the power deposited calculated. Then, this power was multiplied by a '*duty cycle*' representing the proportion of bunches that are present with the 5 Hz pulsing. Figure 7.15 shows the power deposited for the three different fill patterns as a function of the vessel radius. The power deposited due to image current heating must be added to the power due to SR heating.[47]

Experimental measurements of this effect showed a increase in the power deposited compared to the theory by a factor of ∼2 [126]. This was attributed to factors such as the surface roughness of the sample and impurities. For the ILC helical undulator, it is already proposed to use a vessel with an extremely smooth surface to mitigate geometric wakefield effects.[48]

Table 7.5: Power deposited per metre due to resistive wall heating for the different ILC electron bunch fill patterns.

Parameter	Unit	Pattern 1	Pattern 2	Pattern 3
Repetition Rate	Hz	5	5	5
Bunch Spacing	ns	150	300	500
Bunch Length	μm	150	300	500
Particles per Bunch	10^{10}	1	2	2
Peak Bunch Frequency	MHz	6.66	3.33	2
Bunches per pulse		5640	2820	2820
Duty Cycle		1.41×10^{-2}	4.23×10^{-3}	7.05×10^{-3}
Power per metre	W m^{-1}	0.081	0.052	0.022

[47] See Chapter 5.
[48] See Section 8.1.

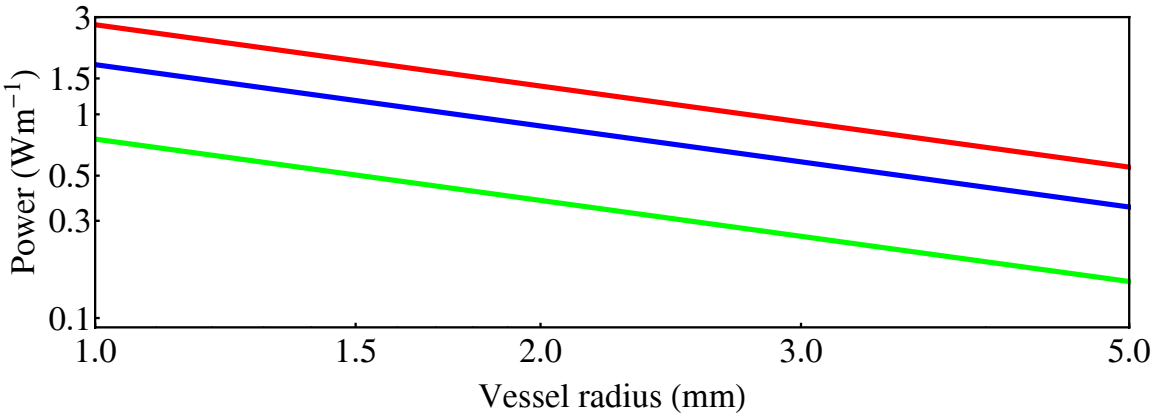

Figure 7.15: Power deposited per metre due to image current heating of copper vessel vs radius for pattern 1 (red), pattern 2 (blue) and pattern 3 (green) from Table 7.5.

7.4 Conclusions and Further Work

For the resistive wall wakefield studies a number of different materials were considered. Calculations were performed using different models of conductivity. The wakes were decomposed transversely and longitudinally. The longitudinal wakes affect the total energy and energy spread of the beam and the transverse wakes give a transverse momentum kick. Any mean energy lost can always be replaced by increasing the number of accelerating cavities in the machine. Increases in energy spread can result in a deterioration in the physics performance of the machine.[49] The energy lost and increase in energy spread are negligible for copper, gold and aluminium. The effects of the transverse momentum kicks on the beam emittance have been calculated and found to be small.

The results shown in Figure 7.10 indicate that a stainless steel vessel should not be used, if the increase in the energy spread is to be kept below 10%. A vessel made of this material would have to be coated with copper or gold to minimise the induced energy spread. Coating such a narrow gap vessel with a smooth layer of copper or gold (for example) would not be easy due to the narrow aperture and long length.

At 77 K aluminium is the best material to use to minimise the increase in energy spread. However, there is a strict requirement on the smoothness of the vessel.[50] Finding such an aluminium vessel from industry has proved difficult: however, there are copper and stainless steel vessels available that meet the smoothness specification. For this reason a smooth copper pipe will be used as the vacuum vessel.

[49] Although in principal as the induced energy spread is correlated with longitudinal position it can be corrected for with downstream elements.

[50] See Section 8.1.

The ILC charge distribution through the undulator is expected to be a Gaussian, or close to a Gaussian. However a trapezium distribution was also considered to show what may happen for non-Gaussian bunches. If, at a later date the charge distribution is found to be non-Gaussian at the undulator then this can easily be modelled.

The temperature dependence of the wakefields for Gaussian and trapezium shaped bunches show that as the temperature decreases so does the induced energy spread. Although reliable numbers are not available for materials at 4 K, the operating temperature of the vessel, it is likely that the effects will continue to improve, or get no worse, as the temperature decreases. Therefore an increase (multiplicative) in energy spread of 1.3% for copper/gold at 77 K can be thought of as a worst case. Further studies could investigate the conductivity properties of vessels at their operating temperature.

The transverse wakefields have been calculated and the kick factor for a gaussian bunch in the undulator is 0.29 eV μm^{-1} m^{-1}. The size of the transverse kick factors is small when compared to the $\sim$150 GeV forward momentum of the beam. Further work should accurately calculate whether this kick contributes to an emittance growth of the electron beam. There is a dedicated team working on the transport of low emittance beams for the ILC using sophisticated algorithms. Their initial studies, including a wakefield kick, have shown that the beam can be transported through the undulator line satisfactorily [125]. These studies need to be kept up to date with the continuing evolution of the undulator lattice.

The image current heating of the vessel is small, although this may change if the electron beam charge distribution is non-Gaussian. Further studies will be required if the charge distribution changes. The results of the SR and image current heating are collated in Chapter 9.

Chapter 8

Geometric Wakefields of the Vacuum Vessel

After discussing the resistive wall wakefield effects in the previous chapter, further effects that may perturb the electron beam traversing the undulator system are now considered; namely wakefield effects due to the vacuum vessel geometry. Two main effects have been studied: those due to the surface roughness of the vessel material and those due to the tapering and shape of the elements in the undulator line. The surface roughness wakefields are discussed first.

8.1 Surface Roughness Wakefields

The surface roughness of the inside of the vacuum vessel creates geometric wakes that must be evaluated to ensure that they do not disrupt any of the beam properties. For a perfectly smooth pipe there would be no induced surface wakefields. Using a pessimistic model of surface roughness features, a stringent specification for the average surface roughness has been calculated [134]. The theoretical results are then compared to measurements of smooth circular vessels available from industry.

8.1.1 Surface Roughness Wakefields Theory

A number of models exist for surface roughness, all of which have been shown to be approximately equivalent [135]. Here, the so-called *inductive impedance model* [136] has been

used, which makes the following assumptions:

- The vessel is cylindrically symmetric.
- The charge distribution is smooth.
- The surface roughness is assumed to have no resistance.
- The length of the bunch is longer than the length of the roughness features.
- As the impedance is purely inductive only surface roughness effects that influence the energy spread of the beam are considered.
- The height of the surface roughness bumps is about the same as the length of the bump.

The model assumes a number of bumps of height δ located on the surface of a vessel with radius b. For an applied field with angular frequency ω, the impedance $Z(\omega)$ per unit length L of a hemispherical bump is given by [137]:

$$\begin{aligned} \frac{Z(\omega)}{L} &= -\mathrm{i}\omega I \\ &= \frac{-\mathrm{i}\omega Z_0 \delta^3}{4\pi c b}. \end{aligned} \tag{8.1}$$

Here I is the inductance of the roughness. The impedance is purely inductive with no resistive part. For different shaped bumps the impedance has to be multiplied by a form factor that depends upon the shape of the bump. Some example bumps with different shapes have been previously modelled and various form factors ascribed to them [138]. Figure 8.1 shows the different shapes considered and Table 8.1 gives their form factors.

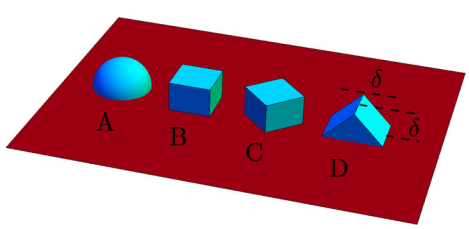

Figure 8.1: Sample bump shapes, A: hemisphere, B: half cube, C: rotated half cube and D: wedge.

As well as considering the shape of the surface bumps, the proportion of the surface area covered by the bumps must be included. For many bumps the total impedance

Table 8.1: Form factors for the different shaped bumps in Figure 8.1.

Bump Shape	Form factor
Hemisphere, A	1
Half Cube, B	2.6
Rotated Half Cube, C	0.6
Wedge, D	1.1

is assumed to be the sum of the impedances of each bump. The total impedance per unit length is then:

$$\frac{Z(\omega)}{L} = \frac{-\mathrm{i}\alpha f \omega Z_0 \delta^3}{4\pi c b} \tag{8.2}$$

where f is the form factor relating to the bump shape and α is the packing factor, giving the fraction of the surface occupied by bumps.

The wake function is then simply the Fourier transform of the impedance. As the impedance is inductive, it only has imaginary components and the Fourier sine integral can be used. Using $\omega = k\,c$, for a Gaussian bunch of rms length σ_z, the wake potential, $W(s)$, is:

$$\begin{aligned} W(s) &= \frac{\alpha f Z_0 \delta c}{2\pi^2 b} \int_0^\infty k \mathrm{e}^{\frac{k^2\sigma_z^2}{2}} \sin(ks)\mathrm{d}k \\ &= \frac{\alpha f Z_0 \delta c}{\pi b \sigma_z^3 \sqrt{2\pi}} s \mathrm{e}^{\frac{s^2}{2\sigma_z^2}}, \end{aligned} \tag{8.3}$$

where $\exp\left(\frac{k^2\sigma_z^2}{2}\right)$ is the Fourier transform of the longitudinal charge distribution.

The induced relative energy spread, σ_E, of a bunch of N electrons of charge e is:

$$\sigma_E = e^2 N \left| \int_{-\infty}^{\infty} \left(\frac{1}{\sigma_z \sqrt{2\pi}} W^2 \mathrm{e}^{\frac{s^2}{2\sigma_z^2}} - k_\parallel^2 \right) \mathrm{d}s \right|, \tag{8.4}$$

where $k_\parallel$ is the longitudinal loss factor and is equal to zero for purely inductive impedances. This gives the total induced energy spread of a round vessel L metres long as:

$$\sigma_E = \alpha f \frac{e^2 N Z_0 \delta c L}{3^{\frac{3}{4}} 2^{\frac{3}{2}} \pi^{\frac{3}{2}} b \sigma_z^2}. \tag{8.5}$$

A similar expression has also been derived, in terms of the inductance, I, and is [139]:

$$\sigma_E = \frac{e^2 N c^2 L I}{3^{\frac{3}{4}} 2^{\frac{1}{2}} \pi^{\frac{1}{2}} \sigma_z^2}, \tag{8.6}$$

where the inductance is determined from measurement and simulation. For the same form factor and packing factor the two expressions give the same result.

8.1.2 Surface Roughness Specification

The parameters given in Table 8.2 have been used to calculate the surface roughness wakefield effects. Only the 150 μm bunch was considered as it produces the worst effect. Using these parameters the induced energy spread was calculated for the various different form factors and surface roughness values, this is shown in Figure 8.2 for a vessel diameter of 5.85 mm. In Figure 8.3, the roughness required to increase the energy spread by 10% of the nominal value as a function of vessel radius is plotted for the different form factors.

Table 8.2: Parameters for the surface roughness calculation.

Parameter	Unit	Value
Energy	GeV	150
Nominal Energy Spread	%	0.05
Undulator Length	m	200
rms Bunch Length	mm	0.15
Number of Particles per Bunch		1×10^{10}
Packing Factor (α)		0.5

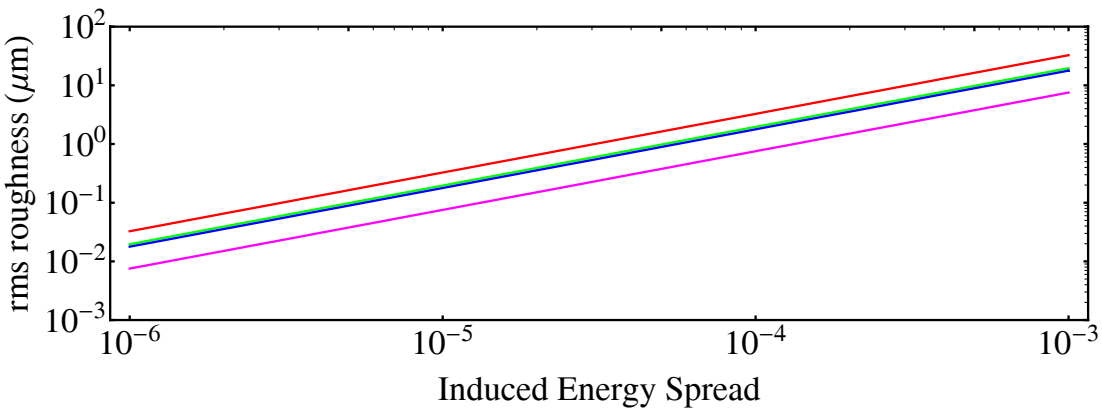

Figure 8.2: Induced energy spread vs the rms roughness of a 5.85 mm diameter vessel for the different shaped bumps in Figure 8.1: A (green), B (magenta), C (red), D (blue).

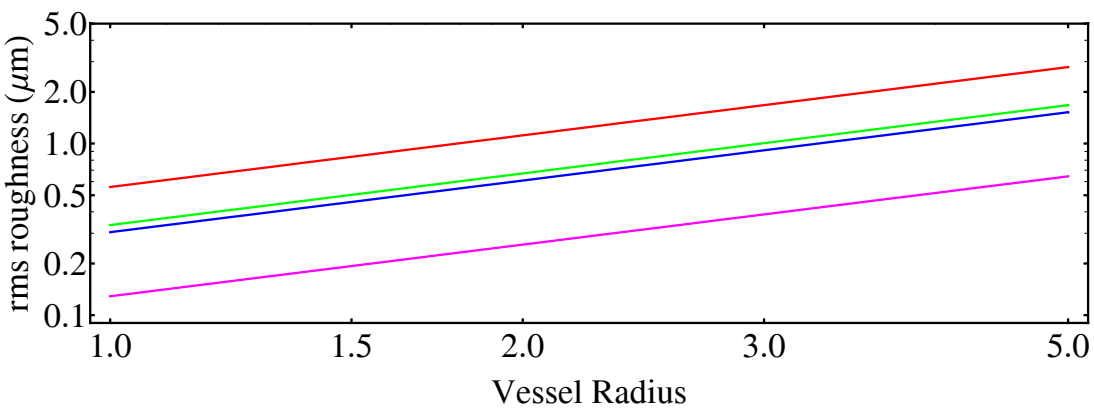

Figure 8.3: The rms surface roughness required to induce an energy spread of 0.5 10^{-4} for different vessel radii and bump shapes, where A (green), B (magenta), C (red), D (blue).

The surface roughness tolerance is not strongly dependent on the radius of the beam tube. It decreases as the inverse of the radius, whereas the resistive wakes[51] vary as an inverse power of the radius. The requirements on the surface roughness seem quite demanding. According to the model, to keep the increase in energy spread below 10% of the nominal value the surface roughness must be less than ∼300 nm, for the worst form factor.

The above calculation was checked by comparing the results with published measurements. The inductance of high quality stainless steel smooth pipes from the VALEX Corporation has been measured [139]. A 2.5 mm radius beam tube gave an inductance of 0.28 pH m^{-1}. The average roughness of the VALEX tube was measured to be ∼125 nm.

[51] Discussed in Chapter 7.2.

Using Equation 8.6 this gives an increase in energy spread of just 4.2×10^{-7}.

The theory is pessimistic compared to measured inductances of real beam tubes. One of the reasons for this is that the assumption that the height of the bumps is approximately the same as the length of the bumps is not confirmed by measurements [139]. If it is assumed that the measured inductance is correct for many metres of pipe, then the corresponding form factor is 0.06 and the height of the bumps required to keep the increase in energy spread less than 10% of the nominal value is ∼12 microns. However, even given all these factors, the conclusions of [139] state that there is an active program underway to improve upon the ∼125 nm surface roughness of the VALEX beam tubes. There are further effects that have not been included that may influence the surface roughness wakefields, such as the true distribution of the bunch charge, which may have features that are approaching the scale of the surface roughness. Also, misalignments of the beam tubes will have some effect. Given these unknowns, it would seem prudent to use the smoothest beam tube possible to help mitigate any deleterious effects of the surface roughness.

The results from resistive wall wakefields calculations[52] suggest that a stainless steel vessel should not be used to keep the induced energy spread low. Therefore the surface roughness of a sample of a smooth copper vessel of ∼6 mm diameter available from Swagelok [140] was measured and found to have an R_a[53] of ∼100 nm [142].

8.2 Wakefields of Tapered Elements in the Undulator Line

In the current design there are two main elements that have tapers, the photon collimators and the transitions between the room temperature vessels and the cold bore of the undulator module (see Figure 8.6). These tapered sections induce wakefields which can kick an off axis beam transversely. There is an active research programme assessing the effects of collimator wakefields. Results from this programme can be used to estimate the effects of the undulator line tapers. There are many references on the subject [143, 144, 145, 146, 147, 148, 149, 150] and the theory is only summarised here.

Generally, the beam will be off-axis due to jitters in the linac and misalignments of elements. The wakefields will kick the beam an amount proportional to the displacement

[52] See Section 7.2.4.2

[53] R_a is a mechanical engineering parameter that characterises the surface based on the vertical deviations of the roughness profile from the mean line. The R_a is the arithmetic average of the absolute values [141].

of the beam off-axis. For small displacements, y, the kick angle, $\Delta y'$, is:

$$\Delta y' = K_b y,$$

where K_b is the bunch kick factor. The off axis displacement and kick angle can be normalised to the rms beam size and divergence $\sigma_{x,y}$ and $\sigma_{x',y'}$, respectively. The quantity:

$$A = K_b \frac{\sigma_{x,y}}{\sigma_{x',y'}},$$

can now be defined which is a factor characterising the strength of the kick. A series of kicks can cause an emittance growth. The relative emittance growth, $\frac{\Delta\epsilon}{\epsilon}$, for a displacement off-axis of n is simply [144]:

$$\frac{\Delta\epsilon}{\epsilon} = (0.4nA)^2, \tag{8.7}$$

where n is in units of $\sigma_{x,y}$. Using these formulae the emittance growth for a given set of alignment tolerances can be calculated.

8.2.1 Electron Beam Properties

The linear lattice functions, calculated in the MAD8 code [151] for the lattice shown in Figure 1.5, are shown in Figure 8.4. The magnitudes of the beta functions in both transverse planes have been optimised to be as similar as possible using the constraints given in reference [152]. The beam sizes can be calculated from these and the normalised emittance values of $\epsilon_x = 8.4$ μm and $\epsilon_y = 24$ nm. They are shown in Figure 8.5. The beam divergences can also be found from the emittance and the lattice functions and reach peak values of 1.99 and 0.11 μrad in the horizontal and vertical directions respectively.

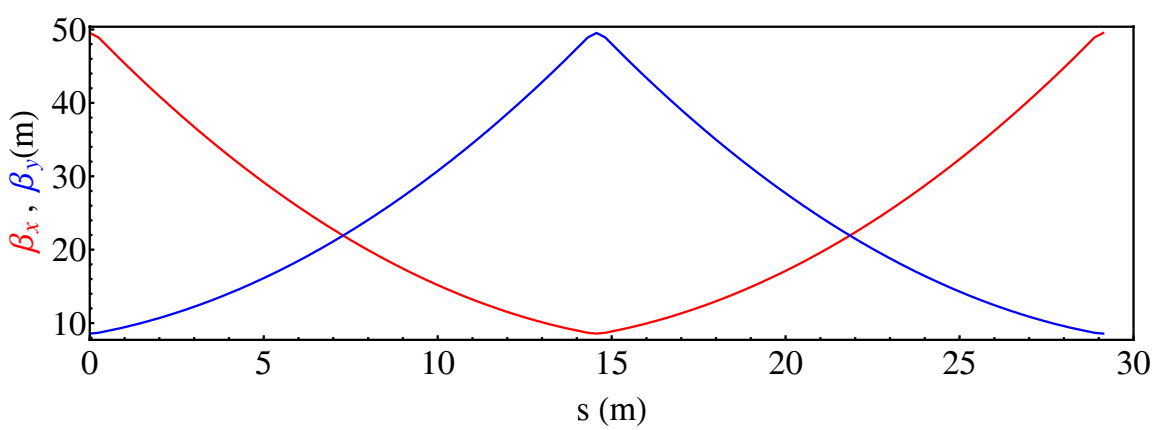

Figure 8.4: The horizontal (red) and vertical (blue) beta functions (β_x, β_y) of the undulator line cell.

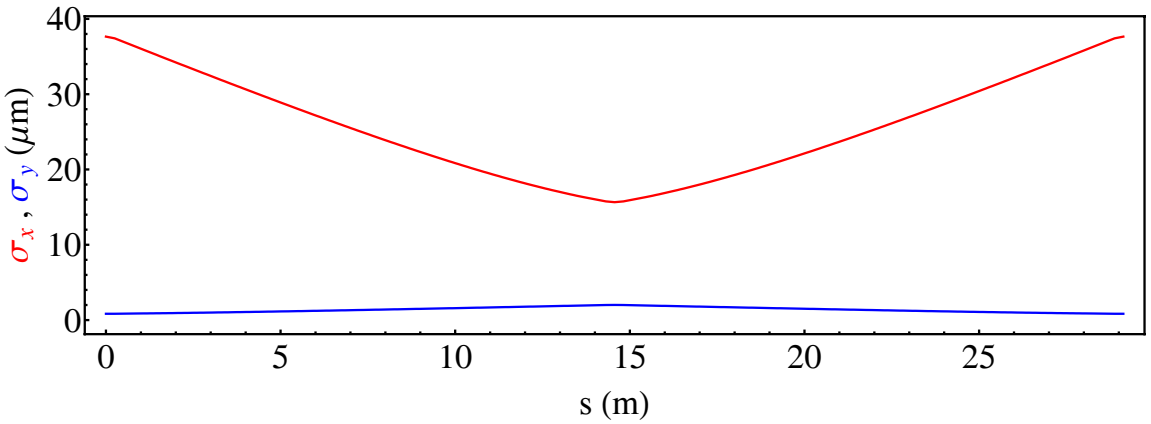

Figure 8.5: The horizontal (red) and vertical (blue) rms electron beam size through the undulator cell.

8.2.2 Geometry of the Tapered Sections

The geometry of each tapered section must be defined to calculate the magnitude of the wakefield kick. There are photon collimators and tapers in the undulator modules to consider.

8.2.2.1 Photon Collimators

The photon collimators are needed to mask undulator photons that would otherwise be incident on the undulator vessel walls and cause a vacuum pressure increase via photon stimulated desorption.[54] They are also required to absorb SR power from upstream undulator modules.[55] To have any effect, these photon collimators must have an aperture less than the undulator vessel (5.85 mm). As yet, there is no engineering design for the collimator, but an assessment of the effects of likely parameters can be made. The collimators are assumed to have an axially symmetric taper with angle 0.1 rad down to a minimum aperture and then a similar taper back up to the nominal vessel radius of 18 mm. There is no flat portion between the two tapers. In order to maintain the necessary vacuum a collimator aperture of 4.4 mm is required, therefore the length of the collimator is ∼0.315 m.

8.2.2.2 Undulator Transitions

The undulator line consists of a FODO cell lattice with three undulator modules between the quadrupoles. The vessels for the quadrupoles are at room temperature and require

[54] See Chapter 4.
[55] See Chapter 5.

traditional pumping solutions with a relatively large bore vessel. The transitions from the large diameter room temperature vessel to the small diameter cold bore undulator vessel are tapered sections at the start and end of each undulator module. A schematic of a layout with unshielded bellows is shown in Figure 8.6. To allow for vacuum pumping, there is a gap between the red bellows and the blue taper. At the corner closest to the red bellows, the taper has a 2 mm radius and is 3.81 mm away from the end of the bellows longitudinally. The dimensions of the tapers are given in Table 8.6, where the flat length is the distance to the next taper. There are 23 corrugations in the bellows with a pitch of 1.4 mm, an inner radius of 17.65 mm and an outer radius of 24 mm. The system is axially symmetric.

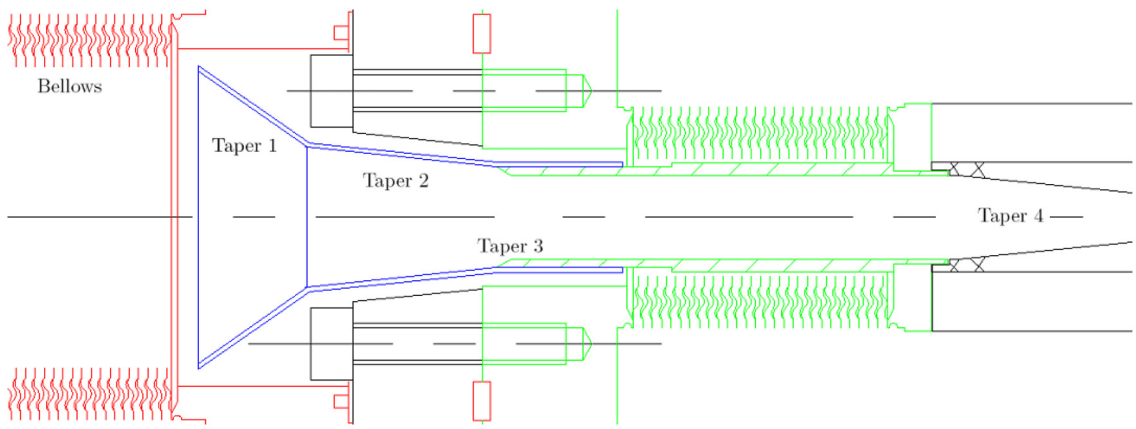

Figure 8.6: Layout of the warm (left) to cold (right) tapered transition of the undulator module. The large bore room temperature vessel is on the left, with the exposed red bellows, and the small cold bore undulator vessel to the right. Taper 1 and taper 2 can be seen on the left in blue, taper 3 is the green chamfer on the sliding joint with the blue taper and taper 4 is where the green vessel enters the undulator magnet on the right.

Table 8.3: Taper dimensions for the unshielded bellows layout.

	Large Diameter (mm)	Small Diameter (mm)	Flat Length (mm)	Taper Angle (mrad)
Taper 1	37.65	17	0	611
Taper 2	17	11.7	0	100
Taper 3	11.7	10	39	524
Taper 4	10	5.85	3700	100

8.2.3 Kick Factors

The bunch kick factor, K_b, is given by [146]:

$$K_b = \frac{4\pi N r_e}{Z_0 c \gamma} k_\perp \tag{8.8}$$

where Z_0 is the vacuum impedance, c is the speed of light, r_e is the classical electron radius, γ is the ratio of total energy to rest mass energy, N the number of particles in the bunch and $k_\perp$ the wakefield kick factor. Generally, there is a contribution from each multipole component of the beam, however only the dipole order transverse kick factor has been considered as this term is the most significant. Values for $k_\perp$ have been calculated using the numerical code ECHO [153], and confirmed using analytic expressions where appropriate.

8.2.3.1 Photon Collimator Wakefield Kick Factors

The analytic expression for the inductive wakefield kick of a Gaussian bunch (of rms length σ_z) passing through an axially symmetric round collimator of large radius b_1, small radius b_2 and taper angle θ is [145]:

$$k_\perp = \frac{Z_0 c}{2\pi^{\frac{3}{2}} b_1} \frac{\theta}{\sigma_z} \left(1 - \frac{b_1}{b_2}\right).$$

where Z_0 is the impedance of free space and c is the speed of light. In Figure 8.7 this expression is compared to the transverse loss factor as calculated in ECHO for b_1 =18 mm and various values of θ and b_2. There is good agreement between the two methods.

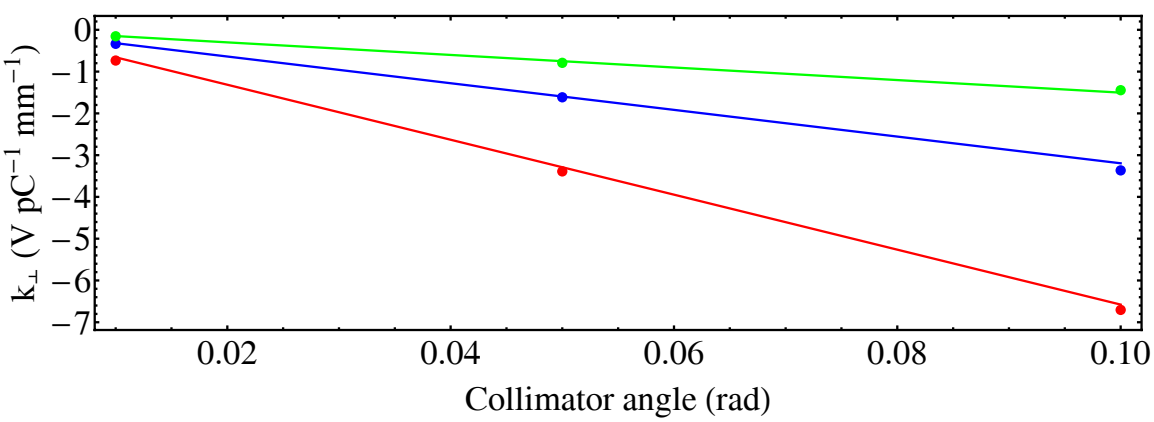

Figure 8.7: Wakefield kick $k_\perp$ calculated using the analytic expression for a short round collimator (lines) and ECHO (points) for different taper angles θ and small collimator aperture of 0.5 mm (red), 1 mm (blue) and 2 mm (green).

8.2.3.2 Undulator Wakefield Kick Factors

The wakefield kick factors for the undulator transitions were calculated using ECHO as there are no analytic expression for the bellows' wakefield. Similar calculations for bellows have previously been performed with ECHO [154]. The total wakefield kick is 0.96 V pC^{-1}mm^{-1}. The bellows only contribute 0.01 V pC^{-1}mm^{-1} to that value.

8.2.3.3 Bunch Kick Factors

The bunch kick factors, K_b, calculated from Equation 8.8, are shown in Table 8.4.

Table 8.4: K_b for the photon collimators and undulator.

Element	K_b (V pC^{-1} mm^{-1})
Photon Collimator	3.19×10^{-5}
Undulator	2.01×10^{-5}

8.2.4 Emittance Growth

The emittance growth for the undulator line can now be calculated using the cell layout from Figure 1.5. Using this layout and the beamsizes from Figure 8.5 the ratios $\frac{\sigma_{x,y}}{\sigma_{x',y'}}$ can be calculated.

8.2.4.1 Emittance Growth with Perfectly Aligned Elements

For perfectly aligned elements, the only contribution to an emittance growth is from the beam jitter. Using the estimate of 0.5 σ in both planes as the transverse displacement jitter of the beam [144], the emittance growth is a factor of $\sim 4.8 \times 10^{-7}$ over 10 cells.

8.2.4.2 Emittance Growth with Misaligned Elements

Each element will be misaligned from the axis. This misalignment has been incorporated into the factor n in Equation 8.7 to give an estimate of the required alignment tolerances for the undulator line. A line consisting of 10 cells was created and each element randomly misaligned by an amount following a Gaussian distribution. Different rms values for the Gaussian distribution were considered, but the misalignments were truncated at 300 μm as this is the typical accuracy reached by a survey team for accelerator components. The line was simulated 10 000 times for each different rms value. An example of the distribution of vertical emittance growth for a standard deviation of 100 μm is shown in Figure 8.8. The mean vertical and horizontal emittance increase for each rms displacement over the 10 000 seeds is shown in Figure 8.9. The mean increase is only 2.7% in the vertical plane for a 300 μm rms displacement of each element.

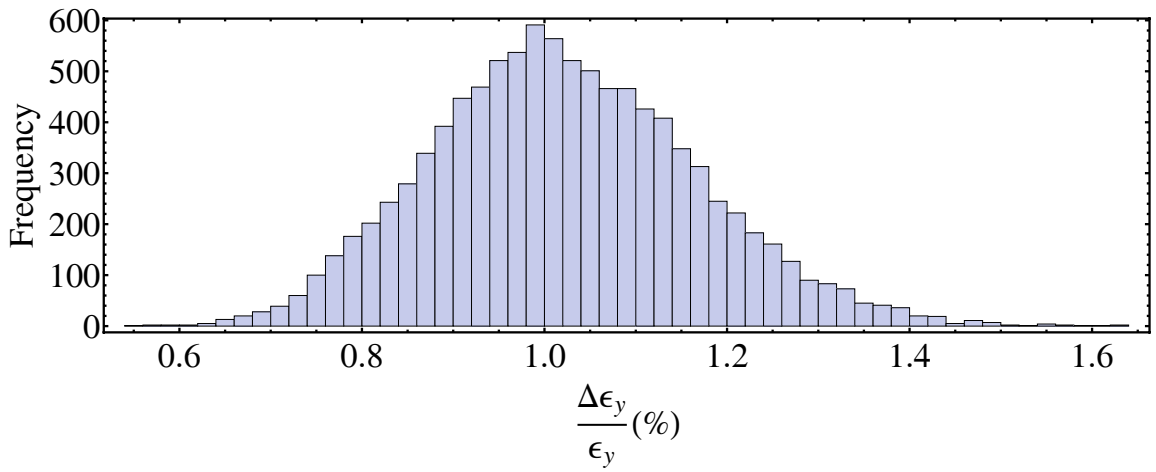

Figure 8.8: Vertical emittance growth in the undulator line for 10 000 seeds with each element randomly displaced an amount from a Gaussian distribution with an rms of 100 μm, truncated at 300 μm.

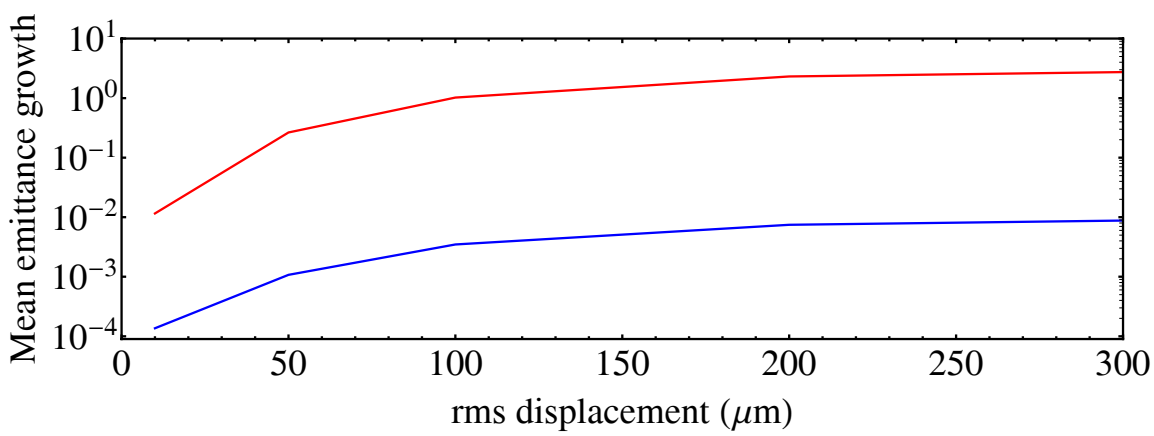

Figure 8.9: Mean emittance growth in the vertical (red) and horizontal (blue) planes vs rms displacement of each element in the undulator line.

8.3 Conclusions and Further Work

In this chapter the geometric wakefields due to the surface roughness of the undulator vessel and the tapered elements in the undulator line have been considered.

The requirements on the surface roughness seem quite demanding. According to the model, to keep the increase in energy spread below 10% of the nominal value, the surface roughness must be less than ∼300 nm, for the worst form factor. The surface roughness tolerance is not strongly dependent on the radius of the vessel; the roughness tolerance decreases as the inverse of the radius[56] therefore increasing the radius is not an effective solution to mitigate the wakefield effects. However, when compared to the measured impedance of a commercially available vessel of similar dimensions required for the ILC the theory seems to be pessimistic. There are a number of companies that can provide smooth vessels of the required dimensions [155, 140]. Typically these vessel are made of stainless steel or copper. The results in Chapter 7 showed that a stainless steel vessel would induce too high an energy spread in the beam and so the smooth copper vessel should be used. Swagelok [140] can provide a copper tube with a surface roughness of ∼100 nm an outer diameter of ∼6.3 mm and an internal diameter of ∼5.85 mm and so this should be used for the undulator vacuum vessel to mitigate the resistive wall and surface roughness wakefield effects.

The other sources of geometric wakefields that have been considered are the photon collimators and undulator transitions from cold to room temperature. For photon collimators with an aperture of 4.4 mm and a taper angle of 0.1 rad and the undulator cold to room temperature transitions as in Figure 8.6 the emittance growth is 2.7% in the vertical plane.

The exact angles for the collimator and undulator tapers may be optimised to allow for the highest packing factor of undulator periods in the available space, without compromising the beam emittance. As yet, there is no specification on the allowable emittance growth, but it seems likely that more undulator periods could be added by increasing the taper angle without dramatically affecting the emittance growth. The number of collimators could also be lower than initially thought, (perhaps by decreasing their minimum aperture or after further vacuum studies using the latest ILC-RDR parameters), thereby increasing the available space in the line for active undulator. Adjusting the taper angle

[56] Other wakefield effects often scale more strongly with radius.

would also free additional space in the line. This additional space could be of the order of 10 metres, which is significant. A specification of the allowable emittance growth is needed before this optimisation process could take place.

The theory assumes that the deviations of the beam or component misalignment off-axis are small. If larger displacements off axis need to be considered then a simulation including higher order terms of the wake potential could be performed [156].

Chapter 9

Summary and Further Study

9.1 Summary

The ILC positron source requires a helical undulator 100s of meters in length. An undulator meeting the initial parameter specifications had not been experimentally demonstrated, and so a programme of work was undertaken to determine realistic parameters. Based on the results of this study a helical undulator with field generated by super-conducting (SC) bifilar wires was chosen as the preferred design. If a PM Ring undulator is to be built in the future, care must be taken to assess the peak reverse fields during assembly of the blocks in order to mitigate any de-magnetisation. After the construction of further SC prototypes the ILC-BCD parameters were altered. The new specifications for the undulator period and K parameter are 11.5 mm and 0.92, respectively. The changes to the specification were to allow for an 80% conductor safety margin[57] in the SC, which had not been allowed for in the ILC-BCD.

The (full) beam aperture of the magnet of 5.85 mm was determined by considering the maximum achievable field, wakefield effects, and the dimensions of commercially available smooth vessels. A copper vessel should be used as the induced energy spread due to resistive wall wakefields is a factor of 10 smaller than with stainless steel. The expected induced correlated energy spread $\frac{\sigma_E}{E}$ is $\sim$1.3% for 200 m of undulator.

To achieve the required vacuum pressure, sufficient to mitigate the fast ion instability with some margin, photon collimators are required. These must be distributed along the length of the undulator, in the current design approximately every 7 m for a collimator

[57] I.e. 80% of the current at which the SC becomes normal conducting.

with (full) beam aperture of 4.4 mm. They are cylindrically symmetric and have a taper angle of 0.1 rad to alleviate geometric wakefields.

The photon collimators are also required to absorb synchrotron radiation (SR) that would otherwise cause the SC magnets to quench. The magnets are also heated by image currents. The total heating of the undulator module, on average and in the worst case, for the current design is given in Table 9.1, the values are acceptable, being less than the 1 Wm^{-1} specification.

Table 9.1: Power (W) heating an undulator module due to image currents and SR.

	ILC-BCD	ILC-RDR
Maximum	1.404	0.604
Mean	0.556	0.38

The effects of magnetic field errors on the electron beam trajectory have been assessed. Deviations of the electron beam off axis up to 0.5 mm are not expected to affect the trajectory significantly. The rms trajectory through the undulator can be corrected to a few microns with simple dipoles placed before an undulator module. The need for such correctors is not well established, but they are relatively simple to implement and would be beneficial during commissioning. It is also probable they will be needed for a polarised positron source to optimise the position of the photon spot on the conversion target.

The resistive wall wakefields have been considered for different materials and conductivity models. The amount of energy lost is negligible when compared to the beam energy and the amount lost via SR. The induced energy spread implies that a stainless steel vessel should not be used, unless it is coated with a high conductivity material such as copper. The resistive wall transverse wakefield kicks are also small and it has been shown that they cause a negligible emittance growth. Of much greater importance is the optics of the undulator line; however with sophisticated steering algorithms the emittance growth can be kept to an acceptable level.

The geometric wakefields have been assessed and an extremely smooth vessel with surface roughness features $\leq$300 nm is recommended. Fortunately, such vessels are readily available from industry. Geometric wakefields from the photon collimators and undulator tapers can cause an emittance growth of a few percent in the vertical direction. If it is later found that this is unacceptable there is scope to further optimise the number of components, taper angles and lengths to minimise the emittance growth. Conversely if a larger emittance

growth is acceptable the collimator taper angles could be increased allowing more space for active undulator to increase the efficiency of the line.

The decision to choose the ILC-RDR undulator parameters was based on the prototype SC devices built by the HeLiCal collaboration and the demonstration that their effects on the beam are acceptable, as presented in this thesis. The programme of prototyping was necessary in order to verify the computer models and to demonstrate the safety margins. There are proposals for using an undulator with a K parameter of 0.4. The reasoning behind this choice is that more of the photons are in the first harmonic of the undulator radiation and so will have a higher degree of circular polarisation. This might be advantageous for the polarised positron source. However there are studies showing that an undulator with a higher K parameter, producing higher energy photons, results in higher positron production. As the efficiency of the positron source is a multi-dimensional problem with many underlying assumptions, such as, the length of undulator, photon spot size, target material and thickness, capture optics, etc. it is very difficult to objectively evaluate all possibilities. Nevertheless, the current consensus of the community is that a high K undulator provides a greater positron intensity per meter of undulator and that this is the preferred solution for the ILC. An undulator with a lower K parameter would have a larger beam aperture which would reduce many of the concerns of the system, such as wakefield effects and alignment. It should also be noted that with a high K SC undulator the K parameter can always be reduced by reducing the current density in the coils.

9.2 Further Study

Further work will look at the construction of a full scale 4 m long module. This will contain two ∼2m long undulators. This module should be tested in a beam to assess the radiation quality, beam-induced heating, reliability and alignment techniques.

The vacuum specification and full engineering design and layout of the photon collimators could be updated with the development of a bespoke code. This code is necessary to calculate the SR at the large angles required. The number of secondary particles also produced in the photon collimators and any influence they have on the electron beam should be investigated. The engineering design of the collimators needs to be completed, this will include looking at possible materials, a more realistic geometry, dissipation of the power deposited and incorporation of the necessary vacuum pumps. As well as updating

the SR calculations for the vacuum system the impact of beam halo particles on the vacuum system needs to be assessed.

The wakefields of the vessel at the operating temperature of 4 K could be calculated by measuring the complex conductivity properties of a real vessel at that temperature.

Analytic studies have shown that the depolarisation of the electron beam through the undulator due to the emission of SR is expected to be small. These results should be checked with a simulation program, although no such program currently exists there are plans to develop one [157].

The main area of further study is in specifying the undulator line for a polarised positron source. For this design a more detailed investigation into the alignment tolerances, beam jitter and affect of magnetic field errors on the polarisation of the SR is required. The radiation from multiple realistic undulator modules needs to be simulated and this too requires further code development.

It should be remembered that the design optimisation of the undulator line must be integrated with the systems engineering of the positron source and ILC. Changes in other components, for example the capture optics, can have consequences on the undulator line specification and must be accounted for.

Appendix A

Electron Spin and the Stern-Gerlach Experiment

In the Stern-Gerlach experiment, a beam of silver atoms are passed through a dipole magnet whose field is tapered so it is stronger at one pole than the other. The dipole field will deflect the beam of silver atoms if they have any magnetic moment, this deflection can be measured by using a photographic screen placed downstream of the dipole.

If the magnetic moment of the silver atoms is assumed to be a bar magnet then there are three possible outcomes of the experiment, the particles could be deflected up, down or not at all. This is because a bar magnet placed in an external field experiences a torque that tends to align it with the field. Due to the tapered nature of the field the force on one pole will be greater than the force on the other pole resulting in a net deflection up or down as shown in Figure A.1. Using classical physics, it is expected that this relative alignment of the two magnet fields can take on any value, giving a continuum of deflections of the silver atoms. However, quantum mechanics predicts that the magnetic moment can only have $2j + 1$ discrete values, where j is a quantum number associated with the total angular momentum of the atom (which is related to the magnetic moment). Therefore, this experiment is measuring the angular momentum of the atom. If $j = 0$ then there will be no angular momentum and therefore no magnetic moment and no deflection. If $j = 1$ then there will be three possible orientations of the magnetic moment and the beam will be deflected into three directions. However in the experiment the beam was split into two, which implies that:

$$2j + 1 = 2,$$

and hence that:

$$j = \frac{1}{2}.$$

This means that the magnetic moment of the silver atom can have only one of two orientations. Although silver atoms were used, in effect it is the magnet properties of a single electron that are being studied. This is because the magnetic effects of all the other particles in the atom cancel each other.

As the angular momentum must come from a single electron in the silver atom, it was postulated in 1925, by Goudsmit and Uhlenbeck, that the electron itself had an intrinsic angular momentum, independent of its motion. This is known as the electron spin, s, and can have values, $s = \pm\frac{1}{2}$. Positive values imply that the spin is parallel to the direction under consideration and negative spin implies antiparallel alignment. In classical physics, a ball of charge could have a magnetic moment if it were spinning such that the charge at the edges produced an effective current loop. This reasoning led to the use of the term 'electron spin' to describe the intrinsic angular momentum, even though the electron is not spinning.

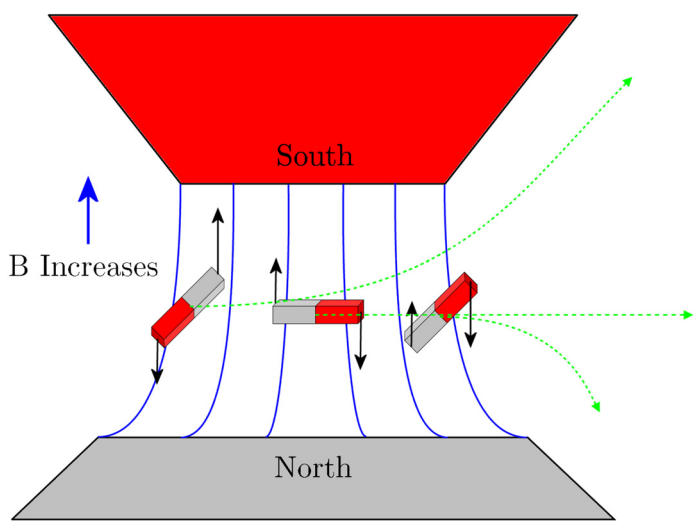

Figure A.1: Bar magnets in an inhomogeneous magnetic field (blue lines) experience a net force (black arrows) that depends upon their orientation with respect to the external field B. This results in a net deflection that also depends upon their orientation (green dashed arrows).

Appendix B

Green's Function for the Time Dependent Wave Equation

The solution to the time dependent wave equation can be found by finding the solution to the differential equation:

$$\Box^2 G(\boldsymbol{r}, t) = \delta(\boldsymbol{r})\delta(t).$$

To find the form of the Green's function, $G(\boldsymbol{r}, t)$, the relationship between delta functions and Fourier transforms can be used:

$$\delta(\boldsymbol{r})\delta(t) = \frac{1}{(2\pi)^4} \int \mathrm{e}^{\mathrm{i}(\omega t - \boldsymbol{k}\cdot\boldsymbol{r})} \mathrm{d}\omega \mathrm{d}^3\boldsymbol{k}.$$

Differentiating gives,

$$G(\boldsymbol{r}, t) = \frac{1}{(2\pi)^4} \int \frac{1}{k^2 - \frac{\omega^2}{c^2}} \, \mathrm{e}^{\mathrm{i}(\omega t - \boldsymbol{k}\cdot\boldsymbol{r})} \mathrm{d}\omega \mathrm{d}^3\boldsymbol{k}, \tag{B.1}$$

as the operator acting on the Green's function must give the same result as that for the δ functions. The integral w.r.t to ω can be carried out using complex analysis. If $kc = q$ then the integral:

$$-\frac{c^2}{(2\pi)^4} \int \frac{\mathrm{e}^{\mathrm{i}(\omega t - \boldsymbol{k}\cdot\boldsymbol{r})} \mathrm{d}\omega \mathrm{d}^3\boldsymbol{k}}{\omega^2 - q^2},$$

is equal to $2\pi\mathrm{i}\sum_j R_j$ where R_j are the residues. There are two poles at $\pm q$. For the pole at $+q$, the residue is:

$$\lim_{\omega \to q} (\omega - q) f(\omega),$$

where:

$$f(\omega) = \frac{\mathrm{e}^{\mathrm{i}\omega t}}{\omega^2 - q^2}.$$

This gives:

$$\lim_{\omega \to q} \frac{(\omega - q)\mathrm{e}^{\mathrm{i}\omega t}}{(\omega - q)(\omega + q)} = \frac{\mathrm{e}^{\mathrm{i}qt}}{2q}.$$

Similarly for the pole at $-q$, the residue is:

$$\begin{aligned} \lim_{\omega \to -q} (\omega + q) f(\omega) &= \frac{(\omega + q)\mathrm{e}^{\mathrm{i}\omega t}}{(\omega - q)(\omega + q)} \\ &= \frac{\mathrm{e}^{-\mathrm{i}qt}}{-2q}. \end{aligned}$$

Therefore the integral of EquationB.1 w.r.t ω is:

$$2\pi\mathrm{i}\left(\frac{\mathrm{e}^{\mathrm{i}qt}}{2q} - \frac{\mathrm{e}^{-\mathrm{i}qt}}{2q}\right).$$

This can be simplified using $\mathrm{e}^{\mathrm{i}\theta} = \cos\theta + \mathrm{i}\sin\theta$, giving:

$$G(\boldsymbol{r}, t) = \frac{c}{(2\pi)^3} \int \frac{1}{k} \mathrm{e}^{\mathrm{i}\boldsymbol{k}\cdot\boldsymbol{r}} \mathrm{d}^3\boldsymbol{k}. \tag{B.2}$$

Equation B.2 is of the form:

$$F(\boldsymbol{r}) = \int f(k) \mathrm{e}^{\mathrm{i}\boldsymbol{k}\cdot\boldsymbol{r}} \mathrm{d}^3\boldsymbol{k},$$

where $f(k)$ depends only upon the magnitude of $\boldsymbol{k}$, not its direction. Therefore, $F(r)$ will also only depend upon the magnitude of $\boldsymbol{k}$. In spherical co-ordinates it can be written as:

$$F(\boldsymbol{r}) = \int_0^\infty k^2 f(k) \mathrm{d}k \int \mathrm{e}^{\mathrm{i}\boldsymbol{k}\cdot\boldsymbol{r}} \mathrm{d}\Omega.$$

The polar axis in $\boldsymbol{k}$ space can be chosen to be in the direction of $\boldsymbol{r}$ giving:

$$\begin{aligned} \int \mathrm{e}^{\mathrm{i}\boldsymbol{k}\cdot\boldsymbol{r}} \mathrm{d}\Omega &= \int_0^{2\pi} \mathrm{d}\phi \int_{-1}^{1} \mathrm{e}^{\mathrm{i}kr\cos\theta} \mathrm{d}\theta \\ &= 2\pi \frac{1}{\mathrm{i}kr} (\mathrm{e}^{\mathrm{i}kr} - \mathrm{e}^{-\mathrm{i}kr}). \end{aligned}$$

This means that:

$$F(\boldsymbol{r}) = \frac{4\pi}{r} \int_0^\infty \sin(kr) \mathrm{d}k.$$

Applying this result to B.2 gives:

$$G(\boldsymbol{r},t) = \frac{c}{4\pi^2 r}\int_{-\infty}^{\infty} \sin(kr)\sin(ckt)\mathrm{d}k.$$

Letting $ck = K$ and therefore $c\mathrm{d}k = \mathrm{d}K$, and using the following trigonometric identity:

$$\sin(a)\sin(b) \equiv \frac{1}{2}(\cos(b-a) - \cos(a+b)),$$

gives:

$$G(\boldsymbol{r},t) = \frac{1}{8\pi^2 r}\int_{-\infty}^{\infty} \left\{\cos\left(Kt - \frac{K\boldsymbol{r}}{c}\right) - \cos\left(Kt + \frac{K\boldsymbol{r}}{c}\right)\right\}\mathrm{d}K,$$

The final integration can be performed using properties of the delta function to give:

$$G(\boldsymbol{r},t) = \frac{1}{4\pi r}\delta\left(t - \frac{\boldsymbol{r}}{c}\right)\delta\left(t + \frac{\boldsymbol{r}}{c}\right). \tag{B.3}$$

Appendix C

Derivation of the Panofsky-Wenzel Theorem

This theorem can be shown by considering the frame of reference where $\frac{1}{\boldsymbol{v}}\frac{\partial}{\partial t} = \frac{\partial}{\partial s}$ and Faraday's law of magnetic induction, Equation 2.2:

$$\frac{\partial \boldsymbol{B}}{\partial t} + \boldsymbol{\nabla} \times \boldsymbol{E} = 0,$$

which can be de-composed into longitudinal and transverse components. For example the electric field can be expressed as:

$$\boldsymbol{E} = E_{\parallel} \cdot \boldsymbol{e}_z + \boldsymbol{E}_{\perp},$$

where $E_{\parallel}$ and $\boldsymbol{E}_{\perp}$ have been expressed in terms of a unit vector in the z direction, $\boldsymbol{e}_z$:

$$E_{\parallel} = \boldsymbol{e}_z \cdot \boldsymbol{E}$$

and

$$\boldsymbol{E}_{\perp} = (\boldsymbol{e}_z \times \boldsymbol{E}) \times \boldsymbol{e}_z.$$

A similar decomposition can be made for the magnetic field. The set of four Maxwell equations now become six in terms of the transverse and parallel components. The relevant part of Faraday's law is:

$$\boldsymbol{e}_z \times \frac{\partial \boldsymbol{B}_{\perp}}{\partial t} = \frac{\partial \boldsymbol{E}_{\perp}}{\partial z} - \boldsymbol{\nabla}_{\perp} \times (E_{\parallel} \cdot \boldsymbol{e}_z).$$

The wake function for a particle of charge q passing through a structure of length L is:

$$\boldsymbol{w} = -\frac{1}{q}\int_{-\frac{L}{2}}^{\frac{L}{2}} (\boldsymbol{E} + \boldsymbol{v}\boldsymbol{e_z} \times \boldsymbol{B})\mathrm{d}z.$$

Taking the partial derivative of the above expression w.r.t. s and considering only the transverse components gives:

$$\frac{\partial}{\partial s}\boldsymbol{w}_\perp = -\frac{1}{q}\int_{-\frac{L}{2}}^{\frac{L}{2}} \left(\frac{\partial}{\partial s}\boldsymbol{E}_\perp + \boldsymbol{v}\boldsymbol{e_z} \times \frac{\partial}{\partial s}\boldsymbol{B}_\perp\right)\mathrm{d}z.$$

Using the fact that $\boldsymbol{v}\frac{\partial}{\partial s} = \frac{\partial}{\partial t}$ gives:

$$\frac{\partial}{\partial s}\boldsymbol{w}_\perp = -\frac{1}{q}\int_{-\frac{L}{2}}^{\frac{L}{2}} \left(\frac{1}{\boldsymbol{v}}\frac{\partial}{\partial t}\boldsymbol{E}_\perp + \boldsymbol{e_z} \times \frac{\partial}{\partial t}\boldsymbol{B}_\perp\right)\mathrm{d}z.$$

Faraday's law can now be used to substitute for $\boldsymbol{B}_\perp$:

$$\frac{\partial}{\partial s}\boldsymbol{w}_\perp = -\frac{1}{q}\int_{-\frac{L}{2}}^{\frac{L}{2}} \left(\left(\frac{1}{\boldsymbol{v}}\frac{\partial}{\partial t} + \frac{\partial}{\partial z}\right)\boldsymbol{E}_\perp - \boldsymbol{\nabla}_\perp E_z\right)\mathrm{d}z.$$

The partial derivative operators can be substituted for an exact derivative by recalling the definition of a partial derivative of a function $F(z,t)$:

$$\mathrm{d}F(z,t) = \frac{\partial}{\partial t}F(z,t)\mathrm{d}t + \frac{\partial}{\partial z}F(z,t)\mathrm{d}z.$$

As $F(z,t)$ is an arbitrary function it can removed to give:

$$\frac{\mathrm{d}}{\mathrm{d}z} = \frac{1}{v}\frac{\partial}{\partial t} + \frac{\partial}{\partial z}.$$

The expression for the wake function is now:

$$\frac{\partial}{\partial s}\boldsymbol{w}_\perp = -\frac{1}{q}\int_{-\frac{L}{2}}^{\frac{L}{2}} \left(\frac{\mathrm{d}}{\mathrm{d}z}\boldsymbol{E}_\perp - \boldsymbol{\nabla}_\perp E_z\right)\mathrm{d}z.$$

The integral of $\frac{1}{q}\boldsymbol{\nabla}_\perp E_z$ is just the longitudinal wake function $w_\parallel$:

$$\frac{\partial}{\partial s}\boldsymbol{w}_\perp = -\boldsymbol{\nabla}_\perp w_\parallel + \left[\frac{\boldsymbol{E}_\perp}{q}\right]_{-\frac{L}{2}}^{\frac{L}{2}}$$

If the transverse electric fields are equal at the beginning and end of the structure considered then

$$\frac{\partial}{\partial s}\boldsymbol{w}_\perp = -\boldsymbol{\nabla}_\perp w_\parallel.$$

This is the Panofsky-Wenzel theorem.

Bibliography

[1] R. Staffin and M. Turner, ed., *"Discovering the Quantum Univerise: The Role of Particle Colliders"*. 2005.
http://www.interactions.org/quantumuniverse/dqu.pdf.

[2] P. Burrows, ed., *"The International Linear Collider: Gateway to the Quantum Universe"*. 2007.
http://www.linearcollider.org/pdf/ilc_gateway_report.pdf.

[3] H. Murayama, "Supersymmetry phenomenology," 2000. arXiv:hep-ph/0002232
http://arxiv.org/abs/hep-ph/0002232.

[4] S. P. Martin, "A supersymmetry primer," 1997. arXiv:hep-ph/9709356
http://arxiv.org/abs/hep-ph/9709356.

[5] G. Guignard, ed., *"A 3 TeV e^+e^- Linear Collider Based on CLIC Technology"*. No. CERN-2000-008, July 2000.
http://preprints.cern.ch/yellowrep/2000/2000-008/p1.pdf.

[6] M. Tigner, "A possible apparatus for electron-clashing experiments," *Nuovo Cimento*, no. 37, pp. 1221–1231, 1965.

[7] H. Wiedemann, *"Synchrotron Radiation"*. Berlin: Springer-Verlag, 2003.

[8] A. Chao and M. Tigner, eds., *"The Handbook of Accelerator Physics and Engineering"*. London: World Scientific, 2nd ed., 2002.

[9] H. Ehrlichmann, S. Guiducci, K. Kubo, M. Kuriki, and A. Wolski, "Recommendations for ILC configuration satisfying timing constraints," tech. rep., ILC, 2006.

[10] H. Ehrlichmann, "Bunch timing aspects for the ILC," Tech. Rep. DESY M 06-01, DESY, 2006.

[11] "The ILC Baseline Configuration Document."
http://www.linearcollider.org/wiki/.

[12] V. Bharadwaj, "The status of existing positron sources." Workshop on Positron Sources for the International Linear Collider, Daresbury Laboratory, 2005.
http://www.astec.ac.uk/id_mag/ID-Mag_Helical_ILC_Positron_Production_Workshop.htm.

[13] A. Ushakov, E. Elsenand, K. Flöttmann, S. Riemann, and K. Sanosyan, "Radiation levels and activation at the ILC positron source," in *Proceedings of the 10th European Particle Accelerator Conference*, (Edinburgh), pp. 2478–2480, June 2006.

[14] J. Clarke, "Positron source recommendations." Snowmass International Linear Colldier Workshop, Snowmass, 2005.
http://www.ippp.dur.ac.uk/~gudrid/source/target/jim_clarke-recommendation.pdf.

[15] K. Flöttmann, *"Investigation Toward the Development of Polarised and Unpolarised High Intensity Positron Sources for Linear Colliders"*. PhD thesis, Hamburg University, November 1993. DESY 92-161.

[16] D. J. Scott, "Geant4 simulations of photon interactions with the target and vacuum vessel." Workshop on Positron Sources for the International Linear Collider, Daresbury Laboratory, 2005.
http://www.astec.ac.uk/id_mag/ID-Mag_Helical_ILC_Positron_Production_Workshop.htm.

[17] V. Balakin and A. Mikhailichenko, "The conversion system for obtaining highly polarized electrons and positrons," tech. rep., BINP, 79-85 1977.

[18] R. Glanz, *"A Feasibility Study of High Intenstiy Positron Sources for the S-Band and TESLA Linear Colliders"*. PhD thesis, Hamburg University, October 1997. DESY 97-201.

[19] R. Brinkmann, K. Flöttmann, J. Rossbach, P. Schüsser, N. Walker, and H. Weise, eds., *"TESLA Technical Design Report"*, vol. II: The Accelerator. DESY, 2001.

[20] N. Phinney, N. Toge, and N. Walker, eds., *"International Linear Collider Reference Design Report"*, vol. 3: Accelerator. August 2007.

http://ilcdoc.linearcollider.org/getfile.py?docid=182&name=ILC_RDR_Volume_3-Accelerator&format=pdf.

[21] J. C. Smith, "Spin transport in the International Linear Collider," in *Proceedings of the 22nd Particle Acclerator Conference*, (Albuquerque), pp. 1955–1957, June 2007.

[22] W. H. McMaster, "Polarization and the Stokes parameters," *Am. J. Phys.*, vol. 22, pp. 351–361, September 1954.

[23] H. A. Tolhoek, "Electron polarization, theory and experiment," *Rev. Mod. Phys.*, vol. 28, pp. 277–297, July 1956.

[24] W. H. McMaster, "Matrix representation of polarization," *Rev. Mod. Phys.*, vol. 3, pp. 8–28, January 1961.

[25] J. Clarke, "S5 positron source." The 9th ACFA ILC Physics and Detector Workshop and ILC GDE Meeting, IHEP, Beijing, 2007. http://ilcagenda.linearcollider.org/getFile.py/access?contribId=155&sessionId=5&resId=0&materialId=slides&confId=1212.

[26] D. Barber. Private communication.

[27] G. A. Moortgat-Pick, T. Abe, G. Alexander, B. Ananthanarayan, A. Babich, V. Bharadwaj, D. Barber, A. Bartl, A. Brachmann, S. Chen, J. Clarke, J. Clendenin, J. Dainton, K. Desch, M. Diehl, B. Dobos, T. Dorland, H. Eberl, J. Ellis, K. Flöttmann, H. Fraas, F. Franco-Sollova, F. Franke, A. Freitas, J. Goodson, J. Gray, A. Han, S. Heinemeyer, S. Hesselbach, T. Hirose, K. Hohenwarter-Sodek, J. Kalinowski, T. Kernreiter, O. Kittel, S. Kraml, W. Majerotto, A. Martinez, H.-U. Martyn, W. Menges, A. Mikhailichenko, K. Mönig, K. Moffeit, S. Moretti, O. Nachtmann, F. Nagel, T. Nakanishi, U. Nauenberg, T. Omori, P. Osland, A. Pankov, N. Paver, R. Pitthan, R. Pöschl, W. Porod, J. Proulx, P. Richardson, S. Riemann, S. Rindani, T. Rizzo, P. Schüler, C. Schwanenberger, D. J. Scott, J. Sheppard, R. Singh, H. Spiesberger, A. Stahl, H. Steiner, A. Wagner, G. Weiglein, G. Wilson, M. Woods, P. Zerwas, J. Zhang, and F. Zomer, "The role of polarized positrons and electrons in revealing fundamental interactions at the linear collider," *Physics Rep.*, vol. 460, pp. 131–243, May 2008.

[28] G. A. Moortgat-Pick, "Physics aspects of polarized e+ at the linear collider," 2006. arXiv:hep-ph/0607173
http://arxiv.org/abs/hep-ph/0607173.

[29] T. Okugi, Y. Kurihara, M. Chiba, A. Endo, R. Hamatsu, T. Hirose, T. Kumita, T. Omori, Y. Takeuchi, and M. Yoshioka, "Proposed method to produce a highly polarized e+ beam for future linear colliders," *Jpn. J. Appl. Phys.*, vol. 35, pp. 3677–3680, June 1996.

[30] T. Omori, M. Fukuda, T. Hirose, Y. Kurihara, R. Kuroda, M. Nomura, A. Ohashi, T. Okugi, K. Sakaue, T. Saito, J. Urakawa, M. Washio, and I. Yamazaki, "Efficient propagation of polarization from laser photons to positrons through compton scattering and electron-positron pair creation," *Phys. Rev. Lett.*, vol. 96, no. 1, p. 114801, 2006.

[31] G. Alexander, P. Anthony, V. Bharadwaj, Y. K. Batygin, T. Behnke, S. Berridge, G. R. Bower, W. Bugg, R. Carr, E. Chudakov, J. E. Clendenin, F.-J. Decker, Y. Efremenko, T. Fieguth, K. Flöttmann, M. Fukuda, V. Gharibyan, T. Handler, T. Hirose, R. H. Iverson, Y. Kamychkov, H. Kolanoski, T. Lohse, C. LuPR, K. T. McDonald, N. Meyners, R. Michaels, A. A. Mikhailichenko, K. Mönig, G. Moortgat-Pick, M. Olson, T. Omori, D. Onoprienko, N. Pavel, R. Pitthan, M. Purohit, L. Rinolfi, K.-P. Schüler, J. C. Sheppard, S. Spanier, A. Stahl, Z. M. Szalata, J. Turner, D. Walz, A. Weidemann, and J. Weisend, "A Two-Stage Proposal to Test Production of Polarized Positrons with the SLAC 50-GeV Beam in the FFTB," tech. rep., SLAC, 2002. SLAC-PROPOSAL-E166.

[32] K.-P. Schüler, "The E166 experiment: Undulator-based production of polarized positrons," in *Proceedings of the 12th International Workshop on Polarized Ion Sources, Targets and Polarimetry*, (Brookhaven National Laboratory), pp. 102–109, September 2007.

[33] G. Alexander, J. Barley, Y. Batygin, S. Berridge, V. Bharadwaj, G. Bower, W. Bugg, F.-J. Decker, R. Dollan, Y. Efremenko, V. Gharibyan, C. Hast, R. Iverson, H. Kolanoski, J. Kovermann, K. Laihem, T. Lohse, K. McDonald, A. Mikhailichenko, G. Moortgat-Pick, P. Pahl, R. Pitthan, R. Pöschl, E. Reinherz-Aronis, S. Riemann, A. Schälicke, K. Schüler, T. Schweizer, D. Scott, J. C. Sheppard, A. Stahl, Z. M. Szalata, D. Walz, , and A. Weidemann, "Observation of polarized positrons from an

undulator-based source," Tech. Rep. CLNS 08/2023, Cockcroft-08-03, DCPT/08/24, DESY 08-025, IPPP/08/12, SLAC-PUB-13145, 2008. Submitted to Phys. Rev. Lett.

[34] S. Agostinelli, J. Allison, K. Amako, J. Apostolakis, H. Araujo, P. Arce, M. Asai, D. Axen, S. Banerjee, G. Barrand, F. Behner, L. Bellagamba, J. Boudreau, L. Broglia, A. Brunengo, H. Burkhardt, S. Chauvie, J. Chuma, R. Chytracek, G. Cooperman, G. Cosmo, P. Degtyarenko, A. Dell'Acqua, G. Depaola, D. Dietrich, R. Enami, A. Feliciello, C. Ferguson, H. Fesefeldt, G. Folger, F. Foppiano, A. Forti, S. Garelli, S. Giani, R. Giannitrapani, D. Gibin, J. J. Gomez-Cadenas, I. Gonzalez, G. Gracia-Abril, G. Greeniaus, W. Greiner, V. Grichine, A. Grossheim, S. Guatelli, P. Gumplinger, R. Hamatsu, K. Hashimoto, H. Hasui, A. Heikkinen, A. Howard, V. Ivanchenko, A. Johnson, F. W. Jones, J. Kallenbach, N. Kanaya, M. Kawabata, Y. Kawabata, M. Kawaguti, S. Kelner, P. Kent, A. Kimura, T. Kodama, R. Kokoulin, M. Kossov, H. Kurashige, E. Lamanna, T. Lampen, V. Lara, V. Lefebure, F. Lei, M. Liendl, W. Lockman, F. Longo, S. Magni, M. Maire, E. Medernach, K. Minamimoto, P. M. de Freitas, Y. Morita, K. Murakami, M. Nagamatu, R. Nartallo, P. Nieminen, T. Nishimura, K. Ohtsubo, M. Okamura, S. O'Neale, Y. Oohata, K. Paech, J. Perl, A. Pfeiffer, M. G. Pia, F. Ranjard, A. Rybin, S. Sadilov, E. D. Salvo, G. Santin, T. Sasaki, N. Savvas, Y. Sawada, S. Scherer, S. Sei, V. Sirotenko, D. Smith, N. Starkov, H. Stoecker, J. Sulkimo, M. Takahata, S. Tanaka, E. Tcherniaev, E. S. Tehrani, M. Tropeano, P. Truscott, H. Uno, L. Urban, P. Urban, M. Verderi, A. Walkden, W. Wander, H. Weber, J. P. Wellisch, T. Wenaus, D. C. Williams, D. Wright, T. Yamada, H. Yoshida, and D. Zschiesche, "GEANT4 a simulation toolkit," *Nucl. Instrum. Methods*, vol. A506, July 2003.

[35] J. Allison, K. Amako, J. Apostolakis, H. Araujo, P. Arce-Dubois, M. Asai, G. Barrand, R. Capra, S. Chauvie, R. Chytracek, G. A. P. Cirrone, G. Cooperman, G. Cosmo, G. Cuttone, G. Daquino, M. Donszelmann, M. Dressel, G. Folger, F. Foppiano, F. Generowicz, V. Grichine, S. Guatelli, P. Gumplinger, A. Heikkinen, I. Hrivnacova, A. Howard, S. Incerti, V. Ivanchenko, T. Johnson, F. Jones, T. Koi, R. Kokoulin, M. Kossov, H. Kurashige, V. Lara, S. Larsson, F. Lei, O. Link, F. Longo, M. Maire, A. Mantero, B. Mascialino, I. McLaren, P. Mendez-Lorenzo, K. Minamimoto, K. Murakami, P. Nieminen, L. Pandola, S. Parlati, L. Peralta, J. Perl, A. Pfeiffer, M. G. Pia, A. Ribon, P. Rodrigues, G. Russo, S. Sadilov, G. Santin, T. Sasaki, D. Smith, N. Starkov, S. Tanaka, E. Tcherniaev, B. Tome, T. A., P. Truscott, L. Ur-

ban, M. Verderi, A. Walkden, J. P. Wellisch, D. C. Williams, and D. W. H. Yoshida, "GEANT4 developments and applications," *IEEE Trans. Nucl. Sci.*, vol. 53, February 2006.

[36] Wolfram Research, Inc., Mathematica, Version 6.0, Champaign, Illinois (2007).

[37] J. D. Jackson, *"Classical Electrodynamics"*. New York: John Wiley & Sons, 2nd ed., 1975.

[38] E. A. Hylleraas, *"Mathematical and Theoretical Physics"*. London: John Wiley & Sons, 1970.

[39] E. A. Hylleraas, *"Mathematical and Theoretical Physics"*, vol. 2. London: John Wiley & Sons, 1970.

[40] L. D. Landau and E. M. Lifshitz, *"The Classical Theory of Fields"*. London: Elsevier, 4th ed., 1975.

[41] J. Clarke, *"The Science and Technology of Undulators and Wigglers"*. Oxford: Oxford University Press, 2004.

[42] H. Onuki and P. Elleaume, eds., *"Undulators, Wigglers and their Applications"*. London: Taylor and Francis, 2003.

[43] R. P. Walker, "Insertion devices: Undulators and wigglers," in *Proceedings of the CERN Accelerator School: Synchrotron Radiation and Free Electron Lasers*, vol. 98-04, pp. 129–190, August 1996.

[44] K. Riley, M. Hobson, and S. Bence, *"Mathematical Methods for Physics and Engineering"*. Cambridge: Cambridge University Press, 1997.

[45] R. Nevels and C.-S. Shin, "Lorenz, Lorentz, and the gauge," *IEEE Antennas Prop. Mag.*, vol. 43, pp. 70–71, 2001.

[46] M. Abramovitz and I. A. Stegun, eds., *"Handbook of Mathematical Functions"*. Dover: Dover Publications, 1965.

[47] B. Kincaid, "A short-period helical wiggler as an improved source of synchrotron radiation," *Journal of Applied Physics*, vol. 48, pp. 2684–2691, July 1977.

[48] R. P. Walker, "Calculation of undulator radiation spectral and angular distributions," *Rev. Sci. Instrum.*, vol. 60, pp. 1816–1819, July 1988.

[49] O. V. Chubar, "Precise computation of electron-beam radiation in nonuniform magnetic fields as a tool for beam diagnostics," *Rev. Sci. Instrum.*, vol. 66, pp. 1872–1874, February 1995.

[50] T. Tanaka and H. Kitamura, "SPECTRA: A synchrotron radiation calculation code," *J. Synchrotron Rad.*, vol. 8, pp. 1221–1228, 2001.

[51] T. Tanaka. Private communication.

[52] K. Flöttmann and S. G. Wipf, "Field enhancement of a superconducting helical undulator with iron," in *Proceedings of the 18th International Linac Conference*, (Geneva), pp. 536–538, August 1996.

[53] D. J. Scott, "A helical undulator for TESLA: A Halbach type design," Tech. Rep. ASTeC-ID-008, CCLRC, 2003.

[54] D. J. Scott, "A helical undulator for TESLA: Super-conducting wires design," Tech. Rep. ASTeC-ID-010, CCLRC, 2003.

[55] D. J. Scott, "A helical undulator for TESLA: Pure permanent magnet planar designs," Tech. Rep. ASTeC-ID-011, CCLRC, 2003.

[56] D. J. Scott, "A helical undulator for TESLA: A Halbach type design 2," Tech. Rep. ASTeC-ID-012, CCLRC, 2003.

[57] D. J. Scott, "A helical undulator for TESLA: Analysis of forces for the Halbach design," Tech. Rep. ASTeC-ID-017, CCLRC, 2003.

[58] D. J. Scott, "A helical undulator for TESLA: Simplification of the Halbach design," Tech. Rep. ASTeC-ID-018, CCLRC, 2003.

[59] D. J. Scott, "A helical undulator for TESLA: Analysis of forces for different Halbach designs," Tech. Rep. ASTeC-ID-021, CCLRC, 2003.

[60] D. J. Scott, S. Appleton, J. Clarke, B. Todd, E. Baynham, T. Bradshaw, S. Carr, Y. Ivanyushenkov, and J. Rochford, "Design considerations for a helical undulator for the production of polarised positrons for TESLA," in *Proceedings of the 9th European Particle Accelerator Conference*, (Lucerne), pp. 458–459, July 2004.

[61] Y. Ivanyushenkov, E. Baynham, T. Bradshaw, S. Carr, J. Rochford, B. J. A. Shepherd, J. A. Clarke, O. Malyshev, D. J. Scott, J. B. Dainton, P. Cooke, T. Greenshaw,

D. P. Barber, and G. A. Moortgat-Pick, "Development of a superconducting helical undulator for a polarised positron source," in *Proceedings of the 21st Particle Accelerator Conference*, (Knoxville), pp. 2295–2297, May 2005.

[62] D. J. Scott, S. Appleton, J. A. Clarke, O. B. Malyshev, B. J. A. Shepherd, B. Todd, D. E. Baynham, T. Bradshaw, A. Brummitt, S. Carr, Y. Ivanyushenkov, J. Rochford, I. R. Bailey, P. Cooke, J. B. Dainton, L. I. Malysheva, D. P. Barber, and G. A. Moortgat-Pick, "Selection of the optimum magnet design for the International Linear Collider positron source helical undulator," *Phys. Rev. ST Accel. Beams*, vol. 10, p. 032401, March 2007.

[63] D. J. Scott, A. Birch, J. A. Clarke, O. B. Malyshev, E. Baynham, T. Bradshaw, A. Brummitt, S. Carr, Y. Ivanyushenkov, A. Lintern, J. Rochford, I. R. Bailey, J. B. Dainton, L. Jenner, L. Malysheva, L. Zhang, D. Barber, and G. A. Moortgat-Pick, "Status of the HeLiCal contribution to the polarised positron source for the International Linear Collider," in *Proceedings of the 22nd Particle Accelerator Conference*, (Albuquerque), pp. 2874–2876, June 2007.

[64] Y. Ivanyushenkov, E. Baynham, T. Bradshaw, A. Brummitt, S. Carr, A. Lintern, J. Rochford, J. A. Clarke, O. B. Malyshev, D. Scott, B. J. A. Shepherd, I. R. Bailey, P. Cooke, J. B. Dainton, L. Malysheva, D. P. Barber, and G. A. Moortgat-Pick, "Status of R&D on a superconducting helical undulator for the ILC positron source," in *Proceedings of the 22nd Particle Accelerator Conference*, (Albuquerque), pp. 2865–2867, June 2007.

[65] P. Campbell, *"Permanent Magnet Materials and their Application"*. Cambridge: Cambridge University Press, 1994.

[66] P. Elleaume, O. Chubar, and J. Chavanne, "Computing 3D magnetic fields from insertion devices," in *Proceedings of the 17th Particle Accelerator Conference*, (Vancouver), pp. 3509–3511, May 1997.

[67] P. Elleaume, O. Chubar, and J. Chavanne, "A 3D magnetostatics computer code for insertion devices," *J. Synchrotron Rad.*, vol. 5, pp. 481–484, 1998.

[68] P. Elleaume and J. Chavanne, "A new powerful flexible linear/helical undulator for soft x-rays," *Nucl. Instrum. Methods Phys. Res.*, vol. A304, pp. 719–724, 1991.

[69] B. Diviacco, "Performance optimization of pure permanent mangent undulators," in *Proceedings of the 15th Particle Accelerator Conference*, (Washington), pp. 1590–1592, May 1993.

[70] S. Sasaki, K. Miyata, and T. Takada, "A new undulator for generating variably polarized radiation," *Jpn. J. Appl. Phys.*, vol. 31, pp. L1794–L1796, December 1992.

[71] J. Bahrdt, W. Frentrup, A. Gaupp, B. Kuske, A. Meseck, and M. Scheer, "Undulators for the BESSY soft-X-ray FEL," in *Proceedings of the 26th International Free Electron Laser Conference*, (Trieste), pp. 610–613, August-September 2004.

[72] A. Hirayo, K. Yoshida, S. Yagi, M. Taniguchi, S. Kimura, H. Hama, T. Takayama, and D. Amano, "Undulators at HiSOR - a compact racetrack-type ring," *J. Synchrotron Rad.*, vol. 5, pp. 445–447, May 1998.

[73] G. V. Rybalchenko, K. Shirasawa, M. Morita, N. V. Smolyakov, K. Goto, T. Matsui, and A. Hiraya, "Performance and future plan of Multi-mode undulator at HiSOR," *Nucl. Instrum. Methods Phys. Res.*, vol. A467-A468, pp. 173–176, July 2001.

[74] K. Halbach, "Physical and optical properties of rare earth cobalt magnets," *Nucl. Instrum. Methods Phys. Res.*, vol. 187, pp. 109–117, 1981.

[75] J. Bahrdt, "APPLE Undulators for HGHG-FELS," in *Proceedings of the 27th International Free Electron Laser Conference*, (Berlin), pp. 521–528, August-September 2006.

[76] K. Halbach, "Design of permanent multipole magnets with oriented rare earth cobalt material," *Nucl. Instrum. Methods*, vol. 169, no. L1794, pp. 1–10, 1980.

[77] M. S. Curtin, S. B. Segall, and P. Diament, "Design of a large-useful-bore permanent-magnet helical wiggler," *Nucl. Instrum. Methods Phys. Res.*, vol. A237, pp. 395–400, June 1985.

[78] O. B. Malyshev. Private communication.

[79] Courtesy of S. Appleton, STFC.

[80] E. D. Cox and B. P. Youngman, "Systematic selection of undulator magnets using the techniques of simulated annealing," *SPIE*, vol. 582, pp. 91–97, 1985.

[81] D. J. Scott, "Magnet block sorting for variably polarising undulators," in *Proceedings of the 9th European Particle Accelerator Conference*, (Lucerne), pp. 461–463, July 2004.

[82] J. Pflüger. Private communication.

[83] L. R. Elias and J. M. J. Madey, "Superconducting helically wound magnet for the free-electron laser," *Rev. Sci. Instrum.*, vol. 50, pp. 1335–1341, 1979.

[84] T. A. Vsevolozhskaya, A. D. Chernyakin, A. A. Mikhailichenko, E. A. Perevedentsev, and G. I. Silvestrov in *Proceedings of the 13th International Conference in High Energy Accelerators*, (Novosibirsk), 1986.

[85] J. Rochford, E. Baynham, T. Bradshaw, A. Brummitt, S. Carr, Y. Ivanyushenkov, J. Clarke, O. Malyshev, D. Scott, I. Bailey, P. Cooke, J. Dainton, L. Malysheva, D. Barber, and G. Moortgat-Pick, "Magnetic modelling of a short-period superconducting helical undulator for the ILC positron source," in *Proceedings of the 10th European Particle Accelerator Conference*, (Edinburgh), pp. 840–842, June 2006.

[86] Vector Fields Ltd, 24 Bankside, Kidlington, Oxford OX5 1JE, UK.

[87] Vacuumschmelze GmbH, D 63412 Hanau, Germany.

[88] D. Baynham, R. Coombs, A. Ijspeert, and R. Perin, "Design of superconducting corrector magnets for LHC," *IEEE Trans. Magn.*, vol. 30, pp. 1823–1826, July 1994.

[89] Arepoc Ltd. Iljusinova 4, 85101 Bratislava, Slovakia
http://www.arepoc.sk/.

[90] J. Clarke, "Report from WP4: Polarised positron source." 2nd EuroTeV Annual Workshop, Daresbury Laboratory, January 2007.
http://ilcagenda.linearcollider.org/getFile.py/access?contribId=47&sessionId=8&resId=1&materialId=slides&confId=1265,.

[91] S. Sasaki, I. Vasserman, C. Doose, E. Moog, and N. Mokhov, "Radiation damage to Advanced Photon Source undulators," in *Proceedings of the 21st Particle Acclerator Conference*, (Knoxville), pp. 4126–4128, May 2005.

[92] T. Bizen, X. Maréchel, T. Seike, H. Kitamura, T. Hara, T. Tanaka, Y. Asano, D. Kim, and H. Leev, "Radiation damage in magnets for undulators at low temperatures," in

Proceedings of the 9th European Particle Acclerator Conference, (Lucerne), pp. 2092–2094, July 2004.

[93] H. Kitamura, T. Hara, T. Tanaka, T. Bizen, X. Maréchel, and T. S. and, "Design criteria and technology challenges for the undulator of the future," in *Proceedings of the 9th European Particle Acclerator Conference*, (Lucerne), pp. 59–63, July 2004.

[94] http://www.astec.ac.uk/id_mag/ID-Mag_Helical.htm.

[95] A. Mikhailichenko, "Test of SC undulator for ILC," in *Proceedings of the 10th European Particle Acclerator Conference*, (Edinburgh), pp. 813–815, June 2006.

[96] W. Gai, "Full scale simulation of the positron production and capturing." Beijing workshop on the International Linear Collider positron source, ICHEP, 2007. http://hirune.kek.jp/mk/ilc/positron/IHEP/program.html.

[97] A. Chambers, R. K. Fitch, and B. S. Halliday, *"Basic Vacuum Technology"*. United Kingdom: Taylor & Francis, 2nd ed., 1998.

[98] A. Chambers, *"Modern Vacuum Physics"*. London: IoP Publishing, 2nd ed., 1998.

[99] J. F. O′Hanlon, *"A Users Guide to Vacuum Technology"*. London: John Wiley & Sons, 1998.

[100] T. O. Raubenheimer and F. Zimmermann, "Fast beam-ion instability. I. Linear theory and simulations," *Phys. Rev. E*, vol. 52, pp. 5487–5498, Nov 1995.

[101] L. Wang. Private communication.

[102] O. B. Malyshev and D. J. Scott, "Vacuum systems for the ILC helical undulator," Tech. Rep. EUROTeV-Report-2006-086, CCLRC, 2006.

[103] O. B. Malyshev, D. J. Scott, I. R. Bailey, D. P. Barber, E. Baynham, T. Bradshaw, A. Brummitt, S. Carr, J. A. Clarke, P. Cooke, J. B. Dainton, Y. Ivanyushenkov, L. I. Malysheva, G. A. Moortgat-Pick, and J. Rochford, "Vacuum systems for the ILC helical undulator," *J. Vac. Sci. Technology A*, vol. 25, pp. 791–801, July/August 2007.

[104] C. Herbeaux, P. Martin, V. Baglin, and O. Grbner, "Photon stimulated desorption of an unbaked stainless steel chamber by 3.75 keV critical energy photons.," *J. Vac. Sci. Technology A*, vol. 17, pp. 635–643, March/April 1999.

[105] C. L. Foerster, H. Halama, and C. Lanni, "Photon-stimulated desorption yields from stainless steel and copper-plated beam tubes with various pre-treatments.," *J. Vac. Sci. Technology A*, vol. 8, p. 28562859, May/June 1990.

[106] O. Gröbner, A. G. Mathewson, and P. Martin, "Gas desorption from an oxygen free high conductivity copper vacuum chamber by synchrotron radiation photons," *J. Vac. Sci. Technology A*, vol. 12, p. 8468539, May/June 1994.

[107] J. C. Billy, J. P. Bojon, B. Henrist, N. Hilleret, M. J. Jimrnrz, I. Laugier, and P. Stubin, "The pressure and gas composition evolution during the operation of the LEP accelerator at 100 GeV.," *Vacuum*, pp. 183–189, 2001.

[108] V. V. Anashin, O. B. Malyshev, V. N. Osipov, and I. L. M. and W. C. Turner, "Investigation of synchrotron radiation-induced photodesorption in cryosorbing quasiclosed geometry," *J. Vac. Sci. Technology A*, vol. 12, p. 29172921, September/October 1994.

[109] O. Malyshev. Private communication.

[110] D. J. Scott, "WP5.1:Helical undulator for a polarised positron source." LC-ABD Collaboration Meeting, Cambridge, 2005.
http://www.astec.ac.uk/lc-abd/cambridgeJuly05/Scott.ppt#1.

[111] T. Bradshaw. Private communication.

[112] R. Aßmann, "Collimators and Cleaning, Could this Limit the LHC Performance?" 12 th Chamonix Workshop: LHC Performance.

[113] O. Chubar. Private communication.

[114] J. P. Blewett and R. Chasman, "Orbits and fields in the helical wiggler," *J. Appl. Phys.*, vol. 48, pp. 2692–2698, July 1977.

[115] A. W. Chao, *"The Physics of Collective Beam Instabilities"*. New York: John Wiley & Sons, 1993.

[116] B. Zotter and S. Kheifets, *"Impedances and Wakes in High Energy Particle Accelerators"*. London: World Scientific, 1998.

[117] H. Schlarb, "Resistive wall wakefields," Tech. Rep. TESLA-97-22, University of Hamburg, 1997.

[118] W. K. H. Panofsky and W. A. Wenzel, "Some considerations concerning the transverse deflection of charged particles in radio-frequency fields," *Rev. Sci. Instrum.*, vol. 27, p. 967, 1956.

[119] N. W. Ashcroft and N. D. Mermin, *"Solid State Physics"*. Philadelphia: W. B. Saunders, 1976.

[120] K. L. F. Bane, "Resistive wall wakefields in the LCLS undulator beam pipe," Tech. Rep. SLAC-PUB-10707, SLAC, 2004.

[121] G. E. H. Reuter and E. H. Sondheimer, "The theory of the anomalous skin effect in metals," *Proc. R. Soc. London, Ser. A*, vol. 195, p. 336, 1949.

[122] K. L. F. Bane and M. Sands, "The short range resistive wall wakefield," Tech. Rep. SLAC-PUB-95-7074, SLAC, 1995.

[123] K. L. F. Bane, "Wakefields of sub-picosecond electron bunches," *Int. J. Mod. Phys. A*, vol. 22, pp. 3736–3758, 2007.

[124] D. Scott and J. Jones, "Transverse resistive wall wakefields of the ILC positron undulator beam tube and their effects on an orbit dependant emittance growth," Tech. Rep. EUROTeV-Report-2007-007, CCLRC, February 2007.

[125] D. Shulte and K. Kubo, "Workshop on Low Emittance Transport for the International Linear Collider," January 2007. Daresbury Laboratory.

[126] W. Chou and F. Ruggiero, "Anomalous skin effect and resistive wall heating," Tech. Rep. LHC Project Note 2 (SL/AP), CERN, 1995.

[127] F. Caspers, M. Morvillo, F. Ruggiero, and J. Tan, "Surface resistance measurements and estimate of the beam-induced resistive wall heating of the LHC dipole beam screen," Tech. Rep. LHC Project Report 307, CERN, 1999.

[128] S. Chouhan, R. Rossmanith, S. Strohmer, D. Doelling, A. Geisler, A. Hobl, and S. Kubsky, "Field error compensation and thermal beam load in a superconductive undulator," in *Proceedings of the 20th Particle Acclerator Conference*, (Portland), pp. 899–901, May 2003.

[129] E. Wallen and G. LeBlanc, "Cryogenic system of the MAX-wiggler," *Cryogenics*, vol. 44, pp. 879–893, 2004.

[130] E. Wallen, J. Chavanne, and P.Elleaume, "Magnetic calculations of a superconducting undulator at the ESRF," *Nucl. Instrum. Methods Phys. Res.*, vol. A541, pp. 630–65093, 2005.

[131] S. Casalbuoni, M. Hagelstein, B. Kostka, R. Rossmanith, E. Steffens, M. Weisser, A. Bernhard, D. Wollmann, and T. Baumbach, "Investigations of the thermal beam load of a superconducting in-vacuum undulator," in *Proceedings of the 10th European Particle Acclerator Conference*, (Edinburgh), pp. 3568–3570, June 2006.

[132] E. Justi and M. Kohler, "Über die elektrische leitfähigkeit der alkalimetalle im magnetfeld," *Annalen der Physik*, vol. 428, no. 3-4, pp. 349–356, 1939.

[133] A. B. Pippard, "The surface impedance of superconductors and normal metals at high frequencies. ii. The anomalous skin effect in normal metals," *Proc. R. Soc. London, Ser. A*, vol. 191, p. 385, 1947.

[134] D. J. Scott, "Surface roughness wakefields for the ILC positron undulator beam tube," Tech. Rep. EUROTeV-Report-2006-085, CCLRC, 2006.

[135] K. L. F. Bane and A. Novokhtaskii, "The Resonator Impedance Model of Surface Roughness Applied to the LCLS Parameters," Tech. Rep. LCLS-TN-99-1, SLAC, March 1999.

[136] K. L. F. Bane, C. Ng, and A. W. Chao, "Estimate of the Impedance Due to Wall Surface Roughness," Tech. Rep. SLAC-PUB-7514, SLAC, May 1997.

[137] S. S. Kurennoy, "Coupling impedance of pumping holes," *Part. Accel.*, vol. 39, p. 1, 1992.

[138] K. L. F. Bane and G. Stupakov, "Wake of a rough beam wall surface," Tech. Rep. SLAC-PUB-8023, SLAC, December 1998.

[139] G. Stupakov, R. Thompson, D. Walz, and R. Carr, "Effects of beam-tube roughness on x-ray free electron laser performance," *Phys. Rev. ST Accel. Beams*, vol. 2, June 1999.

[140] Swagelok Ltd. 29500 Solon Road, Solon, OH 44139, USA
http://www.swagelok.com.

[141] E. A. Avallone and T. Baumeister, *"Marks' Standard Handbook for Mechanical Engineers "*. London: McGraw-Hill Professional, 2006.

[142] A. Brummitt. Private communication.

[143] P. Tenenbaum, "Collimator wakefield calculations for the ILC-TRC report," Tech. Rep. LCC-Note-0101, SLAC, 2002.

[144] NLC Post-Linac Collimation Task Force, "New post-linac collimation system for the Next Linear Collider," Tech. Rep. LCC-Note LCC-0052, SLAC, 2001.

[145] P. Tenenbaum, K. L. F. Bane, L. Eriksson, J. Irwin, R. K. Jobe, D. McCormick, C. K. Ng, T. O. Raubenheimer, M. C. Ross, G. Stupakov, D. Walz, D. Onoprienko, and I. Zagorodnov, "Direct measurement of the transverse wakefields of tapered collimators," *Phys. Rev. ST Accel. Beams*, vol. 10, p. 034401, Mar 2007.

[146] C. Beard and R. Jones, "Numerical simulations of collimator insertions using MAFIA," Tech. Rep. EUROTeV-Report-2006-103, 2006.

[147] G. V. Stupakov, "High-frequency impedance of small-angle collimators," in *Proceedings of the 19th Particle Accelerator Conference*, (Chicago), pp. 1859–1861, June 2001.

[148] I. Zagorodnov, T. Weiland, and K. Bane, "Calculation of collimator wakefields," in *Proceedings of the 20th Particle Accelerator Conference*, (Portland), pp. 3252–3254, May 2003.

[149] I. Zagorodnov and K. Bane, "Wakefield calculations for 3D collimators," Tech. Rep. EUROTeV-Report-2006-074, 2006.

[150] N. Watson, D. Adey, M. Stockton, Y. Kolomensky, M. Slater, D. Angal-Kalinin, C. Beard, C. Densham, G. Ellwood, J.-L. Fernandez-Hernando, J. Greenhalgh, F. Jackson, J. ODell, F. Zimmermann, I. Zagorodnov, D. Burton, N. Shales, J. Smith, A. Sopczak, R. Tucker, R. Barlow, A. Bungau, R. Jones, A. M. G. Kurevlev, T. W. M. Karkkainen, W. Mueller, R. Arnold, C. H. R. Erickson, T. Markiewicz, S. Molloy, M. Ross, S. Seletskiy, A. Seryi, Z. Szalata, P. Tenenbaum, M. Woodley, and M. Woods, "Direct measurment of geometric and resistve wakefields in tapered collimators for the International Linear Collider," in *Proceedings of the 10th European Particle Acclerator Conference*, (Edinburgh), pp. 697–699, June 2006.

[151] H. Grote and F. C. Iselin, "The MAD Program (Methodical Accelerator Design), Version 8.l - User's Reference Manual," Tech. Rep. CERN-SL-90-14 (AP), CERN, May 1990.

[152] US Linear Collider Steering Group: Accelerator Sub-Commitee, US Linear Collider Technical Options Study, March 2004.

[153] I. Zagorodnov and T. Weiland, "TE/TM field solver for particle beam simulations without numerical Cherenkov radiation," *Phys. Rev. ST Accel. Beams*, vol. 8, p. 042001, April 2005.

[154] I. Zagorodnov and N. Solyak, "Wakefield effects of new ILC cavity shapes," in *Proceedings of the 10th European Particle Acclerator Conference*, (Edinburgh), pp. 2862–2864, June 2006.

[155] VALEX Co-orporation USA. 6080 Leland Street, Ventura, CA 93003, http://www.valex.com.

[156] A. Bungau and R. Barlow, "Large simulation of high order short range wakefields," in *Proceedings of the 10th European Particle Accelerator Conference*, (Edinburgh), pp. 2209–2211, June 2006.

[157] D. Barber. Private communication.